Universitat Politècnica de Catalunya
Electrical Engineering Department

Institut de Recerca en Energia de Catalunya
Catalonia Institute for Energy Research

PhD Thesis

Control of voltage source converters for distributed generation in microgrids

Author: **Jordi Pegueroles Queralt**

Advisors: **Fernando D. Bianchi**
Oriol Gomis Bellmunt

Barcelona, July 2015

Catalonia Institute for Energy Research (IREC)
Electrical Engineering Research Area
Jardins de les Dones de Negre 1 2nd floor,
08930 Sant Adrià de Besòs, Barcelona, Spain

Printed in Barcelona by Copiservei Poble Nou, S.L., in June 2015

UNIVERSITAT POLITÈCNICA DE CATALUNYA
BARCELONA**TECH**
Escola de Doctorat

Curs acadèmic:

Acta de qualificació de tesi doctoral

Nom i cognoms

Programa de doctorat

Unitat estructural responsable del programa

Resolució del Tribunal

Reunit el Tribunal designat a l'efecte, el doctorand / la doctoranda exposa el tema de la seva tesi doctoral titulada ____
____.

Acabada la lectura i després de donar resposta a les qüestions formulades pels membres titulars del tribunal, aquest atorga la qualificació:

☐ NO APTE ☐ APROVAT ☐ NOTABLE ☐ EXCEL·LENT

(Nom, cognoms i signatura) President/a	(Nom, cognoms i signatura) Secretari/ària

(Nom, cognoms i signatura) Vocal	(Nom, cognoms i signatura) Vocal	(Nom, cognoms i signatura) Vocal

______________________, _______ d'/de __________________ de _______________

El resultat de l'escrutini dels vots emesos pels membres titulars del tribunal, efectuat per l'Escola de Doctorat, a instància de la Comissió de Doctorat de la UPC, atorga la MENCIÓ CUM LAUDE:

☐ SÍ ☐ NO

(Nom, cognoms i signatura) President de la Comissió Permanent de l'Escola de Doctorat	(Nom, cognoms i signatura) Secretari de la Comissió Permanent de l'Escola de Doctorat

Barcelona, _______ d'/de ____________________ de _________

∀

Abstract

Microgrids are the near future candidate to reduce the dependence on the carbon-based generation, towards a more environmentally friendly and sustainable energy paradigm. The popularization of the use of renewable energy sources has fostered the development of better technologies for microgrids, particularly power electronics and storage systems. Following the improvements in microgrid technologies achieved in the last decade, a new challenge is being faced: the control and management of microgrids for its operation in islanded mode, in addition to its large scale integration into the current electrical power system.

The unregulated introduction of distributed generation based on renewable energy sources into the power system could cause as many problems as it would solve. The unpredictability of the generated power would introduce large disturbances into the electric system, making it difficult to control, and eventually resulting in an unstable system. To overcome these issues, the paradigm of microgrids has been proposed: a small power system, able to operate islanded from the main grid, which will permit the large scale introduction of renewable energy sources interfaced with power electronic converters together with energy storage systems into the distribution grids. Microgrids' ability to allow their users to operate islanded from the utility grid, brings the potential to offer a high quality of service. It is in the islanded operation mode, particularly in microgrids with a high proportion of renewable based generation, where the major technical challenges are found.

This thesis focuses in three of the main challenges of islanded and weak electrical grids: the power converter control of electrical storage systems, its decentralized control design, and also the improvement of power quality in grids disturbed by renewable generation. These topics are addressed from a control point of view, that is, to tackle the electrical problems, modelling them and proposing advanced control strategies to improve performance of microgrids.

Energy storage system are a vital element to permit the islanded operation of microgrids, either in the long or short term. New control strategies are proposed in this thesis for the improvement of the converters' performance. In addition to the control of the converter, the management and control of different energy storage systems for microgrids are also studied. In particular, supercapacitors and batteries have been considered for the short and long term operation, respectively.

Then, the control of islanded microgrids is addressed. Typical controls for islanded microgrids are analysed and new tools for designing stable controllers are proposed. Also, methodologies to analytically obtain the operating point (power flow) of droop controlled grids are studied and proposed.

The high penetration of renewable energy sources in weak low-voltage grids results in undesirable electrical disturbances. This problem in power quality is tackled and innovative solutions to mitigate it are proposed. In particular, a novel power smoothing scheme with simultaneous state of charge regulation of the ESS and power filtering.

The new power smoothing scheme, along with the proposed control strategies for storage systems have been experimentally validated in a laboratory test bench, using a supercapacitor bank and a high power lithium-ion battery available at IREC's facilities.

Resum

Les microxarxes són les candidates en un futur a curt termini, a substituir la generació basada en el carbó, de cara a assolir un sistema energètic més respectuós amb el medi ambient i més sostenible. La popularització de l'ús d'energies renovables ha fomentat la millora de les tecnologies per a microxarxes, en particular els sistemes d'emmagatzematge i l'electronica de potència. Desprès de les millores en tecnologies de microxarxes aconseguides durant l'última dècada, hi ha un nou repte al qual fer front: el control i gestió de microxarxes per la seva operació aïllada, a més de la integració a gran escala dins del sistema elèctric actual.

La introducció descontrolada de fonts de generació distribuides en el sistema elèctric pot causar tants problemes com els que podria sol·lucionar. La incertesa en la producció elèctrica pot introduir grans pertorbacions al sistema elèctric, fent-lo difícil de controlar, i fins i tot el pot arribar a inestabilitzar. Per tal de fer front a aquestes dificultats, es proposa el paradigma de microxarxa: un petit sistema elèctric capaç d'operar de forma aïlla de la xarxa de distribució elèctrica, el qual hauria de permetre la integració a gran escala d'energies renovables a través de l'electrònica de potència, juntament amb sistemes d'emmagatzematge d'energia, dins de les xarxes de distribució. Les microxarxes permeten als seus usuaris a funcionar aillats de la xarxa elèctrica, donant la possibilitat d'oferir una alta qualitat de servei. És en el mode de funcionament aïllat, particularment en microxarxes amb una altra

proporció de generació basada en renovables, on es troben la major part de reptes tecnològics.

Aquesta tesi es centra en tres d'aquests reptes de les xarxes aillades i dèbils: el disseny del control per a convertidors de potència per a sistemes d'emmagatzematge elèctric, el control descentralitzat de les microxarxes i també la millora en la qualitat de subministre elèctric en xarxes afectades per generació renovable. Aquestes temes es tracten des d'el punt de vista de la teoria de control de sistemes, això significa, abordar el problema elèctric, modelar-lo, i proposar estrategies de control avançades per millorar el funcionament de les microxarxes.

Els sistemes d'emmagatzematge són un element vital per permetre l'operació aïllada de les microxarxes, tant a llarg com a curt termini. En aquesta tesi es proposen noves estratègies de control per millorar el funcionament dels convertidors d'electrònica de potència. A més del control del convertidor, també s'estudia la gestió i control de diferents sistemes d'emmagatzematge d'energia per a microxarxes. En particular, supercondensador i bateries s'han considerat per l'operació a curt i llarg termini respectivament.

Seguidament, s'enfila el control de microxarxes aïllades. S'analitzen els controls típics per a microxarxes i es proposen noves eines de disseny que permeten garantitzar l'estabilitat. A més a més, metodologies per a obtenir el punt d'operació (el flux de potènica) per a xarxes amb control tipus *droop* també s'estudien i proposen.

L'alta penetració de fonts d'energia renovables en xarxes de baixa tensió i febles resulta en pertorbacions elèctriques indesitjables. Aquesta problematica en la qualitat de subministrament s'aborda i es proposen solucions inovadores per mitigar els efectes negatius. En particular, s'ha proposat un nou sistema de suavitzat de potència que regula simltaneament l'estat de càrrega del sistema d'emmagatzematge i filtra la potencia fluctuant.

El nou esquema de suavitzat de potència, juntament amb les estrategies proposades per als sistemes d'emmagatzematge elèctric s'han validat experimentalment en un banc de laboratori, emprant superconsadors i una bateria d'alta potència, disponibles a les instal · lacions de l'IREC.

Acknowledgements

This thesis has been supported by Catalonia Institute for Energy Research (IREC), and the research leading to these results has received funding from the European Union seventh framework program FP7-SMARTCITIES-2013 under grant aggreement 608860 in the project IDE4L and from the European Regional Development (ERDF, “FEDER Programa Competitivitat de Catalunya 2007-2013”).

First of all, I would like to express my sincere gratitude to my advisors Dr. Fernando D. Bianchi and Prof. Dr. Oriol Gomis Bellmunt for the supervision, guidance and support they gave me, as well as, for their always useful scientific and personal advices throughout this thesis. Also I would like say thank you to all my current and past colleagues from IREC for their help and friendship. Specially, I am extremely grateful to David, Francisco, José Luis, Lázaro, Lluís, Mikel and Ramon for their invaluable support at all times and their always helpfulness, patience and friendship as well. Likewise, I would like to show my thankfulness to the people of the University of Manchester by graciously welcoming me during my research stay there and for giving me the opportunity to live a great experience. Specially, I greatly appreciated the help of Prof. Dr. Mike Barnes and Dr. Antony Beddard.

Last but not least, I would like to thank my family for their continuous support and for giving me the encouragement whenever I needed it. I would like to express my sincere gratitude to my parents and sister, for their advice. My deepest gratitude is to my girlfriend Maria, who has been by my side throughout this long and intense adventure.

Contents

List of Tables

List of Figures

Acronyms

DER	distributed energy resource.
DG	distributed generation.
DG$_c$	controllable distributed generation.
DG$_{uc}$	uncontrollable distributed generation.
EMS	energy management system.
ESD	energy storage device.
ESS	energy storage system.
ESSC	energy storage side converter.
GSC	grid side converter.
IGBT	insulated gate bipolar transistor.
IS	interconnection switch.
LPF	low pass filter.
LQG	linear-quadratic-Gaussian.
LV	low voltage.

MG microgrid.

MGCC microgrid central controller.

MPPT maximum power point tracking.

PCC point of common coupling.

PI proportional-integral.

PLL phase-locked loop.

PV photo-voltaic.

PWM pulse width modulation.

RES renewable energy source.

RMS root mean square.

RSC renewable energy source side converter.

SG synchronous generator.

SM sliding mode.

SVM space vector modulation.

VSC voltage source converter.

VSS variable structures system.

Nomenclature

$\check{V}_k(t)$	Dynamic phasor with identifier k
$\frac{d}{dt}$	Derivative operator
$\jmath$	Imaginary unit, $\jmath = \sqrt{-1}$
$\mathcal{T}$	Park transformation matrix
ω	Electrical frequency [rad/s]
ϕ	Electrical angle of an AC voltage
f	Electrical frequency [Hz]
I_{DC}	DC current injected to the DC-link
P	Active power [W]
Q	Reactive power [Var]
V_{ESD}	Energy storage device DC voltage
V_{DC}	DC link voltage

1

Introduction

This chapter is a general overview of the research done during the PhD and exposes the motivation, contributions and works related with this thesis.

1.1. Overview

Global concern about sustainability, environmental impact of traditional centralized power generation and the increase of energy demand are driving governments and institutions towards a modernization of power systems. Initiatives like the *20-20-20 objective* [16], impulsed by the European Union, are favouring the introduction of renewable energy sources (RESs) at a large scale. This is, the 20 % of the electrical production share should be based on RES. Moreover distribution networks in many member states of the European Union are getting old and overloaded [39]. To avoid the stress of the current distribution systems and to foster the integration of RESs, a new paradigm has been proposed: the microgrid (MG). A MG can be conceived as a small electrical power system, composed by generation, storage and loads, with the capacity to operate islanded from the utility power grid.

Before the MG concept appeared, many researchers were in pursuit of the integration of distributed generation (DG) based on RES [12, 76]. The scientific community realized that the unregulated introduction of DG based on RES would cause as many problems as it would solve. The unpredictability on the generated power from renewable sources would introduce large disturbances into the electric system, making it difficult to control, and eventually resulting in an unstable system. Microgrids will permit the large scale integration of RES into the electrical distribution system without major disturbances. Moreover, the improvement in electrical energy storage technologies achieved in the last decade, along with the exponential increase in the ratings of power electronic devices, have permitted microgrids to become a feasible solution [123].

Microgrids are controllable power systems with the capability to exchange power with the utility grid according to its operator commands. Three different operation objectives for MG can be identified:

- Microgrid as a power generator. The power produced inside the microgrid is larger than its demand, so it injects its surplus power to the distribution grid.

- Microgrid as a load. The microgrid has less generated power, eventually no generation, than its electrical demand, such that the microgrid consumes power from the utility grid.

- Microgrid as a neutral system. The microgrid is self-sufficient, maintaining a zero net power balance with the utility grid. In this state, it can be differentiated two different operating modes:

- Islanded mode, where the microgrid is electrically isolated from the utility grid [142].
- Connected mode, the microgrid is electrically attached to the utility grid, but without any power exchange [35].

Microgrids allow the production of power from different RESs and maintain the electrical stability with its integrated energy storage systems (ESSs) [115]. Moreover, microgrids can also improve the quality of service in terms of downtime and power quality. All in all, MG potential has aroused the interest of researchers and also industry leaders, which has been continuously increasing for the last decade. This can be observed in Table 1.1, where some relevant projects are listed. In addition to the research projects, different industrial projects are being planned and executed. MG is currently an active topic; much effort is being dedicated to the research of many aspects, from optimal power flow algorithms to advanced control strategies to ensure electrical stability.

Project name	Budget	duration	Promoter	ref.
CERTS	12.2 M USD	from 1999	US	[31]
Microgrids	4.5 M€	2003 to 2006	EU	[37]
More Microgrids	8 M€	2006 to 2010	EU	[38]
IDE4L	8 M€	2013 to 2016	EU	[39]
Microgrid - Alstom	1.2 M USD	from 2014	US	[5]
Positas Microgrid	1.5 M USD	from 2015	US	[83]

Table 1.1.: Some relevant research projects related with microgrids.

Many of these developments are being implemented in test beds spread across the world: an example of some research centres and countries with active research are: INESC[1] in Europe, CERTS[2] in U.S., NEDO[3] in Japan, Canada and India [2, 105, 116]. Some of these test beds and research projects are a reality thanks to the funding provided by governmental agencies. For example, the European Commission has dedicated 5.9 € billion for the Horizon 2020 program [36], for the years 2014 to

---

[1] The Institute for Systems and Computer Engineering of Porto

[2] Consortium for Electric Reliability Technology Solutions

[3] New Energy and Industrial Technology Development Organization

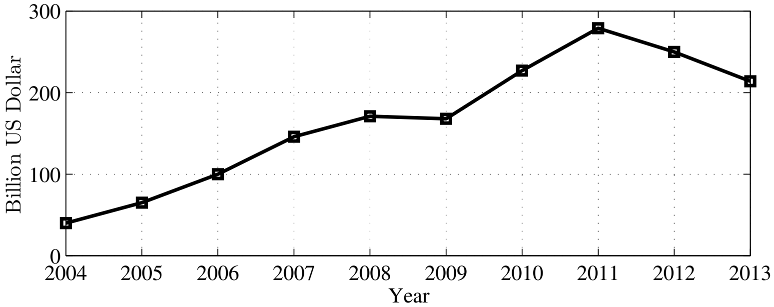

Figure 1.1.: Global new investment in RES, 2004–2013 [139].

2020, in its section dedicated to secure, clean and efficient Energy. Another example is the Department of Energy from the United States of America, which in the fiscal year 2012 has dedicated 6.3 billion USD for clean energy research [79], development, demonstration, and deployment activities.

Figure 1.1 shows the global investment in RESs related projects. This data is collected from [139] Frankfurt School–UNEP Collaborating Centre for Climate & Sustainable Energy Finance and Bloomberg New Energy Finance, Global Trends in Renewable Energy Investment 2014, the sister publication to the Global Status Report. The following renewable energy projects are included: all biomass, geothermal, and wind generation projects of more than 1 MW; all hydro projects of between 1 and 50 MW; all solar power projects, with those less than 1 MW estimated separately and referred to as small-scale projects or small distributed capacity; all ocean energy projects; and all biofuel projects with an annual production capacity of 1 million litres or more. Investment in large hydropower (>50 MW) is not included in the overall total for investment in renewable energy.

1.2. A brief research motivation for microgrids in power systems and contributions

This thesis considers MGs with its generation based on DG with RES. Each DG is interfaced with the electrical network by a power electronics converter. An electrical power system dominated by power electronic interfaces has a very low mechanical inertia associated with the electrical frequency, in contrast with classical power systems composed by large synchronous generators. In addition, compared with traditional power systems, power electronics based MGs permits the implementation of new control strategies to define the electrical behaviour. This implies that the response in the electrical variables, voltage magnitude and frequency, of such systems in front of disturbances are shaped mainly by the control strategy and tuning of its controllers. As a consequence, power electronics converters allow control engineers to propose advanced control strategies to improve the performance and stability margins of the system. This is at the same time an opportunity, but also a responsibility: the robustness and reliability of microgrids depends principally of the control scheme and tuning.

Main contributions contained in this thesis

The objective of this thesis is to investigate advanced control solutions aligned with the three main goals: 1) ESS control and management, 2) design for decentralized microgrid control and 3) power quality improvement. Following there is a list with the main contributions presented in this thesis.

- The proposal of new control strategies for ESS based on lithium-ion batteries and supercapacitors. ESSs are critical elements in an islanded microgrid and requires robust controllers to deal with the intrinsic uncertainties present in microgrids.

- A new a power smoothing strategy using supercapacitor based ESS for weak grids. A low complexity controller is proposed to guarantee a user defined mean state of charge while at the same time attenuates the power oscillations generated by the RES.

- The improvement in the DC–link of power converters voltage transient response by reducing the overshot. To achieve this improvement, it has been proposed to use a reset control scheme in combination with classical linear controllers.

- Design of decentralized controllers for islanded microgrids. New design methodologies for tuning decentralized controllers are proposed. A methodology models the microgrid as an aggregated of subsystems and imposes bounds on their interconnections to guarantee stability and ensure robustness against uncertainties.

- Development of a formulation to obtain the steady state operating point of an islanded grids. The methodology is based on the Newthon-Rhapson method, extended to obtain the equilibrium frequency and the power exchanged by the DG.

The models and simulations performed throughout this thesis has been developed using the commercial software MATLAB/Simulink. To demonstrate the applicability of the proposed control strategies, some of these contributions have been experimentally validated in a laboratory test bench, with especial relevance the development of two energy storage systems for microgrids.

1.3. Scope of the thesis

The MG concept involves not only electrical, but also a wide range of aspects, such as power system regulation, economical analysis and new business models, environmental impact, cyber-security and social interactions among others. In this thesis, the study of microgrids is oriented to the electrical and control engineering, and in particular, to the study and proposal of advanced control strategies for microgrids. Throughout this thesis, the following assumptions have been made:

- The microgrid is assumed to managed by an energy management system (EMS), sending power set-points to individual DG. The design of the EMS is out of the scope of this thesis.
- Every DG considered in this thesis is connected to a low voltage grid using power electronic converters, modelled as two level voltage source converter (VSC) with ideal switches.
- In different applications, such as EMS for microgrids or power smoothing with remote measurement of generated power, communications are required. Such communications among devices are always assumed to be ideal: there is no information loss, and no delay in the data transfer.
- The electrical protection system for microgrids is itself another wide research topic. The lack of fault current (typically fault current is provided by electromechanical generators) in power electronic feed networks imposes the necessity of redesign the protection devices. The protection system has been taken into account, although its design and operation is out of the scope.

1.4. Thesis outline

The first to third chapters present some background material about MGs. The main contributions of the thesis can be found in the next chapters. The last chapter draws some concluding remarks and lists some future research lines. The summary of the chapters follows.

- Chapter 2 exposes the concept of microgrid and presents the devices and systems, such as microgrid management systems and storage systems.

- Chapter 3 exposes the microgrid modelling, problem formulation and electrical notation used throughout this thesis. Then, the current state of the art in the control of islanded microgrids is reviewed.

- Chapter 4 presents the development of a control scheme based on sliding mode control for supercapacitors. The controller is used to regulate the DC current flowing from the battery to the DC–link.

- Chapter 5 presents a DC–link voltage controller to be used in combination with the low level sliding mode current controller. The voltage is regulated from the battery side converter, permitting the implementation of droop control in the microgrid side converter.

- Chapter 6 presents a power smoothing strategy using the energy storage system based on supercapacitors presented in Chapter 4. The power smoothing strategy is applied for the attenuation of flicker in low voltage weak grids.

- Chapter 7 presents the voltage control of the DC-link for back-to-back power converters using a PI control structure with reset to improve transient performance.

- Chapter 8 presents a new design methodology using decentralized control techniques for an improved droop control scheme. The design methodology produces controllers ensuring the stability of the microgrid, requiring only partial information of the microgrid.

- Chapter 9 presents a new methodology to compute the steady state operation point of of islanded grids with droop control, obtaining the equilibrium frequency and power flow.

1.5. PhD related work and activities

This section is an overview of activities related with this thesis, including some industrial and European research projects. The project Charge & Ride involved the development of advanced control strategies for power electronics converters for the DC railway system. This work has been related with the research and development of new control strategies for ESS; the aim is to investigate the control and management of supercapacitors and Li-ion batteries for its inclusion in microgrids. Associated with the ESS research, publications [J1,J2], [C2], listed in Appendix A, were published. The project KIC-SMART-POWER was related with the study of power smoothing techniques, resulting in the publication [J3]. In addition to ESS studies, a more general control for power converters was investigated in collaboration with the ESAII department of the UPC, focusing on the field of repetitive and reset control, which resulted in the publication [J4].

Then, the research continued focusing on the droop control of islanded grids, resulting in publications [J5,J6] and [C1]. Moreover, widening the focus of the research topics related with the thesis, in collaboration with other research lines of the electric and electronic engineering department in IREC, the paper [O1] was written. Then, from August 2014 to November 2014 took place a research stay in the power conversion group, from the school of Electrical and Electronic Engineering, lead by the professor Mike Barnes, in the University of Manchester. During this research stay, the advanced control strategies for islanded grids had been applied to islanded AC grids including large wind farms. Currently, more practical aspects of microgrids are being investigated, collaborating with the FP-7 project *IDE4L grid for all.*

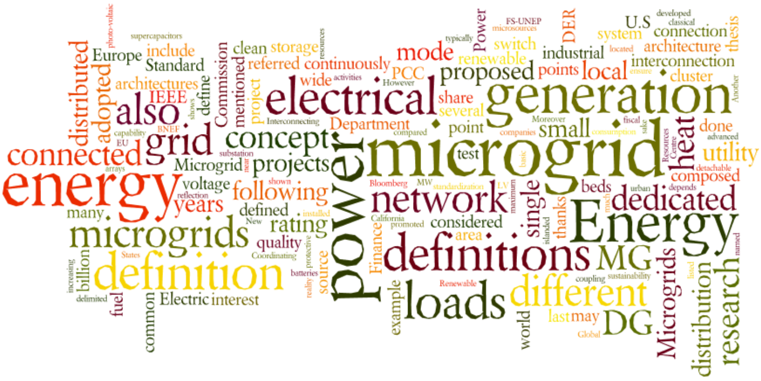

2

Microgrids

In this chapter, some useful concepts to define and understand the operation of microgrids are briefly reviewed. The concepts include a discussion on the formal microgrid definition, its architecture and management scheme. In addition, the final section provides a short review on the storage technologies candidates for its integration in microgrids.

2.1. Microgrid definition

As shown previously, microgrids have been world wide adopted, probably thanks to the simplicity of its concept. However, despite the wide acceptance of the concept, the lack of standardization has led to different interpretations of microgrids in practice. Several formal definitions for microgrids has been proposed in the literature in the recent years. However, the idea behind the concept of microgrid was already present in the literature, some times referred to as autonomous power systems [46, 78]. Since the 2000 decade, no formal definition was proposed; one of the earlier definitions of microgrids was proposed by Lasseter [101] as:

> Microgrid concept assumes a cluster of loads and microsources operating as a single controllable system that provides both power and heat to its local area.

This definition was also adopted by CERTS and used in different projects promoted by the U.S. Department of Energy (DOE) and by the California Energy Commission. In Europe, the first publications concerning microgrids first appeared related with the EU R&D Microgrids project, proposing the following definition by Peças Lopes et al. [124]:

> A microgrid can be defined as a low voltage (LV) network (*e.g.*, a small urban area, a shopping center, or an industrial park) plus its loads and several small modular generation systems connected to it, providing both power and heat to local loads, combined heat and power (CHP).

Other definitions of microgrid has been proposed by industrial companies, such as Siemens [152], whose vision of a microgrid is:

> A microgrid is a regionally limited energy system of distributed energy resources, consumers and optionally storage. It optimizes one or many of the following: Power quality and reliability, sustainability and economic benefits and it may continuously run in off-grid- or on-grid mode, as well as in dual mode by changing the grid connection status.

These three previous definitions and other proposals for microgrids share several common points, such as the idea to combine electrical generation and demand in a small power system connected to electrical distribution system. However, there are some ambiguous terms in microgrid definitions. For instance, in some definitions, the voltage rating is defined, whereas in some others is not mentioned. The same is true for the geographical location, power ratings (a microgrid is not necessarily “small”) and heat generation to list some ambiguous points. On top of them it is the capability of being operated in the islanded mode; in some definitions is not even mentioned. For the sake of conciseness, the following definition of a microgrid has been adopted throughout the thesis:

> A microgrid is a LV electrical network, geographically delimited, composed by a cluster of loads and distributed generation located downstream of the primary distribution grid substation which can operate connected or disconnected from distribution networks.

This definition is suitable for the microgrid test facilities at IREC. See [C3] for more details on this definition.

2.2. Microgrid architecture

In 2008 the Standard 1547, IEEE Standard for Interconnecting Distributed Resources with Electric Power Systems [81] was published. This document exposes the issues and regulation aspects regarding the interconnection of distributed energy resource (DER) with the utility grid, but does not define an architecture for MG. It also states that the installed power generation capacity should not exceed the 10 MW to be considered a microgrid. In the literature there are different architectures proposed for microgrids, see *e.g.* [53, 66]. Most of them, share some basic characteristics:

- MGs are connected to the utility grid in a single electrical connection point, referred to as the point of common coupling (PCC).
- MGs are detachable from the utility grid, typically by a single protective switch. This device will be referred as a the interconnection switch (IS) in this thesis.
- Most DGs are interfaced with power electronic converters.
- Energy storage systems are also commonly considered, to permit a predictable operation of the MG.
- Typically, MGs are managed using a central controller.

To illustrate such characteristics, two topologies for MGs are revised in the following paragraphs. The architecture shown in Figure 2.1 corresponds to the MG concept proposed by Lasseter [101]. The electrical system is radial with several feeders with loads and DG connected to them. Each feeder has an associated power flow controller, and all the controllers are managed centrally by the energy manager. The radial system is connected to the distribution system through an IS, in this case a static switch, at the PCC. This topology has been adopted by numerous authors, see *e.g.* [88] and the references therein.

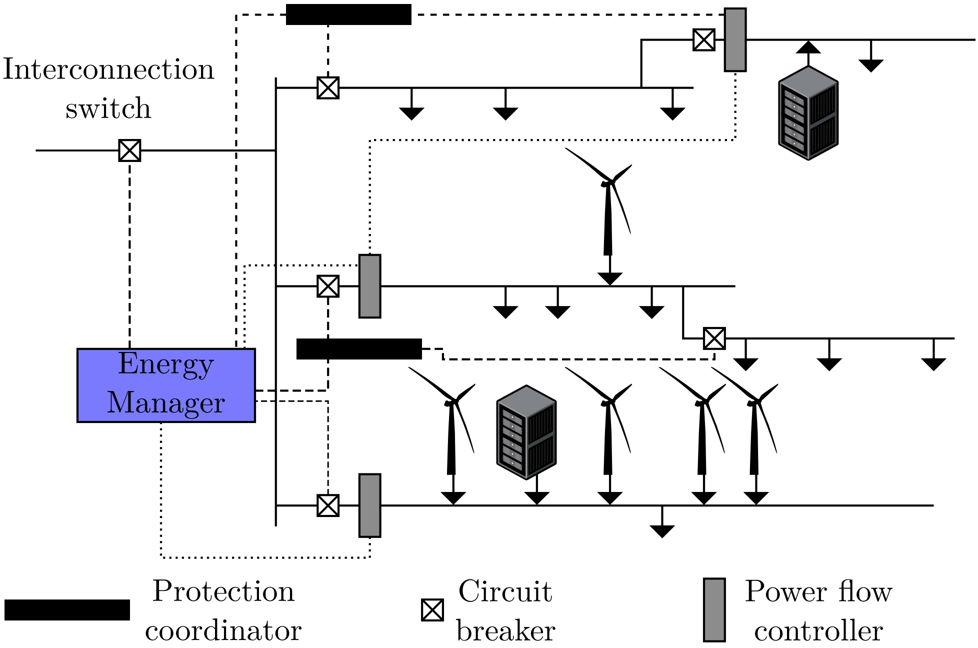

Figure 2.1.: Illustration of the microgrid architecture proposed by CERTS Microgrid project [101].

The european R&D Microgrid project [124] proposed another, though similar, MG concept, with its architecture shown in Figure 2.2. It is composed by a low voltage network, loads (some of them critical), both controllable and non-controllable DG, storage devices, and a hierarchical-type management and control scheme.

These two topologies are the ones followed in this thesis for the proposal of control strategies for energy storage systems and for the design of decentralized stabilizing controllers. The reader will find in the following sections more details on the particular topology adopted throughout the thesis.

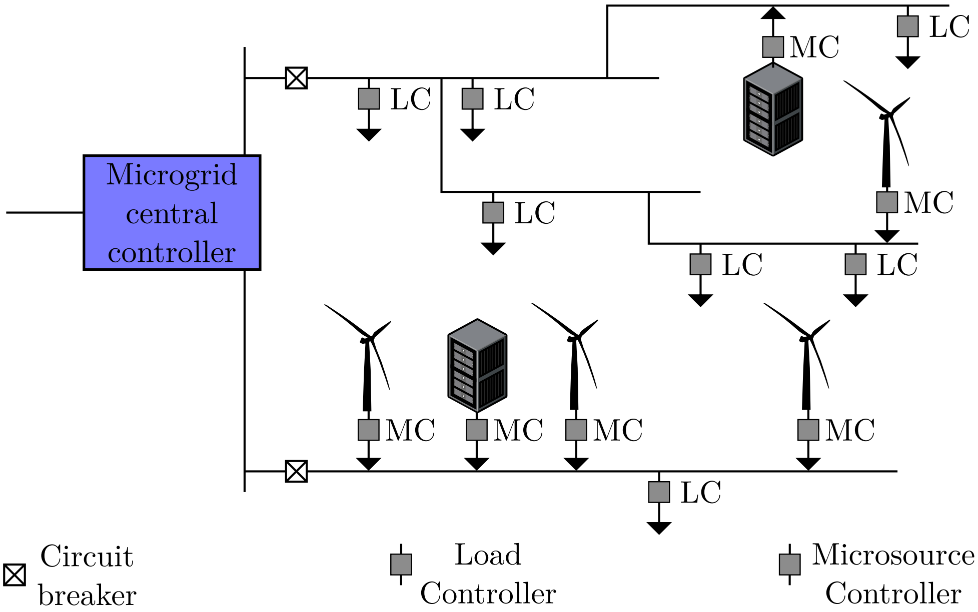

Figure 2.2.: Illustration of the microgrid architecture proposed by EU R&D microgrid project [124].

2.3. Microgrid management

A microgrid is a small electrical power system integrating a high percentage of RES based generation with the capability to control its power exchange with the utility grid. It includes ESS to compensate the variability in power generation of RES in order to permit the regulation of the power flow at the PCC. Moreover, MG operator may define different operation objectives, such as minimization of generation cost, reduction of peak load or reduction in CO_2 emissions. Additionally, a MG might disconnect from the utility grid, becoming an autonomous power system. In islanded mode, a microgrid must not only be able to control the power sharing among generators, but also guarantee the electrical stability of islanded the power system.

The control of microgrids involves a wide range of control levels, from the control of a single power electronic converter, passing through the coordination and planning of the electrical production of an entire microgrid, to the management of a multi-microgrid distribution network. Typically, microgrids are controlled in a hierarchical manner, with two clearly differentiated control levels: *field control level* and *management control level*. Figure 2.3 shows graphically the MG adopted hierarchical control, where can be easily identified the two control levels. This hierarchical control characterization has been adopted by many researchers, see *e.g.* [72, 118, 130, 141].

At the lowest hierarchical level, there is the field control level, also referred to as the primary control. This level is the main focus of this thesis, since most of the contributions are made for this control level. It will be comprehensively treated in the forthcoming chapters. The field control level is responsible for the short term regulation of the microgrid, matching power demand with generation by regulating voltage and frequency, and thus, guaranteeing a stable operation. This primary control is implemented at the the local controllers located at each DG. Local controllers implement the primary control without the need of communication links, thus achieving a decentralized solution for the electrical stabilization of the microgrid, either for grid connected mode and for the

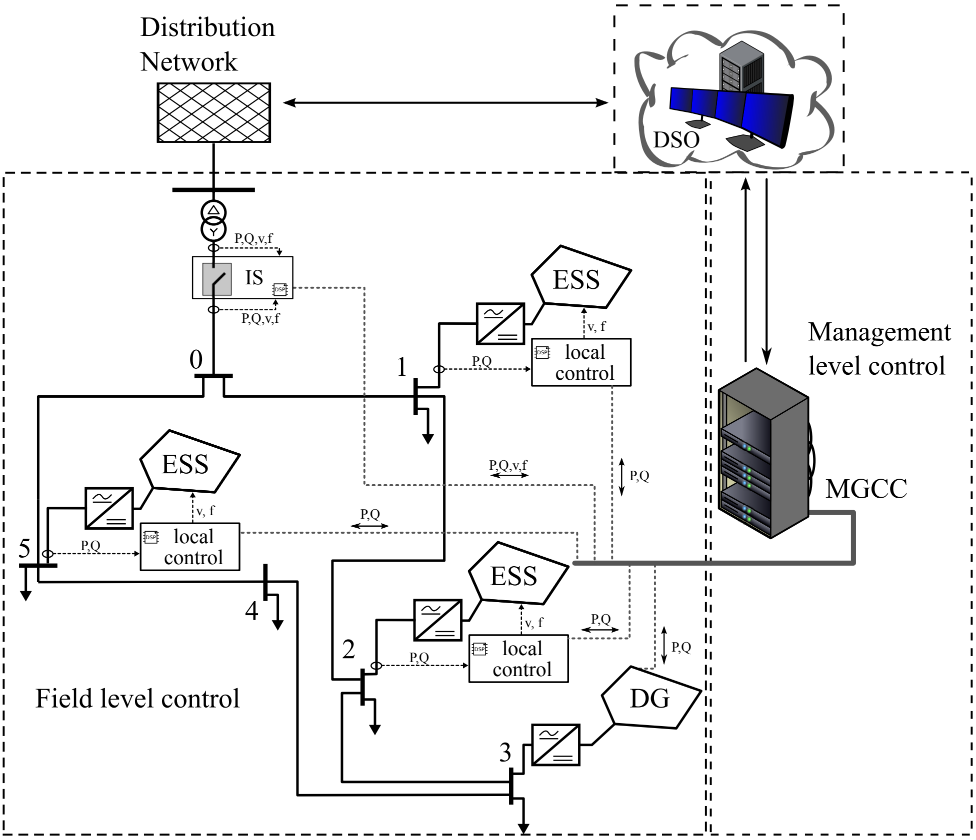

Figure 2.3.: Illustration of the hierarchical control scheme for microgrids adopted throughout this thesis.

islanded mode of operation. However, to achieve an optimal operation of the microgrid, the management control levels is required, and with it, a communication system to link it to the field control level.

Management control level is responsible for the optimal energy dispatching among the different microgrid DG and also the power exchange with the distribution grid in accordance with third parties such as the distribution system operator (DSO) or other commercial agents. The optimization objective depends on the operating state of the microgrid (grid connected or islanded), and other microgrid operator preferences (cost minimization, emission reduction or peak shaving). In order to ensure the joint and optimal operation of all microgrid's components, a possible strategy is to implement the management control level is using a centralized control, commonly located at the microgrid central controller (MGCC) [77]. The management control level can be implemented using an optimal EMS, covering the mid-term decisions in real-time and also providing ancillary services such as monitoring or resynchronization with the distribution grid after an islanding period.

In this thesis, the MG hierarchical control adopted is derived from the electrical dispatching standards found in the literature, to provide smartness and flexibility to MG. The hierarchical control adopted can be divided into the following categories [126].

1. The field control level, located at the local controllers of each DG unit. This local controllers typically regulates the power generation of each unit, ensuring the electrical stability of the microgrid.

2. The management control level, dedicated to the optimization of the power flow in the microgrid

An EMS can be implemented in many different forms. In the following subsection, the EMS adopted in throughout this thesis is described. This EMS is based on three different optimization algorithms dedicated to achieve the objective selected by the MG operator. The field level control is extensively treated in the rest of the chapters.

2.3.1. Energy Management System for IREC microgrid

The adopted optimal EMS is divided into three parallel layers, each layer including an optimization algorithm with different time horizon. On the long-term, we have the tertiary energy management, which is in charge of computing the optimal energy schedule for all microgrid's

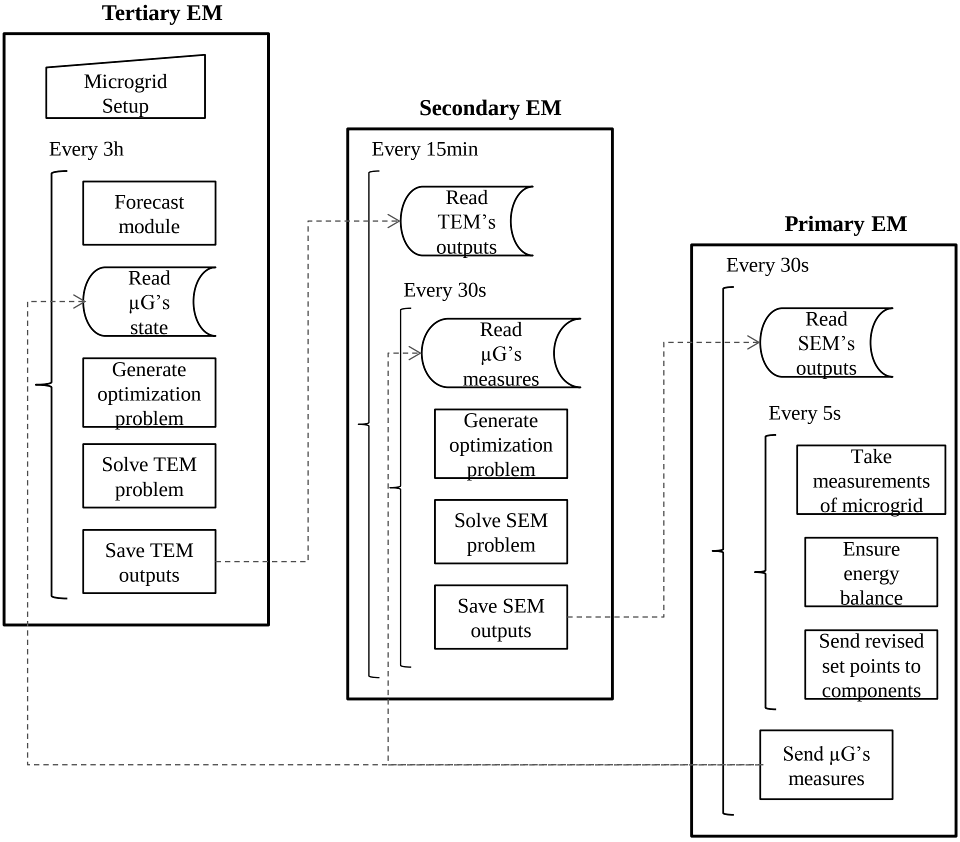

Figure 2.4.: Sketch of an implementation of an energy management system, combining three different optimization problems.

components. In the following layer, the secondary energy management updates the optimal energy schedule taking into account measurements and considering shorter time intervals than the previous layer. The shortest-term layer, updating in real time, typically every 5 seconds, is the Primary Energy Management (PEM), which calculates the necessary power set-points for each DG to achieve an energy balance inside the microgrid. In order to better visualize the EMS structure, Figure 2.4 shows the main algorithms in each layer and their interactions with each other. It is assumed that all loads are equipped with smart measurement units capable of informing the MGCC about the actual demand in real-time.

Tertiary energy management

The main role of tertiary energy management is to solve an optimization problem based on an unit commitment problem, with a 24 hours horizon divided in quarter-hourly intervals (since in most of European countries generation group deviations are calculated on a 15 min basis). The goal of the decision-making problem is to improve the profitability of the supply and the demand balance by minimizing a singular user selectable goal, such as:

- The economic cost.
- The CO_2 emissions.
- The peak load.

To achieve the selected user objective, the system takes advantage of the differences between on-peak and off-peak periods during a day and maximizes the use of renewable energy sources while satisfying several operational constraints. Daily forecasts regarding weather, demand and mobility profiles are used as inputs together with the energy price offered by the energy retailer or generation mix. The optimal energy schedule computed by tertiary energy management for each quarter hour interval within the optimization horizon provides details concerning the operational state and the power amounts generated or consumed for each controllable device of the microgrid [82].

Secondary energy management

Secondary energy management runs every 15 minutes with time periods of 30 seconds. This second layer is in charge of minimizing deviations from tertiary energy management program as far as possible, taking into account actual measurements. For doing so, secondary energy management solves an optimal economic dispatching problem using a cascade procedure with 30 coupled stages within every quarter hour. The inputs for each stage are the computed information by the tertiary energy management and the new measurements taken at the beginning of each stage (weather data and monitored devices' state). The results obtained in each stage are sent to PEM as inputs for the next 30 seconds.

Primary Energy management

The last layer is the PEM and is executed every 5 seconds. Its objective is to ensure balance between generation set-points and demand against any unexpected disturbance. Thus, PEM algorithm indirectly restores voltage and frequency deviations produced by the primary control. Every half a minute, PEM receives the preliminary set-points for each controllable unit computed by the secondary energy management. Moreover, the actual measurements of weather, consumption and state of charge, are taken every 5 seconds. Combining the actual measurements and the preliminary set-points through energy balance equations, the algorithm calculates the surplus power or generation lack. If there is any deviation in the energy balance, PEM carries out an adjustment over the preliminary set-points until the energy balance is achieved. The adjustments are made depending on a list of user's preferences. For instance, if there is an energy surplus, the user should decide whether the surplus is stored or returned to the grid, or the renewable power generation is reduced. Once the set-points ensuring energy balance are computed, PEM is in charge to send new set-points to each DG field controller in the microgrid.

2.4. Storage Devices

A key technology to enable the development of microgrids are the ESSs. Typically, ESSs are the power sources used to implement the grid forming units in a MG. Adding ESSs to a MG with a proper control strategy would have similar effects to the increase of the mechanical inertia in traditional power systems, increasing the robustness of the electrical system, making it less sensitive to disturbances, such as changes in the loading conditions or changes in the electric energy production due to atmospheric variability.

There are many possible technologies to implement an ESS: batteries, flywheels, supeconducting magnetic energy storage, supercapacitors and others [49]. Despite of the wide spectrum of available technologies, none of these technologies offer a clear advantage over the others. Nevertheless, many of these technologies could complement each other in many different applications. For instance, to provide the power and storage capabilities required by the MG with islanding capacity, a combination of short term and long term storage systems is commonly adopted [62].

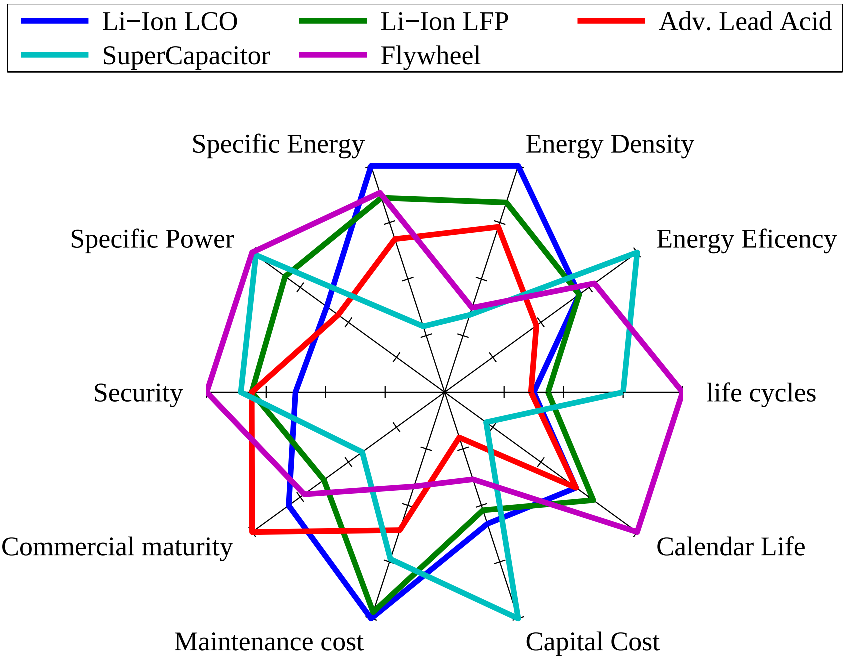

Figure 2.5.: Normalized radar chart comparing the main ESS used in microgrids [49, 80, 136, 156].

To evaluate the potential of each technology, the main storage technologies for MG have been compared taking into account nine different parameters. The following list describes these parameters.

1. Specific Power [W/kg] describes the power per mass unit.
2. Specific Energy [Wh/kg] describes the energy per mass unit.
3. Energy density [Wh/m] indicates the energy per volume unit.
4. Energy efficiency [%] shows the relation between the discharged energy and the amount of energy needed to restore the initial charge state, under specific conditions. It is measured in a percentage.
5. Life cycles [cycles] determines the quantity of consecutive charge and discharge processes that a ESS can undergo while maintaining minimum performance.

6. Calendar life [time] determines the period of time in which the ESS maintains minimum performance without being used.
7. Capital cost [€/Wh] indicates the cost of deploying the ESS.
8. Maintenance cost [€/Wh] indicates the cost of maintenance of the ESS in order to ensure performance.
9. Commercial maturity indicates the period of time in which the technology has been in use and the development experienced in that period.
10. Security represents the safe operation range of the ESS.

Based on the available literature and taking into account the previous parameters, five different technologies have been compared: two li-ion batteries, lithium cobalt oxide ($LiCoO_2$) and Lithium iron phosphate ($LiFePO_4$) based batteries, advanced lead acid batteries, supercapacitor and flywheel [49, 136]. In Figure 2.5 it is shown a comparative chart for the five technology candidates for its integration in MG. Each parameter set has been normalized in order to offer a qualitative comparison among technologies. The comparison revealed that none of the available technologies for ESS offers a clear advantage over the others. However, the comparative led to naturally divide stationary ESS applications into two broad categories:

- *Energy applications* such as power balancing in islanded MG.
- *Power applications* such as power quality.

On the one hand, energy applications involve the charge or discharge of the ESS for periods of hours. On the other hand, power applications involve relatively short periods of discharge (seconds to minutes), short recharging periods, and often require many cycles per day. For these applications, energy storage capacity, power output and lifetime (cycle and calendar) are key performance criteria. Based on this criteria, in this thesis, Li-ion batteries have been considered for energy applications, whereas supercapacitors have been selected for power applications. These ESSs have been considered since they have the potential contribute very positively to the development of microgrids, and in particular to improve the islanded operation. The following section provides a short description of the selected technologies and its relation with this thesis.

2.4.1. Lithium-Ion batteries

In the last decade, the lithium-ion battery technology has imposed itself as the *de facto* technology for portable devices, and is the main technology candidate for the implementation of electric-vehicle and renewable energy applications [156]. The use of Li-ion batteries in stationary energy storage system applications to complement the RES, like photovoltaics and wind energy sources, presents a great interest. The main roles this type of ESS technology used for stationary applications, are identified in the following list [151, 169].

- Increase the grid penetration levels of RES.
- Enable the islanded operation of MG by balancing power generation and load demand.
- Contribute to upward and downward frequency regulation enabling ancillary services for grid connected MG.
- Improve the power quality and reliability of the MG.

In particular, in Chapter 5, a Li-ion battery is used as the storage technology selected to implement an energy storage system for its operation in islanded microgrids. Technical details on the actual battery are briefly described in Appendix D.

2.4.2. Electric double-layer capacitor

An electric double-layer capacitor (EDLC), also known as supercapacitor, supercondenser, electrochemical double layer capacitor, or ultracapacitor, is an electrochemical capacitor with relatively high energy density. Their energy density is typically hundreds of times greater than conventional electrolytic capacitors. A typical D-cell-sized conventional electrolytic capacitor may have capacitance of up to tens of millifarads. The same size EDLC might reach several farads, an improvement of two orders of magnitude. As of 2011 EDLCs had a maximum working voltage of a few volts (standard electrolytics can work at hundreds of volts) and capacities of up to 5 kF. In 2010 the highest available EDLC specific energy was 30 Wh/kg. Up to 85 Wh/kg has been achieved at room temperature in laboratory environment, with the graphene supercapacitor storage record achieved on the 13^{th} of September 2011. This capacity is still lower than rapid-charging lithium-titanate batteries. As of 2012 commercially available EDLCs typically have mass-to-volume ratio between 0.33 and 3.89 kg/l.

As a promising emerging storage technology, it has attracted the attention of many researchers. An example of some applications on power quality improvement for supercapacitors are, for instance, the use of this storage technology to improve the fault ride through capability of wind turbines, as in the work of Abbey and Joos [1] and Jayasinghe and Vilathgamuwa [85]. Supercapacitors have also been implemented for the power smoothing of intrinsically intermittent power sources, such as wave energy converters [120].

In Chapter 4, the supercapacitors have been used to design an ESS. The design includes a power converter control scheme to regulate the charge and discharge of the supercapacitor bank, dealing with its technical constraints. In order to implement high level control strategies to increase power quality in microgrids, in Chapter 6, the supercapacitor based energy storage system has been used for the experimental validation of a novel power smoothing technique, aimed to reduce flicker levels in weak power systems with high penetration of RESs.

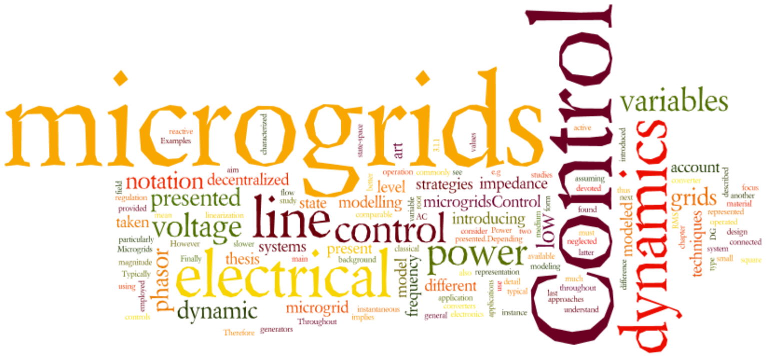

3

Control of microgrids

The aim of this chapter is to present the state of the art on the field level control, particularly for the decentralized control of active and reactive power through the regulation of the voltage magnitude and frequency. To better understand these controls, modeling of microgrids will be introduced and another section will be devoted to the electrical notation. This notation for the electrical variables is presented in Section 3.1, introducing the dynamic phasor. Then, a general microgrid is characterized in Section 3.2, introducing different modelling techniques available for AC grids. Then power converters for microgrids are described in Section 3.3, and its typical control is presented in Section 3.4. Finally, in Section 3.5, the state of the art in decentralized control strategies for microgrid operation is presented.

3.1. Dynamic phasor for low voltage grids

Depending on the type of study, electrical grids can be modeled with different level of detail. For instance, in classical power system studies, where the dynamics of the generators are much slower than the dynamics of the line, the latter can be neglected [149]. However, commonly, in power electronics applications, where the dynamics of the converter are comparable to the dynamics of the line, the last must also be taken into account. This difference implies that the dynamics of the line should be taken into account, and thus modeled. To model the dynamics of the line there are two main approaches.

- The linearization of the line dynamics using an instantaneous representation of the electrical variables. Typically, the model of the line dynamics is presented in the state-space form, see *e.g* [47, 94, 98, 131, 132].

- The use of the dynamic phasor, where the electrical variables are represented by its root mean square (RMS) values, assuming a variable electrical frequency. Examples of application of the dynamic phasor can be found in [4, 45, 54, 112, 170].

Both modelling techniques have been employed throughout this thesis. Therefore, some background material is provided in the next section.

3.1.1. Power flow through an impedance $\hat{Z}$

Microgrids are small electrical power systems which can be operated at medium or low voltage [2]. Throughout this thesis, the focus will be on the design of control strategies for DG connected to low voltage grids. To present the notation of the electrical variables of these systems, consider a low voltage line with an impedance

$$\hat{Z} = R + jX = R + \jmath\omega L = Ze^{\jmath\theta}, \tag{3.1}$$

where $\jmath = \sqrt{-1}$, R is the resistance, L is the inductance and X is the reactance, Z, θ are the modulus and angle respectively, and ω is the voltage frequency. The line with impedance $\hat{Z}$ connects two voltage

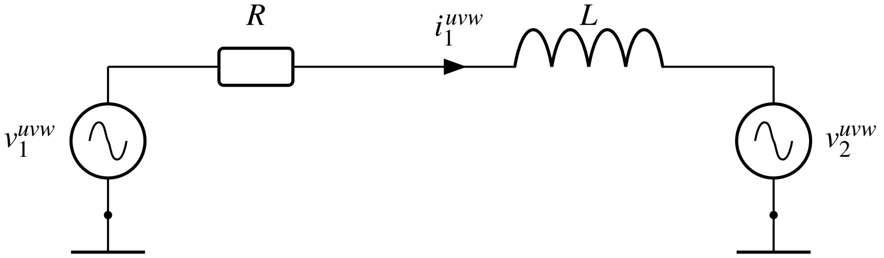

Figure 3.1.: Two voltage sources connected through a line with impedance $\hat{Z} = R + \jmath\omega L$.

sources with the voltage sequence $v_k^{uvw} = \begin{bmatrix} v_k^u & v_k^v & v_k^w \end{bmatrix}^T$ given by

$$\begin{bmatrix} v_k^u \\ v_k^v \\ v_k^w \end{bmatrix} = \sqrt{2} \begin{bmatrix} V_k(t)\cos(\phi_k(t)) \\ V_k(t)\cos(\phi_k(t) + 2/3\pi) \\ V_k(t)\cos(\phi_k(t) - 2/3\pi) \end{bmatrix},$$
$$\check{V}_k(t) = V_k(t)\cos(\phi_k(t)) = V_k(t)e^{\phi_k(t)},$$

where $k = 1, 2$ and $\check{V}_k(t)$ is the phasor representation of the three-phase voltage, V_k, ϕ_k are the time varying amplitude and angle of the k-th voltage source respectively, as illustrated in Figure 3.1.

Let ϕ_{12} denote the difference between angles $(\phi_2 - \phi_1)$. Then the power flowing through impedance $\hat{Z}$ from equation (3.1), can be expressed as [99]

$$\begin{aligned} P + \jmath Q &= \check{V}_1 \mathrm{conj}(\check{I}_1) = \check{V}_1 \mathrm{conj}\left(\frac{\check{V}_1 - \check{V}_2}{\hat{Z}}\right) \\ &= V_1 \left(\frac{V_1 - V_2 e^{\jmath\phi_{12}}}{Z e^{-\jmath\theta}}\right) = \frac{V_1^2}{Z} e^{\jmath\theta} - \frac{V_1 V_2}{Z} e^{\jmath(\theta + \phi_{12})}, \end{aligned}$$

where ˇ indicates the phasorial representation of the variables, the operator conj denotes the conjugate, and P is the active power, Q the reactive power, and $\check{I}_1$ is the current through $\hat{Z}$. Then, the active and reactive power flowing through the line can be expressed as

$$P = \frac{V_1^2}{Z}\cos\theta - \frac{V_1 V_2}{Z}\cos(\theta + \phi_{12}), \tag{3.2}$$

$$Q = \frac{V_1^2}{Z}\sin\theta - \frac{V_1 V_2}{Z}\sin(\theta + \phi_{12}). \tag{3.3}$$

Rearranging (3.2) and (3.3) with $Ze^{j\theta} = R + \jmath X$, it can be obtained

$$\sin\phi_{12} = \frac{XP - RQ}{V_1 V_2}, \qquad V_1 - V_2\cos\phi_{12} = \frac{RP + XQ}{V_1}, \tag{3.4}$$

showing that voltage magnitude and angle are coupled with active and reactive power.

A particularity of low voltage grids is its relatively high R/X ratio, *i.e.* the resistive component of the line impedance is comparable to the inductive component. In order to illustrate this effect, an example based on the system presented in Figure 3.1 has been simulated in the event of a step change in the angle of voltage $\check{V}_2$, this is $\phi_2 = \int_{t=0}^{t=\infty} 2\pi f t \, dt + \psi$, with $\psi = 0 \quad \forall t < 0.01$ s and $\psi = 0.01 \quad \forall t \geq 0.01$ s, and $f = 50$ Hz constant. The values for the line impedance used in the simulation have been obtained from typical values, see *e.g.* [59]. The numerical results of the simulation are shown in Figure 3.2. The parameters used in this example are:

- $\hat{Z} = 0.1342 + \jmath 0.2683, \qquad \check{V}_1 = 230\sqrt{2}\sin(2\pi 50 t)$
- For $t < 0.01$ seconds $\rightarrow \check{V}_2 = 230\sqrt{2}\sin(2\pi 50 t)$
- For $t \geq 0.01$ seconds $\rightarrow \check{V}_2 = 230\sqrt{2}\sin(2\pi 50 t + 0.01)$

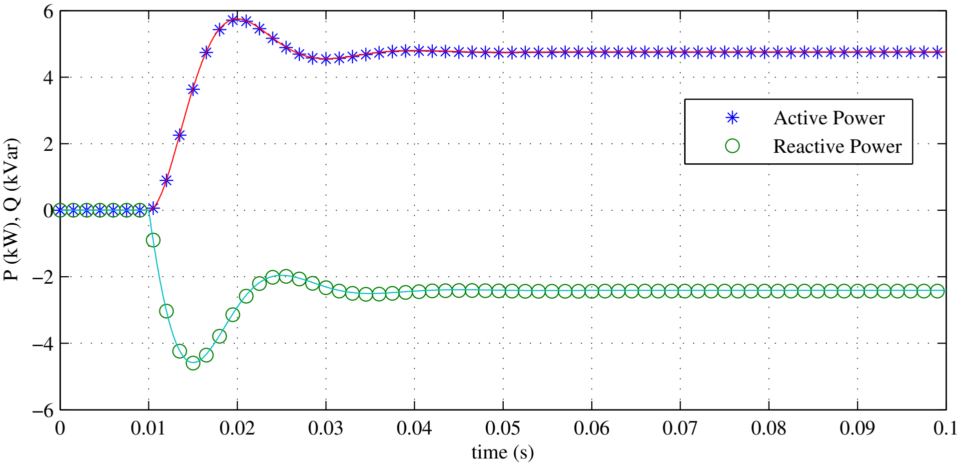

Figure 3.2.: Transient response of power transmission through a low-voltage impedance in front of a step change in the angle difference between its ends.

3.1.2. Dynamics of a line with Z impedance using dynamic phasor notation

Using the Kirchhoff's Voltage Law, the current flowing through the impedance $\hat{Z}$ from equation (3.1) can be obtained as

$$L\frac{d}{dt}i_1^{uvw} = -Ri_1^{uvw} + v_1^{uvw} - v_2^{uvw}. \tag{3.5}$$

The Park transformation matrix $\mathcal{T}$ is

$$\mathcal{T} = \frac{2}{3}\begin{bmatrix} \cos(\phi) & \cos(\phi - \frac{2\pi}{3}) & \cos(\phi + \frac{2\pi}{3}) \\ \sin(\phi) & \sin(\phi - \frac{2\pi}{3}) & \sin(\phi + \frac{2\pi}{3}) \\ \frac{1}{2} & \frac{1}{2} & \frac{1}{2} \end{bmatrix}, \tag{3.6}$$

where $\phi = \omega\, t = 2\pi\, f\, t$. Then, using $\mathcal{T}$, the voltage and current in the uvw frame can be expressed as

$$y_k^{dq0} = \mathcal{T} y_k^{uvw},$$

with $y_k \in \{v_k, i_k\}$, $k = 1, 2$. In the dq frame, equation (3.5) can be expressed as

$$L\frac{d}{dt}i_1^{dq} = -Ri_1^{dq} - L\begin{bmatrix} 0 & -1 \\ 1 & 0 \end{bmatrix}\frac{d}{dt}\phi_1 i_1^{dq} + v_1^{dq} - \Gamma(\phi_{12})^{-1}v_2^{dq},$$

with

$$\Gamma(\cdot) = \begin{bmatrix} \cos(\cdot) & -\sin(\cdot) \\ \sin(\cdot) & \cos(\cdot) \end{bmatrix},$$

and

$$v_k^{dq} = \begin{bmatrix} v_k^d \\ v_k^q \end{bmatrix} = \begin{bmatrix} V_k \\ 0 \end{bmatrix}, \qquad i_1^{dq} = \begin{bmatrix} i_1^d \\ i_1^q \end{bmatrix} = \begin{bmatrix} I_1 \cos(\varphi_k) \\ I_1 \sin(\varphi_k) \end{bmatrix},$$

with $k = 1, 2$ and where φ_k is the time-varying angle difference between the angle of v_k^{uvw} and the angle of the line current i_k^{uvw}.

3.2. Microgrid Modeling

A microgrid can be seen as a complex system composed by numerous elements or subsystems. The dynamics in a MG are defined by key elements, such as the grid, DG and its power electronics interfaces, and electrical loads. A conceptual illustration of a microgrid can be seen in Figure 3.3. Following is an overview on the various models found in the literature used for the control design and stability analysis of microgrids.

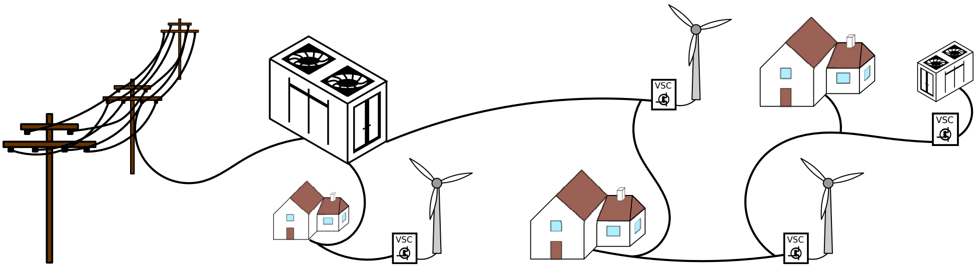

Figure 3.3.: A conceptual illustration of a microgrid with different loads, DG, ESS, lines and an interconnection station.

3.2.1. Microgrid: A system of systems

A microgrid can be composed by a large number of distributed generators, lines and loads, resulting in a high complexity system. In the literature, such systems are referred to as large-scale systems [109, 171]. A system may be considered as a large-scale system when the following conditions are met:

- The system has *high dimensionality*. This is, the system has a large number of state, implying a high computational burden for the design of the controllers.
- The system has *uncertainties*, and thus the properties and behaviour cannot be completely described by a unique model.
- There are *information structure constrains*. This can be a result of the limitations on the communications links among the control units and the sensors of the system.

Microgrids fulfils the conditions to be considered as a large-scale system, with special relevance the high dimensionality, but most importantly, by the uncertainty in different aspects. Through its lifetime, a microgrid can grow in the number of DG connected to it, resulting every time in a new effective system. Moreover, even though no more units are added, as a consequence of the fluctuation of the power generation of RES, a unit might eventually appear as disconnected from the microgrid, modifying the dynamics of the entire microgrid as well. All in all, microgrids are systems with a high uncertainty level.

Let a *subsystem* be a dynamic system composed by a single DG and all the electrical components connected to its PCC (referred as *node* in the sense of Section 3.2.2) of a microgrid. The aggregation of these

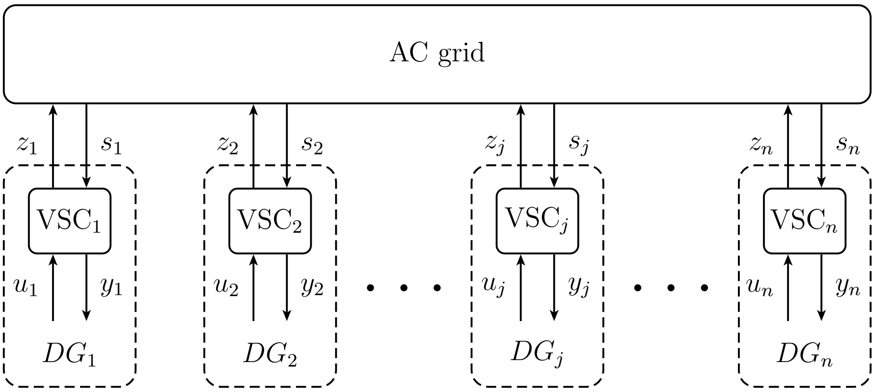

Figure 3.4.: A general control scheme for microgrids using a decentralized structure

subsystems and its interconnections form the microgrid system. Each subsystem may interact with the rest of subsystems through communication links, physical variables, or both simultaneously. Typically, in a MG, interactions are given by the power exchange among subsystems.

A graphical representation of the complete microgrid system is shown in Figure 3.4, where blocks DG$_j$ represents each subsystem, and the block AC grid represents the interconnections among subsystems. The dynamics of the j-th subsystem can be expressed as

$$\frac{d}{dt}x_j = A_j x_j + B_j u_j + E_j s_j, \tag{3.7a}$$

$$y_j = C_j x_j + D_j u_j + F_j s_j, \tag{3.7b}$$

$$z_j = C_{zj} x_j + D_{zj} u_j + F_{zj} s_j, \tag{3.7c}$$

where signals s_j and z_j denote the interaction between subsystem j-th and the rest of subsystems, x_j is the state vector, and u_j and y_j are the inputs and outputs signals of subsystem j used by its local controller. The interconnections of system (3.7) with the rest of the MG are given by

$$s = g(z), \qquad\qquad g : \mathbb{R}^n \to \mathbb{R}^n,$$

where g is in general a non-linear function of the interaction terms $z = \begin{bmatrix} z_1, & \dots, & z_n \end{bmatrix}^T$. Note that signals $s_j\,, z_j\,, u_j\,, y_j$ might be multi-dimensional in general. Matrix A_j typically includes the dynamics of the electrical local load connected to node j.

3.2.2. AC grid models

The model of a microgrid, and in particular the model of the electrical interconnections within the MG, depends on the control strategy implemented in DG elements, on the relative power levels among DG and the coupling between subsystems. The three main models employed to characterize a microgrid are the following:

- The aggregated model. This model is typically used for the design of a controller for a single converter, where the rest of the microgrid is assumed to be electrically much stronger. Analogising with classical power systems, the microgrid is considered as a slack bus, *i.e.* a constant voltage source.

- The model with a common AC bus. In this model, all the converters and loads are assumed to be connected to a unique electrical bus. This is, all units are connected to the same electrical point, observing the same voltage at the other end of the connection impedance.

- The model with arbitrary topology. In this model, the impedance between each pair of elements might be different, as well as the voltage across its interconnection impedance. This is the most general model available for control design or stability analysis.

In the following subsections, these models are described and illustrated.

Aggregated model

The most straightforward model for microgrids is the aggregated model, also referred to as Thévenim equivalent model, due to its similarity with the Thévenim circuit. In this model, all the elements of the microgrid but the converter under design or analysis, are reduced to an ideal voltage source and its equivalent series impedance. Examples of papers employing this model are [107, 132].

This model is applicable when: 1) all DG units are controlled with the same control strategy in a specific MG and 2) the power rating of the DG under design is much lower than the aggregated power rating of the rest of the DG present in the MG. Typically, the voltage source of the Thévenim model is a variable frequency and amplitude voltage source. An example of this model is illustrated in Figure 3.5. The most relevant parameters and variables of the model are listed.

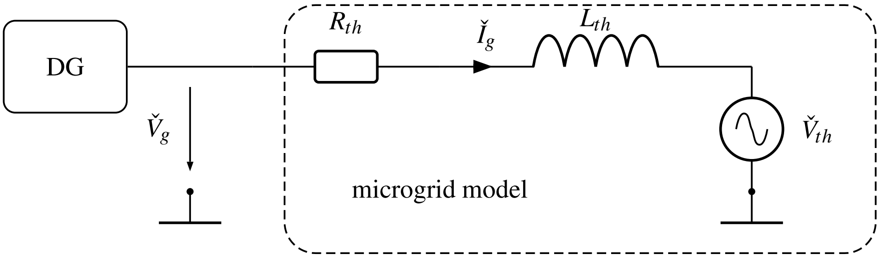

Figure 3.5.: Thévenim model of a microgrid

- $\check{V}_g$ is the MG dynamic phasor at the PCC of the DG under study.
- $\check{I}_g$ is the dynamic phasor of the current from DG to MG.
- $\check{V}_{th}$ denotes the ideal Thévenim voltage dynamic phasor of the MG.
- R_{th}, L_{th} are the Thévenim equivalent impedance of the microgrid at DG PCC.

Single AC bus model

This model is commonly employed in the literature for the modelling of microgrids. This model does not assume an identical and aggregated behaviour of the DG units in the microgrid, *i.e* each power generator can have particular dynamics. This model can be used to analyse the stability of the microgrid, considering the interaction among DG. It is more accurate than the aggregate model, although certain microgrids topologies might not be properly represented. Examples of publications using this model are [22, 67, 111, 114, 141].

In this model, each DG is connected to a common AC bus through typically a line, with its own impedance. An illustration of this model is shown in Figure 3.6, with the main parameters labeled for three different units. In contrast with the Thévenim model, in this model, each DG has a particular voltage at its PCC, as well as a different impedance connecting DG and the AC voltage bus. Considering a microgrid with n the number of DG units, and $j \in \{1 \dots n\}$ the index indicating the j-th unit, the parameters and variables are:

- $\check{V}_j$ is the dynamic phasor of the voltage at the PCC of DG j-th.

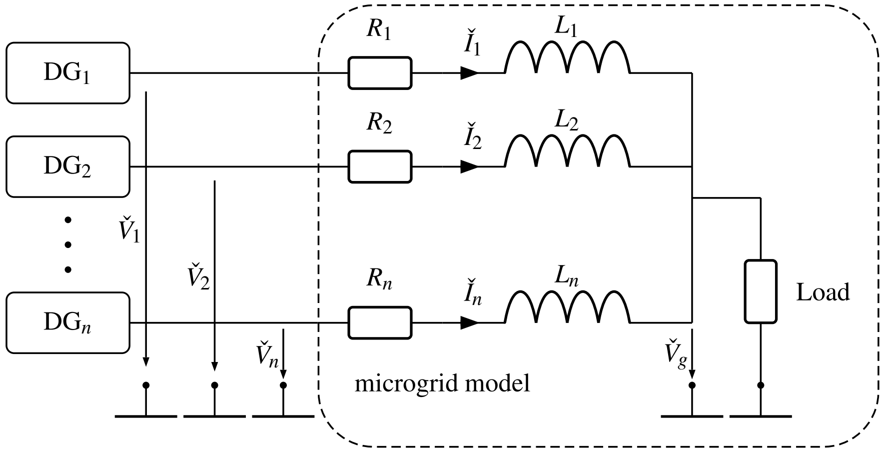

Figure 3.6.: Microgrid model with single AC bus

- $\check{I}_j$ is the dynamic phasor of the current injected to the microgrid AC bus from the j-th DG.
- R_j, L_j are the resistance and inductance respectively, between the j-th DG and the microgrid AC voltage bus.
- $\check{V}_g$ denotes the dynamic phasor of the voltage at the AC bus of the microgrid. Typically this voltage is the reference for the angle difference between voltages.

Meshed microgrid model

In addition to the previous two models, there is a third model to represent the electrical connections of a microgrid. This is the most general model, where the topology of the microgrid can be represented with high fidelity. This model is typically used when the previous two models fail to reproduce the dynamics of the microgrid. See *e.g.*, the following publications where a microgrid is modelled using the complete topology information [93, 124, 131, 148, 162].

Figure 3.7 shows an example of a meshed microgrid with complete topology information. Commonly, following the classical approach in conventional power system studies, it is assumed that loads are modeled by constant impedances. Microgrid networks can be modeled including load impedance information and obtain a set of differential equations.

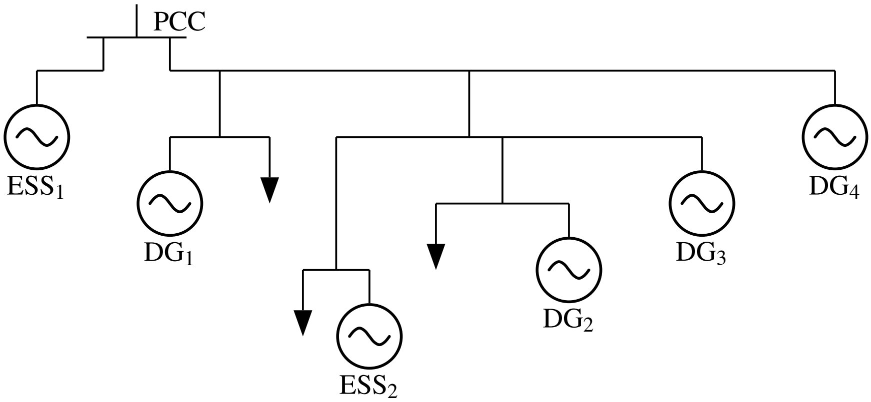

Figure 3.7.: Microgrid model with arbitrary grid topology.

The microgrid is then formed by $n \geq 1$ nodes, each of which represents a DG unit interfaced via a VSC. Let $\mathcal{N}$ denote the set of network nodes, and associate a time-dependent dynamic phasor $\check{V}_j(t) = \sqrt{2}V_j(t)\cos(\phi_j(t))$ with phase angle ϕ_j as well as a voltage amplitude V_j to each node $j \in \mathcal{N}$ in the microgrid. Typically, $\check{V}_j$ can be expressed in the DQ reference frame with either local angle reference or a common angle reference for the whole MG.

Depending on the study performed to the microgrid, the AC grid can be modelled including dynamics or not. If the dynamics are not considered, the impedance information of the microgrid can be expressed as the common admittance matrix Y used in conventional power system analysis. Matrix Y can be obtained easily with standard procedures [99]. Let $\mathcal{N}_j$ denote the set of nodes connected to node j (usually called neighbours) as $\mathcal{N}_j = \{k \in \mathcal{N} \mid k \neq j\,, Y_{jk} \neq 0\}$, where $Y_{jk} = G_{jk} + \jmath B_{jk}$ is the admittance between nodes j and k. With this information, one can obtain the power flow injected at j-th node of the microgrid by solving

$$\begin{aligned} P_j &= G_{jj}V_j^2 - \sum_{k \in \mathcal{N}_j} V_j V_k \left(G_{jk}\cos(\phi_{jk}) + B_{jk}\sin(\phi_{jk})\right), \\ Q_j &= -B_{jj}V_j^2 - \sum_{k \in \mathcal{N}_j} V_j V_k \left(G_{jk}\sin(\phi_{jk}) - B_{jk}\cos(\phi_{jk})\right), \end{aligned}$$

with G_{jk} and B_{jk} the conductance and susceptance, respectively, between nodes j and k.

As mentioned before, the microgrid network may be modeled including its dynamics. In such case, assume a network with n nodes and m lines. On a common DQ reference referred to DG j, the state equations for current of line connecting nodes j and k are

$$\frac{d}{dt} i^d_{jk} = -\frac{R_{jk}}{L_{jk}} i^d_{jk} + \omega i^q_{jk} + \frac{1}{L_{jk}} v^d_j - v^d_k \cos(\phi_{jk}) \tag{3.8a}$$

$$\frac{d}{dt} i^q_{jk} = -\frac{R_{jk}}{L_{jk}} i^q_{jk} - \omega i^d_{jk} + \frac{1}{L_{jk}} v^q_j - v^q_k \cos(\phi_{jk}), \tag{3.8b}$$

where ω is the frequency of the microgrid. Equation (3.8) can be linearized and expressed in the state-space as

$$\frac{d}{dt} \Delta i^{dq} = A_{net} \Delta i^{dq} + B_{1net} \Delta v^{dq} + B_{2net} \Delta \omega,$$

where Δ indicates the variation around the operation point, with

$$\Delta v^{dq} = \begin{bmatrix} \Delta v^{dq}_1 & \ldots & \Delta v^{dq}_n \end{bmatrix}, \qquad \Delta i^{dq} = \begin{bmatrix} \Delta i^{dq}_1 & \ldots & \Delta i^{dq}_m \end{bmatrix},$$

the vector of voltages in all nodes in $\mathcal{N}$, and the vector of line current between two nodes, respectively. Matrices are defined as

$$\begin{aligned} A_{net} &= \operatorname{diag}(A_{line_1}, \ldots, A_{line_m})_{2m \times 2m}, \\ B_{1net} &= \begin{bmatrix} B_{1line_1} & \ldots & B_{1line_m} \end{bmatrix}^T_{2m \times 2n}, \\ B_{2net} &= \begin{bmatrix} B_{2line_1} & \ldots & B_{2line_m} \end{bmatrix}^T_{2m \times 1}, \end{aligned}$$

where

$$A_{line_l} = \begin{bmatrix} -\frac{R_{jk}}{L_{jk}} & \omega_0 \\ -\omega_0 & -\frac{R_{jk}}{L_{jk}} \end{bmatrix},$$

$$B_{1line_l} = \begin{bmatrix} \cdots & \frac{1}{L_{jk}} & 0 & \cdots & -\frac{1}{L_{jk}} & 0 & \cdots \\ \cdots & 0 & \frac{1}{L_{jk}} & \cdots & 0 & -\frac{1}{L_{jk}} & \cdots \end{bmatrix}, \quad B_{2line_l} = \begin{bmatrix} i^q_{jk_0} \\ -i^d_{jk_0} \end{bmatrix},$$

with $l = 1, \ldots, n$ and the subindex 0 indicates the steady state value.

3.3. Distributed generators power electronics interfaces for microgrids

One of the most important microgrid enabling devices is the power electronic interface of the DG. This power electronic interface, typically a VSC, permits to implement advanced control solutions to enhance the operation of electrical systems. VSC can be arranged in different configurations. A common configuration, and the one used in this thesis, is the back-to-back configuration, where two VSC are connected through the DC–link, interfacing the two electrical systems. The DC–link refers to a common DC bus, where the DC capacitors of each VSC are connected. A sketch of a back-to-back configuration is shown in Figure 3.8, where the main components and electrical signals are labeled.

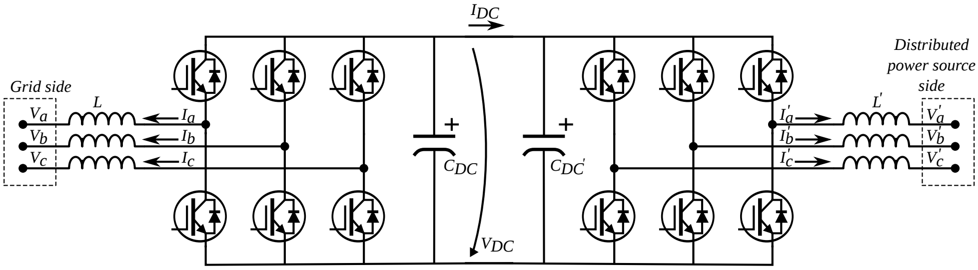

Figure 3.8.: Sketch of a back-to-back VSC configuration for interfacing distributed power resources

The back-to-back VSC configuration in Figure 3.8 is composed of two VSC, each with six insulated gate bipolar transistor (IGBT), three output arm inductors with inductance L, and two equivalent DC–link capacitors with C_{DC} capacitance. The voltage across the DC–link is V_{DC}, the DC current is I_{DC} and the phase voltage and currents are v^{uvw} and i^{uvw} respectively.

3.3.1. VSC simplified averaged model

Most of the current commercially available power electronic converters used for low voltage grid connection are based on the voltage-source

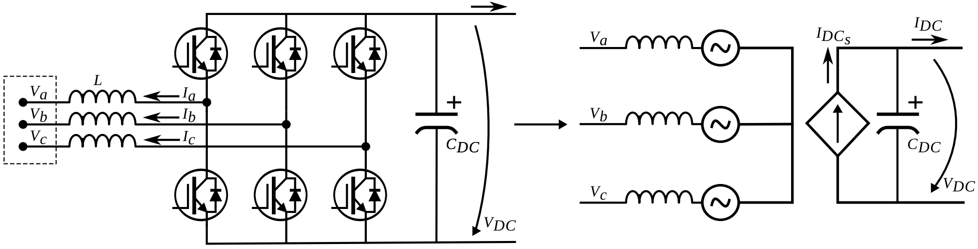

Figure 3.9.: VSC simplified average model

two-level VSC. An LCL filter is commonly used [86, 173], although L filters have been also used [140]. Pogaku, Prodanovic, and Green [131] demonstrates that with the DC voltage fixed, the switching process can be neglected and the inverter produces the reference voltage, thus the VSC can be modeled as an ideal voltage source for design purposes.

The simplified averaged model of the VSC, shown in Figure 3.9, assumes that the electrical angle ϕ can be either measured or computed. In many applications, a phase-locked loop (PLL) synchronized with the AC grid is used to provide the measure of the time varying angle of the electrical grid. In some control schemes, the reference angle of the output voltage is given by the control law of the converter, and does not require to be measured. Given the electrical angle, the three phase voltage and current can be expressed in a rotating DQ0 frame applying the park transformation $\mathcal{T}$ (see equation (3.6)). Then, using the instantaneous power theory [3] and assuming the three phase system is balanced (*i.e.* the homopolar component, x^0, is zero), the active and reactive power can expressed as

$$P_{AC} = \frac{3}{2}(v^d i^d + v^q i^q), \tag{3.9}$$

$$Q_{AC} = \frac{3}{2}(v^d i^q - v^q i^d), \tag{3.10}$$

where P_{AC} and Q_{AC} are the active and reactive power respectively, and v^{dq} and i^{dq} are the grid voltage and current respectively. Neglecting the converter losses, and applying the principle of energy conservation, the DC current of the source can be computed as

$$I_{DC_s} = \frac{P_{AC}}{V_{DC}}, \tag{3.11}$$

with I_{DC_s} the DC current injected by the current source of the averaged model, and V_{DC} the DC voltage of the DC–link.

3.3.2. Controllable and non-controllable distributed generation

Depending on DG capability and the control objectives, DG power sources can be classified in two different main groups [141]:

- *Grid feeding* DG.
- *Grid forming* DG.

An example of the two different configurations is illustrated in Figure 3.10. Depending on the microgrid operating mode, grid connected or islanded mode, power sources may change its functionality, with a special relevance for the grid forming sources. When a grid forming power source, such as the one in Figure 3.10a, is connected to the grid, it can be arbitrarily commanded to exchange active and reactive power. However, when it is islanded from the main grid, its role changes to grid forming power source. In islanded mode, all grid forming DG units will exchange the required amount of active and reactive power to guarantee the electrical stability of the islanded microgrid. When there are several grid forming units working in parallel, different strategies can be proposed to define the sharing of the electrical demand among them. Independently of the chosen strategy, when grid forming sources are paralleled, they typically have the capacity to regulate the active and reactive power.

In the grid feeding configuration of Figure 3.10b, the power source injects power to the electrical grid, regardless of the electrical demand and regardless of the operation mode of the microgrid. Typically, the grid feeding power sources implement a maximum power point tracking

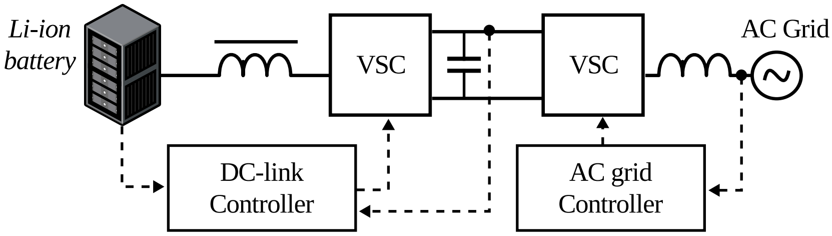

(a) Grid forming power source with the grid side converter controlling the DC–link voltage.

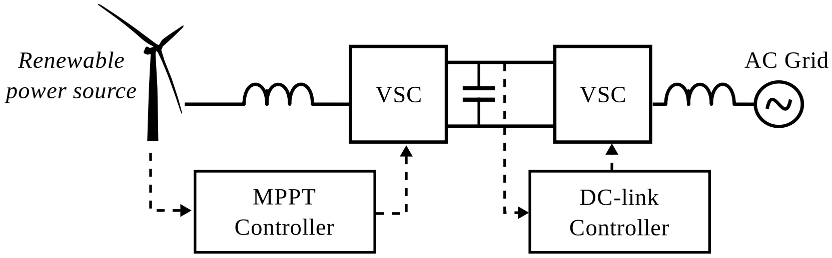

(b) Grid feeding power source, with the battery side converter controlling the DC–link voltage.

Figure 3.10.: Examples of grid feeding and grid forming power sources.

(MPPT) control scheme. Examples of common grid feeding sources are wind turbines and photo-voltaic (PV) generation. In addition to the pure grid forming and feeding schemes, power converters can be equipped with grid supporting functions as well. In this case, grid feeding power sources can modify its power output according to current the electrical demand. A summary of the controlled variables in the different operation modes of the microgrid and the different power sources is shown in Table 3.1, with the grid side converter (GSC) and renewable energy source side converter (RSC); P is the active power and Q is the reactive power; V_{AC} is the AC voltage and V_{DC} is the DC–link voltage.

	Grid connected	Islanded mode
Grid forming (single)	GSC: P, Q RSC: V_{DC}	GSC: V_{AC} RSC: V_{DC}
Grid forming (paralleled)	GSC: P, Q RSC: V_{DC}	GSC: V_{AC}, P, Q RSC: V_{DC}
Grid feeding	GSC: V_{DC}, Q RSC: P	GSC: V_{DC}, Q RSC: P

Table 3.1.: Summary of the controlled variables by back-to-back VSC for DG in different operation modes.

From the point of view of the control design of the MG elements, and from herein in this thesis, let controllable distributed generation (DG$_c$) denote the power sources acting in grid forming, and let uncontrollable distributed generation (DG$_{uc}$) denote the power sources acting as grid feeding and grid supporting. This distinction responds to the assumption that grid feeding and grid supporting power sources will be deployed by a third party, and do not contribute actively to the electrical stability of the MG.

3.4. VSC control for distributed generation

As discussed in section 3.3, the power electronics of VSC are modeled using the simplified averaged model, neglecting the IGBT dynamics. In the following subsections, two typical control objectives for power converters are presented.

3.4.1. Converter with inner control loop dynamics

Power converters for RES are typically composed in a back-to-back structure, connected by the DC–link. The two converters are the GSC and the RSC. Power electronic interfaces provide a more flexible operation compared to the direct connection of synchronous and induction generators to the grid [93]. On the one hand, the power electronic inverters permits to shape the voltage waveform, allowing, for instance, the decoupled control of active and reactive power, or the design of active filters to improve the power quality of the electrical grid. On the other hand, the DC–link provides a certain degree of decoupling from the dynamics of the power source to the dynamics of the electrical grid. The DC–link permits the implementation of decoupled controls for the grid side converter and the power source side converter. This permits the design of control schemes for the electrical stabilization of the microgrid independently of the DG nature. In this section it will be assumed that the RSC control perfectly regulates the DC–link voltage, and thus the dynamics of the DC–link can be neglected [124].

GSC is typically controlled with a cascaded control scheme [95]. The objective of the control scheme is to: 1) control the output AC current i^{uvw} and 2) regulate the output voltage v^{uvw} to the given set-point. This structure permits to easily limit the output current to avoid potential dangerous over-currents produced by the voltage controller transients. Assume a VSC, modelled using a simplified average model, connected to an ideal AC voltage source $\check{V}_g = \sqrt{2}V_g \cos(\phi)$, through an LCL filter, as in Figure 3.11. The output filter is composed by:

- Inductor filter: $\hat{Z}_f = R_f + \jmath\omega L_f$, with a current $\check{I}$ through it,
- Capacitor filter: C_f, with a voltage $\check{V}$ across it,
- Coupling inductor: $\hat{Z}_c = R_c + \jmath\omega L_c$, with a current $\check{I}_g$ through it.

Assume also that the voltage $\check{V}$ and current $\check{I}$, $\check{I}_g$ can all be measured and transformed using Park transformation with an ideal PLL, obtaining v^{dq}, i^{dq}, i_g^{dq} and $\omega = 2\pi f$. Applying the transformation $\mathcal{T}$ (see equation (3.6)) to the electrical variables, one can express the model of the system as

$$\frac{d}{dt}\begin{bmatrix} i^d \\ i^q \end{bmatrix} = \begin{bmatrix} -\frac{R_f}{L_f} & \omega \\ -\omega & -\frac{R_f}{L_f} \end{bmatrix} \begin{bmatrix} i^d \\ i^q \end{bmatrix} + \frac{1}{L_f}\begin{bmatrix} v_o^d - v^d \\ v_o^q - v^q \end{bmatrix},$$

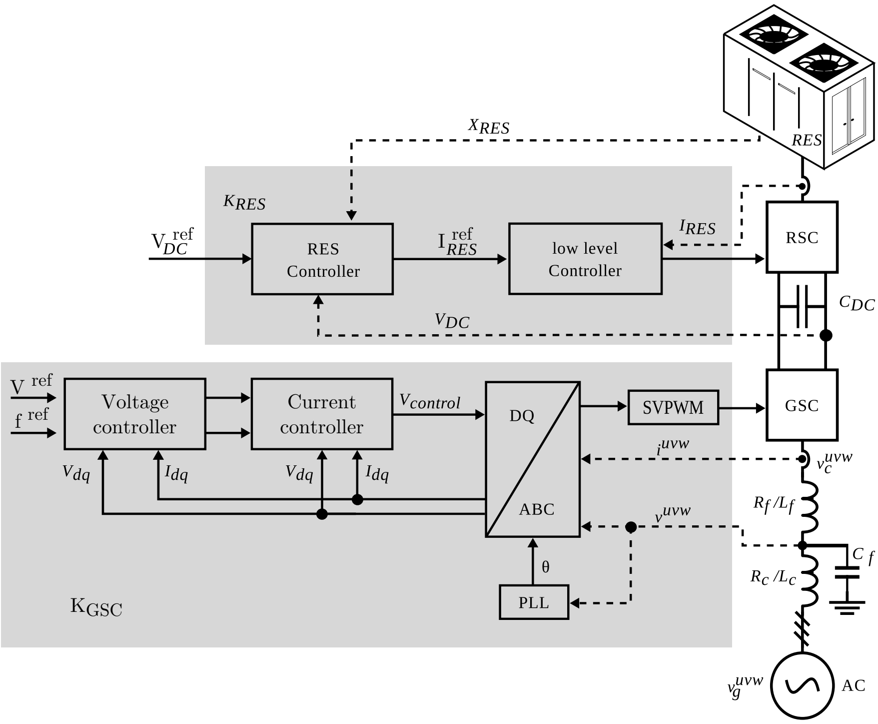

Figure 3.11.: Typical control scheme for VSC interfacing a RES with a microgrid.

with v_o^{dq} the output voltage of the VSC. Using a standard proportional-integral (PI) controller, as shown in Figure 3.12, which can be expressed as

$$\frac{d}{dt}\begin{bmatrix} x_i^d \\ x_i^q \end{bmatrix} = ki_c \begin{bmatrix} i^{d,ref} - i^d \\ i^{q,ref} - i^q \end{bmatrix},$$

$$\begin{bmatrix} v_o^d \\ v_o^q \end{bmatrix} = \begin{bmatrix} x_i^d \\ x_i^q \end{bmatrix} + kp_c \begin{bmatrix} i^{d,ref} \\ i^{q,ref} \end{bmatrix} - \begin{bmatrix} kp_c & -\omega L_f \\ \omega L_f & kp_c \end{bmatrix} \begin{bmatrix} i^d \\ i^q \end{bmatrix} + \begin{bmatrix} v^d \\ v^q \end{bmatrix},$$

where $\begin{bmatrix} x_i^d & x_i^q \end{bmatrix}^T$ are the states of the controller, and kp_c and ki_c are the controller parameters. Notice that the controller includes a feedforward term, $\begin{bmatrix} v^d & v^q \end{bmatrix}^T$, and a decoupling term, ωL_f. The controller parameters can be selected as

$$kp_c = \frac{L_f}{\tau_c}, \qquad ki_c = \frac{R_f}{\tau_c}$$

where τ_c is the time constant of the closed current loop. The resulting

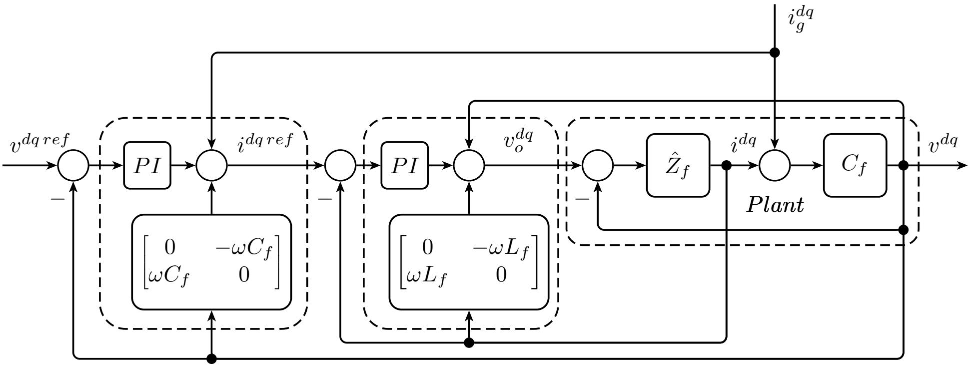

Figure 3.12.: Classical control scheme for current and voltage used in VSC with PI, feed-forward and decoupling terms.

closed loop system can be written as

$$\frac{d}{dt}\begin{bmatrix} i^d \\ i^q \end{bmatrix} = \begin{bmatrix} -1/\tau_c & 0 \\ 0 & -1/\tau_c \end{bmatrix}\begin{bmatrix} i^d \\ i^q \end{bmatrix} + \begin{bmatrix} 1/\tau_c & 0 \\ 0 & 1/\tau_c \end{bmatrix}\begin{bmatrix} i^{d,\,ref} \\ i_{q,\,ref} \end{bmatrix},$$

which corresponds to a first order transfer function, where i^d and i^q are the AC currents through inductor L_f in the DQ framework with $i^{d,ref}$ and $i^{q,ref}$ the corresponding set-points.

Let G_I denote the transfer function from $i^{dq,ref}$ to i^{dq}, and K_v be the voltage controller. Then, one can express closed loop voltage control scheme as the block diagram shown in Figure 3.13, were the coupling of the DQ variables is not included for the sake of clarity. The grid impedance is included in the block $\frac{1}{sL_c+R_c}$ along with the coupling inductor R_c, L_c of the VSC. Signals V_g and I_g are the grid voltage and current respectively, while V^{ref} is the AC voltage reference for the converter, and K_v is the controller to be designed.

To provide closed loop AC voltage regulation at the capacitor output filter point, another PI controller is typically used to implement K_v, including also decoupling and feed-forward terms to generate the reference current $I^{ref} = \begin{bmatrix} i^{dq,ref} \end{bmatrix}$. The dynamics of the voltage at the capacitor filter C_f are given by

$$\frac{d}{dt}\begin{bmatrix} v^d \\ v^q \end{bmatrix} = \begin{bmatrix} 0 & \omega \\ -\omega & 0 \end{bmatrix}\begin{bmatrix} v^d \\ v^q \end{bmatrix} + \frac{1}{C_f}\begin{bmatrix} i^d - i_g^d \\ i^q - i_g^q \end{bmatrix}.$$

Then, similarly to the current controller, the voltage controller can be

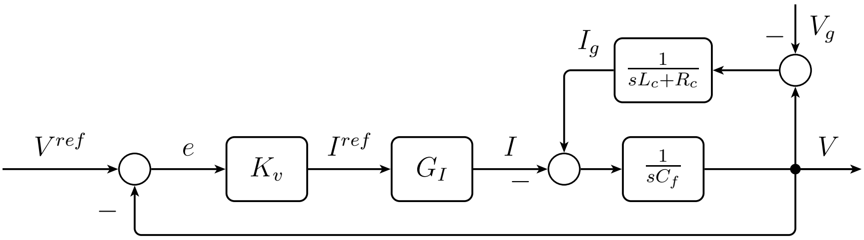

Figure 3.13.: A conceptual AC voltage control scheme for VSC.

expressed as

$$\begin{aligned}
\frac{d}{dt}\begin{bmatrix} x_v^d \\ x_v^q \end{bmatrix} &= ki_v \begin{bmatrix} v^{d,\,ref} - v^d \\ v^{q,\,ref} - v^q \end{bmatrix}, \\
\begin{bmatrix} i^{d,\,ref} \\ i^{q,\,ref} \end{bmatrix} &= \begin{bmatrix} x_v^d \\ x_v^q \end{bmatrix} + kp_v \begin{bmatrix} v^{d,\,ref} \\ v^{q,\,ref} \end{bmatrix} - \begin{bmatrix} kp_v & -\omega C_f \\ \omega C_f & kp_v \end{bmatrix} \begin{bmatrix} v^d \\ v^q \end{bmatrix} + \begin{bmatrix} i_g^d \\ i_g^q \end{bmatrix},
\end{aligned}$$

where $\begin{bmatrix} x_i^d & x_i^q \end{bmatrix}^T$ are the states of the controller, kp_v , ki_v are the proportional and integral gains, respectively.

3.4.2. Simplified AC voltage source model for GSC

Assuming the voltage controller K_v has been properly designed, it is possible to obtain a simplified equivalent dynamic model of the VSC. For details on the implementation see *e.g.* [43, 74, 90, 127].

The model simplification has been analyzed in [117], concluding that the simplified model is accurate enough for stability studies. In this model, the inner control of the VSC is modelled as an ideal voltage source with variable frequency [58]. Power electronics converters can change the frequency of the generated voltage instantaneously, however the voltage magnitude cannot be changed instantaneously. The voltage control loop is modelled by a first order transfer function parametrized by τ_V. The dynamics of the inner control loop can be expressed as

$$\begin{aligned}
\frac{d}{dt}\phi(t) &= \omega^{ref}(t), \\
\frac{d}{dt}v^d(t) &= \frac{1}{\tau_v}(-v^d(t) + v^{d,ref}(t)).
\end{aligned}$$

where ω^{ref} and $v^{d,ref}$ are the set-point signals for the power converter obtained from the higher level power controller.

3.5. Power control in Microgrids

In conventional power systems, where the generators are based on large synchronous machines, the voltage frequency of the electrical system is electro-mechanically coupled with the dispatched active power. As electrical load increases, the torque load on the generator shaft increases as well, which translates into reduction of the rotating speed and thus decreases the voltage frequency. Acting on the power feeding of the prime mover, the shaft torque can be controlled, and therefore it is possible to restore the system frequency. This natural characteristic of synchronous generators leads to the well-known speed droop control of traditional power systems, permitting generators units to operate in parallel [99].

In contrast, in electric power systems composed only by RES interfaced with power electronic converters, VSC, there is no physical connection between the generated power and the grid frequency. When this kind of systems become electrical islands, disconnected from the utility grid, the electrical demand and the islanded grid voltage frequency are decoupled by nature. The typical solution to link voltage frequency and electrical demand in power electronic interfaced power systems in island operation is to implement the so-called droop control. In opposite to traditional power systems, the droop control in power electronics converter does not regulate the electrical frequency, but modifies it by emulating the droop characteristic of synchronous generators. This is, regulates the active and reactive power by modifying the voltage frequency and magnitude respectively.

In this section, the proposals found in the literature for the implementation of field controller K_{DG_i} (see Chapter 2) are reviewed. Although a large number of proposals can be found in the literature, only those focussed mainly on the decentralized control are presented. Please note that throughout this thesis, a distinction between decentralized and distributed has been considered:

Decentralized The individual controllers of each subsystem does not communicate with each other. Only local information from subsystem j (signal y_j in equation (3.7)) is used to operate the controller.

Distributed Local controllers in each subsystem may have a communication link with an arbitrary number of other local controllers in the microgrid. Thus, a local controller may use information from other subsystems besides the local information (some signals from $\{y_1, \dots, y_j, \dots, y_n\}$ in equation (3.7)).

3.5.1. Voltage and Frequency control in microgirds

Although microgrids are a promising paradigm, some technical challenges should be overcome prior to the large scale integration [130]. The most relevant technical challenge presented in low voltage microgrids is the achievement of a correct grid regulation by sharing the power demand among multiple parallel DG when working isolated from the main grid. This challenge has been addressed by numerous authors presenting different conceptual solutions; see *e.g.* [66, 110, 153, 177].

Being accepted by the majority of the scientific community, droop control is the *de facto* technique for paralleling VSC working in islanded conditions. Droop controllers, which emulate the droop characteristic of synchronous generators, has been adopted as power sharing controllers of microgrid generators by numerous authors, see *e.g* [44, 70, 93, 118, 119, 124, 131, 141, 148, 172].

From herein, let *classical droop control* denote the control proposed by Chandorkar, Divan, and Adapa [32] in 1993. This control consists of a proportional relation between active power and voltage frequency and between reactive power and voltage amplitude. The major benefit of the droop control is its decentralized structure which allows to control the microgrid electrical variables in absence of communications among units, achieving a highly reliable system.

Classical droop control

Grid forming power sources, such as the one in Figure 3.10a, must exchange the required active and reactive power to guarantee the electrical stability of the islanded microgrid. This functionality can be achieved with a control scheme based on the droop control, permitting also a seamless transfer from grid connected to islanded operation mode. The classical droop control law (see Figure 3.14) is defined by

$$f^{ref} = f^{nom} - k_p(P - P^{ref}) \tag{3.12}$$

$$V^{ref} = V^{nom} - k_q(Q - Q^{ref}), \tag{3.13}$$

where f^{ref} and V^{ref} are the reference values of voltage frequency and magnitude for the VSC control (see Figure 3.13), f^{nom} and V^{nom} are

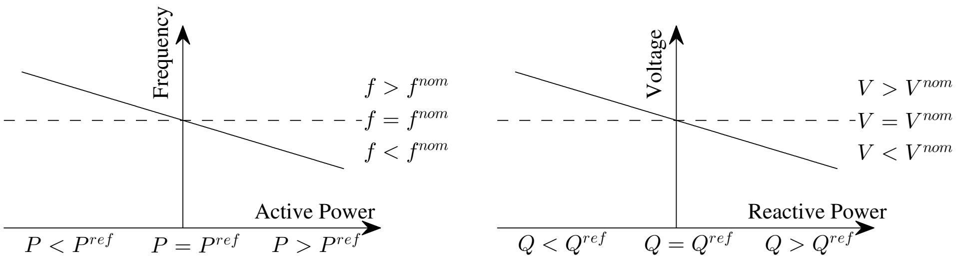

(a) Frequency droop characteristic. (b) Voltage droop characteristic.

Figure 3.14.: Classical droop control graphical characteristics.

the nominal values for frequency and voltage for the MG, and P^{ref} and Q^{ref} are the power set-points given the EMS (see Chapter 2), and k_p and k_q are the active and reactive power droop coefficients, respectively.

3.5.2. Droop control variants

Despite its wide acceptance, droop control presents some important drawbacks [119]. The most important drawback is the impact of line impedance in the dynamic response of the microgrid. This dependence makes non-trivial the control design to guarantee power sharing accuracy and/or stability [110].

Different approaches has been proposed in the literature to circumvent the effects of line impedance. Among the decentralized approaches based on the modification of the droop control it can be distinguished:

- The virtual impedance method by Guerrero, García de Vicuña, Matas, Castilla, and Miret [68].
- The parametric droop with a rotation matrix based on R/X line impedance ratio by Brabandere, Bolsens, Van den Keybus, Woyte, Driesen, and Belmans [22].
- The droop control with improved transient behavior [67].
- The emulation of mechanical inertia [55].
- Variations of these methods detailed in [119, 130].

Most of the proposed improvements to the droop control share several common characteristics, such as the fact that the design of the controller requires previous knowledge of the entire microgrid. This fact limits the implementation of flexible microgrids where different DG would be deployed in arbitrary locations modifying the microgrid topology. Moreover, the stability analysis of the above proposals makes strong hypothesis about the microgrid topology and DG behavior, such as a unique common AC bus where all units are connected or identical behavior of all DG units in the microgrid. Following is a brief overview of proposed variations to classical droop control scheme.

Droop control by virtual impedance method

Typically, line impedance is considered inductive for droop design, but this is not true in the case of low voltage microgrids. Moreover, the inverter output impedance also depends on the control strategy adopted [20, 71, 174]. This method proposes to increase the VSC output impedance to reduce the uncertainty on the total output impedance. This is achieved by adding a virtual impedance in the control loop, as if it would be just before the physical output impedance of the converter.

In the lines connecting parallel inverters, circulating currents through inverters can easily appear due to small variations on the output impedance respect to the model used during the design phase. By adding a virtual complex impedance such circulating current can be reduced, as the system becomes less sensitive to line impedance unbalance and parameter mismatching. Another important aspect is the ability to supply harmonics to non-linear loads. By emulating a virtual impedance in the time domain good harmonic current sharing can be achieved [155].

The virtual impedance $\hat{Z}_v = R_v + \jmath\omega L_v$ is equivalent to the series impedance of a synchronous generator. However, since it is virtual, there are no real losses. There are different proposals to implement virtual impedance. For instance, Guerrero, Matas, García De Vicuña, Castilla, and Miret [70] explores the control of active and reactive power flow through the analysis of the output impedance of the inverters and its impact on the power sharing. As a result, adaptive virtual output impedance is proposed in order to achieve a proper reactive power sharing, regardless of the line-impedance unbalances. A soft-start operation is also included, avoiding the initial current peak, which results in a seamless hot-swap operation. Linear and nonlinear loads can be properly shared due to the addition of a current harmonic loop in the control strategy.

A later implementation is proposed by Brabandere, Vanthournout, Driesen, Deconinck, and Belmans [23] using a more advanced control scheme compared with the classical droop control. In his proposed scheme, a combined error of voltage magnitude and grid current is used to estimate the disturbance and internal states of the VSC to feed an optimal state-feedback linear-quadratic-Gaussian (LQG) gain for controlling the electrical variables. This approach allows this converter to be used in a MG with a line impedance ranging from 0 to ∞.

Droop control taking into account line impedance

In the case of low voltage MG, the classical assumption where the line inductance is much higher than the resistance component ($X >> R$) in the impedance of the power line is no longer true. To deal with this situation, [23] propose a transformation that is an orthogonal linear rotational transformation matrix $\mathbf{T}$ to create a new active and reactive power, P' and Q', which can be expressed as

$$\begin{bmatrix} P' \\ Q' \end{bmatrix} = \mathbf{T} \begin{bmatrix} P \\ Q \end{bmatrix} = \begin{bmatrix} X/Z & -R/Z \\ R/Z & X/Z \end{bmatrix} \begin{bmatrix} P \\ Q \end{bmatrix},$$

with $Z = \sqrt{R^2 + X^2}$ the grid impedance observed from the VSC. Applying this transformation to equations (3.4) results in

$$\sin\phi_{12} = \frac{ZP'}{V_1 V_2}, \qquad V_1 - V_2\cos\phi_{12} = \frac{ZQ'}{V_1}.$$

Then, by regulating P', only the power angle ϕ_{12} is affected, whereas regulating Q' acts on the voltage magnitude. The new droop equations become

$$\begin{aligned} f^{ref} &= f^{nom} - k_p(P' - P'^{ref}), \\ V^{ref} &= V^{nom} - k_q(Q' - Q'^{ref}), \end{aligned}$$

or equivalently

$$\begin{aligned} f^{ref} &= f^{nom} - k_p\frac{X}{Z}(P - P^{ref}) + k_p\frac{R}{Z}(Q - Q^{ref}), \\ V^{ref} &= V^{nom} - k_q\frac{R}{Z}(P - P^{ref}) + k_q\frac{X}{Z}(Q - Q^{ref}). \end{aligned}$$

Notice that knowledge on the ratio R/X of the line impedance is enough to achieve the droop control.

Droop control with improved transient behavior

Typically droop coefficients are selected based on an electrical consideration rather than stability criteria. It is for this reason that an additional loop to the *classical droop control* is being proposed [50, 67, 117]. Guerrero, García de Vicuña, Matas, Castilla, and Miret [67] proposes a power sharing droop controller with a modified droop function with controllable gain transient droop characteristics. This configuration leads to a 2-DOF tunable controller, where the droop gain is selected to determine the frequency/voltage regulation performance and the transient gains can be adaptively tuned to damp the oscillatory modes at different operating conditions.

To provide active damping for the low frequency power oscillations and to increase the controllability of the reactive power sharing-controller, the following droop functions are proposed

$$\begin{aligned} f^{ref} &= f^{nom} - k_p(P - P^{ref}) - \hat{k}_p \frac{d}{dt} P \\ V^{ref} &= V^{nom} - k_q(Q - Q^{ref}) - \hat{k}_q \frac{d}{dt} Q \end{aligned}$$

where $\hat{k}_p$ and $\hat{k}_q$ are transient droop gains. With this structure, the dynamics of the microgrid can be controlled by adjusting the transient droop gains. Since the new term is the derivative of the active and reactive power, the steady state is not modified respect the classical droop control, preserving the power sharing proportional to the electrical ratings of the converter.

Further studies on the modified droop control with improved transient were performed by other authors. On the one hand, Divshali, Alimardani, Hosseinian, and Abedi [50] proposed that a single DG maintains the microgrid voltage and frequency, applying a compensation based on the derivative term of the power to improve the transient response, without considering multiple parallel DG. On the other hand, multiple DG are considered by Mohamed and El-Saadany [117], where control parameters are designed using the small signal model of the microgrid, and the same model is used for the stability analysis.

Synchronous Generator Emulation

The parallel operation of DG could benefit from characteristics of synchronous generator (SG) such as the kinetic energy stored in rotor (*i.e.* inertia). With this end, droop control of VSC in MG could mimic SG behaviour in classical power systems. Beck and Hesse [14] proposes an autonomous controller based on the model of SG for microgrid inverter to mimic the characteristic of SG. Moreover, the converter is designed to operate seamlessly as either grid feeding or grid forming DG in microgrids by integrating a virtual primary frequency regulator and a virtual excitation regulator. The simulation results presented reveal good performance of the proposed control strategy on voltage regulation, power sharing and operation mode transfer, with seamless transition.

Recently, D'Arco and Suul [42] have demonstrated that a VSC with droop control emulating inertia, can be modelled equivalently as a SG. The control scheme shown in Figure 3.15 illustrates the implementation of a droop control with virtual inertia. The block $\mathcal{V}I$ is the virtual inertia, which can be in the form of

$$\mathcal{V}I(s) = \left(1 + \tau_v/k_p\, s\right)^{-1},$$

where τ_v is the time mechanical constant of the equivalent virtual SG. Then, it can be demonstrated that

$$\tau_v/k_p = 2H,$$

where H is moment of inertia of the emulated synchronous generator.

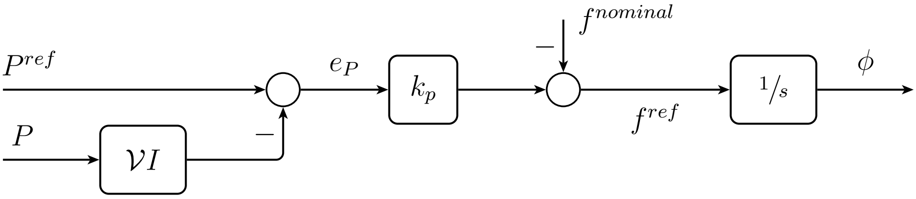

Figure 3.15.: Droop control scheme using virtual inertia to generate the voltage reference for the VSC.

3.5.3. Design of stabilizing droop considering interactions

When the interactions with other DG are considered, the droop design reduces to the decentralized control problem of MGs. The design seeks to obtain a set of controllers K_{DG_j}, $j \in \{1 \ldots n\}$ such that the MG is stable and satisfies a certain performance requirement. In general, the decentralized control requires to design a structured controller in the form

$$K_{mg} = \begin{bmatrix} K_{DG_1} & 0 & \cdots & 0 \\ 0 & K_{DG_2} & \cdots & 0 \\ \vdots & \vdots & \ddots & \vdots \\ 0 & 0 & \cdots & K_{DG_n} \end{bmatrix},$$

where K_{mg} is the controller of the complete microgrid. The optimal design of this control results in a non-convex optimization problem, which may be complex to solve in general.

Recently, a new approach has been proposed for the decentralized design of a robust droop control for microgrid DG units [147, 153]. This approach models the microgrid as an aggregate of interconnected subsystems [176], deriving the stability of the entire system by analyzing each subsystem stability and placing bounds on the nonlinear interconnections between subsystems. In [153] bounds on the droop coefficients are derived for the *classical droop control* to ensure stability and states the worst case synchronization rate.

Alternatively, the interactions among different DER are analyzed and a decentralized control scheme guaranteeing stability is proposed in [147]. However, the proposed control strategy does not focus on the droop control of voltage and frequency, but on an outer loop to enable decentralized restoration of the nominal frequency and voltage. The design on the controller parameters assumes that every DG behaves in a exact manner and the synchronization among DG relies on external GPS signals. Based on this approach, a new decentralized design for droop control is proposed in Chapter 8.

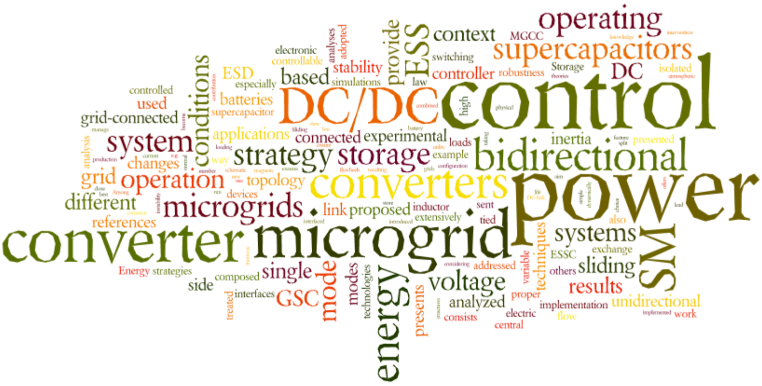

4

Control of a supercapacitor energy storage system for microgrid applications

This chapter presents the control of an ESS based on supercapacitors in the context of grid-connected microgrids. A single sliding mode strategy is proposed to control a bidirectional DC-DC converter, capable of working properly under all operating conditions. The switching devices are commanded by a single sliding function, dynamically shaped by references sent from the microgrid central controller. This feature facilitates the implementation and design of the control law and simplifies the stability analysis over the entire operating range. The effectiveness of the proposed control strategy is illustrated by experimental results.

4.1. Introduction

As seen in Chapter 2, in the context of microgrids, an ESS based on supercapacitors consists of a GSC and a bidirectional DC-DC converter referred to as energy storage side converter (ESSC). In the case of grid connected microgrids, the GSC is a voltage source converter that ensures the power transfer between the microgrid and the ESS by regulating the voltage of the DC–link, as introduced also in Chapter 3. The control of bidirectional DC-DC converters has been widely analyzed in the literature, but not so extensively in microgrid applications. Among other control techniques, nonlinear techniques based on variable structures system (VSS) and sliding mode (SM) theories result especially suitable for switched systems like power converters [154, 166]. Sliding mode techniques permit the combination of designs with different objectives and also provide a quite simple implementation. Therefore, for power converters subjected to high variable operating conditions, SM algorithms become a natural choice considering their large signal capability.

Several articles have analyzed and proposed SM control strategies for DC-DC converters in a variety of applications, for example [17, 34, 56, 64, 84, 160, 168]. However, the use of bidirectional DC-DC converters controlled by SM to ensure a proper power exchange in a microgrids is not common. In [56, 160, 168], unidirectional converters with resistive loads as a single isolated stage are analyzed. For example, El Aroudi, Robert, and Leyva [56] presents the control of a high voltage two-cell buck converter, where SM is used to control the inductor current and a PI control is added to regulate the output voltage. This configuration is unidirectional in power and the results are evaluated by numerical simulations. Gee, Robinson, and Dunn [64] proposes a bidirectional buck-derived converter is controlled by hysteresis to extend the battery life through the charge/discharge of a supercapacitor. Ciccarelli and Lauria [34] addresses the sliding mode control of a coupled inductor bidirectional DC-DC converter and results are presented by simulations for a DC tramway application. Stability analyses are not addressed in [34, 56, 64, 160, 168]. Bianchi, Battista, and Mantz [17] and Inthamoussou, Mantz, and Battista [84] has addressed the stability analysis for unidirectional converters as isolated stages.

The main contribution of this chapter is to propose an SM control strategy for a bidirectional DC-DC converter for an ESS based on supercapacitors in the context of microgrid applications. The strategy covers all operating conditions: startup, constant power and voltage limitation. The whole strategy is implemented under the SM theory in contrast with other proposals that combine different strategies and do not provide all these operating modes. This characteristic offers the robustness of SM control and flexibility to easily get different operation modes. With this aim, different sliding surfaces are combined resulting in a single switching control law. Thus, the system is able to run from a zero energy stored state, exchange power with the microgrid in normal operation and shut down without the necessity of human intervention. The controller changes automatically between these modes, taking into account the references sent by the MGCC. A stability analysis and experimental results at maximum operating conditions are also presented. The control of a supercapacitor in the previously mentioned way, in the microgrid context and with exhaustive experimental tests, has not been treated deeply in the literature.

4.2. Energy storage systems based on supercapacitors

Figure 4.1 presents a schematic view of the interface topology adopted to control the power flow between the energy storage device (ESD) and the microgrid. It consists of a GSC, a DC–link, and a bidirectional DC-DC converter and the ESD. The last one is the physical device used to store energy (supercapacitors in the present chapter). Another type of ESD, a Li-on battery, is used with a similar converter topology in the next chapter.

The controller of the ESSC, K_{ESSC}, regulates the power exchanged between the ESD and the DC–link. The controller design strongly depends on the configuration of the microgrid at which the ESS is connected, as well as on the particular ESD used. In the configuration of Figure 4.1, K_{ESSC} receives instructions from the MGCC (in the form of a power reference, P^{ref}), which determines when the ESS must store energy and when it must inject energy into the grid. Figure 4.2 presents the bidirectional DC-DC topology adopted to implement the ESSC. For this topology, voltage is always higher on the left side (V_{DC}) than on the right side (V_{ESD}), but energy can flow in both directions. This converter can

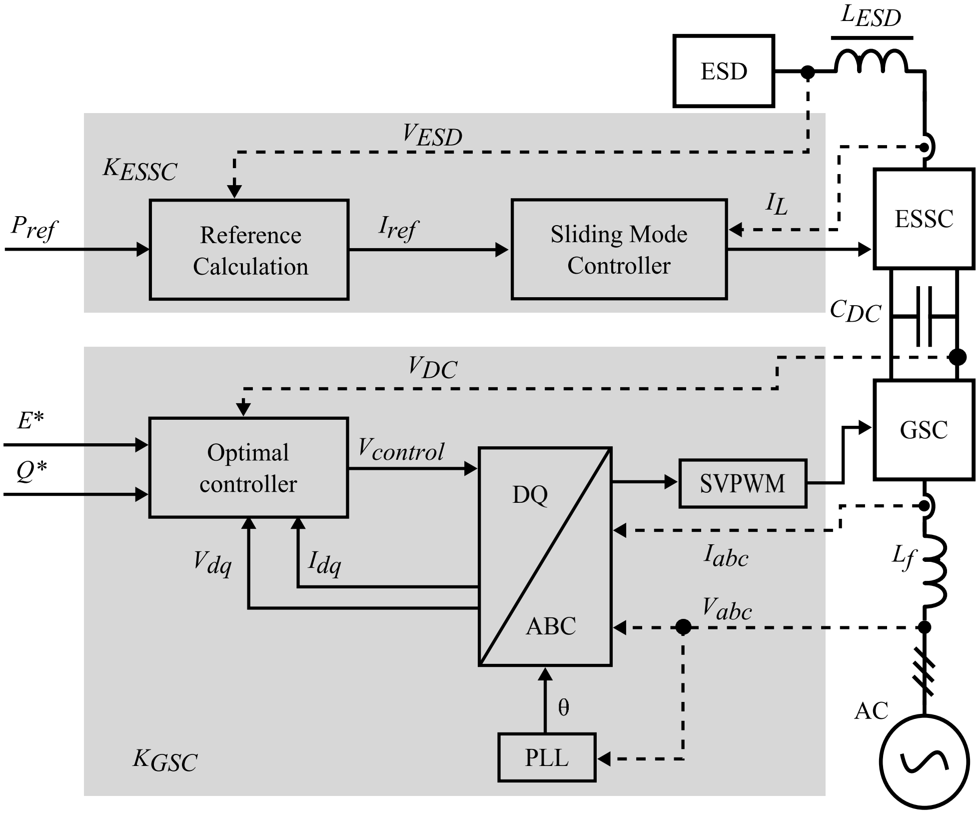

Figure 4.1.: Adopted converter topology to interface the ESS with the microgrid.

work in buck mode delivering energy to the storage device or in boost mode draining energy from the storage device. Each operating mode is achieved by setting the proper duty cycle on each switch. Switches S_{w1} and S_{w2} are operated in a complementary manner. This switching scheme avoids discontinuous operation for low current set-points. In both modes, the anti-parallel diodes act as free-wheeling diodes.

The DC–link provides a certain degree of decoupling between both converters, permitting the design of each controller separately. Commonly, the GSC in grid connected mode is controlled with a cascaded control scheme. For details on the control of the GSC, see Chapter 3. The controller of the ESSC is described in detail in the next section.

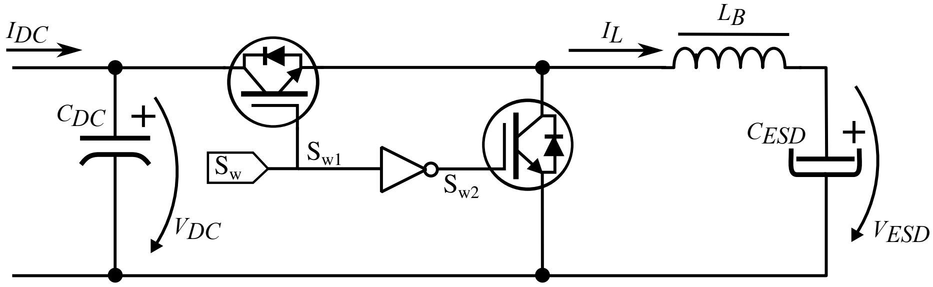

Mode Buck: S_{w1} duty cycle $> 50\%$ $S_{w2} = \overline{S_{w1}}$
Mode Boost: S_{w1} duty cycle $< 50\%$ $S_{w2} = \overline{S_{w1}}$

Figure 4.2.: Bidirectional DC-DC converter used in the ESSC.

4.3. Sliding mode control of the ESS

Clearly, the system in Figure 4.2 is a VSS, *i.e.*, a system with dynamic changes in the conduction state of the switches. It is well known that SM techniques provide quite effective control strategies in the case of VSS [128, 166]. For further details on background of SM control, refer to Appendix B.2.

For control algorithms, such as SM control, an instantaneous model of the switches is utilized. From Figure 4.2, it is possible to see that the structure and dynamics of the system strongly depend on the switch conducting state, even the energy flow direction can be changed with the switch operation. Actually, the DC-DC converter can be seen as formed by two subsystems (buck and boost) that can be selected according to the duty cycle applied to the switches S_{w1} and S_{w2}. These two operation modes can be synthetically described by the following unified model

$$\begin{cases} \dfrac{d}{dt} I_L = -\dfrac{V_{ESD}}{L_{ESD}} + \dfrac{V_{DC}}{L_{ESD}} S_w, \\ \dfrac{d}{dt} V_{ESD} = \dfrac{I_L}{C_{ESD}}, \end{cases} \tag{4.1}$$

where C_{ESD} is the capacitance of the super-capacitor and

$$S_{w1} = S_w, \qquad S_{w2} = \overline{S_w},$$

where the overline denotes the logic inverse state, *i.e.* if $S_w = 1$ (switch closed) then $\overline{S_w} = 0$ (switch open). This equation represents the DC-DC converter dynamics for both operation modes. When the duty cycle of S_w is lower than 50%, the DC-DC converter works as buck and otherwise it works in boost mode.

The ESSC must fulfill several operation objectives depending on the microgrid and the supercapacitor states. Three clear objectives can be identified.

- Startup: the supercapacitors are charged from zero initial condition at constant current.
- Constant Power: I_L is controlled so that there is a power transfer from/to the grid according to a power reference P^{ref} imposed by the MGCC. Power mismatch between P^{ref} and the actual power transferred to the microgrid, due to power losses, is assumed to be compensated by the MGCC.
- Voltage Limitation: once V_{ESD} reaches the maximum or minimum operation voltage, V_{ESD} is maintained constant.

As mentioned above, these objectives are accomplished by the ESSC by controlling the inductor current I_L. In the rest of the section, it will be shown that these objectives can be achieved with a single, simple and easy to implement sliding surface whose reference is modified in correspondence with the pursued objective.

4.3.1. Startup

The target of this stage is to pre-charge the supercapacitors in order to be able to run automatically from a zero initial charge condition. To achieve this goal the current through inductor L_{ESD} is regulated at a constant value $I_{\max}$, the current limit of the supercapacitors. Here, the DC-DC converter works in buck mode. The following sliding surface

$$\mathcal{S}(I_L) = I_{\max} - I_L = 0 \tag{4.2}$$

is proposed associated with the switching logic

$$S_w = \frac{\operatorname{sign}(I_{\max} - I_L) + 1}{2}, \tag{4.3}$$

where sign denotes the sign function. Then, it must be verified if (4.2) qualifies as a sliding surface, *i.e.*, if it satisfies the necessary and sufficient condition for sliding mode establishment, also known as transversality condition ($\mathcal{L}_g\mathcal{S} = -V_{DC}/L_{ESD} < 0$), where $\mathcal{L}$ is the Lie derivative [166]. If this condition is fulfilled, it can be ensured that the state trajectories point toward the manifold from both sides. The existence condition can be obtained by the equivalent control method. The equivalent control is obtained from the invariance condition ($\mathcal{S} = 0$ and $\dot{\mathcal{S}} = 0$) and in the case of the switching law (4.3), the equivalent control is

$$S_{w_{eq}} = \frac{V_{ESD}}{V_{DC}}. \tag{4.4}$$

SM regimen exists on the manifold whenever the equivalent control satisfies that $0 \leq S_{w_{eq}} \leq 1$. That is, there exists SM on the manifold if $0 \leq V_{ESD} \leq V_{DC}$ (SM domain). This condition is always satisfied in the DC-DC converter topology in Figure 4.2.

The dynamics in SM is obtained by substituting S_w with the equivalent control in (4.1), resulting in

$$\begin{cases} \dfrac{d}{dt}I_L = 0 \\ \dfrac{d}{dt}V_{ESD} = \dfrac{I_{\max}}{C_{ESD}} \end{cases} \tag{4.5}$$

This equation reveals that there is no dynamics in the regulated current (positive constant current) and that the supercapacitor voltage increases linearly with time.

Notice that other current references can be used. Moreover, a similar SM control can be used to discharge the super-capacitor. In this case, the current reference is negative and the ESSC works in boost mode. Therefore, the switching logic is identical to (4.3) but now S_{w1}'s duty cycle is lower than S_{w2}'s. In this way, the system can be turned off for maintenance purposes, for example.

4.3.2. Power control model

In this stage, the control law is similar to the previous case but the maximum current reference is substituted with the current needed to transfer the power demanded by the MGCC. The power reference depends on the particular microgrid operation and can be positive or negative. Therefore, the DC-DC converter must work in buck mode and boost mode to allow a bidirectional power transfer.

In this stage, the surface utilized is

$$\mathcal{S}(I_L) = \frac{P^{ref}}{V_{ESD}} - I_L = 0 \tag{4.6}$$

which verifies the transversality condition since $-V_{DC}/L_{ESD} < 0$ holds. Hence, the switching logic

$$S_w = \frac{\text{sign}(\frac{P^{ref}}{V_{ESD}} - I_L) + 1}{2} \tag{4.7}$$

ensures the SM regimen.

The equivalent control results

$$S_{w_{eq}} = \frac{V_{ESD}}{V_{DC}} - \frac{(P^{ref})^2 L_{ESD}}{V_{ESD}^3 C_{ESD} V_{DC}}. \tag{4.8}$$

The SM domain,

$$\frac{(P^{ref})^2 L_{ESD}}{V_{ESD}^3 C_{ESD}} \leq V_{ESD} \leq V_{DC} + \frac{(P^{ref})^2 L_{ESD}}{V_{ESD}^3 C_{ESD}},$$

is always accomplished.

The dynamics during the SM regimen are obtained by substituting (4.8) in (4.1) and is given by

$$\begin{cases} \quad \dfrac{d}{dt} I_L = -\dfrac{I_L^3}{P^{ref} C_{ESD}}, \\ \dfrac{d}{dt} V_{ESD} = \dfrac{I_L}{C_{ESD}} = \dfrac{P^{ref}}{V_{ESD} C_{ESD}}. \end{cases} \tag{4.9}$$

The trajectory of the states in SM regimes is illustrated in Figure 4.3. It can be observed that for all positive values of I_L, its derivative is negative and for all for negative values, its derivative is positive. Therefore, from all initial conditions, the inductor current converges to the stable equilibrium point $I_L = 0$. For the supercapacitor voltage, its derivative is always positive (for positive inductor currents, buck mode) and then V_{ESD} will increase if the power reference remains with positive values. This is a characteristic of the system and is independent of the control strategy. For this reason, a voltage limitation mode is necessary to prevent the super-capacitor from being damaged, which is explained in the next subsection.

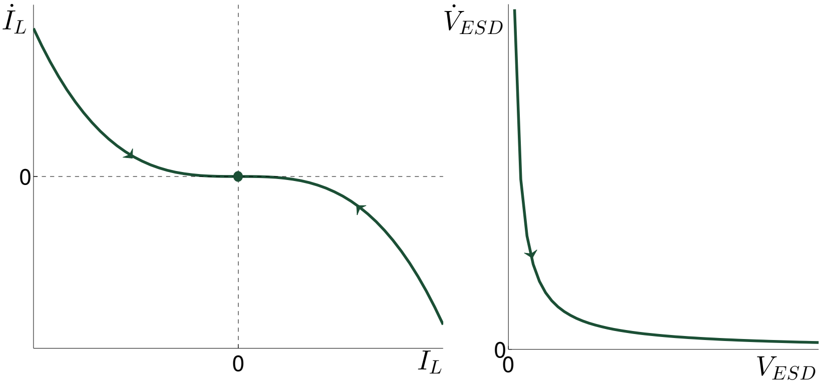

Figure 4.3.: Sliding mode dynamics in constant power.

In both modes, the switching law is the same whether working as buck delivering energy to the storage device or working as boost consuming energy from the storage device. This is because of an inversion of the sign in the inductor current and reference.

Remark 1 *It is important to note that the surface remains as a current surface. The only difference is that the reference is shaped dynamically.*

4.3.3. Voltage limitation

For operative and safety reasons, supercapacitors must operate within a voltage range limited by upper $\overline{V}_{ESD}$ and lower $\underline{V}_{ESD}$ limits. The upper limit is to protect the integrity of the supercapacitors. The lower limit is due to the fact that the supercapacitors cannot store much energy below this voltage and also, high current references could arise for high power references. To guarantee that these values are reached smoothly, an additional sliding surface is proposed, which is applied when V_{ESD} is in the transition regions $\mathcal{R}_l := \{V_{ESD} \,|\, \underline{V}_{ESD} < V_{ESD} < \underline{V}_{ESD} + V_\Delta\}$ and $\mathcal{R}_u := \{V_{ESD} \,|\, \overline{V}_{ESD} - V_\Delta < V_{ESD} < \overline{V}_{ESD}\}$, where V_Δ defines the width of the transition regions.

Therefore, when the supercapacitor voltage is in the transition region $\mathcal{R}_u$, the sliding surface is

$$\mathcal{S}(I_L) = \frac{P^{ref}(\overline{V}_{ESD} - V_{ESD})}{(\overline{V}_{ESD} - V_\Delta)V_\Delta} - I_L = 0, \tag{4.10}$$

which verifies the transversality condition since $-V_{DC}/L_{ESD} < 0$ holds. In this case, the switching logic is given by

$$S_w = (\text{sign}\left(\frac{P^{ref}(\overline{V}_{ESD} - V_{ESD})}{(\overline{V}_{ESD} - V_\Delta)V_\Delta} - I_L\right) + 1)/2. \tag{4.11}$$

The equivalent control results

$$S_{w_{eq}} = \frac{V_{ESD}}{V_{DC}} - \frac{(P^{ref})^2 L_{ESD}(\overline{V}_{ESD} - V_{ESD})}{(\overline{V}_{ESD} - V_\Delta)^2 V_\Delta^2 C_{ESD} V_{DC}}. \tag{4.12}$$

The SM domain is

$$\frac{(P^{ref})^2(\overline{V}_{ESD} - V_{ESD})L_{ESD}}{(\overline{V}_{ESD} - V_\Delta)^2 V_\Delta^2 C_{ESD}} < V_{ESD} < V_{DC} + \frac{(P^{ref})^2(\overline{V}_{ESD} - V_{ESD})L_{ESD}}{(\overline{V}_{ESD} - V_\Delta)^2 V_\Delta^2 C_{ESD}},$$

that is always accomplished.

Substituting (4.12) in (4.1), the dynamics in the SM regimen can be obtained

$$\left\{\begin{aligned} \frac{d}{dt}I_L &= -\frac{P^{ref}}{(\overline{V}_{ESD} - V_\Delta)V_\Delta}\frac{I_L}{C_{ESD}}, \\ \frac{d}{dt}V_{ESD} &= \frac{P^{ref}}{C_{ESD}(\overline{V}_{ESD} - V_\Delta)V_\Delta}(\overline{V}_{ESD} - V_{ESD}). \end{aligned}\right. \tag{4.13}$$

These expressions can be seen in Figure 4.4. It is clear that for all initial conditions, the current approaches the stable equilibrium point $I_L = 0$. In addition the supercapacitor voltage converges to the final value $V_{ESD} = \overline{V}_{ESD}$ without overpassing the limit, whereas the inductor current goes to zero smoothly.

In the case of a negative power reference, the ESSC operates in boost mode. In this circumstance, when the voltage reaches the lower transition region $\mathcal{R}_l$, a switching law similar to (4.11) can be used.

Notice that this operating mode is necessary, first, to avoid dissconnecting the inductor when non-zero current is flowing through it, and second, to compensate supercapacitor losses, for example, if the system does not absorb energy for a long period of time.

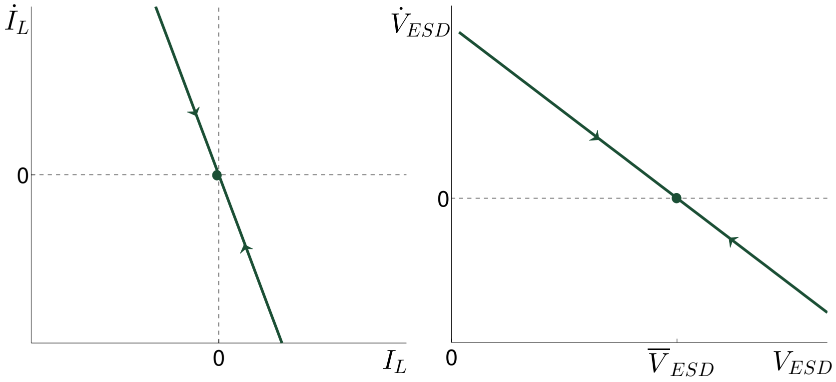

Figure 4.4.: Sliding mode dynamics in voltage limitation mode.

4.3.4. Complete control strategy

Observing the SM surfaces (4.2), (4.6) and (4.11), it is clear that the different operation objectives can be fulfilled with the same switching law

$$S_w = \frac{\operatorname{sign}(I_{ref,i} - I_L) + 1}{2} \tag{4.14}$$

with

- startup
$$I_{ref1} = I_{\max}, \tag{4.15}$$

- constant power mode
$$I_{ref2} = P^{ref}/V_{ESD}, \tag{4.16}$$

- voltage limitation mode (lower limit)
$$I_{ref3} = \frac{P^{ref}}{(\underline{V}_{ESD} + V_{\Delta})V_{\Delta}}(V_{ESD} - \underline{V}_{ESD}), \tag{4.17}$$

- voltage limitation mode (upper limit)
$$I_{ref4} = \frac{P^{ref}}{(\overline{V}_{ESD} - V_{\Delta})V_{\Delta}}(\overline{V}_{ESD} - V_{ESD}). \tag{4.18}$$

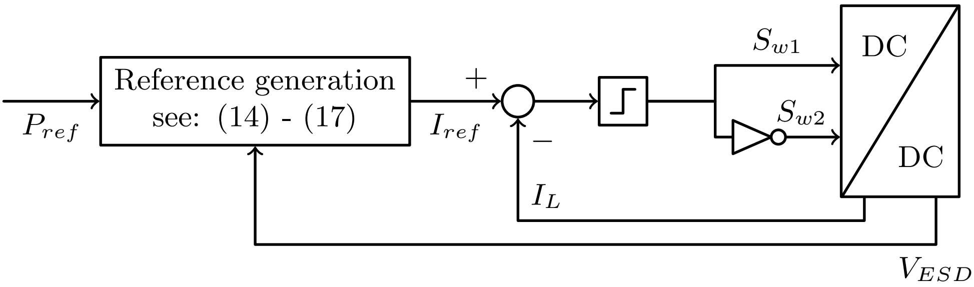

Figure 4.5.: Sketch of the proposed control strategy based on sliding mode control.

For the system startup, the control strategy imposes a constant current reference. The same surface, but with a negative reference can be utilized to discharge the supercapacitors. The discharge of the supercapacitors is necessary in order to ensure a safe operation. In constant power stage, the current reference is computed according to the current supercapacitor voltage in order to provide the amount of power indicated by the MGCC. Finally, when the supercapacitors reach the lower or upper voltage limits, a transition sliding surface is used to smoothly lead the inductor current to zero. A schematic representation of the control strategy is illustrated in Figure 4.5. In Figure 4.6, the different operating mode can be seen in the voltage-current plane.

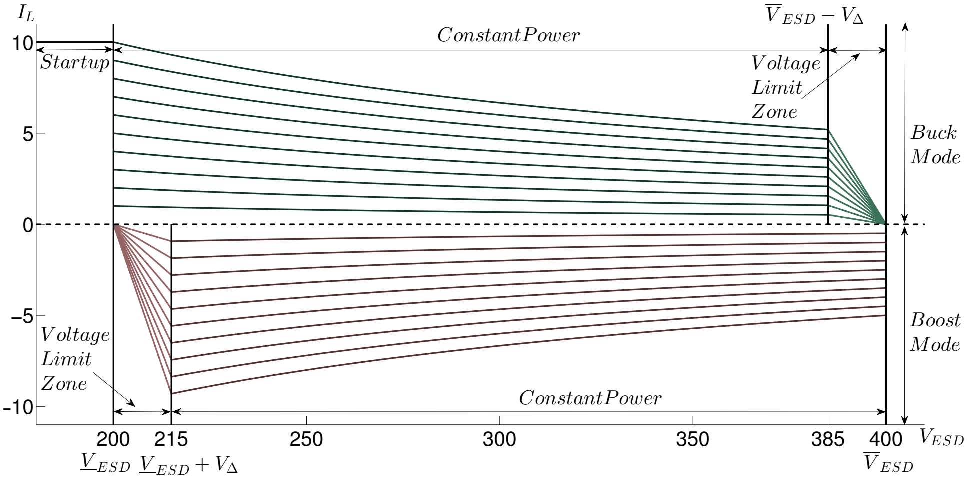

Figure 4.6.: Representation of sliding surfaces under the different operating modes and objectives.

Remark 2 *In all cases there exists only one stable equilibrium point for the inductor current regulation. Therefore, from the previous analysis it can be concluded that the point is globally reached.*

Remark 3 *It is worth mentioning that the grid, the inverter along with the DC link capacitor and the controller* K_{GSC} *are considered a system that is perturbed by the rest of the system (ESSC). This consideration is a consequence of the robustness against variability of the DC link voltage and the supercapacitor voltage provided by the SM control. Hence, providing that a correct design of* K_{GSC} *ensures that the DC link voltage is higher than the maximum supercapacitor voltage plus the operation voltage of the converter (a requirement of DC-DC converter to work properly), the controller* K_{ESSC} *will work correctly (performance and stability) under SM control. This is one of the advantages of SM control.*

4.4. Test bench implementation

The proposed SM control strategy has been implemented in the set-up shown in Figure 4.7. The DC link voltage, V_{DC}, is set at 700 V, the inductance, L_{ESD}, is 4.27 mH and the DC link capacitance, C_{DC}, is 2 mF. The DC-DC converter has been implemented using IGBTs, with each IGBT rated at 20 A maximum. The firmware has been written using ANSI-C language, compiled with speed optimizations, running on a TMS320F2808 DSP.

The GSC shown in Figure 4.1 is not the main contribution of this work. A detailed explanation of the control algorithm and the implementation can be found in [18, 165]. Notice that the switching frequency of the GSC is 12 kHz, higher than the maximum switching frequency produced by the SM controller. Different switching frequencies on both converters helps to reduce noise on the sampled signals. This noise is produced by the electromagnetic interferences between the converters.

The supercapacitor bank is composed of thirty five modules[1] of 16.2 V and 58 F each, connected in series. For safety reasons, the bank has a maximum operating voltage of 400 V and a capacity of 1.7 F. Details on the experimental platform are summarized in Appendix D.3.

---

[1] MAXWELL BMOD0058 E016 B02

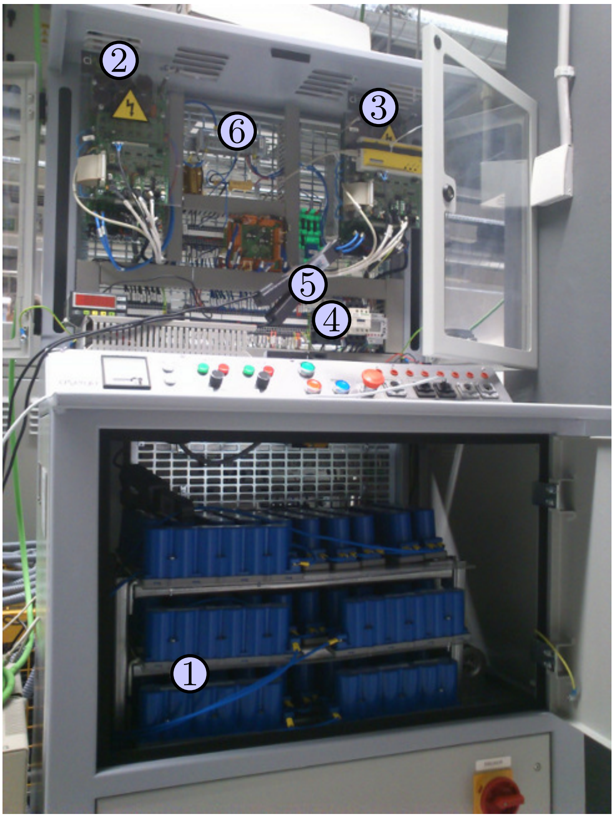

Figure 4.7.: Experimental set-up for the implementation of the proposed SM control strategy. (1) supercapacitor bank, (2) DC-DC converter, (3) grid side converter, (4) protections, (5) current prove, (6) DC–link.

4.4.1. Control algorithm

The control algorithm implemented in the DSP can be summarized in the following pseudocode.

```
while ($V_{ESD} < \underline{V}_{ESD}$) do                                ▷ Startup
    $S_w = (\text{sign}(I_{ref1} - I_L) + 1)/2$
end while
Shutdown=FALSE
while (shutdown=FALSE) do
    Read $V_{ESD}$
    if ($V_{ESD} > \overline{V}_{ESD} - V_{\Delta}$) AND ($P^{ref} > 0$) then
                                                         ▷ Voltage Limitation
        $S_w = (\text{sign}\,(I_{ref4} - I_L) + 1)/2$
    else if ($V_{ESD} < \underline{V}_{ESD} + V_{\Delta}$) AND ($P^{ref} < 0$) then
```

```
                                                        ▷ Voltage Limitation
        $S_w = (\text{sign}\,(I_{ref3} - I_L) + 1)/2$
    else if $(\underline{V}_{ESD} < V_{ESD} < \overline{V}_{ESD})$ then
                                                        ▷ Constant Power
        $S_w = (\text{sign}\,(I_{ref2} - I_L) + 1)/2$
    end if
    if $(V_{ESD} > \overline{V}_{ESD} + V_\Delta)$ then                ▷ Protection
        Shutdown=TRUE
    end if
    if $(V_{ESD} < \underline{V}_{ESD} - V_\Delta)$ then                ▷ Protection
        Shutdown=TRUE
    end if
end while
```

For the DC-DC converter in the implementation, the pre-charge current I_{ref1} is set to 10 A, the maximum operating voltage $\overline{V}_{ESD}$ to 400 V, the minimum operating voltage $\underline{V}_{ESD}$ to 200 V and the voltage threshold V_Δ to 15 V. Current references are computed using equations (4.15) to (4.18).

4.5. Experimental results at full ratings

Three scenarios were analyzed in order to evaluate the proper operation of the proposed ESS: the startup, the tracking of several power references and the voltage limitation. For the experiment, the converter was operated at its nominal values to evaluate the proposed control strategy in a real situation.

Startup

During the startup scenario, the supercapacitors were pre-charged at constant current until a minimum operating voltage was reached. Figure 4.8 shows the current and the voltage in this scenario. The supercapacitor pre-charge current set-point was 10 A. It can be seen in Figure 4.8 that the controller achieves a suitable regulation of the current at the desired set-point. The minimum current ripple amplitude is a consequence of the hysteresis band used in the SM control, the inductance L_{ESD} and

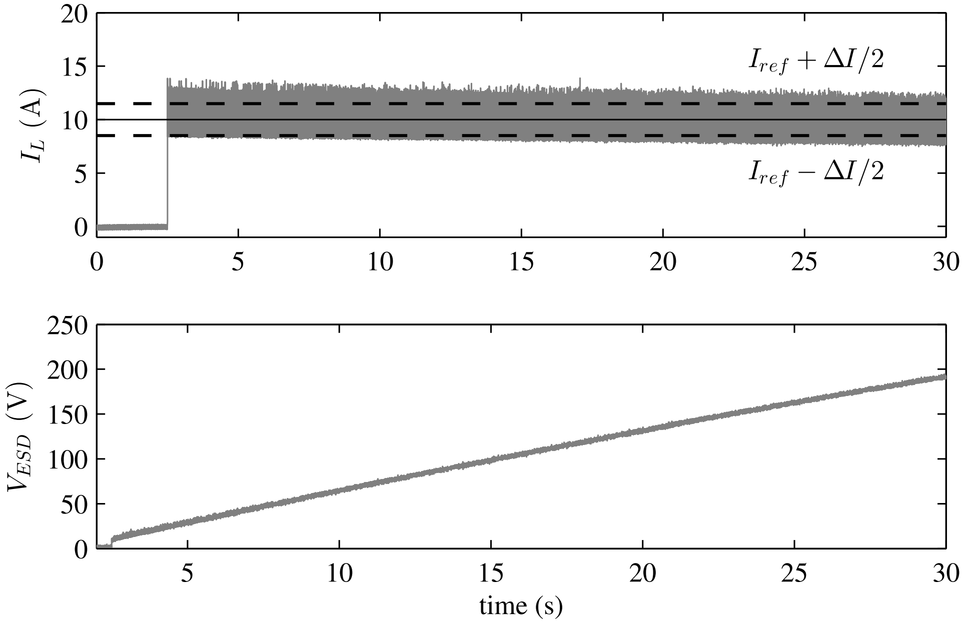

Figure 4.8.: Current I_L and voltage V_{ESD} during pre-charge stage. Dashed lines are the bounds of the current ripple.

the voltage difference between V_{ESD} and V_{DC}. The ripple setting of the controller (ΔI) is 3.5 A, shown with dashed lines.

Figure 4.9 presents a detail of the current to show the reaching mode. This is the current trajectory starting from the initial conditions $I_L = 0$ to the SM surface $\mathcal{S}(I_L) = 10\ \text{A} - I_L = 0$. The current slightly overpasses the hysteresis band as a result of the limited sampling frequency of the DSP and also measure noise. From Figure 4.9 it is possible to see that the current slope when S_{w1} is closed is much larger than when open. If the current rises too fast, the DSP is not able to achieve an acute computation of the switching law (4.3). The slope of the current depends on the voltage difference between the supercapacitors and the DC link. Therefore, the phenomenon is more noticeable at the initial state, where the voltage difference between supercapacitors and the DC link is very high, in this case 700 V. This fast variation of the current results in a small delay in the detection of the crossing of the current with the upper limit of the hysteresis band. This is a limitation of the hardware employed, although the performance is suitable for the selected application. This phenomena is evidenced in Figure 4.8. When the supercapacitor voltage approaches the operating values, the current

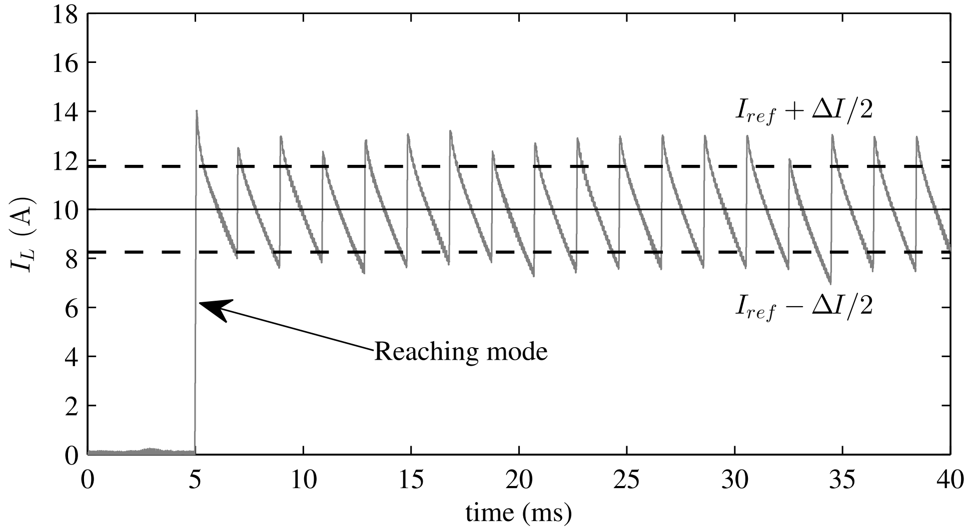

Figure 4.9.: Detail of the reaching mode during the system startup. Dashed lines are the bounds of the current ripple.

better fits the desired ripple bands. It is important to note that the startup stage is not a permanent mode of operation and the performance achieved is suitable for the discussed application.

Constant Power

The usual operation of the supercapacitors on the microgrid is to track the power set-points given by MGCC. The power is measured as the product of the supercapacitor voltage times the current flowing through the inductor L_{ESD}. By convention, positive power means that the power is being transferred from the DC link to the supercapacitors, and vice-versa, negative power means that the power is being supplied to the DC link. The average supercapacitor power is shown in Figure 4.10, as the interest of this application is on the mean value of the transferred power. Notice that the actual power transferred to the grid is lower than the supercapacitor power due to power losses.

The gray line of the I_L current in Figure 4.10 is the instantaneous current flowing through the DC inductor, and the black line is the current reference I^{ref}. It can be seen that I_L converges rapidly to the new SM surface when there is a change in the power reference. To show that the AC power consumed or injected to the microgrid is kept constant, Figure 4.10 shows the phase-a AC current during the tracking of six different

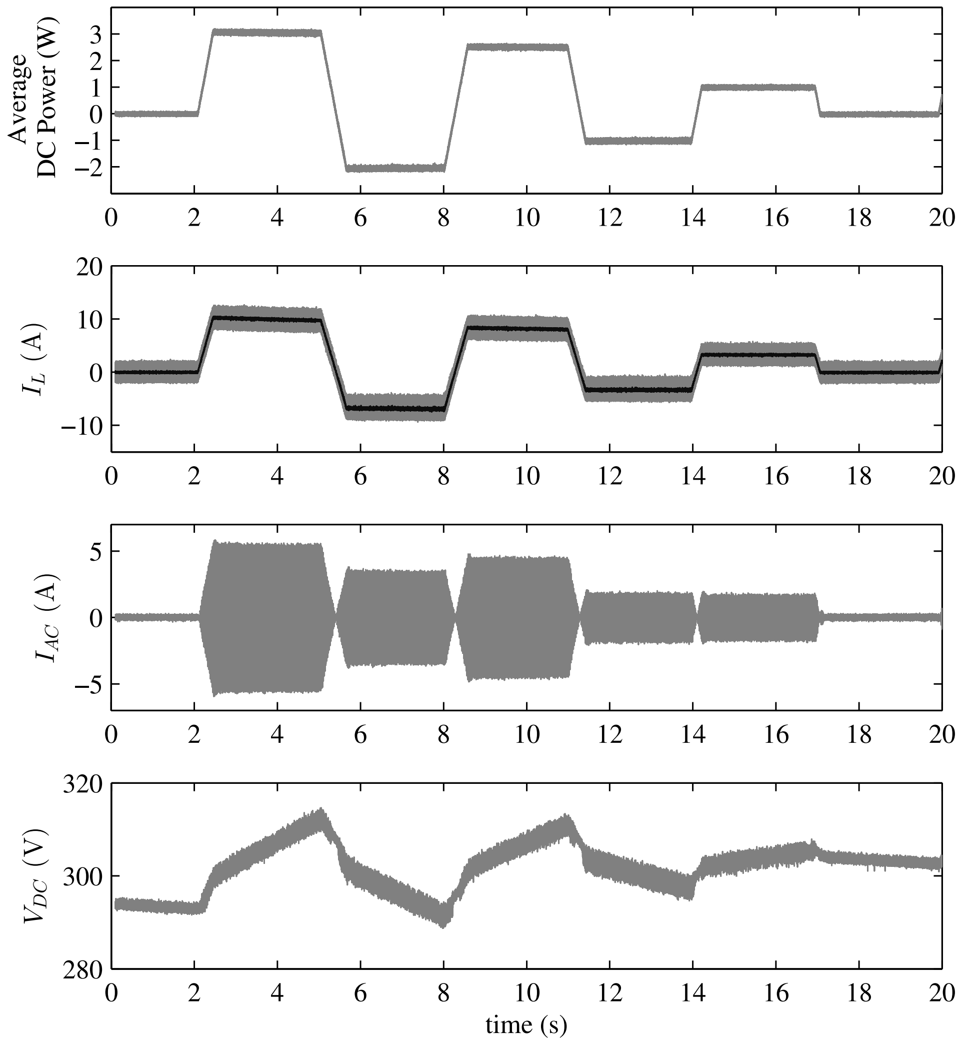

Figure 4.10.: Extract of most relevant states of the converter during normal operation. From top to bottom, the measured states are: average supercapacitor DC power, I_L current, AC current corresponding to phase-a of a tri-phase system and the voltage of supercapacitor bank.

power set-points, $P_{ref_1} = 0$ kW, $P_{ref_2} = 3$ kW, $P_{ref_3} = -2$ kW, $P_{ref_4} = 2.5$ kW, $P_{ref_5} = -1$ kW, $P_{ref_6} = 1$ kW. As a consequence of the current ripple, the super-capacitor bank voltage also has a small ripple.

It must be noted that although the SM controller is capable of an extremely fast transition between sliding surfaces with the reaching mode, the hardware of the experimental set-up cannot withstand such an abrupt change on the current flowing into the DC link, resulting in trips of the protections. For this reason the transition between different power set-points has been implemented with a ramp. The transition is fast and presents no overshoot. The tracking error is zero since the SM control strategy ensures zero steady state error.

A close lookup of the AC and DC currents of the converter are shown in Figure 4.11. The current I_L presents a constant ripple imposed by the hysteresis band of the sliding mode controller. The minimum current ripple and maximum switching frequency are a consequence of the DC inductance L_{ESD}, the voltage difference between the V_{ESD} and V_{DC}, and the sampling frequency of the controller. For this experimental set-up, the average current ripple is about 15% of the current limit and the switching frequency varies form 8 kHz to 11 kHz during normal operation. If lower ripple or higher frequency are required, some of the aforementioned parameters should be improved.

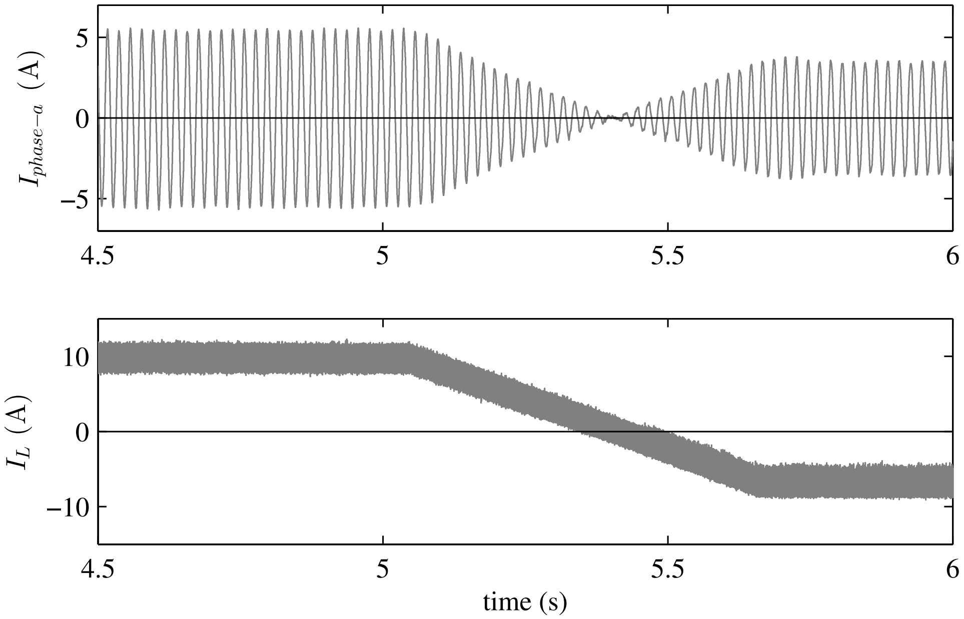

Figure 4.11.: Detail of the phase-a AC current and the DC I_L current during a sign change in the power flow.

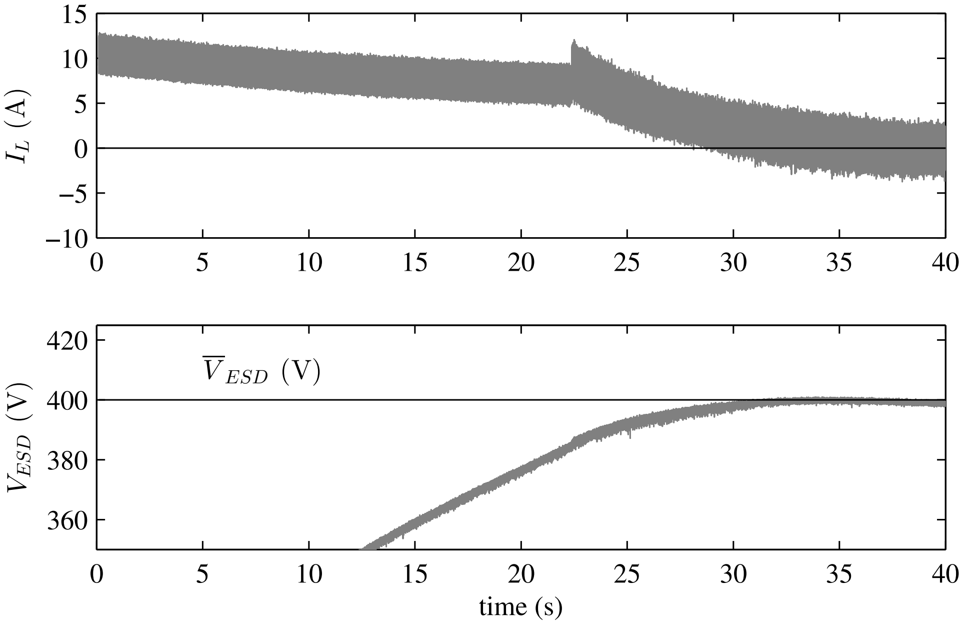

Figure 4.12.: Detail of the current I_L and voltage V_{ESD} during the voltage limitation mode.

Voltage limitation validation

The sliding surface defined in equation (4.10) is responsible for driving V_{ESD} to $\overline{V}_{ESD}$ smoothly and with no overshoot. The results of the implementation of the surface are shown in Figure 4.12. The supercapacitor voltage V_{ESD} is kept at 400 V ($\overline{V}_{ESD}$) in this experiment, guaranteeing the integrity of the supercapacitor bank. The voltage is kept constant at $\overline{V}_{ESD}$, maintaining the supercapacitors at the desired capacity until a negative power reference is received from the MGCC. Upon the reception of the discharge command, the controller re-enters in the constant power stage, starting a new cycle.

4.6. Conclusion of the chapter

A new control strategy for a bidirectional AC/DC converter to control the power exchange between a supercapacitor bank and a grid connected microgrid was presented. The proposed strategy is based on a unique SM surface which is able to cover all the operating conditions, even the startup of the supercapacitor bank. Different current references, depending on the particular objective, were used to produce a commanding law for the switching devices. The proposed control is simple to implement in the DSPs commonly used in power converters and also ensures proper operation in different conditions, even under changes in the system parameters. Also, as the whole strategy is based on sliding mode techniques, no slope compensation is needed for duty cycles above 50% as is required in fixed frequency current mode control. The proper operation and robustness were experimentally corroborated. Several scenarios covering all operating conditions, including the startup and extreme situations in which the supercapacitor reaches the maximum voltage, were analyzed. These results show that the proposed control strategy exhibits a suitable performance even in the presence of adverse conditions. Some hardware limitations can affect the system performance (ripple levels), especially during the startup. These limitations can be circumvented by increasing the inductor and using a more powerful ADC/DSP. This is a limitation of the laboratory hardware that can be avoided with non-expensive modifications in the equipment. Nevertheless, in microgrid applications such improvement in the ripple level might not be necessary.

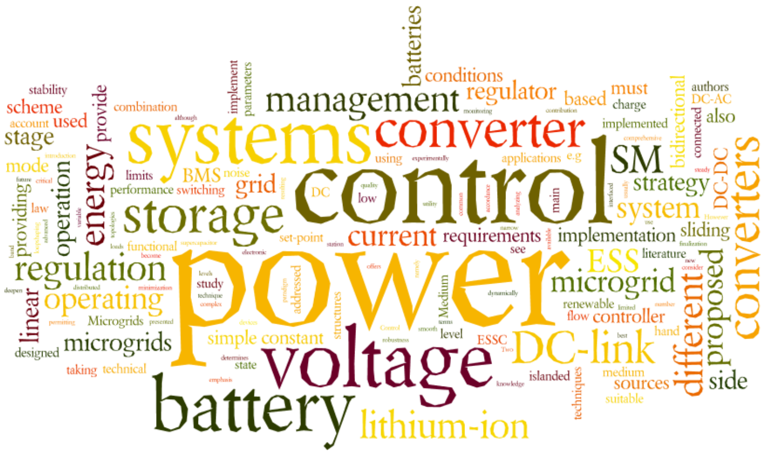

5

Control of a lithium-ion battery storage system for microgrid applications

This chapter presents the control scheme for a lithium-ion battery bidirectional DC/AC power converter intended for microgrid applications. The switching devices of a bidirectional DC converter are commanded by a single sliding mode control law, dynamically shaped by a linear voltage regulator in accordance with the battery management system. The sliding mode controller facilitates the implementation and design of the control law and simplifies the stability analysis over the entire operating range. Control parameters of the linear regulator are designed to minimize the impact of commutation noise in the DC–link voltage regulation. The effectiveness of the proposed control strategy is illustrated by experimental results.

5.1. Introduction

Microgrids combine a number of different power sources and loads together with a coordinated management system providing the capability of maintaining the operation even with the microgrid disconnected from the utility [96]. To provide high power quality, the fluctuating renewable power sources must be compensated with storage systems [48, 69]. Medium power lithium-ion batteries are suitable storage systems for providing islanding capabilities [104, 135, 146].

The main functional requirement of an ESS depends on the microgrid state, either grid connected or islanded. On the one hand, when working grid connected, a central EMS sets the power set-point to every local controller in each ESS in the microgrid in order to optimize the power flow in terms of energy costs. On the other hand, when islanded, the field level control in each ESS determines locally its own power set-point by regulating the voltage and frequency. This local power set-point can be modified by the central EMS, to reorganize the power flow in the islanded microgrid. Notice that the field level control has priority over the management level control in order to ensure the islanded MG stability. For more details on the implementation of microgrid hierarchical control, see Chapter 2.

Medium power lithium-ion batteries are equipped with a battery management system (BMS) monitoring critical parameters of the battery, providing technical limits for the battery current and voltage. To implement the functional and technical requirements, ESS can be interfaced with a two stage bidirectional power converter to the microgrid [100]. Two stage power converters are necessary in DC-AC systems with different voltage levels at the converter input and output. The first stage is a power electronic DC-AC inverter implementing a droop control [113]. The DC–link voltage must be kept in a narrow band to provide an almost constant DC voltage source to the GSC, as described in Chapter 3. The second stage, a DC-DC voltage regulator, namely the ESSC, controls the DC–link voltage through the regulation of the battery current. The ESSC must also guarantee that the BMS limits are never exceeded, performing a tight regulation of the charging and discharging current over all the operating range and conditions as required by lithium-ion batteries [25].

Different topologies of DC-DC converters are available in the literature, ranging from simple buck or boost converters [29, 89, 143] to more complex structures based on dual active bridge [122]. The application of power converters to energy storage system has also been addressed. For example, the control of hybrid battery/supercacitor systems is addressed in [89]. In [100], a battery charge station for electrical vehicle is presented but the charge algorithm is limited to a constant current and constant voltage operation. Other authors (see *e.g.* [51, 103, 134]) study the management of storage systems, but do not deepen in the low level control of such systems. In Chapter 4, a power control for supercapacitor storage systems based on sliding mode (SM) control is proposed. A comprehensive study of SM controlled DC-DC converters has been reported in [13], analysing the performance and stability of the battery side current regulation.

The main contribution of this chapter is to propose a new control strategy for the regulation of the DC–link voltage using the battery side converter, taking into account the requirements and limitations of medium power lithium-ion batteries when used in microgrids applications. The proposed strategy covers all ESS operating conditions: DC–link precharge, DC–link regulation and battery charge/discharge finalization. The strategy is implemented combining the SM control proposed in Chapter 4 and linear regulators. In contrast with Chapter 4, where the focus has been stressed on the DC current control, in this chapter, the focus is on the voltage control of the DC–link.

Sliding mode permits the combination of designs with different objectives and also provide a quite simple implementation [161]. This combination of different techniques offers the robustness of SM control, a smooth transition between operating conditions and a simple implementation and tuning. The linear voltage regulator is designed using loopshaping techniques, making special emphasis in the minimization of the switching noise, which would reduce the steady state performance of the controller. For more details on the robust control and loopshaping technique, see Appendix B. The analysis of the voltage noise generated by the switching of the IGBT is reported in Appendix C. The proposed controller changes automatically the set-points according to the BMS, permitting the operation of the power converter in the different operating modes. The proposed ideas are experimentally implemented in a 4 kVA power converter interfacing a 240 V DC, 20 kW lithium-ion battery with a 400 V AC grid.

5.2. Energy storage systems based on lithium-ion batteries for microgrids

To supply the electrical power demand in RESs based microgrids, renewable energy sources need to be supported by ESSs, equipped with droop control to maintain the island voltage magnitude and frequency, as explained in Chapter 3. ESSs are usually composed by an ESD and a power electronic converter for the management and electrical interconnection of the DC voltage storage device and the AC grid. The adopted topology for the control of the power flow between the battery and the microgrid is illustrated in Figure 5.1. The DC-AC converter is composed by a DC-DC ESSC with a controller K_{ESSC} regulating the DC–link voltage and the GSC with controller K_{GSC} regulating the active and reactive power.

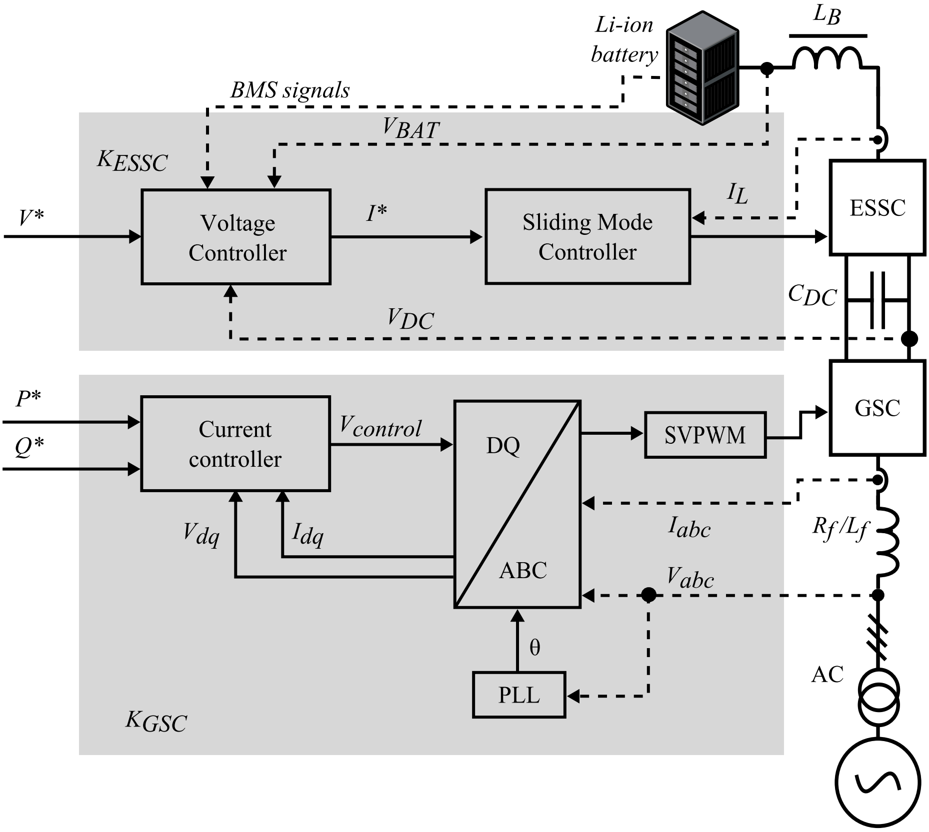

Figure 5.1.: Converter topology for interfacing lithium-ion batteries in microgrids.

5.2.1. Ancillary services of batteries in microgrids

When batteries are used in islanded microgrids, there are some functional requirements that must be met. This functions are implemented in the power electronic interface, by means of the control algorithms implemented in K_{ESSC} and K_{GSC}, and also in the microgrid central controller. The following services should be implemented.

1. Regulation of the AC active and reactive power. The droop control is commonly used as the power sharing mechanism for isolated micorgrids, see *e.g.* [124]. Typically, the power set-points for the droop control are given by a high level microgrid energy management system. The high level EMS must take into account the battery state for producing power references P^{ref} and Q^{ref}. This is, the EMS must ensure that the battery is neither completely discharged nor charged, in order to avoid loosing capacity to regulate the DC–link.

2. Black-start capability. The DC–link voltage must be pre-charged from the battery, with the DC-DC converter acting as a boost.

3. Safety protections in case of over/under discharge. The ESSC must limit the charging or discharging current in accordance with the BMS signals.

In the following sections, these functions will be analysed in detail, altogether with the control strategies and implementation details.

5.2.2. Grid side converter

The GSC is a three–phase, two–level voltage source converter. The model of the GSC with the inductive output filter L_f can be expressed in the DQ frame as (see Chapter 3.4)

$$\frac{d}{dt}\begin{bmatrix} i^d \\ i^q \end{bmatrix} = \begin{bmatrix} \frac{-Rf}{Lf} & \omega \\ -\omega & \frac{-Rf}{Lf} \end{bmatrix} \begin{bmatrix} i^d \\ i^q \end{bmatrix} + \frac{1}{Lf} \begin{bmatrix} v_o^d - v^d \\ v_o^q - v^q \end{bmatrix},$$

where $i_{d,q}$ are the AC currents in DQ frame, R_f and L_f are the resistance and inductance of the output filter respectively, v_{d,q_o} are the output voltage of the converter and $v_{d,q}$ are grid voltages, both in DQ frame, and ω is the AC voltage frequency.

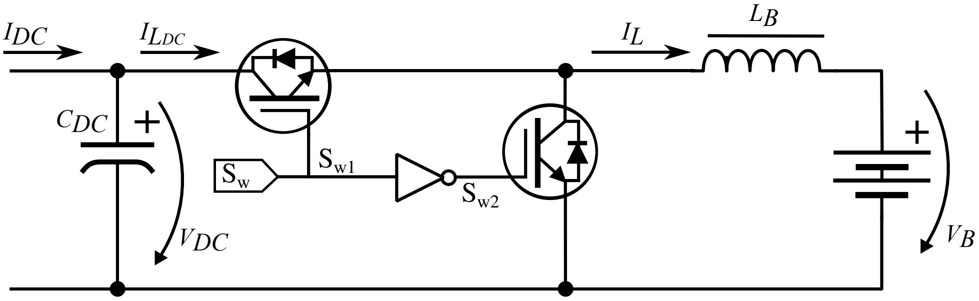

Figure 5.2.: Bidirectional DC-DC converter used in the ESSC.

For the sake of simplicity and to focus on the control strategy of the ESSC, we will use K_{GSC} as an AC active and reactive power controller, using a single current control loop in the DQ axis. This control scheme is much simpler than the typical droop control scheme used in islanded microgrids. However, this power loop and the droop control behaves identically from the K_{ESSC} control design point of view, acting as a DC current source for the DC–link.

5.2.3. Energy storage side converter

The topology selected for this application is a buck-boost converter based on a switched branch with an L-filter inductance, shown in Figure 5.2. In the literature it can also be found implementations using an output LCL-filter [13]. In this chapter, an L-filter has been chosen as it is the most common filter type for low voltage DC-DC converters adopted by industry [61].

In medium power battery systems, the BMS provides the charging sequence, indicating the instantaneous maximum dynamic charge and discharge current (MCC, MDC) and the battery maximum charge and discharge voltages (MCV, MDV). To preserve the battery life, the current must remain below MCC and over MDC, and the battery voltage must lie between MCV and MDV, as shown in the charge profile in Figure 5.3.

To derive an instantaneous model of the DC-DC power converter, it can be assumed that the voltage is always higher on the DC–link (V_{DC}) than on the battery side (V_B), although energy can flow in both directions. Switches S_{w1} and S_{w2} are operated in a complementary manner, avoiding discontinuous operation for low current set-points. The DC-DC converter can be seen as formed by two subsystems that can operate as

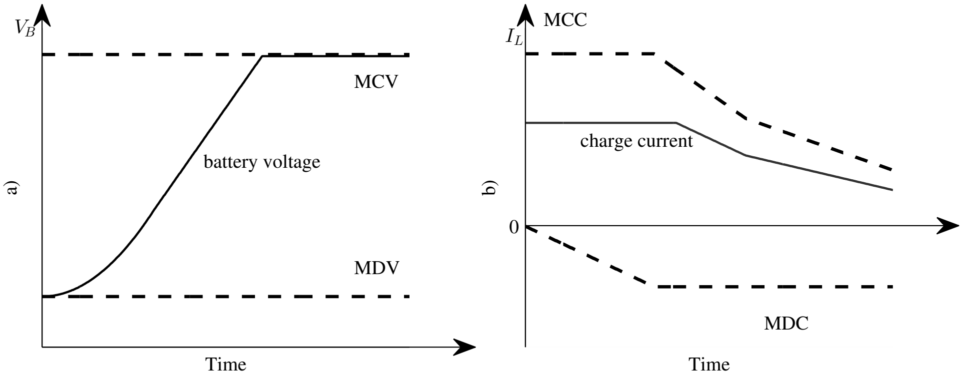

Figure 5.3.: Typical charge profile for medium power lithium-ion batteries with BMS.

buck or boost converters, which can be synthetically described by the following unified model

$$\begin{cases} \frac{d}{dt} I_L = -\frac{V_B}{L_B} + \left(\frac{V_{DC}}{L_B}\right) S_w, & (5.1a) \\ \frac{d}{dt} V_B = g(I_L, \vartheta), & (5.1b) \\ \frac{d}{dt} V_{DC} = \frac{1}{C_{DC}} \left(I_{DC} - I_{L_{DC}}\right), & (5.1c) \end{cases}$$

with $I_{L_{DC}} = I_L S_w$, where I_L is the inductor current, and S_w is the switch state, with $S_w = S_{w1} = \overline{S_{w2}}$, with the over-line denoting the logic inverse state (*i.e.* $S_w = 1$ represents switch closed and $\overline{S_w} = 0$ switch open). The function $g(\cdot)$ is the voltage dynamics of the battery in the linear region, and can be expressed as [25]

$$g(I_L, \vartheta) = \frac{1}{Q_B} I_L + R_{int} \frac{d}{dt} I_L + \epsilon(I_L, \vartheta),$$

with ϑ the temperature of the battery, $\epsilon(I_L, \vartheta)$ a function of the parasite capacitance and other non-linearities, R_{int} the internal resistance of the battery, and Q_B is the capacity of the battery. Since $I_L/Q_B + R_{int}\frac{d}{dt} I_L \gg \epsilon(I_L)$ for the operating range of the battery voltage, $g(I_L, \vartheta)$ can be approximated by

$$g(I_L, \vartheta) \approx \frac{I_L}{Q_B} + R_{int} \frac{d}{dt} I_L = \frac{I_L}{Q_B} + \frac{R_{int}}{L_B}(V_{DC} S_w - V_B). \qquad (5.2)$$

5.3. Control of the ESS

The energy stored in the ESS is governed by controllers K_{GSC} and K_{ESSC} according to the demanded active power P^{ref} and reactive power Q^{ref}. To track the power references, K_{GSC} injects or demands DC current from the DC–link. The DC–link voltage is regulated by the controller K_{ESSC}, which is formed by a linear voltage regulator producing the current set-point for the faster SM current regulator. This scheme allows the explicit limitation of the current reference to avoid over-current in the power electronic devices and in the battery. The DC–link permits to decouple the design of K_{GSC} and K_{ESSC}; the design of K_{GSC} assumes a constant voltage in the DC–link of the back-to-back converter.

5.3.1. Grid side converter: power control

The GSC exchanges active and reactive power with the microgrid, according to the power set-points given by the EMS. For the design of the GSC control, K_{GSC}, it is assumed that the DC–link voltage is constant. The AC power control is typically implemented by regulating the AC current. This current regulator is designed using a PI structure in a rotating DQ frame, a controller widely used with this inverter topology (see *e.g.* [141]). The current controller is

$$\frac{d}{dt}\begin{bmatrix} x_c^d \\ x_c^q \end{bmatrix} = \begin{bmatrix} k_{i_c} & 0 \\ 0 & k_{i_c} \end{bmatrix} \begin{bmatrix} e_c^d \\ e_c^q \end{bmatrix},$$

$$\begin{aligned} \begin{bmatrix} v_o^d \\ v_o^q \end{bmatrix} = \begin{bmatrix} 1 & 0 \\ 0 & 1 \end{bmatrix} \begin{bmatrix} x_c^d \\ x_c^q \end{bmatrix} &+ \begin{bmatrix} k_{p_c} & 0 \\ 0 & k_{p_c} \end{bmatrix} \begin{bmatrix} i^{d,ref} \\ i^{q,ref} \end{bmatrix} \\ &+ \begin{bmatrix} -k_{p_c} & L_f\omega_n \\ L_f\omega_n & -k_{p_c} \end{bmatrix} \begin{bmatrix} i^d \\ i^q \end{bmatrix} + \begin{bmatrix} 1 & 0 \\ 0 & 1 \end{bmatrix} \begin{bmatrix} v^d \\ v^q \end{bmatrix}, \end{aligned}$$

where e_c^{qd} is the difference between the current set-point $i^{dq,ref}$ and the actual current i^{dq}; x_c^{dq} are the states of the controller, v^{dq} are the grid voltages in DQ frame and v_o^{dq} are the converter voltages generated by the space vector modulation module. The controller parameters K_{I_c}, K_{P_c} are selected as [75]

$$K_{P_c} = \frac{L_f}{\tau_c}, \qquad K_{I_c} = \frac{R_f}{\tau_c},$$

where τ_c is the time constant of the inner current loop. The current references in DQ are computed as

$$\begin{bmatrix} i^{d,ref} \\ i^{q,ref} \end{bmatrix} = \begin{bmatrix} \frac{2}{3v_d} & 0 \\ 0 & \frac{2}{3v_d} \end{bmatrix} \begin{bmatrix} P^{ref} \\ Q^{ref} \end{bmatrix} \tag{5.3}$$

assuming v^q is zero, *i.e.* the the phase-locked loop (PLL) is synchronized with the grid voltage. The resulting closed loop system can be approximated by

$$\begin{aligned} \frac{d}{dt} \begin{bmatrix} i^{d} \\ i^{q} \end{bmatrix} &= \begin{bmatrix} \frac{-1}{\tau_c} & 0 \\ 0 & \frac{-1}{\tau_c} \end{bmatrix} \begin{bmatrix} i^{d} \\ i^{q} \end{bmatrix} + \begin{bmatrix} \frac{2}{\tau_c 3v_d} & 0 \\ 0 & \frac{2}{\tau_c 3v_d} \end{bmatrix} \begin{bmatrix} P^{ref} \\ Q^{ref} \end{bmatrix}, \\ I_{DC} &= \frac{P^{grid}}{V_{DC}} = \frac{3v^d i^d}{2V_{DC}}, \end{aligned} \tag{5.4}$$

where I_{DC} (see Figure 5.2) is the current drawn from the DC–link by the GSC, and P^{grid} is the actual power exchanged with the microgrid.

5.3.2. Control of energy storage side converter

The objectives of K_{ESSC} are to regulate the DC–link voltage to V_{DC}^{ref}, minimizing voltage excursions in front of the current disturbances produced by K_{GSC}, and to regulate the inductor current I_L. The current I_L must be precisely regulated to avoid over-currents on the sensitive power electronic switches. To fulfill these requirements, a cascaded control scheme is used, as shown in Figure 5.1, consisting in a linear voltage regulator and a SM current control. Moreover, K_{ESSC} must provide a very fast transient response in its operation as a voltage regulator, as islanded operation of the microgrid demands fast dynamic responses in front of load or generation changes.

One of the advantages of using SM for the control of the battery DC current is that, during the design of the linear voltage regulator, it can be assumed that dynamics of the DC current loop are much faster than the one on the voltage loop. That is, it can be assumed that the current tracks perfectly the set-point produced by the linear regulator. This characteristic of the SM is true provided that the current lies in the sliding surface. This assumption permits to simplify the converter model used for the design and tune of the linear regulator. Conditions for the operation of K_{ESSC} are given in next subsections.

Current control with SM

The DC-DC converter shown in Figure 5.2 is clearly a variable structure system, *i.e.*, a system with dynamic changes depending on the conduction state of the switches. It is well known that SM techniques provide quite effective control strategies in the case of variable structures systems [166]. SM has been chosen instead of linear techniques for the control of the battery current for its performance, robustness and ease of implementation. The DC-DC converter controlled using SM technique provide very fast response without neither overshoot nor risk of modulator saturation but at the expense of a variable switching frequency.

The current regulation can be achieved with a single, simple and easy to implement sliding surface whose reference is modified in correspondence with the voltage controller and the BMS. The power demand can be positive or negative depending on the microgrid operating conditions. Therefore, the DC-DC converter must work in buck mode and boost mode to allow a bidirectional power transfer. To cover all operating modes, the following sliding surface

$$\mathcal{S}(I_L) = I^{ref} - I_L = 0 \tag{5.5}$$

is proposed associated with the switching logic

$$S_w = \frac{\text{sign}(I^{ref} - I_L) + 1}{2}, \tag{5.6}$$

where sign denotes the sign function and the reference I^{ref} is the setpoint given by the voltage regulator. It must be noted that the control law (5.6) results in infinite variable frequency operation of the power switches. To limit the switching frequency, the current I_L is confined in the region $\{I_L \quad | \quad I^{ref} - \Delta I_L < I_L < I^{ref} + \Delta I_L\}$ where ΔI_L is the desired ripple band. The resulting switching frequency depends on the DC voltage levels at both ends of inductance L_B and on the inductance itself, and can be expressed as

$$f_{sw} = \frac{V_{DC}V_B - V_B^2}{2L_B\Delta I_L V_{DC}}, \tag{5.7}$$

where f_{sw} is the switching frequency. Expression (5.7) is deduced from Figure 5.2 and

$$2\Delta I_L = \frac{\Delta V_L^{sw}}{L_B}\Delta t^{sw},$$

where ΔV_L^{sw} is the voltage difference across the output inductance, which depends on the switch state, and Δt^{sw} is the time required to produce a variation of $2\Delta I_L$ on the output current.

The sliding surface (5.5) satisfies the necessary and sufficient condition for sliding mode establishment, a.k.a. transversality condition

$$\mathcal{L}_g\mathcal{S} = -V_{DC}/L_B < 0,$$

where $\mathcal{L}$ is the Lie derivative [166]. To see this point, the equivalent control is obtained from the invariance condition ($\mathcal{S} = 0$ and ${}^{d}\!/\!{}_{dt}\mathcal{S} = 0$) and in the case of the switching law (5.6) it results

$$S_{w_{eq}} = \frac{V_B}{V_{DC}}. \tag{5.8}$$

SM regimen exists on the manifold whenever the equivalent control satisfies that $0 \leq S_{w_{eq}} \leq 1$. According to (5.8), this implies that

$$0 \leq V_B \leq V_{DC}, \tag{5.9}$$

which is guaranteed by the voltage regulator of the DC–link. The dynamics during SM regimen are obtained by substituting (5.8) in (5.1) and are given by

$$\begin{cases} \dfrac{d}{dt}I_L = 0, & \text{(5.10a)} \\ \dfrac{d}{dt}V_B = I^{ref}/Q_B, & \text{(5.10b)} \\ \dfrac{d}{dt}V_{DC} = \dfrac{1}{C_{DC}}(I_{DC} - I_{L_{DC}}). & \text{(5.10c)} \end{cases}$$

It is worth to mention that SM control eliminates the influence of the battery internal resistance (see (5.2)) over the battery voltage dynamics (5.10c).

The stability of the SM controlled system (5.10) is guaranteed for all initial conditions provided condition (5.9) is satisfied. Despite ${}^{d}\!/\!{}_{dt}V_B$ is not bounded by the SM control, it is indirectly bounded by the BMS. The dynamics of the battery voltage, ${}^{d}\!/\!{}_{dt}V_B$, are illustrated in Figure 5.4, for three different constant charge currents: $I_{L_1} < I_{L_2} < I_{L_3}$, respecting the BMS limits. As can be seen, ${}^{d}\!/\!{}_{dt}V_B$ converges to zero as the voltage reaches the MCV limit. Further details on the prove of stability can be found in Chapter 4.

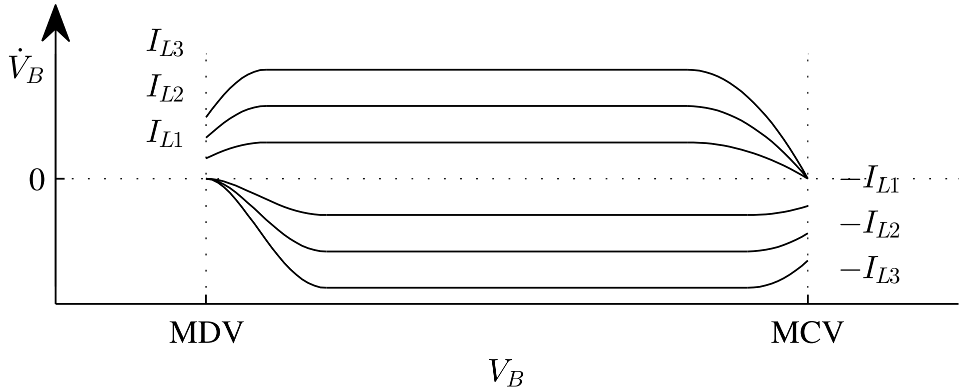

Figure 5.4.: Battery dynamics for three different constant charge currents.

Voltage regulation of the DC–link

The DC–link voltage is regulated with a PI control structure with anti-windup compensation, the block K_{DC} in Figure 5.5. The output of K_{DC} is the current set-point I^{ref} for the sliding surface (5.5). For design purposes, the current loop can be assumed in SM regime. Therefore, $I_L = I^{ref}$ and the dynamics of the system to be controlled are given by (5.10c), denoted as G in Figure 5.5

The voltage regulator K_{DC} must reject the current disturbances I_{DC} generated by the GSC, as described in (5.4), and produce a current set-point $\tilde{I}^{ref}$ for the SM control. This current reference $\tilde{I}^{ref}$ is bounded by the battery lower and higher limits, MDC and MCC respectively, and the current limits of the power electronic switches $\underline{I}$ and $\overline{I}$, *i.e.*

$$\max(\underline{I}, MDC) \leq I^{ref} \leq \min(\overline{I}, MCC). \tag{5.11}$$

The PI controller K_{DC} is governed then by

$$\frac{d}{dt}x_{K_{DC}} = K_{I_{DC}} e_{DC}, \tag{5.12}$$

$$\tilde{I}^{ref} = x_{K_{DC}} + K_{P_{DC}} e_{DC}, \tag{5.13}$$

where $e_{DC} = V_{DC}^{ref} - V_{DC}$, with V_{DC}^{ref} the DC voltage reference, $x_{K_{DC}}$ is the integrator state and $K_{I_{DC}}$ and $K_{P_{DC}}$ are the integral and proportional gains.

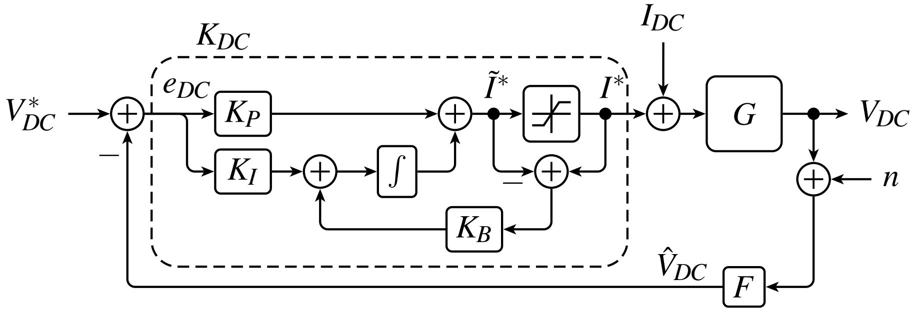

Figure 5.5.: Control scheme for the V_{DC} DC–link voltage regulation.

Power converters applying standard pulse width modulation (PWM) switching schemes are prone to produce electromagnetic radiation because of the hard switching of the power switches [178]. This electromagnetic radiation can interfere in the voltage sensors, introducing high frequency noise. See Appendix C for more details on the harmonics produced by PWM on the VSC. As a consequence of the noise, it is advisable to limit the controller bandwidth. PI controllers may amplify the high frequency noise. To avoid this undesirable effect, the controller bandwidth is limited by inserting a low-pass filter F into the control loop, Moreover, the controller gains are tuned using loopshaping ideas. For background on robust control and loopshaping, see Appendix B.

Let be

$$L(s) = F(s)K_{DC}(s)G(s),$$

$$S(s) = \frac{1}{1+L(s)}, \qquad T(s) = \frac{L(s)}{1+L(s)},$$

the open loop, sensitivity and complementary sensitivity transfer functions, respectively, where $G(s)$ is the transfer function from I^{ref} to V_B. The sensitivity S is the transfer function from V_{DC}^{ref} to e_{DC} and the complementary sensitivity T is the transfer function from the measurement noise n to V_{DC} (see Figure 5.5). In order to achieve a satisfactory voltage regulation, the magnitude of S should be below 0 dB in low frequencies. On the other hand, the magnitude of T should be below 0 dB in the high frequencies to attenuate the effect of the measurement noise on the controlled variable V_{DC}. Since $S+T=1$, a compromise must be reached to fulfil both objectives.

Loopshaping allows translating the constraints on the closed loop transfers into constraints on the open loop transfer function L. The constraint on S implies that the magnitude of L must be large in low frequencies, whereas the constraint on T demands small gain in high frequencies. These constraints on the magnitude of L are illustrated in Figure 5.6. The magnitude of the open loop transfer function must remain outside the shadows areas. The design based on loopshaping consists in shaping the magnitude of L by selecting proper controller to fulfill the frequency constraints.

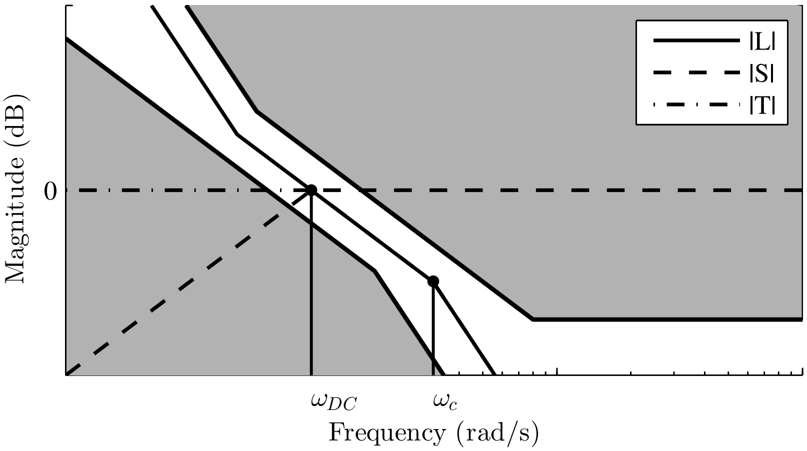

Figure 5.6.: Loopshaping using magnitude of L, S, T and the magnitude of constraints (shadow area).

Assuming that the close loop bandwidth ω_{DC} is much lower and than the switching frequency $\omega_{sw} = 2\pi f_{sw}$, the dynamics (5.10c) can be expressed by an average model. Energy balance between battery and DC–link implies

$$\overline{I}_{L_{DC}} V_{DC} = \overline{I}_L V_B,$$

where overline denotes the average value. Thus, (5.10c) can be expressed in terms of I^{ref} resulting in

$$G(s) = \frac{1}{sC_{DC}} \frac{V_{DC}}{V_B},$$
$$K(s) = k_{P_{DC}} + \frac{k_{I_{DC}}}{s}$$

and assuming the cut-off frequency of filter F, ω_c, is much higher than the closed loop bandwidth ω_{DC}. Since the model of the DC–link depends mainly on the battery voltage V_B (assuming V_{DC} is tightly regulated), the design of the controller parameters can be based on a worst case scenario, this is taking $V_B = \text{MDV}$. This assumption permits to keep the control structure simple and easy to implement. Then the parameters $k_{P_{DC}}$ and $k_{I_{DC}}$ must be chosen in order that the magnitude of

$$L(s) = \frac{k_{P_{DC}}}{C_{DC}} \left(\frac{s + k_{I_{DC}}/k_{P_{DC}}}{s^2} \right) \frac{V_{DC}^{ref}}{\text{MDV}}$$

remains in the non-shadow area in Figure 5.6. It is advisable that L crosses the 0 dB line with a slope of -20 dB/decade in order to obtain a damped transient response. Therefore, $k_{I_{DC}}/k_{P_{DC}} \ll \omega_{DC}$ and the gain $k_{P_{DC}}$ is chosen such that the magnitude of L crosses the 0 dB line at ω_{DC}. The bandwidth ω_{DC} should be much lower than filter cutoff frequency ω_c.

Anti-windup scheme

Since, the control variable $\tilde{I}^{ref}$ is limited to protect the battery and the electronic switches, large voltage oversteps could occur as a result of PI windup. Therefore, the voltage controller is completed with a simple anti-windup compensation by back-calculation. As proposed in [6], the back-calculation coefficient is chosen as $K_B = K_{I_{DC}}$. It should be noted that I_L is limited by (5.11), as a consequence this imposes limits on I_{DC} which depends on the battery current state. These limits are taken into account by the external power control, which produces the power set-point P^{ref} respecting the state and power limits of the battery; *i.e.* the power demanded to the battery must not exceed the limits given by the BMS.

5.4. Experimental Results at full ratings

To illustrate the effectiveness of the proposed control law, it has been implemented in the experimental test bench shown in Figure 5.7. The test bench consists of a two stage power converter, composed by the ESSC and the GSC, with its associated controllers. The set-up of this experiment is similar to its homologous in Chapter 4.

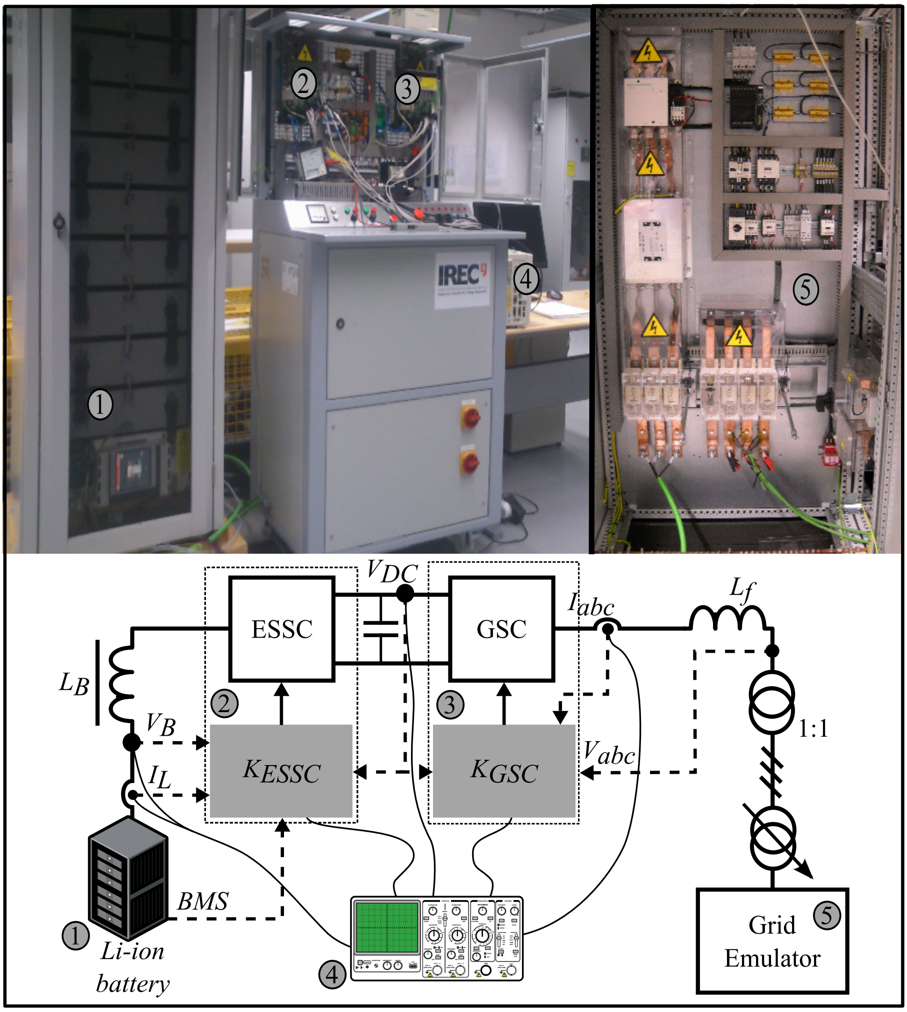

Figure 5.7.: Experimental setup used to evaluate the proposed control law with an illustration of the converters, controllers, passive components and measuring points.

The maximum rated direct current of the ESSC is 20 A, with a total rated power of 4 kW. The battery used in the experimental setup is composed by ten *Synerion (SAFT)* 24 V, 2 kWh module rated at 34 A for charging and 160 A for discharging, with a total capacity of 20 kWh and 240 volts [144]. The GSC is interfaced with the grid with an a auto-transformer (1), and an isolating transformer (2) for safety reasons (see Figure 5.7). The isolation transformer provides galvanic isolation between the AC grid and the power converter.

Parameter	Value	Units	Description
f_{sw}	12.21	kHz	GSC switching frequency (PWM)
$f_{sw_{ESSC}}$	[7-10]	kHz	ESSC switching frequency (variable)
τ_c	10	ms	Power loop response time
ω_c	250	Hz	low pass filter cut-off frequency
ω_{DC}	100	rad/s	K_{DC} bandwidth
$k_{P_{DC}}$	0.364	-	K_{DC} proportional gain
$k_{I_{DC}}$	22.491	-	K_{DC} integral gain

Table 5.1.: Design and control parameters of the Li-ion battery experimental set-up.

The control and design parameters used are shown in Table 5.1. The parameters of the experimental test bench are summarized in Appendix D. To evaluate the proper operation of the proposed control law, the ESS is evaluated in four different scenarios: the black-start operation, positive and negative current disturbance rejection during voltage regulation and low voltage fault.

5.4.1. Black-start operation

The black-start operation consists in the pre-charge of the DC–link with the ESS being disconnected from the grid. This procedure allows re-energizing the microgrid in case of a black-out in the power system or in the microgrid itself. The pre-charge procedure is divided in two steps. First, the battery is connected to the DC–link through a pre-charge resistor, rising V_{DC} up to V_B. This state, $V_{DC} = V_B$, is the limit operating condition that guarantees the stability of the SM current control, as shown in equation (5.9). In the second step of the pre-charge, the SM controller is activated along with the DC–link voltage controller, rising and regulating V_{DC} to V_{DC}^{ref}. The step response of the system can be seen in Figure 5.8, where signals V_{DC}, I_L and V_B has been acquired simultaneously.

The signal V_{DC} has been acquired using a differential voltage probe attached directly to the DC–link bus bar; the signal I_L has been acquired using a hall effect DC current probe placed in the cable linking the battery positive pole with the power converter output inductance L_B; the signal V_B has been acquired using a differential voltage probe attached

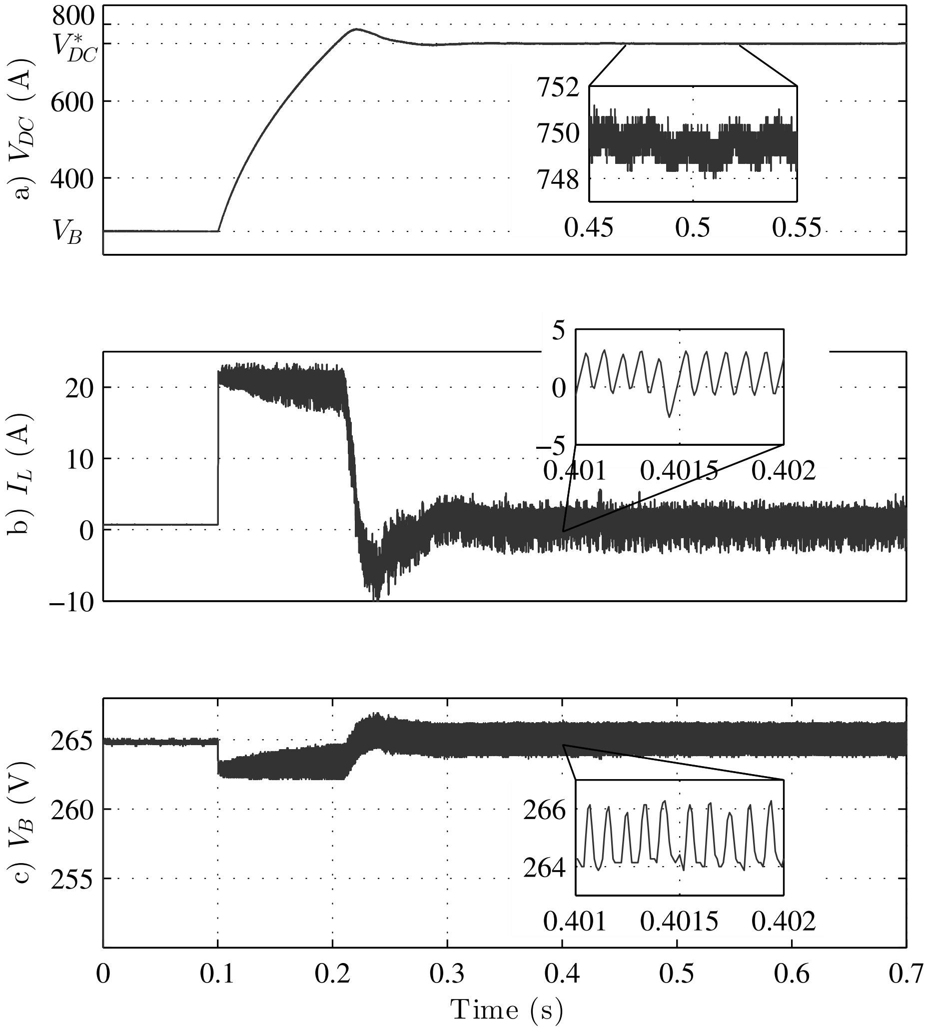

Figure 5.8.: Experimental results during the pre-charge of the DC–link: a) DC–link voltage V_{DC}; b) battery current I_L; c) Battery voltage V_B.

directly to the battery's terminals. Positive currents are defined as the currents delivered by the battery. Note that due to internal losses of the power converter, the average current needed for regulating the voltage to V_{DC}^{ref} is about 2 A. As a consequence of the current ripple and the battery internal resistance R_{int}, the battery voltage also presents a small ripple of 2 V, lower than 0.75%.

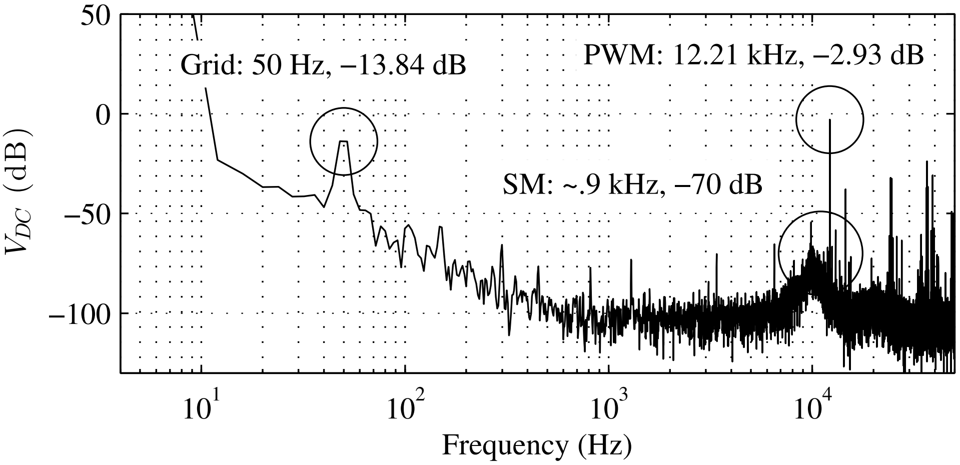

Figure 5.9.: Frequency spectrum of V_{DC}, with the DC–link voltage being regulated by ESSC and the GSC regulating power to zero.

Voltage regulation with GSC switching

Lets analyze the interaction between the GSC and the ESSC with the spectrum of V_{DC} shown in Figure 5.9. The spectrum corresponds to the DC–link voltage being regulated by ESSC and the GSC regulating active and reactive power to zero. It can be detected three sources of electromagnetic perturbations which deforms the voltage waveform: the grid, the ESSC switching and the GSC switching. In two-level voltage source inverters the grid frequency ripple is induced to the DC–link intrinsically when regulating the AC power to a constant value. This implies that a minimum voltage ripple at the grid frequency will always be present in the DC–link. The variable switching frequency of the SM control scheme results in a flatter spectrum, with the peak value at −70 dB, which doesn't produce significant noise. However, the PWM switching implemented in the GSC results in a high power spike at the switching frequency of 12.21 kHz, with a value of −2.93 dB. This frequency component is attenuated by the low pass filter F to avoid its aliasing in the control loop.

5.4.2. Current disturbance rejection

During normal operation, the battery can inject or draw power from the microgrid, consuming or injecting current from the DC–link. The task of K_{ESSC} is to regulate the DC–link voltage by rejecting the current disturbances produced by the GSC. In order to evaluate the performance of the proposed control scheme, the GSC is stepped with a power change from 0 to 100% (0 to 4 kW), and from 0 to -100%. The measured battery power is the product of the battery voltage times the current flowing through the inductor L_B; the grid power is obtained from (5.3).

Injection of 4 kW to the grid

To evaluate the effectiveness of the ESSC control scheme, a step of 4 kW is applied at $t = 0.1$ s. The post-disturbance evolution of signals a) V_{DC}, b) I_L, c) battery voltage V_B, d) AC current and e) active power can be seen in Figure 5.10. In contrast to Figure 5.8 where the GSC is no yet operating, in Figure 5.10 the GSC is switching at 12.2 kHz. This power converter produces electromagnetic interferences, resulting in a noisier operation, particularly noticeable in I_L. However, the proper design of K_{DC} and the low pass filter F reduces significantly the signal noise level.

The power set-point change is reflected in the DC–link voltage producing a drop the 2.5 % of V_{DC}^{ref}. The PI voltage regulator produces a current reference that rapidly rejects the disturbance from the GSC, which in turn is perfectly tracked by the SM current controller, as can be seen in Figure 5.10. The AC current signals shown correspond to the phase-a current (gray line) and i_d (black line). The instantaneous grid power is shown (black line) in Figure 5.10. It must be noted that the actual grid power and the battery drawn power different due to the power losses of the power converter.

Consumption of 4 kW from the grid

During the islanded mode of operation, the ESS can be also charged, consuming power from the microgrid. This situation is analyzed in this scenario, where a set-point of -4 kW is send to the GSC at $t = 0.1$ s. The results of this scenario are shown in Figure 5.11, which is analogous to Figure 5.10, showing signals a) V_{DC}, b) I_L, c) battery voltage V_B, d) AC current and e) Active power. In this scenario, the voltage V_{DC} rises up to 770 V, 2.5 % higher than V_{DC}^{ref}. The rest of the signals I_L, AC current and active power present characteristics similar to the previous scenario.

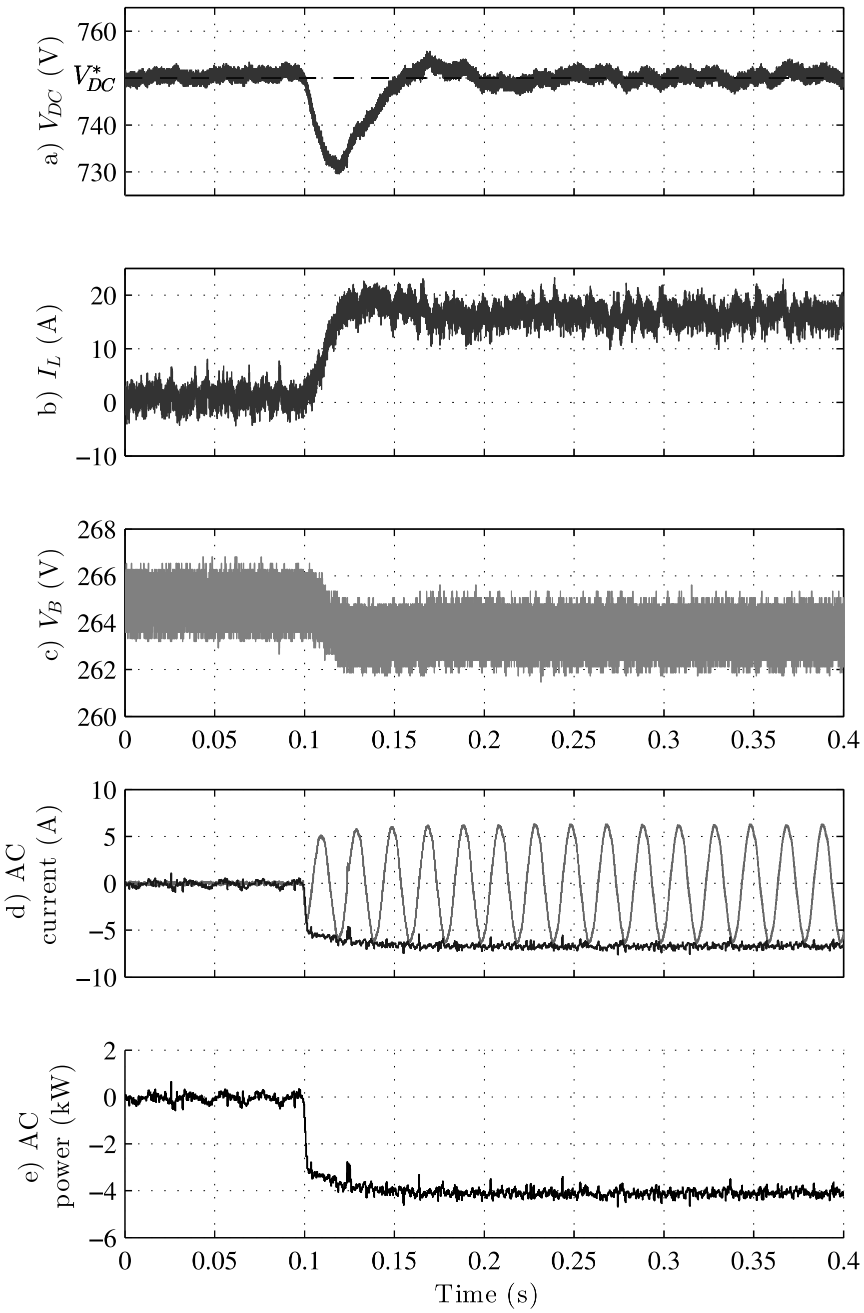

Figure 5.10.: System response for a 4 kW power injection disturbance: a) DC–link voltage; b) battery current I_L; c) battery voltage V_B; d) AC current (phase-a, gray; D-axis, black) and e) grid power.

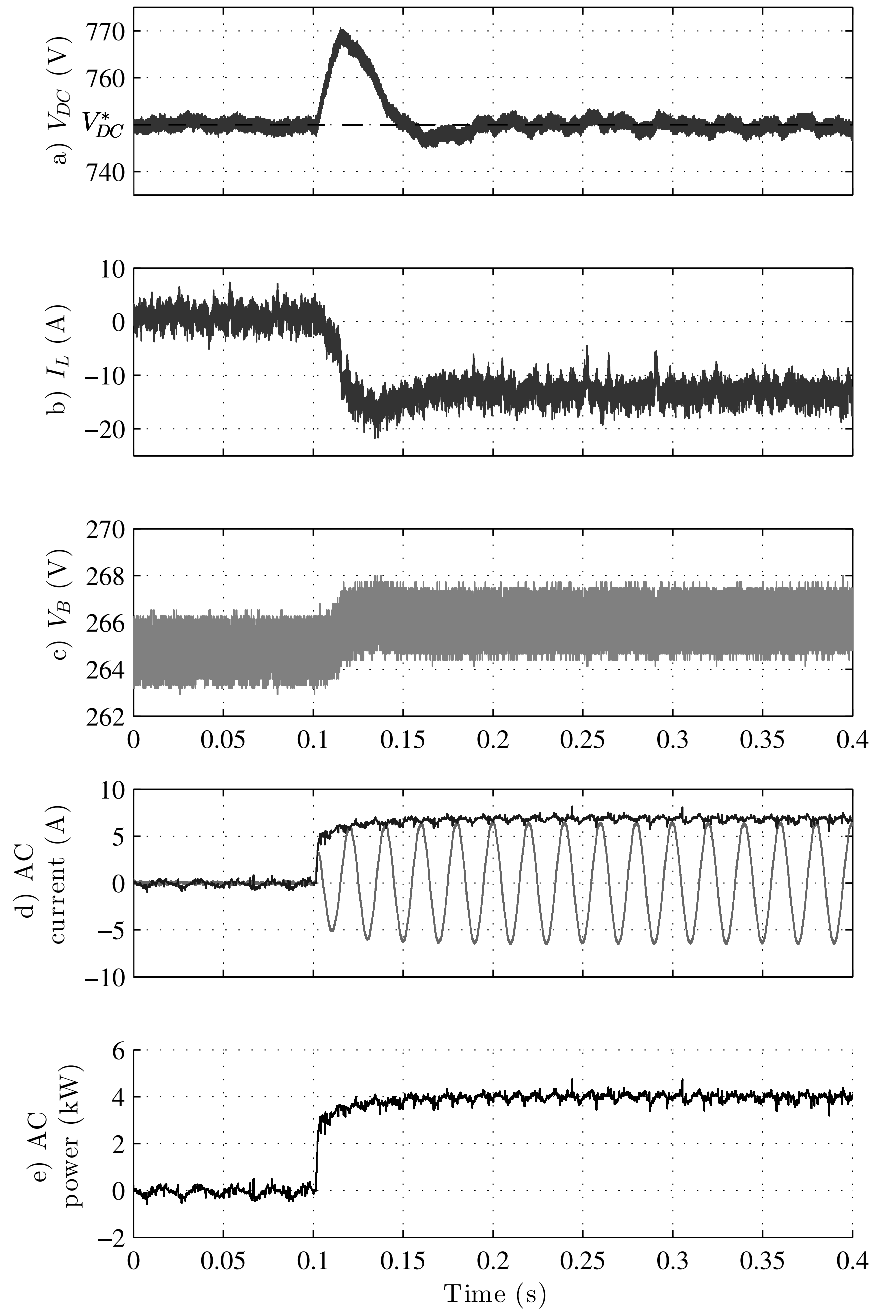

Figure 5.11.: System response for a 4 kW power consumption disturbance: a) DC–link voltage; b) battery current I_L; c) battery voltage V_B; d) AC current (phase-a, gray; D-axis, black) and e) grid power.

5.4.3. Fault ride through capability

In [60] it is defined a Network Code that defines a common framework of grid connection requirements for electrical generators. The technical specification of this network code is used to analyse the impact of distribution grid low voltage faults into the DC–link of the proposed energy storage system. The fault applied to the ESS is a voltage sag of 80 % depth with a duration of 250 ms, with a sudden voltage recovery. The fault is generated by a 200 kVA power grid emulator, shown in Figure 5.7, composed by a three-phase active rectifier in series with a three-phase inverter. This power grid emulator is operated as a variable voltage source capable of generating symmetric three-phase voltage sags.

A current limitation in the grid side power converter is necessary for the fault ride through capability. Thus, current references $i^{dq,ref}$ are bounded to avoid over-currents during faults. The procedure upon detection of voltage sag is to set the active power reference to zero $i^{d,ref} = 0$ and inject reactive current according the grid code. When the fault is cleared, the active and reactive power reference are slowly restored to the pre-fault value to minimize post-fault transients.

In Figure 5.12 it can be seen the time response of the a) DC–link voltage (V_{DC}) and b) battery current (I_L) in front of a c) AC voltage fault (V_{abc}). In this scenario, the converter's power set point is -4 kW. During the fault ($t = 0$ s to $t = 0.25$ s), current set-points are temporally modified, such that $i^{d,ref} = 0$ and $i^{q,ref} = 5$ A, to inject reactive current. Since the regulated AC current is limited by the control, it can be seen in plot d) that the AC current (phase-a) is bounded during the fault, presenting two transients, one at the fault occurrence and another at the clearance. It can be observed that the proposed control is capable of achieving a fast restoration of the DC–link voltage even under extreme scenarios like a voltage sag. The DC–link presents a fast transient at the fault occurrence with an overshoot smaller than 2 %, and a higher overshoot of 6 % at the fault recovery. The DC–link is constrained around V_{DC}^{ref} by reducing the battery current (b) in concordance with instantaneous exchanged AC active power (e). Due to the transient during the voltage recovery, the inrush power to the DC–link is much higher than the rated power of battery the DC/DC converter, causing the saturation of I_L.

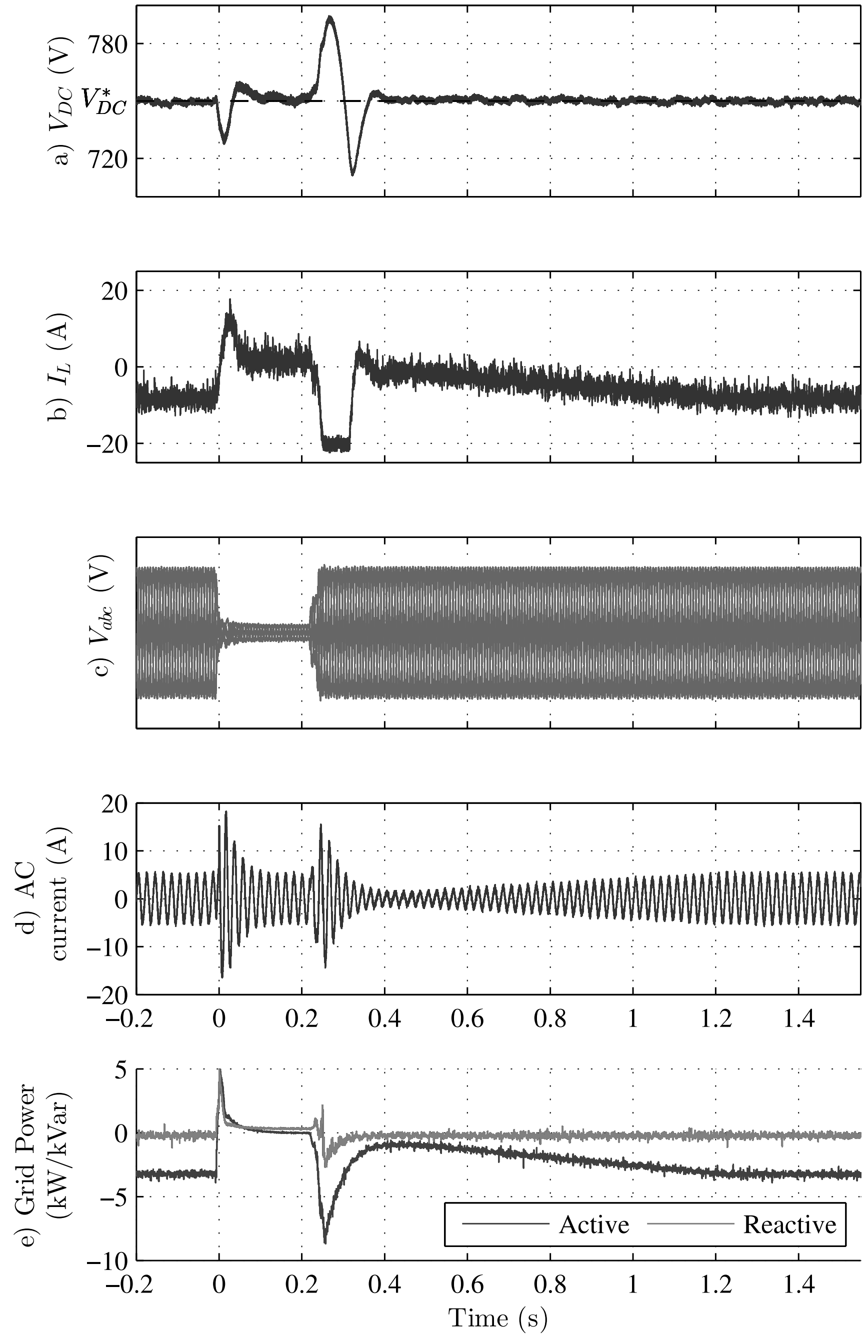

Figure 5.12.: System response in front of a low voltage fault: a) DC–link voltage; b) battery current I_L; c) AC grid voltage (V_{abc}); d) AC current (phase-a) and e) grid power.

5.5. Conclusion of the chapter

This chapter has presented a new control strategy for a bidirectional AC/DC converter to control the power exchange between a battery and a microgrid. The power converter has been designed with the aim to control the DC–link voltage entirely from the ESSC, in contrast with the converter design in Chapter 4. The porpoise of this research is to obtain a converter capable to operate in combination with the droop control on the AC MG side.

The proposed strategy combines, in a cascade configuration, a SM control for the current loop and linear regulator designed using loopshaping ideas in the DC–link voltage loop. The combination of these controllers ensures robustness and a suitable compromise between voltage regulation and measurement noise rejection. Besides, the control schemes results in a simple implementation, which is an important point considering the fast responses demanded to power converters.

The scheme was experimentally tested in several representative scenarios, both in normal and fault operation conditions. The experimental results show that the proposed control strategy exhibits a suitable performance under typical microgrid scenarios, including black-start operation, power injection and battery charging. The results obtained under conditions imposed by the grid codes also show that the scheme exhibits good ride-through capability to handle voltage sags in the grid. This is faulty condition that a converter connected to a grid must be able to cope.

It can be seen a slightly high ripple amplitude in the DC current. The ripple might be reduced by employing advanced commutation techniques such as interleaving. However, this leads to more complex converters and the ripple is adequate for a battery charger.

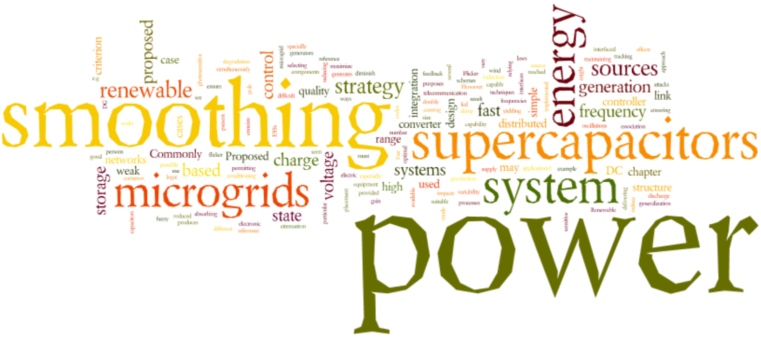

6

A power smoothing system based on supercapacitors for microgrids

This chapter presents a simple power smoothing strategy based on supercapacitors for power conditioning of DG. The power smoothing controller generates the power reference for the DC-DC converter which has a power tracking control implemented with sliding mode techniques, as described in chapter 4. The proposed strategy consists on a voltage controller capable of maintaining the optimal state of charge and reducing high frequency components of the power coming from renewable energy sources. A generalization of the PI structure is used to ensure simple design and implementation. With the proposed control structure, the tuning is reduced to find a state feedback gain based on a pole placement criterion. In addition, a criterion for selecting supercapacitors' size is provided.

6.1. Introduction

Renewable distributed generation impacts on power systems in a number of ways, with special relevance the variability of the electrical production. The penetration of distributed generation may result in degradation of the power quality, especially in the case of weak networks [137, 145] or microgrids [133]. Fast fluctuation of power generation produces voltage oscillations (flicker), with frequency range between 1 and 10 Hz [19]. Its effects can vary from electric disturbances to epileptic attacks in photosensitive persons. Flicker may also affect sensitive electronic systems, such as telecommunication equipment or industrial processes, relying on high quality power supply [138].

A possible approach to diminish voltage fluctuations in weak networks, such as microgrids, is to actively damp the specific frequency by only employing the energy stored in the capacitors of the DC–link [65]. However, the smoothing of a wider range of frequencies requires the use of ESSs. As seen in Chapter 2, several storage technologies are available for smoothing purposes. In particular, supercapacitors are an emerging technology specially suitable for power applications[1], this is, cases demanding fast charge and discharge cycles, such as the power smoothing of renewable energy sources [92]. Storage systems for power smoothing present different interfaces with the grid. In the case of individual renewable energy sources power generators interfaced with a full power back-to-back power converter, it is common to attach the energy storage system to the DC–link [1, 8, 27, 28, 106, 120]. In other cases, the energy storage system is equipped with its own inverter, permitting its association with one or more sources simultaneously, or its integration in a microgrid. Commonly, the ESS is connected at the PCC of the renewable source, see *e.g.* [11, 66, 91, 159].

In power smoothing, a compromise must be reached between the attenuation of the fast variation in power and the regulation of the state of charge. This last objective is necessary to maximize the capability of absorbing and delivering energy, ensuring a good power smoothing. Commonly, to achieve these objectives, two control laws are used yielding to schemes that might be difficult to design [1, 11, 159, 175]. For example, the integration of supercapacitors in a doubly fed induction generator to reduce the fast wind–induced power variations is considered in [1]. The proposed fuzzy logic based energy management system

---

[1] in the sense of Section 2.4

is used to set the power set-point of the wind turbine combined with storage in order to optimize the overall operation of the system. The energy manager uses the predicted wind power production, energy storage device status and history, and AC voltage measurements. Kamel et al. propose to combine pitch control of wind power and ESS based on supercapacitors for smoothing power fluctuations in microgrid applications [91]. A filter extracts the mean wind power, which is used as the power reference for the system wind turbine with storage. The supercapacitor system compensates the power mismatch between the computed average power reference and the actual wind power, leaving the state of charge unconstrained. The problem of finding the correct size of the supercapacitor bank tied to the output of a direct wave energy converter to ensure a smooth power profile is analyzed in [8]. In this application the ESS power setpoint is the result of a fuzzy rule combining both the difference between a constant grid power reference and the actual produced power, and the state of charge of the ESS. A different approach is presented by Jayasinghe and Vilathgamuwa [85], where clamped supercapacitors are used, in the DC–link of a three-level voltage source converter, to remove the fast fluctuations in wind power applications. The smoothing is accomplished by the inertia introduced by the supercapacitors in the converter.

In this chapter, in contrast with the previous approaches of power tracking problems found in the literature, the power smoothing is expressed as a filtering problem. With this approach, the power smoothing consists in attenuating the high frequency components of the power delivered by the renewable source. Then, the power smoother results in a rather simple voltage control scheme, which permits to specify the cut-off smoothing frequency, while guaranteeing optimal state of charge of the storage system, without the requirement of additional filters or prediction algorithms. The proposed control design helps to find a trade-off between state of charge regulation and smoothing capability. The power smoothing system is connected directly to the AC grid to obtain a flexible implementation for smoothing different variable power sources. Guidelines to determine the size of the storage element according to the cut-off frequency and power levels of the application are also provided. The power smoothing scheme has been implemented in a supercapacitor based ESS to smooth wind power. This application has been evaluated by simulations and experimental tests in a laboratory environment.

6.2. Power smoothing with supercapacitors

Consider an aggregation of renewable energy sources injecting a fast varying power P_{ren} into the grid. The idea of power smoothing is to generate a power profile P_{ESS} to compensate the fast varying components of P_{ren} and to produce a slow varying power output ($P_{out} = P_{ren} + P_{ESS}$) delivered to the low voltage grid or microgrid. In other words, power smoothing consists in attenuating the components of P_{out} for frequencies greater than a boundary value λ^d, *i.e.*

$$|P_{out}(j\lambda)| < \epsilon, \qquad \forall\, \lambda > \lambda^d,$$

where λ is the frequency and ϵ is a small arbitrary value. If the objective of the power smoothing would be to suppress flicker, the value λ^d should be in the range of frequencies of the voltage oscillations (1 to 10 Hz).

The topology adopted in this chapter to reduce the variability in the electric production of an aggregation renewable sources is sketched in Figure 6.1. The constructive details of the ESS can be found in Chapter 4. The ESS is interfaced with the rest of the network through a GSC controlled by K_{GSC}, which regulates the voltage V_{DC} maintaining energy balance in the DC–link. The controller of the ESSC, K_{ESSC}, regulates the power exchanged between the ESD and the DC–link. Figure 4.2 presents the bidirectional DC-DC topology adopted to implement the ESSC. In this application, the voltage V_{DC} (on the left side) is always higher than V_{ESD} (on the right side), but energy can flow in both directions. This converter can work in buck mode delivering energy to the storage device or in boost mode draining energy from the storage device.

As the DC–link provides a certain degree of decoupling between ESSC and GSC, the design of each controller can be independent. Usually, the GSC is controlled with a cascaded control scheme. For details on the control of the GSC, see *e.g.* Chapter 3. The DC-DC controller K_{ESSC} is implemented using sliding mode techniques. A single sliding surface, which is used as the switching law, is shaped dynamically to achieve one of the three operating modes: pre-charge, power tracking or voltage limitation. More details on the ESSC design can be found in Chapter 4.

For power smoothing analysis, the supercapacitors can be assumed pre-charged and in power tracking operation. In this state, ESS can absorb or deliver power to the grid tracking a power reference P_{ESS}^{ref}. In

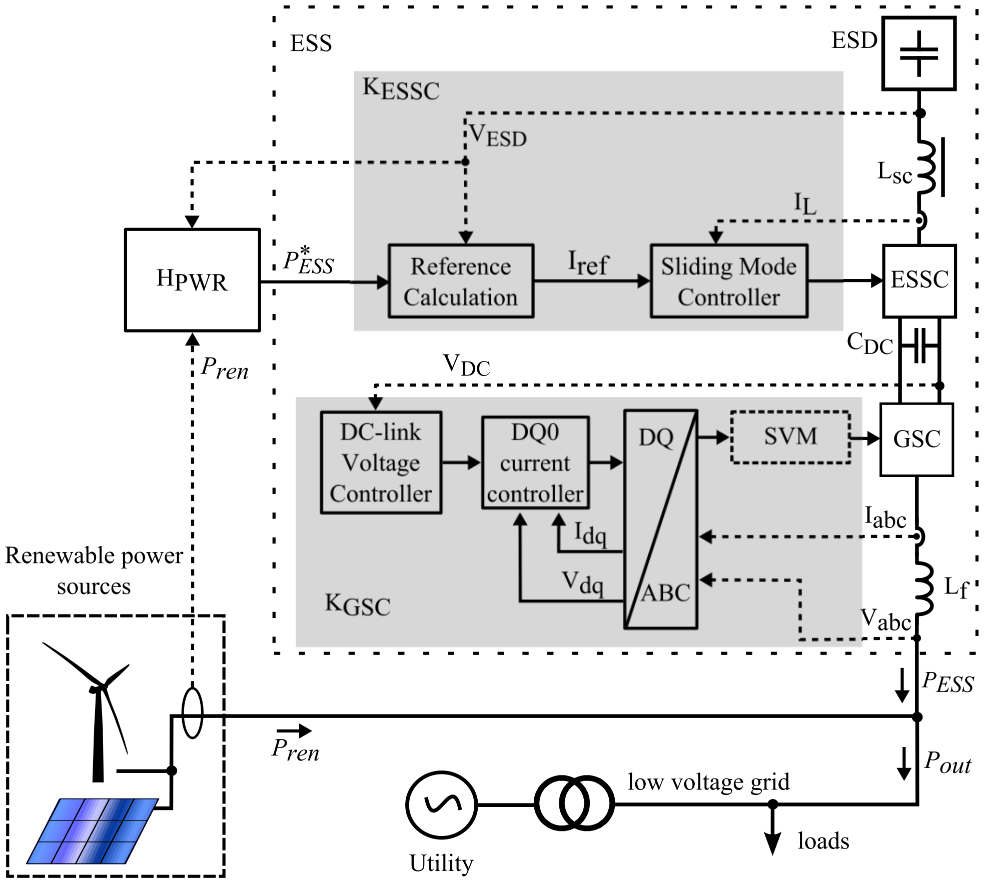

Figure 6.1.: Sketch of the power smoothing system.

power tracking mode, the dynamics of the ESS can be described by

$$G_{ESS} : \begin{cases} \dfrac{d}{dt} V_{ESD} = \dfrac{P_{ESS}^{ref}}{V_{ESD} C_{ESD}}, \\ \dfrac{d}{dt} P_{ESS} = \dfrac{P_{ESS}^{ref} - P_{ESS}}{\tau_{GSC}}, \end{cases} \tag{6.1}$$

where P_{ESS}^{ref} is the power reference for the ESS, V_{ESD} and C_{ESD} are the supercapacitors' voltage and capacity respectively, and τ_{GSC} is the time constant of the GSC.

For security reasons, the voltage of the supercapacitor bank must be constrained in the operating range

$$V_{ESD_{min}} < V_{ESD} < V_{ESD_{max}}, \tag{6.2}$$

as high current could arise if voltage V_{ESD} decreases to small values and an upper limit must be imposed to preserve the integrity of the supercapacitors. The control developed in chapter 4 has been designed to ensure the voltage V_{ESD} is constrained to its operating range.

The state of charge SoC of the ESD is defined as

$$SoC = \frac{V_{ESD}^2 - V_{ESD_{min}}^2}{V_{ESD_{max}}^2 - V_{ESD_{min}}^2}.$$

Maintaining a 50 % SoC is important to maximize smoothing capability of the ESS. A low value of SoC limits the system to deliver the necessary energy to the grid. Otherwise, an ESS with a high SoC could not be able to absorb the amount energy needed for power smoothing.

6.3. Proposed power smoothing strategy

The main component of the power smoothing system is the controller H_{PWR}. In Figure 6.1, the power smoothing controller H_{PWR} produces a power reference P_{ESS}^{ref}, the setpoint for the ESS, by measuring the total output power from renewable sources P_{ren} and monitoring the SoC of the ESS. In order to guarantee a long term operation, the power smoothing controller must ensure that the SoC of the ESD is at 50 % in average. This prevents the voltage from reaching the saturation limits ensuring a better capability to absorb or deliver power in any situation.

The proposed structure for the power smoothing controller H_{PWR} is shown in Figure 6.2, where G_{ESS} are the dynamics described in (6.1). The core of H_{PWR} is the voltage controller $K_{V_{ESD}}$ producing a control signal $\hat{u}$ with its bandwidth limited to λ_c. The power reference P_{ESS}^{ref} sent to the ESS is the power P_{ren} delivered by the renewable energy source subtracted from $\hat{u}$. The voltage controller $K_{V_{ESD}}$ must be designed to maintain V_{ESD} close to the reference ${V_{ESD}^{ref}}$[2] in low frequencies to ensure a proper SoC of the supercapacitors. Simultaneously, the controller H_{PWR} must also produce a high frequency signal P_{ESS} capable of attenuating P_{ren} for frequencies above λ^d, *i.e.*

$$|P_{ren}(j\lambda) + P_{ESS}(j\lambda)| < \epsilon, \qquad \forall\, \lambda \geq \lambda^d \geq \lambda_c, \tag{6.3}$$

where λ_c is the bandwidth of the power smoothing control.

---

[2] see subsection 6.3.1 for the definition of V_{ESD}^{ref}.

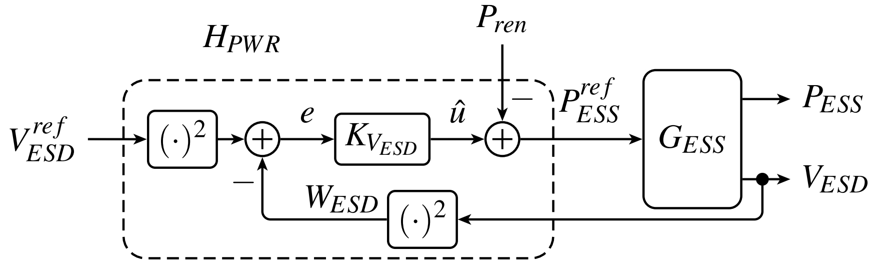

Figure 6.2.: Proposed power smoothing controller H_{PWR} structure.

Clearly, the key point to achieve these objectives is the design of the voltage controller $K_{V_{ESD}}$ and the correct selection of the supercapacitors capacity. These points are analyzed in detail in the following subsections.

6.3.1. ESS sizing

Taking into account voltage limits of the supercapacitors and current limits of the converter, it is important to select a supercapacitor bank with the proper capacity and voltage for achieving the best power smoothing at lower cost. In this subsection, a selection criterion is proposed based on a worst case scenario.

The energy that the supercapacitor can absorb or deliver for smoothing purposes is given by

$$E_{useful} = \frac{1}{2} C_{ESD} V_{ESD_{max}}^2 - E_{min}, \tag{6.4}$$

where $E_{min} = \frac{1}{2} C_{ESD} V_{ESD_{min}}^2$ denotes the energy required to raise the voltage up to $V_{ESD_{min}}$, *i.e.* E_{min} is the amount of energy not used due to the lower voltage limit. To have the largest possible amount of energy available for smoothing purposes, the voltage reference V_{ESD}^{ref} is selected as the value corresponding to 50 % of the SoC, *i.e.*

$$V_{ESD}^{ref} = \sqrt{\frac{V_{ESD_{max}}^2 + V_{ESD_{min}}^2}{2}}. \tag{6.5}$$

These values of energy and voltage are illustrated in Figure 6.3.

Considering the previous analysis, the following criteria can be used to determine the capacity of the energy storage element. First, it must

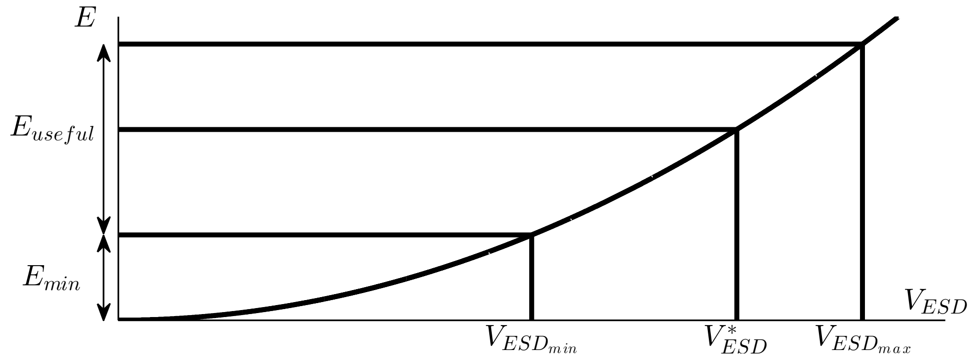

Figure 6.3.: Relation between the supercapacitors voltage V_{ESD} and the energy stored.

be decided the cut-off frequency λ_c based on the particular needs of the application. Then, in the worst case scenario, the filtering element would have to generate a power

$$P_{ESS} = P_{ESD}\sin(\lambda_c t).$$

That is, the disturbance to attenuate is a pure sinusoidal signal of maximum power, with P_{ESD} the nominal power of the ESS. In order to be able to completely cancel this signal, the ESD must store or inject the energy

$$E_{WC} = P_{ESD}\int_0^{\frac{\pi}{\lambda_c}} \sin(\lambda_c \tau)d\tau = 2\frac{P_{ESD}}{\lambda_c}$$

If the supercapacitor voltage is maintained at V_{ESD}^{ref}, the energy stored is $E_{useful}/2 + E_{min}$ (50 % of its capacity). Thus, to guarantee an energy level of E_{WC} available for power smoothing, supercapacitor must be sized such that

$$E_{useful} = 2E_{WC}.$$

Therefore, from (6.4),

$$C_{ESD} = \frac{4E_{WC}}{V_{ESD_{max}}^2 - V_{ESD_{min}}^2}. \tag{6.6}$$

Notice that this criterion is based on the assumption of perfect filtering, therefore the lower frequency to be generated by the smoother is λ_c. In practice, this is not completely true since other frequencies will be present. However, this approximation provides a useful guideline to select the capacity of the storage device.

6.3.2. Design of voltage regulator $K_{V_{ESD}}$

In order to design a simple voltage controller, equation (6.1) is linearized by the change of variable $W_{ESD} = V_{ESD}^2$. Thus, voltage dynamics is governed by

$$W_{ESD} = \frac{2}{C_{ESD}} P_{ESS}^{ref},$$

with a control signal expressed as $P_{ESS}^{ref} = \hat{u} - P_{ren}$, where $\hat{u}$ is the control law

$$\hat{u} = K_{V_{ESD}}(W_{ESD}^{ref} - W_{ESD}),$$

with $W_{ESD}^{ref} = V_{ESD}^{ref\ 2}$. Finally the controlled signal W_{ESD} is given by

$$W_{ESD} = G_{eq}(s)(\hat{u} - P_{ren}),$$

where $G_{eq} = 2/sC_{ESD}$.

To design the power smoother, two transfer functions are of interest: $T_H(s)$ from P_{ren} to P_{ESS} and $T_V(s)$ from W_{ESD}^{ref} to W_{ESD}. From Figure 6.2, these transfer functions are derived as

$$T_H(s) = \frac{P_{ESS}(s)}{P_{ren}(s)} = \frac{-G_2(s)}{1 + G_{eq}(s)K_{V_{ESD}}(s)},$$
$$T_V(s) = \frac{W_{ESD}(s)}{W_{ESD}^{ref}(s)} = \frac{G_{eq}(s)K_{V_{ESD}}(s)}{1 + G_{eq}(s)K_{V_{ESD}}(s)},$$

with

$$G_2(s) = \frac{P_{ESS(s)}}{P_{ESS}^{ref}(s)} = \frac{1}{s\tau_{ESD} + 1}.$$

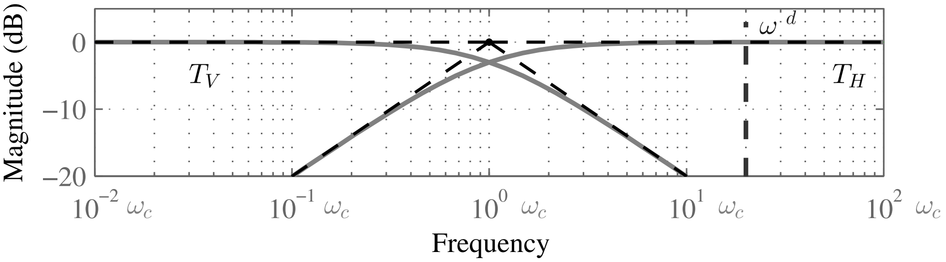

Figure 6.4.: Desirable asymptotic frequency responses of the transfer functions $T_H(s)$ and $T_V(s)$.

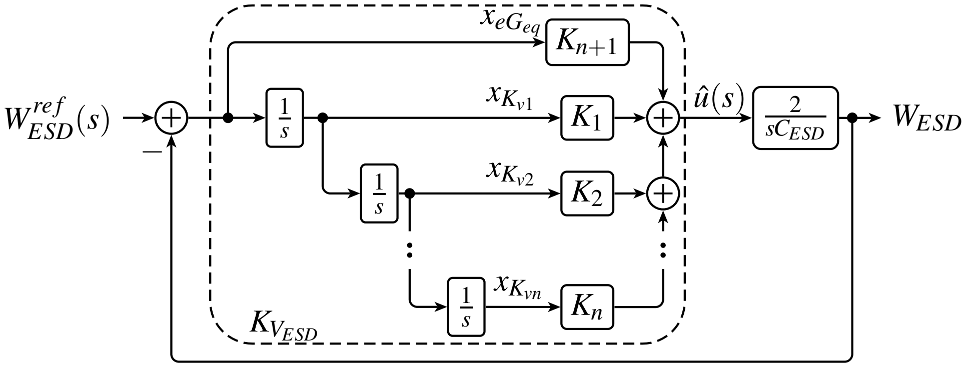

Figure 6.5.: General block diagram of the voltage controller $K_{V_{ESD}}$.

To fulfill the control objectives aforementioned, the frequency responses of these transfer functions should be as illustrated in Figure 6.4. That is, $T_H(s)$ should be a high pass filter with a cut-off frequency ω_c, to reproduce in P_{ESS} the high frequency components of P_{ren}. On the other hand, $T_V(s)$ should be a low pass filter with at least one pole located in $s = 0$ to maintain the supercapacitor voltage close to V_{ESD}^{ref} and guarantee a proper SoC.

The proposed structure for the controller $K_{V_{ESD}}$ is shown in Figure 6.5, where K_i $(i = 1, \dots, n+1)$ are scalar parameters to be designed. This structure is a generalization of the classical PI that allows a simple design of a n-order filter. The order depends on the needed accuracy of the bandwidth limitation. As will be shown, the controller structure in Figure 6.5 reduces the design to the computation of a simple state feedback gain $K_{sf} = \begin{bmatrix} K_1 & K_2 & \dots & K_n & K_{n+1} \end{bmatrix}$ to place the closed loop poles in a desired location.

Let $x_{K_{vi}}$ $(i = 1, \dots, n)$ be the controller states, then the open loop system formed with the proposed controller structure and $G_{eq}(s)$ is given by

$$\dot{x} = \begin{bmatrix} A_{st} & \Upsilon \\ 0 & 0 \end{bmatrix} x + \begin{bmatrix} 0 & B_{st} \\ 2/C_{ESD} & 0 \end{bmatrix} \begin{bmatrix} \hat{u} \\ W_{ESD}^{ref} \end{bmatrix},$$

where

$$A_{st} = \begin{bmatrix} 0 & 0 & \cdots & 0 \\ 1 & 0 & \cdots & 0 \\ \vdots & \ddots & \ddots & \vdots \\ 0 & \cdots & 1 & 0 \end{bmatrix}, \qquad \Upsilon = \begin{bmatrix} -1 \\ 0 \\ \vdots \\ 0 \end{bmatrix}, \qquad B_{st} = \begin{bmatrix} 1 \\ 0 \\ \vdots \\ 0 \end{bmatrix},$$

and $x = \begin{bmatrix} x_{K_{v1}}, & \ldots, & x_{K_{vn}}, & W_{ESD} \end{bmatrix}^T$. In this scheme, the control signal is given by

$$\hat{u} = K_{sf} x.$$

This state feedback control law can be computed *e.g.* by solving a standard pole placement problem [33]. More precisely, the closed loop matrix is given by

$$A_{cl} = \begin{bmatrix} A_{st} & \Upsilon \\ 2\tilde{K}_{sf}/C_{ESD} & K_{n+1} \end{bmatrix},$$

where $\tilde{K}_{sf} = [K_1 \; K_2 \; \ldots \; K_n]$. Using a similarity transformation T, this closed loop matrix in the controllable realization results

$$A_{cl}^c = T^{-1} A_{cl} T = \begin{bmatrix} 0 & & I_n \\ K_1^c & \ldots & K_{n+1}^c \end{bmatrix},$$

where $K_{sf}^c = [K_1^c \; K_2^c \; \ldots \; K_{n+1}^c] = K_{sf} T$. The characteristic polynomial of A_{cl}^c is given by

$$\det(sI_{n+1} - A_{cl}^c) = s^{n+1} + K_{n+1}^c s^n + \cdots + K_2^c s + K_1^c. \tag{6.7}$$

If all closed loop poles are located in $s = -\lambda_c$, the desired closed loop characteristic polynomial is

$$(s + \lambda_c)^{n+1} = s^{n+1} + \alpha_1 s^n + \alpha_2 s^{n-1} + \cdots + \alpha_n s + \alpha_{n+1}. \tag{6.8}$$

By comparing (6.7) and (6.8), the state feedback results

$$K_{sf} = \begin{bmatrix} \alpha_{n+1} & \alpha_n & \ldots & \alpha_1 \end{bmatrix} T^{-1}.$$

The controller $K_{V_{ESD}}(s)$ can be obtained as

$$K_{V_{ESD}}(s) = \tilde{K}_{sf}(sI_n - A_{st})^{-1} B_{st} + K_{n+1}.$$

For example, for $n = 2$, the state feedback gain is

$$K_{sf} = \begin{bmatrix} \frac{3\lambda_c^2 C_{ESD}}{2} & \frac{\lambda_c^3 C_{ESD}}{2} & \frac{3\lambda_c C_{ESD}}{2} \end{bmatrix}$$

and the voltage controller

$$K_{V_{ESD}} = \frac{3\lambda_c C_{ESD}}{2} + \frac{3\lambda_c^2 C_{ESD}}{2s} + \frac{\lambda_c^3 C_{ESD}}{2s^2}.$$

Then, the closed loop transfer functions become

$$T_H(s) = \frac{s^3}{(s+\lambda_c)^3(s\tau_{ESD}+1)}, \tag{6.9}$$

$$T_V(s) = \frac{3\lambda_c s^2 + 3\lambda_c^2 s + \lambda_c^3}{(s+\lambda_c)^3}. \tag{6.10}$$

Transfer functions (6.9) and (6.10) obey the requirement on frequency response shown in Figure 6.4. It is also clear that the transition region of the two filters are overlapped. These regions are smaller when the order of the controller is higher, achieving a more accurate frequency filtering. However, the order of the controller increases the complexity of the implementation.

The controller must be discretized to be implemented in a digital platform, such as a digital signal processor. The state-space realization of the discrete version is then balanced and expressed in the modal canonical form to avoid quantification effects and numerical issues [102]. This is important especially in digital platforms with fixed-point arithmetic. The discrete implementation results then in

$$\begin{aligned} x(k+1) &= x(k) + B_c(W_{ESD}^{ref}(k) - W_{ESD}(k)), \\ \hat{u}(k) &= C_c x(k) + d_c(W_{ESD}^{ref}(k) - W_{ESD}(k)). \end{aligned}$$

where $B_c = [b_1 \ldots b_n]^T$ and $C_c = [c_1 \ldots c_n]$.

6.3.3. Guidelines for selecting the power smoothing controller parameters

In the scheme previously presented, the cut-off frequency, the controller order, the energy storage capacity and rated power are parameters to be selected in accordance to the power level to be smoothed. In the sequel, some general guidelines are given to help to select these parameters.

- The cut-off frequency λ_c determines the bandwidth of the power smoother and can be selected arbitrarily lower than the desired smoothing frequency λ^d. The filter order n determines the steepness of the transition region. The higher the order the more accurate is the component cancellation in the power spectrum. Selecting λ_c close to λ^d can result in a high order controller, and low value of λ_c requires a high capacity of the ESS. The separation between λ_c and λ_d defines the magnitude of T_H at λ_d, see Figure 6.4. With the pole placement given in equation (6.8) and assuming that $\lambda_d \ll 1/\tau_{ESD}$,

  $$|T_H(\lambda_d)| \approx \left(\lambda_c/\sqrt{\lambda_d^2+\lambda_c^2}\right)^{n+1}.$$

  Therefore, it is straightforward to prove that by setting the cross-frequency as

  $$\lambda_c = \sqrt{1-\varepsilon^{2/(n+1)}}\lambda_d,$$

  the attenuation at λ_d is approximately ε. This formula can be used to select the suitable λ_c depending on the controller order.

- There is a trade-off between capacity of the ESS and smoothing capabilities. The higher the capacity C_{ESD}, the smoother the power output. High capacities also prevents reaching capacity limits; if the limits are reached, the filter is disabled until the voltage is restored to the operating range defined in equation (6.2), either by charging or discharging supercapacitors.

- The energy storage rated power P_{ESD} is given by the power converter limits and typically is chosen between $10-40$ % of the rated power of renewable energy source [24].

6.4. Case study: Wind power smoothing

To illustrate the design of the proposed scheme, the technique is used to smooth the power injected into the grid by a wind turbine of 373 kW. The smoothing controller is evaluated by simulation and experiment (in a scaled version).

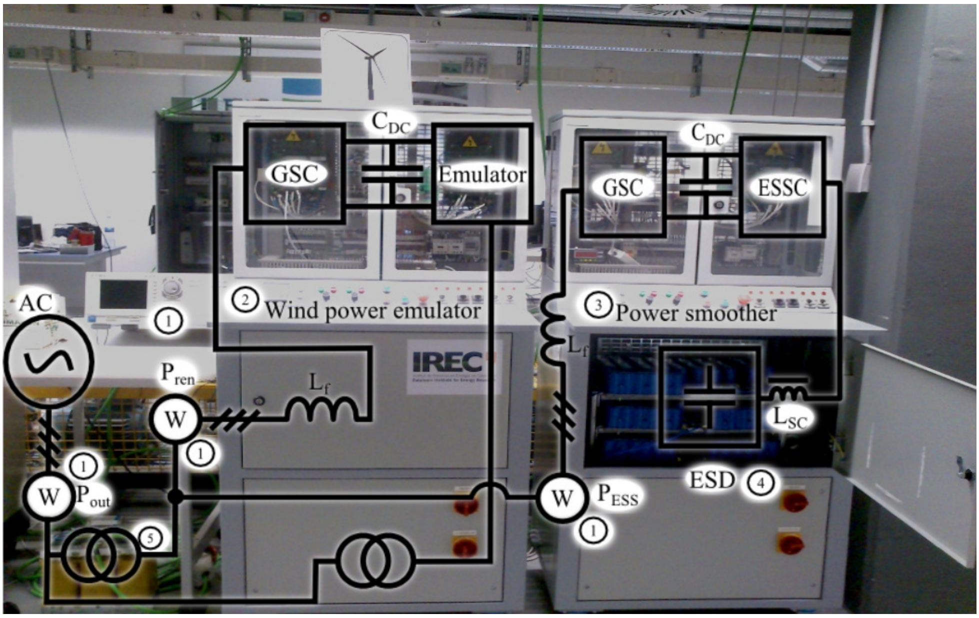

Figure 6.6.: Experimental setup for the implementation of the power smoothing controller. Set-up includes: 1, power meter; 2, wind turbine emulator; 3, power smoother cabinet; 4 , supercapacitor bank; 5, transformer at the point of common coupling.

The experimental set-up is shown in Figure 6.6, which emulates the smoothing scheme in Figure 6.1. The objective is to reduce the power oscillations injected by the wind turbine. Basically, the experimental setup consists of two back-to-back converter, with a DC–link voltage of 650 V, connected to a 400 V AC grid through an isolating transformer. One power converter emulates the power profile of a wind turbine of 373 kW. The other converter implements the power smoother proposed in this chapter. The storage device of the power smoothing system is a supercapacitor bank of 400 V_{DC}, 4 kW and 60 Wh, with $V_{ESD_{min}} = 250\ V$ and $V_{ESD_{max}} = 450\ V$. For more details on the hardware of the experimental set-up see Appendix D. It is worth mentioning that due to hardware limitations on the available equipment to emulate the wind turbine [142], the power ratings in the experimental set-up are lower than the ratings used in simulation case.

The power injected by the wind turbine emulator presents the typical short-term spectrum shown in Figure 6.7. This spectrum was obtained from the model presented in [121, 129] taking into account the studies carried out by Thringer and Dahlberg [163]. The wind profile corresponds to a mean wind speed of 8 m/s and a turbulence intensity of 18 %. The turbulence intensity quantifies the variability of wind speed within 10 minutes. The wind turbine rated power is 373 kW, and the rated wind speed is about 11 m/s. It can be observed in the spectrum in Figure 6.7 that the wind power presents a prominent component close to 1.1 Hz, which is transferred to the grid as a power ripple of several kilowatt.

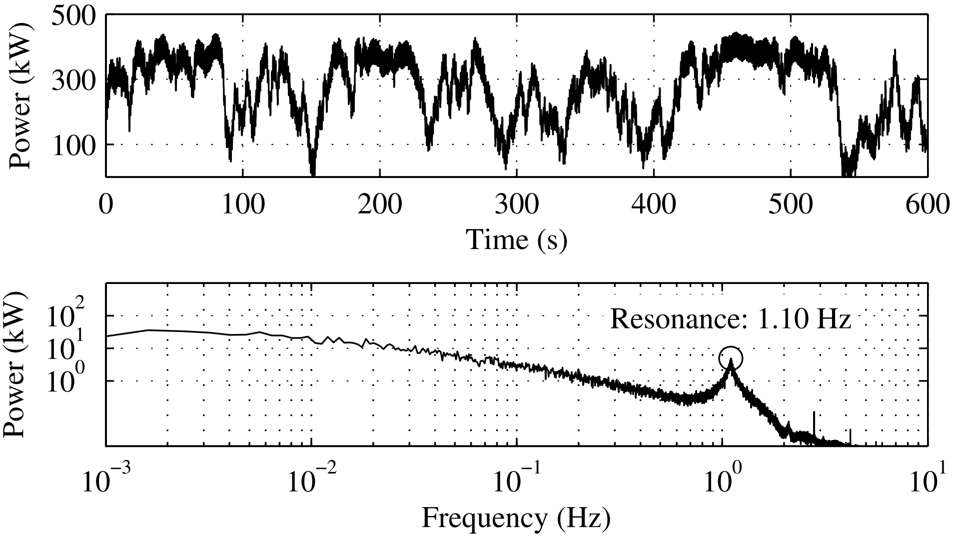

Figure 6.7.: Profile of P_{ren}, the signal emulating the power injected by a 375 kW wind turbine with mean wind speed of 8 m/s, and the corresponding spectrum.

In order to design the power smoother for this particular case, the first step is to decide the cut-off frequency λ^d. It is clear from the spectrum of P_{ren} in Figure 6.7 that λ^d is 6.91 rad/s (1.1 Hz). To attenuate the output power P_{out} in frequencies above λ^d, the magnitude of the frequency response of transfer function $T_H(s)$ should be one at 6.91 rad/s. To achieve this with a reasonable controller order, λ_c is set at 0.3462 rad/s.

A power smoother of order 3 has proved to be sufficient to suppress the 1.1 Hz component without oversizing the supercapacitors for this particular application. The ESS rated power P_{ESD} is set at the 25 % of the nominal power of the renewable source, 100 kW. By applying equations (6.4) to (6.6), the required energy to generate the spectrum is 80.51 Wh. With the procedure described in section 6.3.2 a filter with the frequency response shown in Figure 6.8 is synthesized. The bode plot in Figure 6.8 shows the closed loop transfer functions T_V and T_H corresponding to the designed voltage controller.

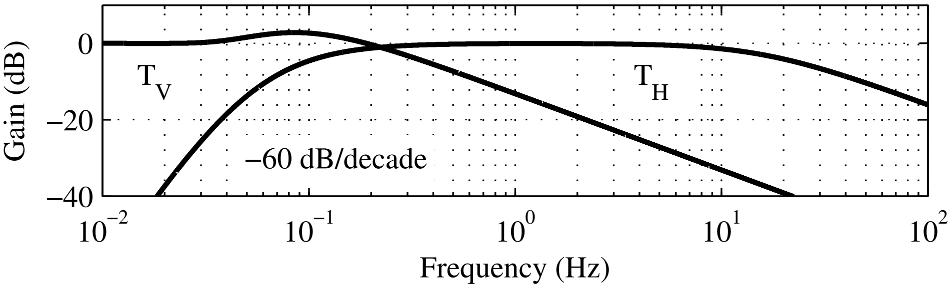

Figure 6.8.: Frequency responses of the closed loop transfers T_H and T_V, the voltage controller has a bandwidth of 0.5857 Hz.

6.4.1. Simulation results

The power smoother designed in the previous subsection is first evaluated by simulation. The scenario includes a wind turbine model generating the power profile shown in Figure 6.7 connected to an AC network with a short circuit ratio of 2.5 (weak network). Power and supercapacitors voltage obtained by simulation can be seen in Figure 6.9. The gray lines correspond to the power injected by the wind turbine P_{ren} (top plot) and the voltage reference V_{ESD}^{ref} (bottom plot), respectively. The rest of lines correspond to the results obtained with a smoother controller of order one and three (dashed and solid lines, respectively).

In the first seconds, in both cases, supercapacitors voltage V_{ESD} reaches the low voltage limit (250 V, in this example) due to the initial transient. Nevertheless, clearly the third order controller is more effective to regulate the voltage than the simple PI. The better effectiveness of the third order controller can also be observed in the power

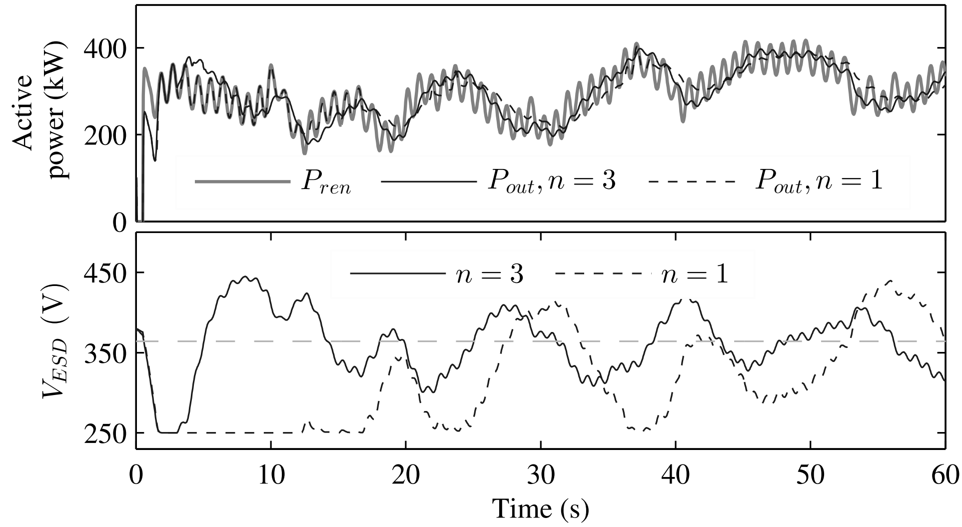

Figure 6.9.: Simulation results corresponding to the 3^{rd} order (solid black lines) and PI (dashed black lines) controllers with $\lambda_c = 0.3462$ rad/s. The gray lines corresponds to P_{ren} in the top plot, and V_{ESD}^{ref} in the bottom plot.

smoothing. The PI power smoothing controller exhibits less attenuation in frequencies below λ^d than the third order controller. Such low attenuation causes larger deviations in the voltage reaching the limits in some points. In contrast, the third order controller is capable of blocking low frequencies, resulting in a smaller voltage variation. If a smoother output power P_{out} is needed, the filter parameter λ_c could be reduced, at the expense of a higher energy capacity required by the storage element.

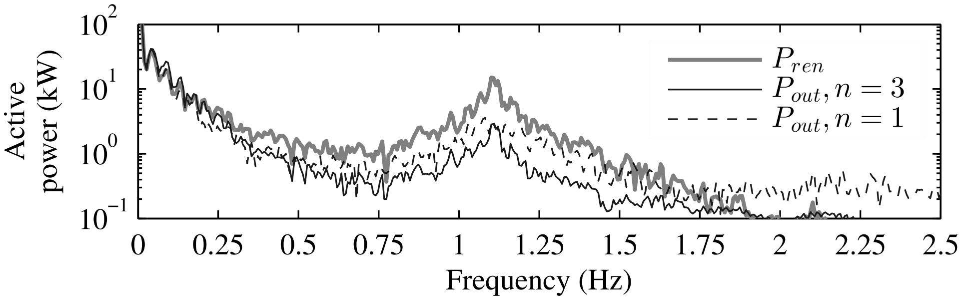

Figure 6.10.: Spectrum of P_{ren} and P_{out}, for the 3^{rd} and 2^{nd} order controllers, respectively.

Figure 6.10 presents the frequency analysis of two simulations showing the differences between the two controllers. The resonance frequency of 1.1 Hz in P_{ren} has been effectively damped by both power smoothing controllers. Nevertheless, higher order controller is more capable of discerning the two control objectives. The attenuation at the frequency of 1.1 Hz is similar, although the PI controller exhibits more energy in the rest of the frequencies. This is translated in a more oscillating power as shown in Figure 6.9. If such behavior is not acceptable for a particular application, a higher order filter should be used.

6.4.2. Experimental results

The power smoother is also evaluated experimentally. In this case, with the aim of obtaining a good resolution, the wind power profile in Figure 6.7 is scaled to fit the emulator limits (±4 kW in this case). As a consequence, the wind power profile has a mean value near zero. In simulations, it has already been validated that the power filter is capable of smoothing a generation with a mean power different from zero. The power smoother implemented in the experimental set-up has the same parameters than the simulated model to produce comparable results. In both cases, the capacity of filtering element is the same. Only the results of the third order controller are presented to avoid a long exposition.

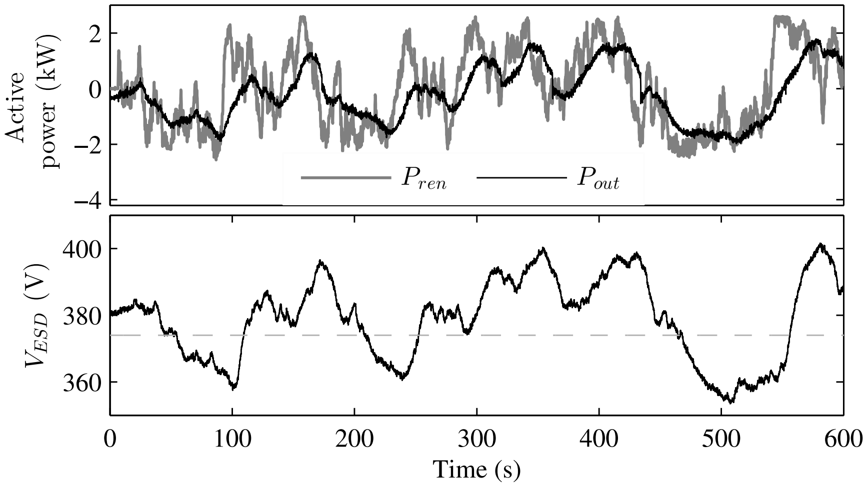

Figure 6.11.: Experimental results corresponding to a 3^{rd} order smoother controller with $\lambda_c = 0.3462$ rad/s.

The generated power P_{ren} with the resulting power P_{out} and the supercapacitor bank voltage V_{ESD} obtained in the experiments can be seen in Figure 6.11. It is clear that the proposed smoothing scheme is able to achieve an effective attenuation of high frequency components in the power while maintain voltage close to the reference value. It must be noted that supercapacitors are oversized for this particular application, as in the available equipment, the rated power of both converters are close. As a consequence, the voltage magnitude could vary less than in a real application.

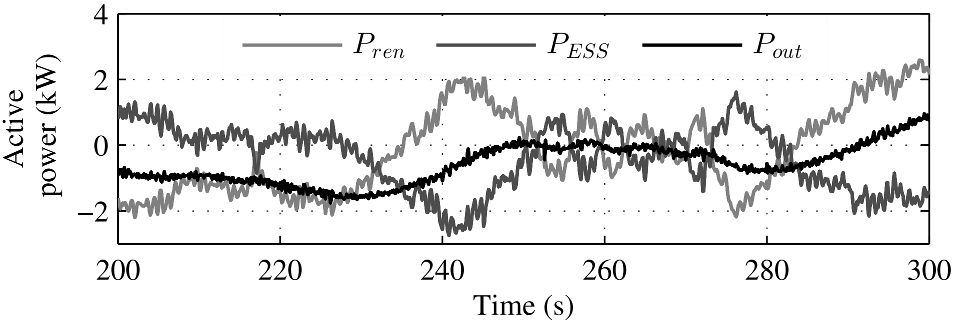

Figure 6.12.: Details of the three power of interest: P_{ren} (light gray), P_{ESS} (dark gray) and P_{out} (black), obtained with the experimental set-up.

Figure 6.12 presents a detail of the three power of interest: P_{ren}, P_{ESS} and P_{out}. This figure serves to show the cancellation of high frequency components of P_{ren}. Fast variations on the power P_{ren} can be observed (lighter line) being compensated by the power generated by the smoothing controller (dark gray) resulting in a smooth power output (black line). The spectrum of P_{out} shown in Figure 6.13 (black line) is the resulting smoothed power injected to the grid. It can be observed that the resonance at 1.1 Hz present in P_{ren} (gray line) is effectively damped in P_{out}. As a consequence of acquisition noise, the signals presented in Figure 6.13 have more variability than its counterparts in Figure 6.10.

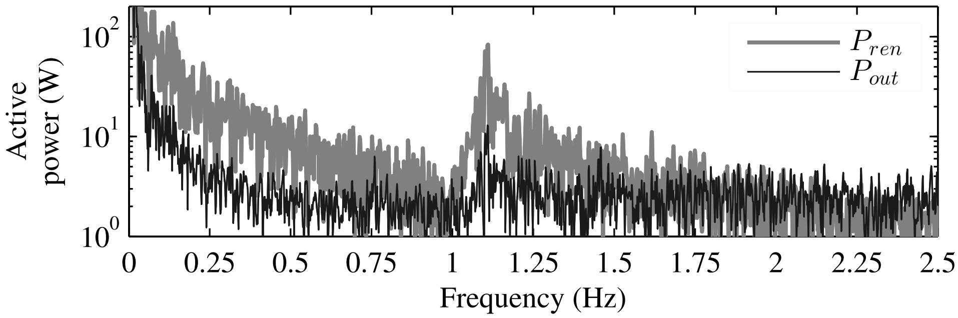

Figure 6.13.: Spectrum of P_{ren} and P_{out}, for the 3^{rd} and 2^{nd} order controllers, respectively.

6.5. Conclusion of the chapter

This chapter has presented a power smoothing strategy based on supercapacitors for its application in weak AC networks or microgrids. The power smoothing strategy has been based on a voltage controller that manages the supercapacitors state of charge while at the same time generates a power profile capable of smoothing the varying power of renewable sources. The proposed voltage controller has been aimed to simplify the implementation, even higher order than the presented in the case of study could be easily implemented in typical digital signal processor used in power converter. The design procedure has been reduced to a standard pole placement problem and guidelines for selecting the storage element have been provided. It is worth noticing the simplicity of the proposed scheme, since it only requires the design and implementation of a voltage controller for supercapacitors, besides the lower current loops, to smooth power injected by an arbitrary source.

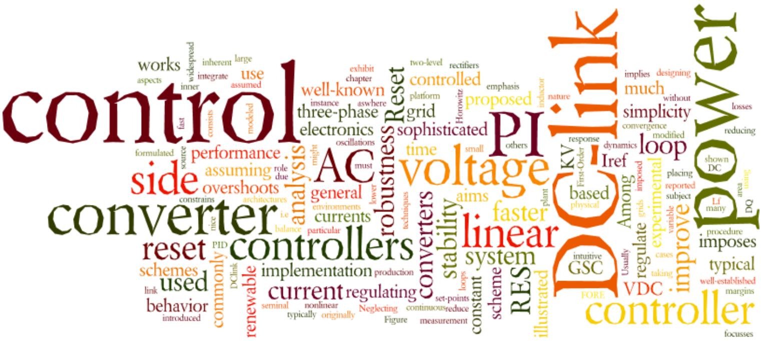

7

DC–link voltage regulation using reset control

This chapter presents the use of reset control to improve the DC–link voltage (V_{DC}) regulation in three-phase rectifiers. The proposed scheme achieves a faster response with lower overshoots preserving the simplicity of the typical PI controllers. The tuning procedure is illustrated in an experimental platform placing special emphasis on the implementation aspects.

7.1. Introduction

In general, and in power electronics in particular, most control loops are based on the well-known and well-established linear control. Among others, PI or PID control is one of the most popular control architectures [7], typically used to regulate a physical variable to a constant value [114, 167]. This type of controllers is widespread also in power electronics [26, 63, 125]. Among other applications, it is commonly used to control the DC–link in power converters, as seen in the previous chapters. Clearly, any performance improvement of PI controllers is quite convenient as it can reduce bus oscillations and improve robustness, and in some cases might allow reducing the required link capacitance.

Although PI controllers exhibit in general a nice behavior, they are subject to inherent constrains due to their linear nature [41]. As it is well-known, a linear second order system with fast convergence implies large overshoots and small robustness margins. This is imposed by the location of the closed-loop poles. Reset control permits taking profit from the PI controller properties and simplicity while overcoming some of its limitations. Reset control was originally introduced by the seminal works of Horowitz on the Clegg-integrator and First-Order Reset Element (FORE), since then many works on this area have been reported [9, 15]. The application of reset techniques in linear controllers imposes a nonlinear behavior to the linear controlled system. This helps to improve performance and robustness but transforms the stability analysis into a more sophisticated affair [9]. Usually an intuitive stability analysis can be based on the describing function, but a formal stability analysis requires the use of more sophisticated tools [9].

In this chapter, a PI controller with reset control is proposed to regulate the DC–link of a power converter. Contribution focusses on the experimental implementation. Most reset control schemes are formulated in continuous time and assuming measurement without noise. As it will be shown, these schemes must be modified before using them in a real environments.

7.2. DC–link in power converters

The plant to be controlled is the DC–link of back-to-back power converters, similar to those used in this thesis, and described in Chapter 3. These converters are commonly used, among other applications, to inte-

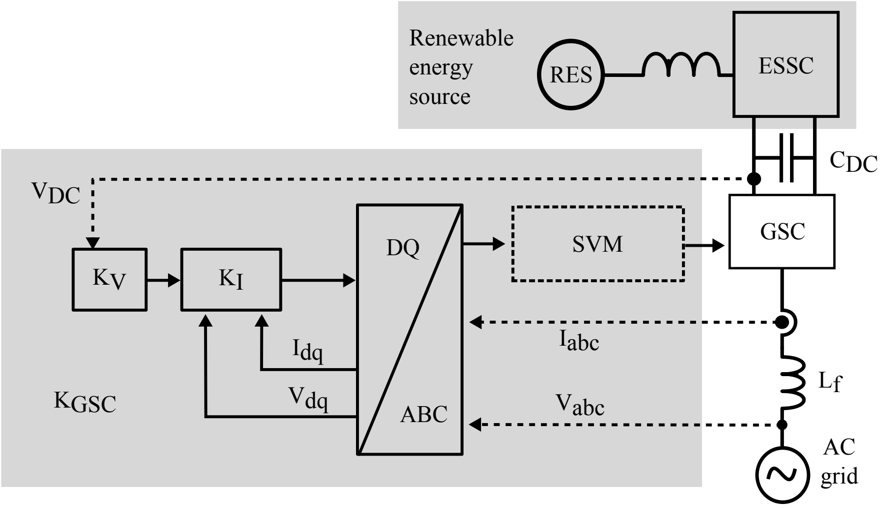

Figure 7.1.: Control scheme of a typical grid side converter.

grate RES into microgrids. The system consists of two power converters connected through a DC–link. The converter on the RES side aims at regulating the renewable power production. The role of the grid side converter (GSC) for grid feeding[1] DG is to inject the power into the AC grid by regulating the DC–link voltage. The GSC is a DC-AC three-phase two-level voltage source converter (VSC).

A typical control scheme of the DC–link for back-to-back converters for RES applications is illustrated in Figure 7.1. The PI controller K_V regulates the DC–link voltage V_{DC} and the controller K_I the AC currents. The controller K_V aims at rejecting the current disturbances caused by the RES side converter. The inner current loop can be assumed much faster than the voltage loop. Then, for purpose of designing the DC–link voltage control, it can be modelled as (see Chapter 3)

$$\frac{d}{dt}\begin{bmatrix} i^d \\ i^q \end{bmatrix} = \begin{bmatrix} \frac{-1}{\tau_I} & 0 \\ 0 & \frac{-1}{\tau_I} \end{bmatrix} \begin{bmatrix} i^d \\ i^q \end{bmatrix} + \begin{bmatrix} \frac{1}{\tau_I} & 0 \\ 0 & \frac{1}{\tau_I} \end{bmatrix} \begin{bmatrix} i^{d,ref} \\ i^{q,ref} \end{bmatrix},$$

where i^d and i^q are the AC currents through inductor L_f in the DQ framework with $i^{d,ref}$ and $i^{q,ref}$ are the corresponding set-points, and τ_I is the time constant.

Neglecting the converter losses and assuming that the current loop is much faster than the DC–link dynamics (*i.e.* $i^{d,ref} \approx i^d$ and $i^{q,ref} \approx i^q$),

---

[1] see Section 3.3 for description of grid feeding DG

the power balance between the AC side and the DC side imposes that

$$\frac{3}{2}(v^d i^d + v^q i^q) = I_{DC} V_{DC},$$

where v^d and v^q are the AC grid voltages expressed in the rotating DQ reference frame, with $v^q = 0$, as the DQ reference is aligned with v^q. Then, the dynamics of the DC–link voltage can be expressed as

$$C_{DC} \frac{d}{dt} V_{DC} = \frac{P_{RES}}{V_{DC}} - \frac{3}{2} \frac{v^d i^d}{V_{DC}}, \tag{7.1}$$

where C_{DC} is the DC–link capacitance and P_{RES} is the power injected (or consumed) from the RES side converter (disturbance) in watts. Multiplying equation (7.1) both sides by V_{DC} and defining $E = V_{DC}^2$, the dynamics of DC–link voltage can be modelled by the linear differential equation

$$C_{DC} \frac{d}{dt} E = P_{RES} - \frac{3}{2} v^d i^d. \tag{7.2}$$

In the Laplace domain results in

$$E(s) = \frac{1}{sC_{DC}} P_{RES}(s) - \frac{K_g}{s} i^d(s), \tag{7.3}$$

with $K_g = 1.5 v^d / C_{DC}$, which in the discrete time is

$$E(z) = \hat{K}_d \frac{1}{z-1} P_{RES}(z) - \hat{K}_g \frac{1}{z-1} i^d(z), \tag{7.4}$$

where T_s is the sampling time, and $\hat{K}_d = \frac{T_s}{C_{DC}}$, $\hat{K}_g = K_g T_s$.

7.3. PI controllers with reset control

PI controllers are composed by two control actions, proportional and integral, while the proportional action most relevant role is to guarantee stability and shaping the step response, integral action guarantees null steady-state error. Under this hypothesis, most discrete PI controllers have an integral gain much lower than the proportional one and consequently the proportional action becomes the most relevant one when the error is close to zero. Unfortunately, at this point the integrator stores a value that depends on the previous evolution and that might be far from the value required in steady-state. This is in most cases the reason of the overshoot produced by PI controllers when a fast convergence is required.

The idea behind the Clegg integrator [9] is to reset to 0 the integrator in the PI controller as the error ($e = E^{ref} - E$) becomes 0. This would in general reduce or even extinguish the overshoot while preserving the settling time. Although tracking reference and rejecting disturbance are closely related problems in linear system, it is not the case in nonlinear control in general, and reset control in particular. When K_V controller aims to reject constant (or piecewise constant) disturbances, the Clegg integrator is not usually used alone. It is commonly used in parallel with a regular integrator. Both integrators have the same gain K_i but an additional parameter α ($0 \leq \alpha \leq 1$) is added to set the resetability degree. Figure 7.2 shows the complete architecture of the PI control plus the Clegg integrator. From the reference tracking problem point of view, a complete reset ($\alpha = 1$) offers the best performance but this might not be the case for the disturbance rejection problem, as depending on the reset logic, the best performance can be typically achieved with $\alpha \neq 0$.

Most real systems are subject to measurement noise, which might generate an undesired integrator reset. To deal with this problem the error is passed through a low pass filter (LPF) to clean it and properly detect the appropriate moment to reset the integrator. As this low-pass filter introduces a phase lag, similar to those systems subject to time delay, it is convenient to use a band reset logic [10] instead of one previously introduced ($e = 0$). The band detection must also deal with phenomena like quantification and sampling. This might cause large changes in the variables from one sample to the following. Consequently, the reset band must be set greater than the maximum expected change of e_f between two samples. Then, the following reset logic is proposed

$$\text{reset} = \begin{cases} TRUE, & \text{if } e_f \leq -\gamma \text{ AND } \frac{d}{dt}e_f \leq 0, \\ TRUE, & \text{if } e_f \geq \gamma \text{ AND } \frac{d}{dt}e_f \geq 0, \\ FALSE, & \text{otherwise,} \end{cases}$$

where γ is the reset band size. That is, the integrator is reset when the filtered error e_f crosses the band defined around $e_f = 0$ with increasing amplitude.

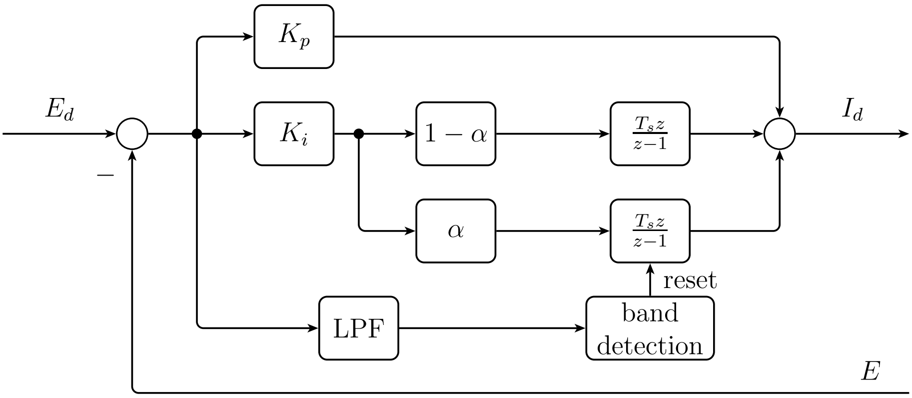

Figure 7.2.: PI controller with reset control for the GSC.

7.4. Experimental implementation

The implementation of the control scheme in Figure 7.2 and the tuning of the different parameters are illustrated in the case of an experimental platform composed of a 4 kW DC/DC converter connected to a three-phase 4 kW VSC operated at 12.21 kHz ($T_s = 0.819$ μs). Further details of the experimental set-up can be found in Appendix D. Then, for this particular system, the parameters from (7.4) results in $\hat{K}_g = 26.5840$ and $\hat{K}_d = 0.0443$ and the controller is

$$K_V(z) = \frac{i^d(z)}{E^{ref}(z) - E(z)} = K_p + K_i \frac{T_s z}{z-1}.$$

With this controller, the closed-loop transfer function from the desired set-point E^{ref} to the output E is

$$T_{EE^{ref}}(z) = \frac{\hat{K}_g\left(\left(K_i T_s + K_p\right) z - K_p\right)}{z^2 + \left(K_i T_s \hat{K}_g + K_p \hat{K}_g - 2\right) z - K_p \hat{K}_g + 1},$$

while the closed-loop transfer function from the power disturbance P_{RES} to the output E results

$$T_{ED}(z) = \frac{\hat{K}_d\,(z-1)}{z^2 + \left(K_i T_s \hat{K}_g + K_p \hat{K}_g - 2\right) z - K_p \hat{K}_g + 1}.$$

The PI parameters were tuned as $K_p = 0.1233 \cdot 10^{-3}$ and $K_i = 8.9074 \cdot 10^{-3}$ in order to achieve a fast step response. This choice places the closed-loop poles at $0.99835 \pm \jmath 0.004085$ and the zero of $T_{EE^{ref}}$ at $z = 0.99411$. The location of the closed-loop poles corresponds to an overshoot of 0.282 V^2 for one unit change at the set-point and a settling time of 0.2 s approximately. The zeros in $T_{EE^{ref}}$ and T_{ED} increase the overshoot to 0.385 V^2 for $T_{EE^{ref}}(z)$ and to 6.245 V^2 for $T_{ED}(z)$.

Figure 7.3 shows the DC–link voltage V_{DC} when the power P_{RES} consumed by the DC/DC converter changes from 3.5 kW to −3.5 kW (a step of 7 kW). Clearly, the response is fast but with a significant overshoot, as expected from the PI tuning.

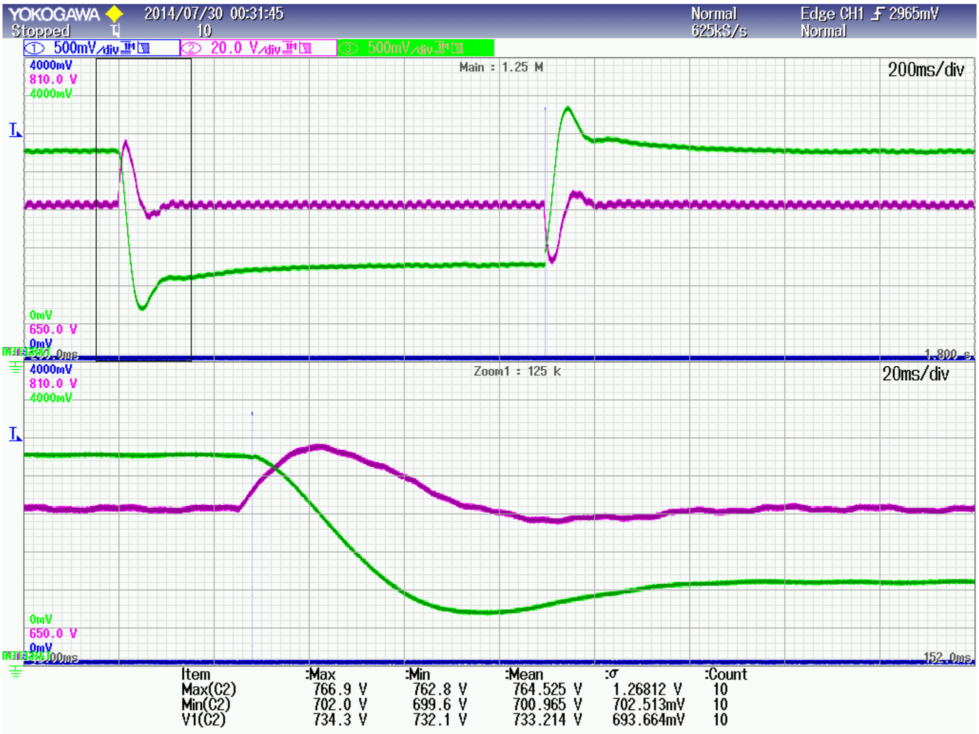

```
Item        :Max      :Min      :Mean       :σ           :Count
Max(C2)      766.9 V   762.8 V   764.525 V   1.26812 V    10
Min(C2)      702.0 V   699.6 V   700.965 V   702.513mV    10
V1(C2)       734.3 V   732.1 V   733.214 V   693.664mV    10
```

Figure 7.3.: Closed-loop system response without reset control under a 7 kW power step disturbance. The purple line is V_{DC}, and the green line is the K_V integrator state.

Using linear controllers, reducing the overshoot implies increasing the settling time and a slower disturbance rejection. As discussed in section 7.3, this can be circumvent by adding reset control to the linear controller. The first step in the implementation of the reset control scheme in Figure 7.2 is to select an appropriate low-pass filter in order to avoid undesirable reset caused by the measurement noise in the DC

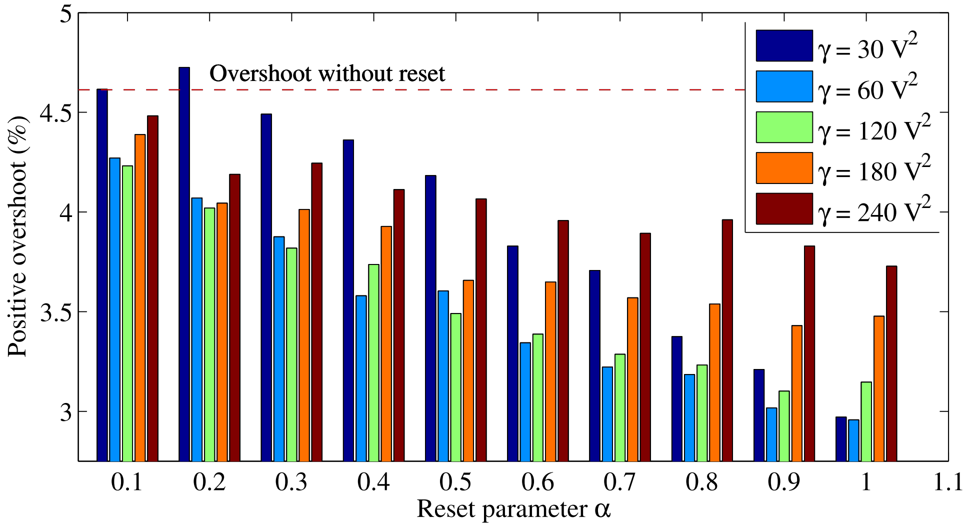

Figure 7.4.: Response comparison for different reset parameter values and reset bands.

voltage. The spectrum of V_{DC} measured during constant full load operation reveals high energy components in the frequencies 50, 150 and 12210 Hz. The combined effect of these components results in a noise amplitude of 4.18 V around the nominal value. To attenuate this noise, a second order Butterworth filter with a bandwidth of 50 Hz was used for the low-pass filter in Figure 7.2.

The second step in the reset implementation is to select the reset band. The selection must consider the delay due to the low-pass filter and the quantification and sampling issues. As a result, the reset band γ was selected after evaluating several values and analyzing the effect on the overshoot. Figure 7.4 summarizes these tests. These were conducted for five different bands with nine different values of the parameter α. It can be observed, for each band, that the overshoot decreases as the reset parameter α increases. For the present application, with the particular reset logic and low-pass filter, the best results are obtained with $\alpha = 1$ and $\gamma = 60$ V^2.

Figure 7.5 shows the closed-loop response for a similar power disturbance (a step of 7 kW) in case of using the proposed reset control scheme. Clearly, the DC voltage exhibits a significantly reduction in the overshoot, approximately 30% lower w.r.t the case without reset control. It is worth noticing that the settling time is not affected.

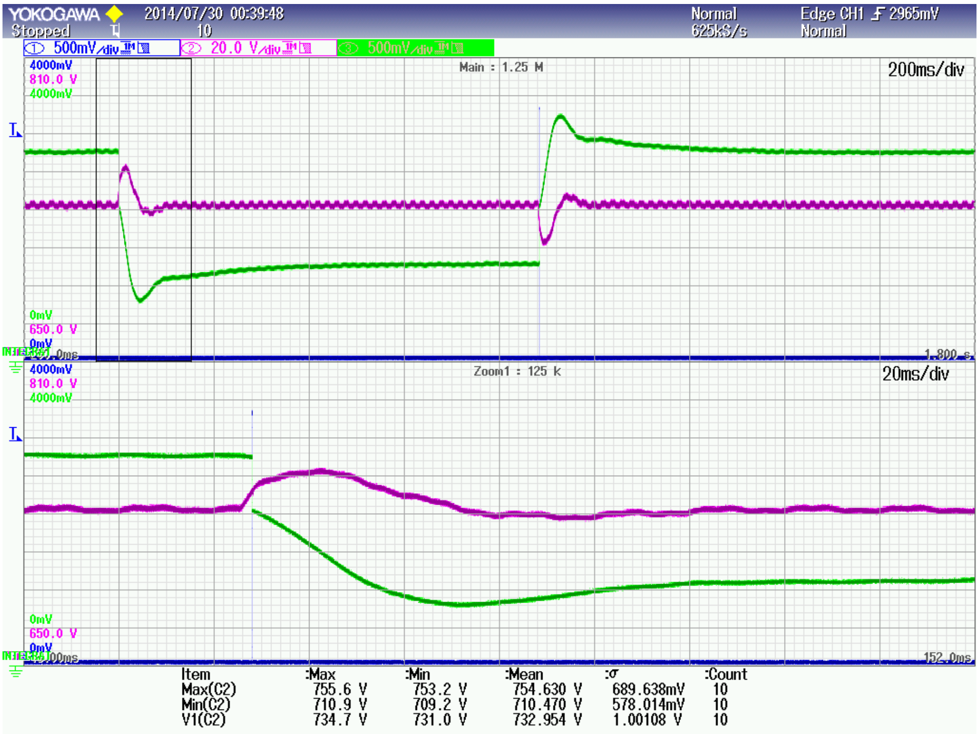

```
Item      :Max      :Min      :Mean       :σ          :Count
Max(C2)   755.6 V   753.2 V   754.630 V   689.638mV   10
Min(C2)   710.9 V   709.2 V   710.470 V   578.014mV   10
V1(C2)    734.7 V   731.0 V   732.954 V   1.00108 V   10
```

Figure 7.5.: Closed-loop system response with reset control under a 7 kW power step disturbance. The purple line is V_{DC}, and the green line is the K_V integrator state.

7.5. Conclusion of the chapter

The addition of reset control to the typical PI controller used to regulate the DC–link voltage in VSC can reduce the overshoot without affecting the settling time. The proposed control scheme keep the controller simplicity and is capable of properly working under noisy environment like power converter as shown in the experimental results. The proposed architecture and methodology can be easily extended to other types of applications.

8

Robust decentralized droop control design for islanded microgrids

This chapter addresses the problem of decentralized droop control design with stability guarantee for the parallel operation of DG in low voltage microgrids. The design procedure is derived for an advanced decentralized droop control scheme with derivative term to improve transient response and stability margins. The decentralized control offers two advantages over typical centralized schemes: on the one hand permits to modify the microgrid topology without redesigning the controllers. On the other hand, the proposed procedure guarantees the stability of the microgrid with multiple units working in parallel without communications, yielding to a more reliable system. Control parameters are obtained solving a optimization problem with LMI constraints, using three tuning parameters.

8.1. Introduction

Although MG is a promising paradigm, some technical challenges should be overcome prior to its large scale integration [130]. One of the most relevant technical challenges to be faced in low voltage microgrids is the electrical stabilization by means of sharing the power demand among multiple parallel DG when working islanded from the main grid. This challenge has been addressed by numerous authors [66, 153, 177], presenting different conceptual solutions; see Chapter 3 for more details. Being accepted by the majority of the scientific community, droop control is the *de facto* technique for paralleling VSC working in islanded conditions [119]. The classical droop control proposed by Chandorkar, Divan, and Adapa [32] consists of a proportional relation between active power and voltage frequency and between reactive power and voltage amplitude. The major benefit of the droop control is its decentralized structure which allows to control the microgrid electrical variables in absence of communications among units, achieving a highly reliable system. Despite its wide acceptance, it presents some important drawbacks [119]. One of the most important drawbacks is the impact of line impedance in the dynamic response of the microgrid. This dependence can lead to undesired behaviors, ranging from low power sharing accuracy to instability.

Different approaches has been proposed in the literature to circumvent the effects of line impedance. Among the decentralized approaches based on the modification of the droop control it can be distinguished the virtual impedance method [68], the parametric droop with a rotation matrix based on R/X line impedance ratio [22], the emulation of mechanical inertia [148], the recent droop based on $\mathcal{H}_\infty$ theory [58], and variations of these methods [119, 130]. In addition to these proposals, an additional loop to the conventional droop control has been proposed in [67] to improve the transient performance and stability margins. This additional derivative loop is studied in [67] in a system where a DG is connected to a stiff AC system. The proposed design guidelines of the new control loop parameters are based on the small signal system root locus. Later, multiple DG units are considered in [117], where the design procedure is also based on the small signal model of the complete microgrid. Since the performance of the DG units depends on the delivered power level, an adaptive gain is proposed in [50, 117]. As a novelty to previous works, the dynamics of the power source is taken into account in [50].

In parallel to the proposed improvements to the droop control, a different approach for the decentralized and robust design for droop control of microgrids has been proposed [147, 153]. This approach models the microgrid as an aggregate of interconnected subsystems, deriving the stability of the entire system by analyzing each subsystem stability and placing bounds on the non-linear interconnections between subsystems. In [153], bounds on the droop coefficients are derived for the conventional droop control to ensure stability and states the worst case synchronization rate. Alternatively, the interactions among different DER are analysed and a decentralized control scheme guaranteeing stability is proposed in [147].

The aim of this chapter is to provide a new design procedure to obtain a decentralized robust stabilizing droop controller taking into account the interactions among DG. The controller structure is based on the modifications to the droop control found in the literature, this is, adding virtual inertia and a derivative term for stabilization. Unlike previous results, the proposed procedure tunes the control parameters for each unit without knowing the entire microgrid configuration. The synchronization among DG is performed by the droop control, ensuring a deterministic power sharing without communications. Moreover, the design procedure takes into account the possibility that a external supervisor changes the droop set-points of each DG to restore the system frequency or synchronize with the distribution grid. The operation of a sample microgrid implemented with controllers designed using the proposed control design procedure is analysed by numerical simulation.

8.2. Droop control in microgrid applications

Consider a microgrid with n_{DG_c} controllable units, $n_{DG_{uc}}$ uncontrollable units and n_L loads with a total of $n_{mg} = n_{DG_c} + n_{DG_{uc}} + n_L$ units. With the aim of modeling the microgrid for control design purpose, controllable and uncontrollable DG units, and loads without associated generation will be considered as nodes of the microgrid. The set of all nodes in the microgrid is defined as

$$\mathbb{N}_{mg} \triangleq \{1, \dots, n_{mg}\} = \mathbb{N}_{DG_c} \cup \mathbb{N}_{DG_{uc}} \cup \mathbb{N}_L,$$

with $\mathbb{N}_{DG_c}$ the subset of controllable DG nodes, $\mathbb{N}_{DG_{uc}}$ the subset of uncontrollable DG nodes and $\mathbb{N}_L$ the subset of independent loads.

Conventional droop control seeks to achieve a proper power generation sharing among the controllable DG$_c$ units in response to variations in the electrical demand. To this end, the control strategy imposes frequency and voltage set-points to the VSC proportional to the deviations of the active and reactive powers from the set-points given by the MGCC, *i.e.* for all $j \in \mathbb{N}_{DC_c}$,

$$\omega_j^c = \omega^{ref} - k_{pP_j}(P_j^c - P_j^{ref}), \tag{8.1a}$$

$$V_j^c = V^{ref} - k_{pQ_j}(Q_j^c - Q_j^{ref}), \tag{8.1b}$$

with k_{P_j} and k_{Q_j} the droop coefficients. Superscript ^{ref} denotes set-point values. This scheme produces voltage and frequency variations around the global references V^{ref} and ω^{ref}, taking into account the power set-points P_j^{ref} and Q_j^{ref} given by the MGCC. Typically, droop coefficients k_{pP_j} and k_{pQ_j} are fixed and selected according the power rating of each DG$_c$ as

$$k_{pP_j} = \frac{\Delta\omega}{S_j^n}, \qquad k_{pQ_j} = \frac{\Delta V}{S_j^n},$$

where $\Delta\omega$ and ΔV are the maximum frequency and voltage admissible deviations respectively, and S_j^n is the nominal power of the j-th DG.

Active and reactive powers can be passed through a low pass filter. Typically, the filter may remove the fast oscillations obtained from the power computation. However, by increasing the time constant of the filter, it can be introduced a fictitious inertia to the power converter, miming traditional synchronous generators [148]. Such fictitious inertia provides a time scale separation between the droop control and the line dynamics. The dynamic equations of this low pass filter are given by

$$\frac{d}{dt}P_j = \frac{1}{\tau_{I_j}}(-P_j + z_{1,j}), \tag{8.2a}$$

$$\frac{d}{dt}Q_j = \frac{1}{\tau_{I_j}}(-Q_j + z_{2,j}), \tag{8.2b}$$

where τ_{I_j} is the time constant [55].

As droop gain is selected according to power sharing objectives, the stability of the entire microgrid is not guaranteed and frequency and voltages responses after a disturbance may be rather oscillatory before reaching the steady-state values. In order to add additional degrees of freedom, the control law (8.1) can be modified by adding derivative terms

[67, 117]. The aim of these terms is to produce signals capable of helping in the damping of power oscillations caused by the interactions among DG. The control law is sketched in Figure 8.2 and can be expressed as

$$\omega_j^c = \omega^{ref} - k_{pP,j}(P_j - P_j^{ref}) - k_{dP,j}P_j^d, \tag{8.3a}$$

$$V_j^c = V^{ref} - k_{pQ,j}(Q_j - Q_j^{ref}) - k_{dQ,j}Q_j^d, \tag{8.3b}$$

with

$$\frac{d}{dt}P_j^d = (-P_j^d + \frac{d}{dt}P_j)/\tau_{D_j}, \tag{8.4a}$$

$$\frac{d}{dt}Q_j^d = (-Q_j^d + \frac{d}{dt}Q_j)/\tau_{D_j}, \tag{8.4b}$$

for all $j \in \mathbb{N}_{DG_c}$. Power set-points are assumed in the range: $P_{\min,j} \leq P_j^{ref} \leq P_{\max,j}$ and $Q_{\min,j} \leq Q_j^{ref} \leq Q_{\max,j}$.

As the droop gains $k_{pP,j}$ and $k_{pQ,j}$ are selected according a power sharing criteria, the gain of the derivative terms, k_{dP_j} and k_{dQ_j}, can be designed to ensure the global stability of the microgrid, without affecting the steady-state power sharing. The time constant $\tau_{D,j}$ is selected smaller than $\tau_{I,j}$ in order to achieve a proper derivative effect in the frequencies of interest.

8.3. Microgrid Modeling

The active and the reactive powers flowing from a DG associated to the node j are given by

$$P_j^c(t) = P_j^{ld}(t) + P_j^g(t), \tag{8.5a}$$

$$Q_j^c(t) = Q_j^{ld}(t) + Q_j^g(t), \tag{8.5b}$$

where P_j^{ld} and Q_j^{ld} are the active and reactive powers corresponding to a local load and P_j^g and Q_j^g are the active and reactive powers flowing into the rest of the microgrid, as illustrated in Figure 8.1.

The voltage at the node $j \in \mathbb{N}_{mg}$ can be expressed as a time-varying complex number, namely a dynamic phasor[1] which represents the voltage as a sine wave $\check{V}_j(t) = \sqrt{2}V_j(t)\cos\phi_j(t)$, where V_j is the magnitude and ϕ_j is the angle determined with respect the j-th local reference frame. Note that it is assumed that no communications are available among DG$_c$ for synchronization, thus each angle ϕ_j is independent.

---

[1] see Chapter 3 for more details

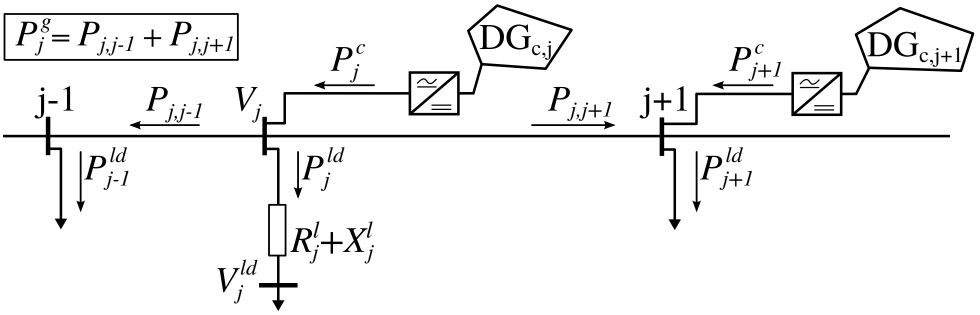

Figure 8.1.: Labelling a generic node of a microgrid.

Considering that the node j is connected to another node h through an admittance $Y_{jh} = G_{jh} + \jmath B_{jh}$ ($\jmath = \sqrt{-1}$), the active and reactive powers flowing from node j to the rest of the grid are given by [149]

$$\begin{aligned} P_j^g(t) &= G_{jj} V_j^2(t) \\ &\quad - V_j(t) \sum_{h \in \mathcal{N}_j} V_h(t)(G_{jh} \cos \phi_{jh}(t) + B_{jh} \sin \phi_{jh}(t)), \end{aligned} \tag{8.6a}$$

$$\begin{aligned} Q_j^g(t) &= -B_{jj} V_j^2(t) \\ &\quad - V_j(t) \sum_{h \in \mathcal{N}_j} V_h(t)(G_{jh} \sin \phi_{jh}(t) - B_{jh} \cos \phi_{jh}(t)), \end{aligned} \tag{8.6b}$$

where $\phi_{jh}(t) = \phi_h(t) - \phi_j(t)$, and $\mathcal{N}_j = \{h : h \in \mathbb{N}_{mg}, h \neq j, Y_{jh} \neq 0\}$ denotes the set of nodes directly connected through an admittance Y_{jh} with the node j (these nodes are usually called neighbours). Moreover,

$$G_{jj} = \hat{G}_{jj} + \sum_{h \in \mathcal{N}_j} G_{jh}, \qquad B_{jj} = \hat{B}_{jj} + \sum_{h \in \mathcal{N}_j} B_{jh},$$

and $\hat{G}_{jj}$ and $\hat{B}_{jj}$ are the shunt conductance and susceptance, respectively.

To formulate the local dynamics of node j-th, these are the dynamics of the power flowing from node j to the local aggregated loads, voltage $\check{V}_j(t)$ and $\check{V}_j^{ld}$ can be expressed in a rotating DQ reference frame, choosing ϕ_j as the reference angle, such that

$$\begin{aligned} v_j^d(t) &= V_j(t), & v_j^q(t) &= 0, \\ v_j^{d,ld}(t) &= V_j^{ld}(t) \cos(\phi), & v_j^{q,ld}(t) &= V_j^{ld}(t) \sin(\phi), \end{aligned}$$

where $\phi = \phi_j(t) - \phi_j^{ld}(t)$, d and q denote the direct and quadrature components, and $\check{V}_j^{ld}$ is the dynamic phasor representing the load voltage.

In this reference frame and using the instantaneous power theory, the local load power is expressed as

$$P_j^{ld}(t) = \frac{3}{2} v_j^d(t) i_j^{d,ld}(t), \tag{8.7a}$$

$$Q_j^{ld}(t) = \frac{3}{2} v_j^q(t) i_j^{q,ld}(t), \tag{8.7b}$$

where $i_j^{dq,ld}$ is the current flowing into the local loads. The Kirchhoff voltage law allow us to relate the load voltage and current as

$$L_j^l \frac{d}{dt} I^{ld}(t) = -R_j^l I^{ld}(t) + \check{V}_j(t) - \check{V}_j^{ld}(t), \tag{8.8}$$

where R_j^l and L_j^l is the impedance of the line connecting the loads and the j-th bus. Expressing (8.8) in the previously defined DQ reference frame, it can be obtained

$$\frac{d}{dt} i_j^{d,ld}(t) = -\frac{R_j^l}{L_j^l} i_j^{d,ld}(t) + \omega_j(t) i_j^{q,ld}(t) + \frac{v_j^d(t) - v_j^{d,ld}(t)}{L_j^l}, \tag{8.9a}$$

$$\frac{d}{dt} i_j^{q,ld}(t) = -\frac{R_j^l}{L_j^l} i_j^{q,ld}(t) - \omega_j(t) i_j^{d,ld}(t) - \frac{v_j^{q,ld}(t)}{L_j^l}, \tag{8.9b}$$

where $\omega_j(t) = \frac{d}{dt}\phi_j(t)$ is the voltage frequency at node j.

The generic power equations (8.5) can be particularized for each type of node as:

- *Loads*, $j \in \mathbb{N}_L$, $P_j^c = 0$ and $Q_j^c = 0$, as it is assumed that there is no generation in this kind of node.

- *Uncontrollable nodes*, $j \in \mathbb{N}_{DG_{uc}}$, P_j^c and Q_j^c are considered as external disturbances to the microgrid, as the power injected by this kind of nodes cannot be controlled.

- *Controllable nodes*, $j \in \mathbb{N}_{DG_c}$, P_j^c and Q_j^c are variables that can be controlled by acting on the power converters. Controllable DG units are interfaced with VSC operated in AC voltage source mode [124]. To analyze the stability the microgrid, the inner control of the VSC is modeled as an ideal voltage source with variable frequency [58]. The model simplification has been analyzed in [117] concluding that the simplified model is accurate enough for stability studies. Power electronics converters can change the frequency of the generated voltage instantaneously, however the voltage magnitude control loop introduces a delay represented by τ_{V_j}. The dynamics of the inner control loop, as seen in Chapter 3, can be expressed as

$$\frac{d}{dt}\phi_j(t) = \omega_j^c(t), \tag{8.10a}$$

$$\frac{d}{dt}V_j(t) = \frac{1}{\tau_{V_j}}(-V_j(t) + V_j^c(t)). \tag{8.10b}$$

where ω_j^c and V_j^c are the set-point signals for the power converter obtained from the droop control law.

With the previous considerations, the entire microgrid system can be modelled as the aggregation of all nodes by combining equations (8.5). The interactions among nodes are given by the signals P_j^c and Q_j^c, which

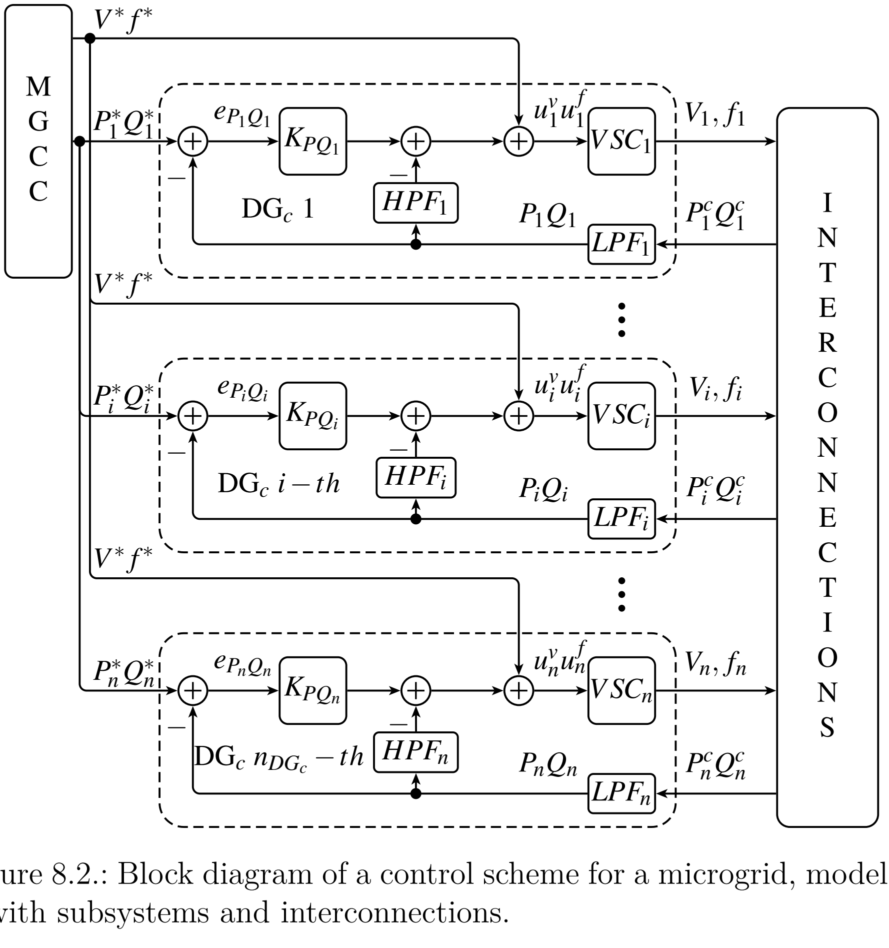

Figure 8.2.: Block diagram of a control scheme for a microgrid, modelled with subsystems and interconnections.

reflect the grid topology and the particular DG units and loads as shown in Figure 8.2. This subdivision is useful to study the stability of the whole system and to propose a decentralized control design procedure establishing bounds on the interconnections among the subsystems.

With the aim of studying the stability of the microgrid, local dynamics (8.9), for every controllable DG$_c$, are linearised around the steady-state values $\bar{\phi}_j$, $\bar{V}_j$, $\bar{i}_{dq,j}$ defined by the local power flow conditions. To obtain the steady state values, it is assumed that DG$_c$ is only connected to its local load, *i.e.* $P_j^g(t) = 0$. To calculate the steady state values, a procedure such as de one proposed in Chapter 9 might be used. Hereafter time has been drop to shorten the expressions. Then, the small-signal dynamics for a generic node j are given by

$$\begin{aligned}
\frac{d}{dt}x_{1,j} &= -\frac{R_j^l}{L_j^l}x_{1,j} + \omega^{ref}x_{2,j} - \frac{\bar{V}_{d,j}^{ld}\sin(\bar{\phi}_j - \bar{\phi}_j^{ld})}{L_j^l}x_{3,j} \\
&\quad + \frac{\bar{V}_{d,j}}{L_j^l}x_{4,j} + 2\pi\bar{i}_{q,j}u_j^{\omega}, && (8.11a) \\
\frac{d}{dt}x_{2,j} &= -\omega^{ref}x_{1,j} - \frac{R_j^l}{L_j^l}x_{2,j} + \frac{\bar{V}_{q,j}^{ld}\cos(\bar{\phi}_j - \bar{\phi}_j^{ld})}{L_j^l}x_{3,j} \\
&\quad - 2\pi\bar{i}_{q,j}u_j^{\omega}, && (8.11b) \\
\frac{d}{dt}x_{3,j} &= u_j^{\omega}, && (8.11c) \\
\frac{d}{dt}x_{4,j} &= \frac{1}{\tau_{V,j}}\left(-x_{4,j} + u_j^{v}\right), && (8.11d) \\
z_{1,j} &= \frac{3}{2}\bar{V}_{d,j}x_{1,j} + \frac{3}{2}\bar{i}_{d,j}x_{4,j} + d_{P,j}, && (8.11e) \\
z_{2,j} &= \frac{3}{2}\bar{V}_{d,j}x_{2,j} + \frac{3}{2}\bar{i}_{q,j}x_{4,j} + d_{Q,j}, && (8.11f)
\end{aligned}$$

where

$$\begin{aligned}
x_{1,j} &= i_{d,j} - \bar{i}_{d,j}, & x_{2,j} &= i_{q,j} - \bar{i}_{q,j}, \\
x_{3,j} &= \phi_j - \bar{\phi}_j, & x_{4,j} &= V_{d,j} - \bar{V}_{d,j}, \\
u_j^{\omega} &= \omega_j^c - \omega^{ref}, & u_j^{v} &= V_j^c - V_j^{ref} \quad \text{(see (8.3))} \\
d_{P,j} &= P_j^g - \bar{P}_j^g, & d_{Q,j} &= Q_j^g - \bar{Q}_j^g,
\end{aligned}$$

with u_j^{ω} and u_j^{v} the variations of the control signals with respect to its set-point values. The dynamics of (8.6) and (8.9) depends on ω_j, which is determined by the droop control law defined in (8.3). Given

$\omega^{ref} \gg k_{pP_j}(P_j^c - P_j^{ref}) + k_{dP,j}P_j^d$, the reactance of $\omega_j L_j^l$ and B_{jh} can be assumed constant with its nominal value. From the viewpoint of the dynamics of all nodes $j \in \mathbb{N}_{DC_c}$, the variables $d_{P,j}$ and $d_{Q,j}$ are disturbances caused by the interaction with the rest of the nodes.

Defining the state variables

$$\begin{aligned} x_{5,j} &= P_j - \bar{P}_j, & x_{6,j} &= Q_j - \bar{Q}_j, \\ x_{7,j} &= \tau_{D,j}P_j^d - x_{5,j}, & x_{8,j} &= \tau_{D,j}Q_j^d - x_{6,j}, \end{aligned}$$

the small-signal dynamics corresponding of the entire grid is governed by

$$\frac{d}{dt}x_j = A_j x_j + B_j u_j + E_j d_j(x), \qquad j \in \mathbb{N}_{DG_c} \tag{8.12}$$

where

$$\begin{aligned} x_j^T &= \begin{bmatrix} x_{1,j} & \dots & x_{8,j} \end{bmatrix}, \quad x^T = \begin{bmatrix} x_1^T & \dots & x_{n_{DG_c}}^T \end{bmatrix}, \\ u_j^T &= \begin{bmatrix} u_j^\omega & u_j^v \end{bmatrix}, \quad d_j^T = \begin{bmatrix} d_{P,j} & d_{Q,j} \end{bmatrix}, \end{aligned}$$

with

$$A_j = \begin{bmatrix} -\frac{R_j}{L_j} & 2\pi\bar{f} & \frac{\bar{V}_{d,j}^{ld}\sin(\bar{\delta}_j - \bar{\phi}_j^{ld})}{L_j} & \frac{\bar{V}_{d,j}}{L_j} & 0 & 0 & 0 & 0 \\ -2\pi\bar{f} & -\frac{R_j}{L_j} & \frac{\bar{V}_{q,j}^{ld}\cos(\bar{\phi}_j - \bar{\phi}_j^{ld})}{L_j} & 0 & 0 & 0 & 0 & 0 \\ 0 & 0 & 0 & 0 & 0 & 0 & 0 & 0 \\ 0 & 0 & 0 & \frac{-1}{\tau_{V_i}} & 0 & 0 & 0 & 0 \\ 0 & \frac{3\bar{V}_j}{2\tau_{I_j}} & 0 & \frac{3\bar{i}_{d,j}}{2\tau_{I,j}} & \frac{-1}{\tau_{I,j}} & 0 & 0 & 0 \\ 0 & \frac{3\bar{V}_j}{2\tau_{I_j}} & 0 & \frac{3\bar{i}_{d,j}}{2\tau_{I,j}} & 0 & \frac{-1}{\tau_{I,j}} & 0 & 0 \\ 0 & 0 & 0 & 0 & \frac{-1}{\tau_{D_j}} & 0 & \frac{-1}{\tau_{D_j}} & 0 \\ 0 & 0 & 0 & 0 & 0 & \frac{-1}{\tau_{D_j}} & 0 & \frac{-1}{\tau_{D_j}} \end{bmatrix},$$

$$B_j = \begin{bmatrix} 2\pi\bar{i}_{q,j} & 0 & 1 & 0 & 0 & 0 & 0 & 0 \\ 2\pi\bar{i}_{d,j} & 0 & 0 & 1/\tau_{V_j} & 0 & 0 & 0 & 0 \end{bmatrix}^T,$$

$$E_j = \begin{bmatrix} 0 & 0 & 0 & 0 & 1/\tau_{I_j} & 0 & 0 & 0 \\ 0 & 0 & 0 & 0 & 0 & 1/\tau_{I_j} & 0 & 0 \end{bmatrix}^T.$$

It is assumed that the dynamics of nodes in $\mathbb{N}_{DG_{uc}}$ and $\mathbb{N}_L$ are negligible compared with the dynamics of nodes in $\mathbb{N}_{DG_c}$. It is worth noticing that the first two terms in (8.12) depend only on local variables (*i.e.*, variables from node j) and the interaction with other DG$_c$ is governed only by the last term.

With the previous definitions, the control law (8.3) results

$$u_j = -K_j x_j = -K_{p,j} x_j - K_{d,j} C x_j \quad \forall\, j \in \mathbb{N}_{DG_c}, \tag{8.13}$$

where

$$K_{p,j} = \begin{bmatrix} 0 & 0 & k_{pP,j} & 0 & 0 & 0 & 0 & 0 \\ 0 & 0 & 0 & k_{pQ,j} & 0 & 0 & 0 & 0 \end{bmatrix},$$
$$K_{d,j} = \begin{bmatrix} k_{dP,j} & 0 \\ 0 & k_{dQ,j} \end{bmatrix}, \quad C = \begin{bmatrix} 0 & 0 & I_2 & 0 \end{bmatrix},$$

with I_2 the identity matrix of dimension 2 × 2.

The control law (8.13) is decentralized as only uses information from the own node. As it will be shown in the next section, the control parameters are tuned using only local information. The first term in (8.13) ensures the proper power sharing and the latter is a derivative term in order to improve the stability characteristics of the systems without affecting the power balance of the system. That is, the parameters $k_{pP,j}$ and $k_{pQ,j}$ are designed to meet the electrical requirements of power sharing, and the parameters $k_{dP,j}$ and $k_{dQ,j}$ are designed to robustly stabilize the system.

8.4. Design of robust decentralized stabilizing droop control

The aim of this section is to present a design procedure to find the gains $K_{d,j}$ that ensure stability for the whole microgrid using only the dynamic equations of the nodes corresponding to the controllable DG units. The purpose is to avoid using explicitly the interaction terms, which would lead to high order closed-loop systems and numerical issues in the computation of the gains $K_{d,j}$.

With the notation of the previous section and with the purpose of control design, the closed-loop system corresponding to the entire microgrid can be expressed as

$$\frac{d}{dt} x_j = (\tilde{A}_j - B_j K_{d,j} C) x_j + E_j d_j(x), \quad \forall\, j \in \mathbb{N}_{DG_c}, \tag{8.14}$$

where $\tilde{A}_j = A_j - B_j K_{p,j}$. Notice that the interactions with the independent loads and uncontrollable DG units are included in the third term of (8.14).

In order to ensure the stability of system (8.14), we define the Lyapunov function [87]

$$\Upsilon = \sum_{j \in \mathbb{N}_{DG_c}} \Upsilon_j = \sum_{j \in \mathbb{N}_{DG_c}} x_j^T \Psi_j x_j,$$

where Ψ_j is a symmetric positive definite matrix (which will be denoted as $\Psi_j \succ 0$). Then, the states evolution of the system is asymptotically stable and with decay rate lower than $\zeta_j > 0$, *i.e.*,

$$\lim_{t \to \infty} e^{\zeta_j t} \parallel x_j(t) \parallel = 0$$

for all trajectories x_j if the condition

$$\frac{d}{dt}\Upsilon_j + 2\zeta_j \Upsilon_j < 0 \tag{8.15}$$

holds. Substituting the state evolution governed by expression (8.14) in (8.15), the previous condition is equivalent to

$$\begin{aligned}
\frac{d}{dt}\Upsilon_j + 2\zeta_j\Upsilon_j &= \frac{d}{dt}x_j^T\Psi_j x_j + x_j^T\Psi_j\frac{d}{dt}x_j + 2\zeta_j x_j^T\Psi_j x_j = \\
&= x_j^T((\tilde{A}_j - B_jK_{d,j}C)^T\Psi_j + \Psi_j(\tilde{A}_j - B_jK_{d,j}C) \\
&\quad + 2\zeta_j\Psi_j)x_j + d_j^T(x)E_j^T\Psi_j x_j + x_j^T\Psi_j E_j d_j(x) < 0.
\end{aligned}$$

Using of the Young's inequality [147]

$$q^T r + r^T q \leq \frac{1}{\epsilon}q^T q + \epsilon r^T r,$$

for any $\epsilon > 0$, condition (8.15) can be bounded by

$$\begin{aligned}
\frac{d}{dt}\Upsilon_j + 2\zeta_j\Upsilon_j \leq x_j^T \Big(& (\tilde{A}_j - B_jK_{p,j}C)^T\Psi_j + \\
& \Psi_j(\tilde{A}_j - B_jK_{p,j}C) + 2\zeta_j\Psi_j\Big) x_j + \\
& \epsilon x_j^T\Psi_j E_j E_j^T\Psi_j x_j + \frac{1}{\epsilon}d_j^T(x)d_j(x).
\end{aligned}$$

In this inequality, the interaction among DG is reflected in the last term $d_j^T(x)d_j(x)$. In order to decouple the inequalities, this term can be covered with an uncertainty represented by α_j. It is a common approach to consider $d_j(x)$ as piecewise-continuous function in x, satisfying the quadratic inequalities (see *e.g.* [57, 176])

$$d_j^T(x)d_j(x) \leq \alpha_j^2 x^T \tilde{H}_j^T \tilde{H}_j x, \quad j \in \mathbb{N}_{DG_c} \tag{8.16}$$

where $\alpha_j > 0$ is a scalar parameter and $\tilde{H}_j$ is a constant matrix. Provided the converters are operated with a low level voltage and current controller, the maximum power $|P_j^g|$ exchanged by node j is bounded by $|P_{max,j}| - |P_j^{ld}|$. Additionally, the voltage in all nodes in $\mathbb{N}_{DG_c}$ are limited to $|x_{4,j}| < V_{\max} - \bar{V}_j$, where $V_{\max}$ is the maximum allowed voltage. The non-linear term can be explicitly written as

$$\begin{aligned} d_j(x) = V_j \sum_{h\in\mathcal{N}_j} & V_h(G_{jh}\cos\phi_{jh} + B_{jh}\sin\phi_{jh}) - \\ \overline{V}_j \sum_{h\in\mathcal{N}_j} & \overline{V}_h(G_{jh}\cos\overline{\phi}_{jh} + B_{jh}\sin\overline{\phi}_{jh}), \end{aligned}$$

and can be bounded by the worst case, when $V_h = V_{\max}$ as

$$d_j(x) \leq (V_j - \overline{V}_j)V_{\max} \textstyle\sum_{h\in\mathcal{N}_j} \sqrt{G_{jh}^2 + B_{jh}^2},$$

with $(G_{jh}\cos\phi_{jh} + B_{jh}\sin\phi_{jh}) \leq \sqrt{G_{jh}^2 + B_{jh}^2}$. Then, it is straightforward to express the bounds on $d_j^T(x)d_j(x)$ in the form (8.16) as

$$d_j^T(x)d_j(x) \leq \alpha_j^2 x_j^T H_j^T H_j x_j, \tag{8.17}$$

where $H_j = \begin{bmatrix} 0_3 & V_{\max}\sum_{h\in\mathcal{N}_j}\sqrt{G_{jh}^2 + B_{jh}^2} & 0_4 \end{bmatrix}$. Then, applying (8.17) results in

$$\begin{aligned} \frac{d}{dt}\Upsilon_j \leq x_j^T \Big(& (\tilde{A}_j - B_jK_{p,j}C)^T\Psi_j + \Psi_j(\tilde{A}_j - B_jK_{p,j}C) \\ & + 2\zeta_j\Psi_j + \epsilon\Psi_jE_jE_j^T\Psi_j \Big) x_j + \frac{\alpha_j^2}{\epsilon} x_j^T H_j^T H_j x_j. \end{aligned} \tag{8.18}$$

Notice that parameter α_j in Lyapunov function (8.18) can be interpreted as a stability margin. Then, by maximizing α, the design procedure permits to minimize the impact of grid impedance on the system response.

Condition (8.18) is satisfied if matrix

$$\begin{aligned} (\tilde{A}_j - B_jK_{p,j}C)^T\Psi_j + \Psi_j(\tilde{A}_j - B_jK_{p,j}C) + 2\zeta_j\Psi_j & \\ + \epsilon\Psi_jE_jE_j^T\Psi_j + \frac{\alpha_j^2}{\epsilon}H_j^TH_j \prec 0, & \end{aligned} \tag{8.19}$$

i.e. the matrix is negative definite. After applying a congruent transformation $\Phi_j = \Psi_j^{-1}$ (multiplying at left and right by Φ_j) and using Schur's complements [21], condition (8.19) results in the following bilinear matrix inequality (BMI) in the unknowns Φ_j and $K_{d,j}$, for all $j \in N_{DG_c}$,

$$\begin{bmatrix} \Sigma_j - B_j K_{d,j} C\Phi_j - (B_j K_{d,j} C\Phi_j)^T & \Phi_j H_j^T \\ H_j \Phi_j & -\gamma\epsilon \end{bmatrix} \prec 0, \tag{8.20}$$

where $\gamma_j = 1/\alpha_j^2$ and

$$\Sigma_j = \tilde{A}_j \Phi_j + \Phi_j \tilde{A}_j^T + 2\zeta_j \Phi_j + \epsilon E_j E_j^T.$$

In order to simplify the design, condition (8.20) can be covered using the sufficient condition proposed in [40]. Although it introduces conservativism in the design, this leads to an efficient solution for the problem of designing the derivative term of the control law (8.3). The relaxation consists in defining the matrix W_j with suitable structure such that $W_j = C\Phi_j$ and adding the equality constraint $Z_j C = C\Phi_j$. Then, the derivative gain $K_{d,j}$, for all $j \in N_{DG_c}$ can be found by solving (not necessary simultaneously) the following convex optimization problems with Linear Matrix Inequalities (LMI).

$$\begin{aligned} \text{minimize}\ & \gamma_j \\ \text{subject to}\ & \Phi_j \succ 0 \\ & Z_j C = C\Phi_j \\ & \begin{bmatrix} \Sigma_j - B_j W_j C - (B_j W_j C)^T & \Phi_j H_j^T \\ H_j \Phi_j & -\gamma\epsilon \end{bmatrix} \prec 0, \end{aligned} \tag{8.21}$$

Then, the derivative gain can be computed from

$$K_{d,j} = W_j Z_j^{-1}.$$

This is a convex optimization problem that can be efficiently solved with software like Sedumi [158] and Yalmip [108].

8.5. Illustrative example

In this section it will be analyzed the dynamic response of a five bus sample microgrid with a control designed using the procedure proposed in this paper. The system under study is illustrated in Figure 8.3. It

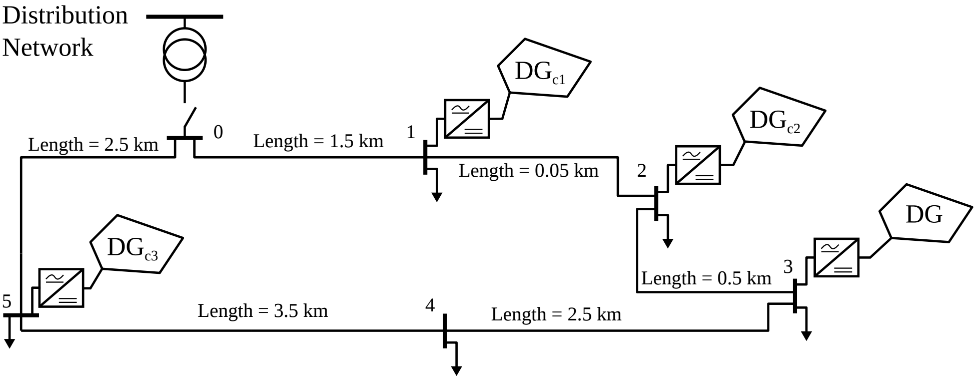

Figure 8.3.: Sample 5-bus microgrid to test the control scheme designed with the proposed procedure.

consists on a low voltage, three phase microgrid composed by three DG$_c$ and one DG$_{uc}$. The three DG$_c$ are electrical storage systems governed by the improved droop control. Set-points to DG$_c$ are given by the energy management system as discussed in Chapter 2.

8.5.1. Microgrid AC network, load and DG$_c$ parameters

The microgrid is composed of three DG$_c$ and one DG$_{uc}$ connected in a ring configuration, as shown in Figure 8.3. The nominal operating voltage is 400±10% V and 50±2% Hz. Line impedance values (see [157] for typical values) for the sample microgrid are listed in Table 8.1.

Each bus $j \in \mathbb{N}_{mg} = \{1, .., 5\}$ has associated a local load, with the total load of the system 50 kVA (43 kW). The sum of the power rating of all DG$_c$ is 50 kVA and the DG$_{uc}$ power rating is 45 kVA. DG$_c$ are equipped with different energy storage technologies: DG$_{c1}$ is a supercapacitor bank, DG$_{c2}$ is a fuel-cell and DG$_{c3}$ is a lithium-ion battery. The parameters for each node are summarized in Table 8.2. After solving the

Line	01	12	23	34	45	50
section (mm^2)	85	85	85	85	170	170
resistance (Ω)	0.201	0.013	0.134	0.668	0.468	0.334
reactance (Ω)	0.062	0.004	0.042	0.208	0.145	0.104

Table 8.1.: Line impedance values of the example microgrid.

optimization problem (8.21) for the particular example, the following derivative gains have been obtained

$$\hat{k}_{P_1} = 1.392, \qquad \hat{k}_{P_2} = 3.369, \qquad \hat{k}_{P_5} = 4.641 \qquad \mathrm{Hz}^2/\mathrm{kW},$$
$$\hat{k}_{Q_1} = 8.655, \qquad \hat{k}_{Q_2} = 13.726, \qquad \hat{k}_{Q_5} = 17.088 \qquad \mathrm{VHz}/\mathrm{kVar},$$

with parameters

$$\alpha_1 = 88.94, \qquad \alpha_2 = 82.325, \qquad \alpha_3 = 77.063,$$

indicating high stability margins against uncertainties on the line impedance and grid topology.

8.5.2. Simulation results

Three different scenarios were analyzed: a step change in load conditions, one by one load disconnection, and the introduction of a variable power source. The improvement relative to the conventional droop with low pass filter, is shown in Figs. 8.4, 8.5 and 8.6, where black lines correspond to the system designed using the proposed procedure and gray lines correspond to same controller without derivative terms. It is worthily to note that in this example, the microgrid is unstable with the conventional droop scheme, without the inertia emulation.

Step change in load conditions

In this scenario loads from buses 1 to 5 are connected simultaneously at instant $t = 0.1$ s. As it can be seen in the simulation results in

Node j	1	2	3	4	5	
P_j^{ld}	3	9	12.45	16.6	2	kW
Q_j^{ld}	0	1	2.55	3.4	0	kVar,
S_{N_j}	5	15	45	-	30	kVA
τ_{P_j}	1.053	4.000	-	-	1.333	s
τ_{V_j}	50	75	-	-	100	ms
k_{P_j}	0.2	0.066	-	-	0.033	Hz/kW
k_{Q_j}	4	1.333	-	-	0.667	V/kVar

Table 8.2.: Control and design parameters used in the simulation example.

Figure 8.4, $DG_{c1,c2,c3}$ share the total power demand proportionally to each power rating, in steady state. In full load demand, the microgrid deviates its frequency to 49.23 Hz. The power transient corresponding to improved droop control, exhibits a less oscillatory response than the conventional droop.

Response to changing load conditions

Similarly to the previous scenario, at instant $t = 0.1$ s all load are connected simultaneously, making the frequency to drop. One by one, loads at buses 1 to 5 are disconnected at $t = 2, 4, 6, 8, 9$ s respectively.

In Figure 8.5 it can be seen how $DG_{c1,c2,c3}$ rapidly accommodates the new load conditions, with a more damped response compared to the conventional droop.

Primary control regulation with variable power generation from DG$_{uc}$

In this scenario a 45 kVA variable power source (DG$_{uc}$), corresponding to a low inertia wind turbine, is connected to the microgrid. The wind profile used in this simulation is a turbulent wind with high variability. The aim of this scenario is to show how multiple DG$_c$ units working in parallel with a completely decentralized primary control are capable to maintain the system stability and bound the microgrid frequency and voltage. Figure 8.6 also shows that the microgrid is able to operate in case of a contingency in a DG$_c$ unit. In this case, DG$_{c2}$ was disconnected at $t = 5$ s. Despite the loss of DG$_{c2}$ the control is capable of maintaining the voltage and frequency within the bounds.The larger load power fluctuations are a consequence of the decrease in the power capacity of the microgrid, as has been weakened by a 30 % due to the loss of DG$_{c2}$.

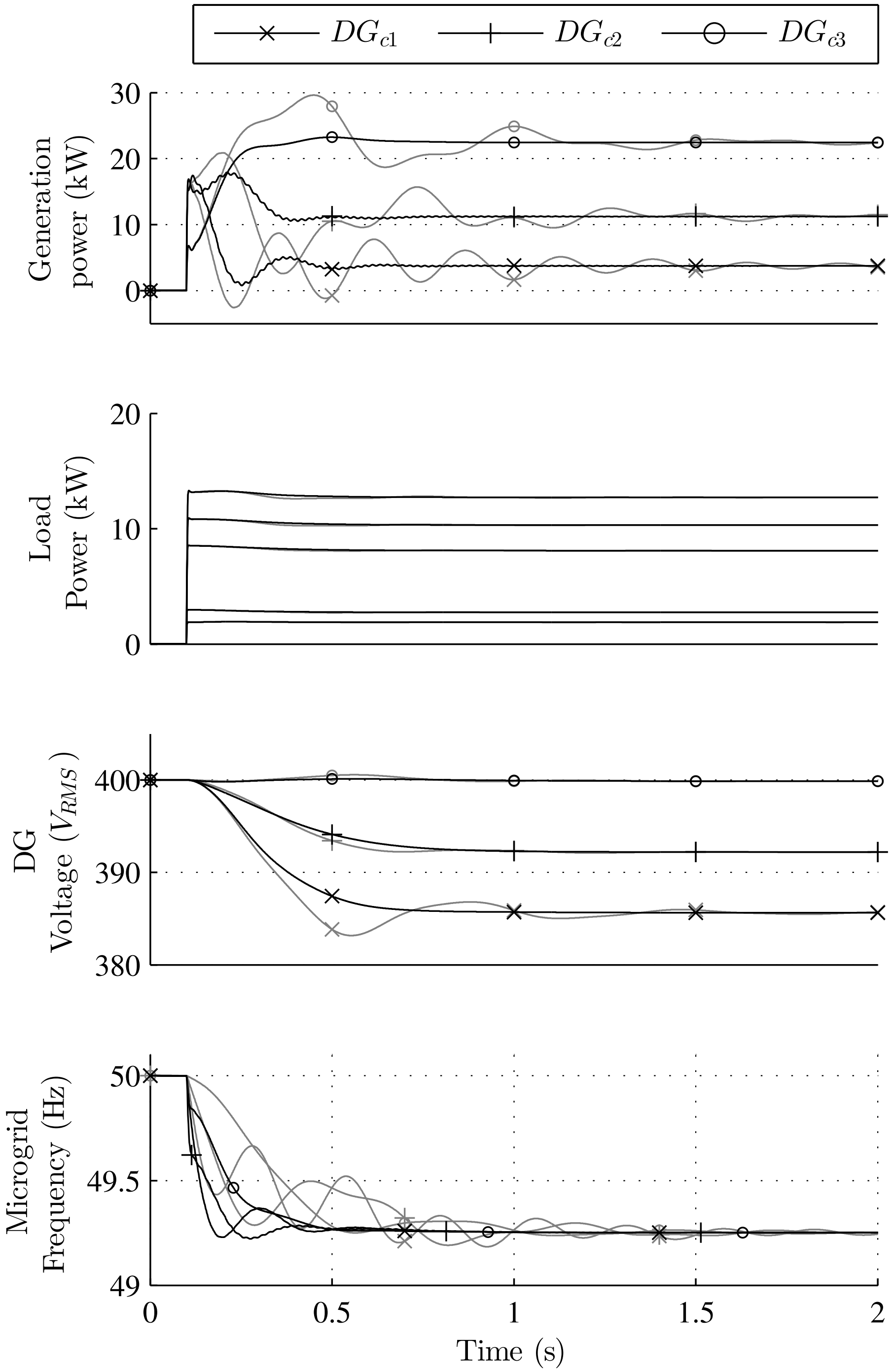

Figure 8.4.: Scenario 1 results: full load at $t = 0.1$ s. Black lines correspond to the proposed control design and gray lines correspond to conventional droop without derivative term.

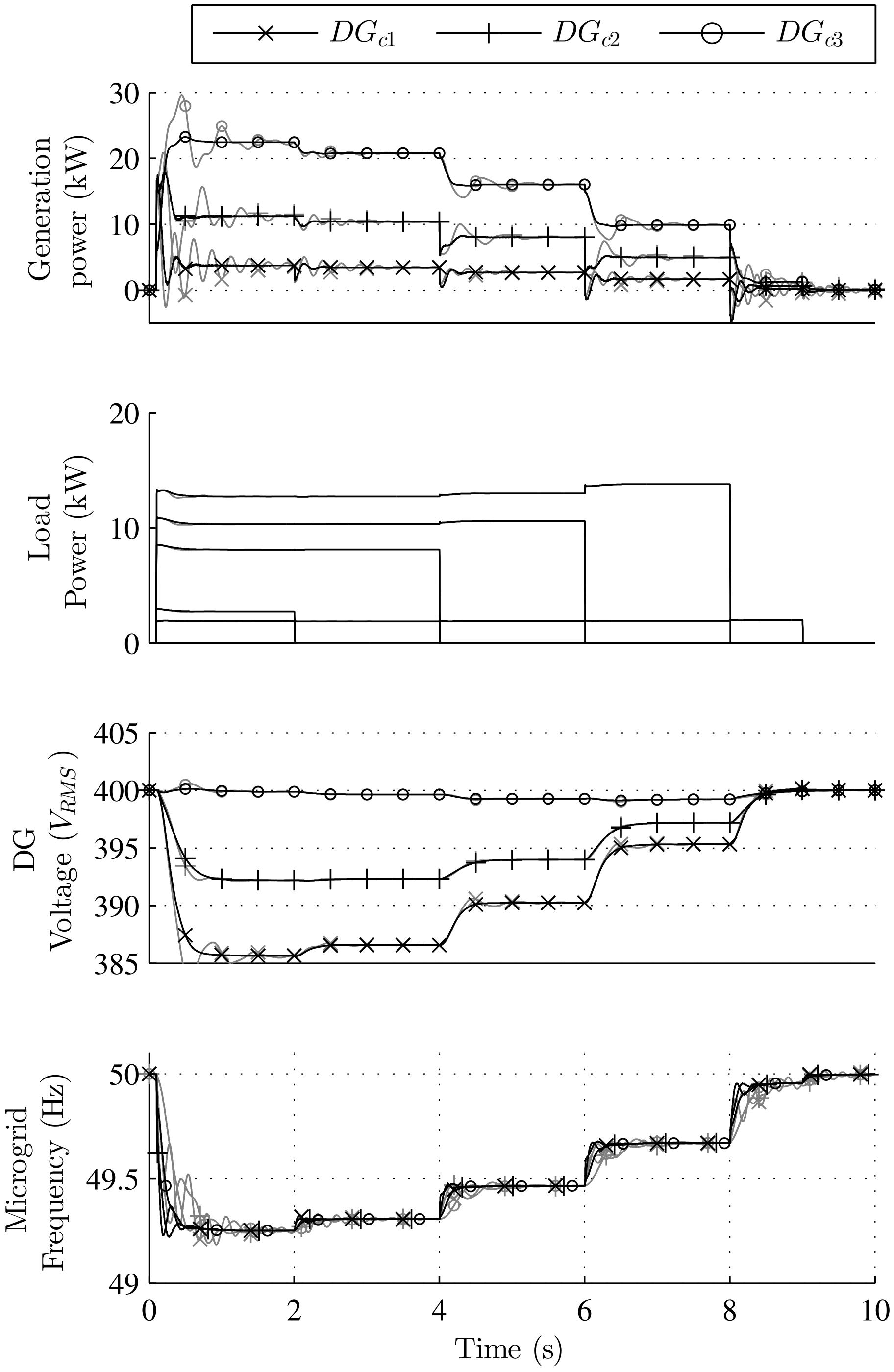

Figure 8.5.: Scenario 2 results: full load at $t = 0.1$ s; loads at buses 1-5 are disconnect at $t = 2, 4, 6, 8, 9$ s respective and sequentially. Black lines correspond to the proposed control design and gray lines correspond to conventional droop without derivative term.

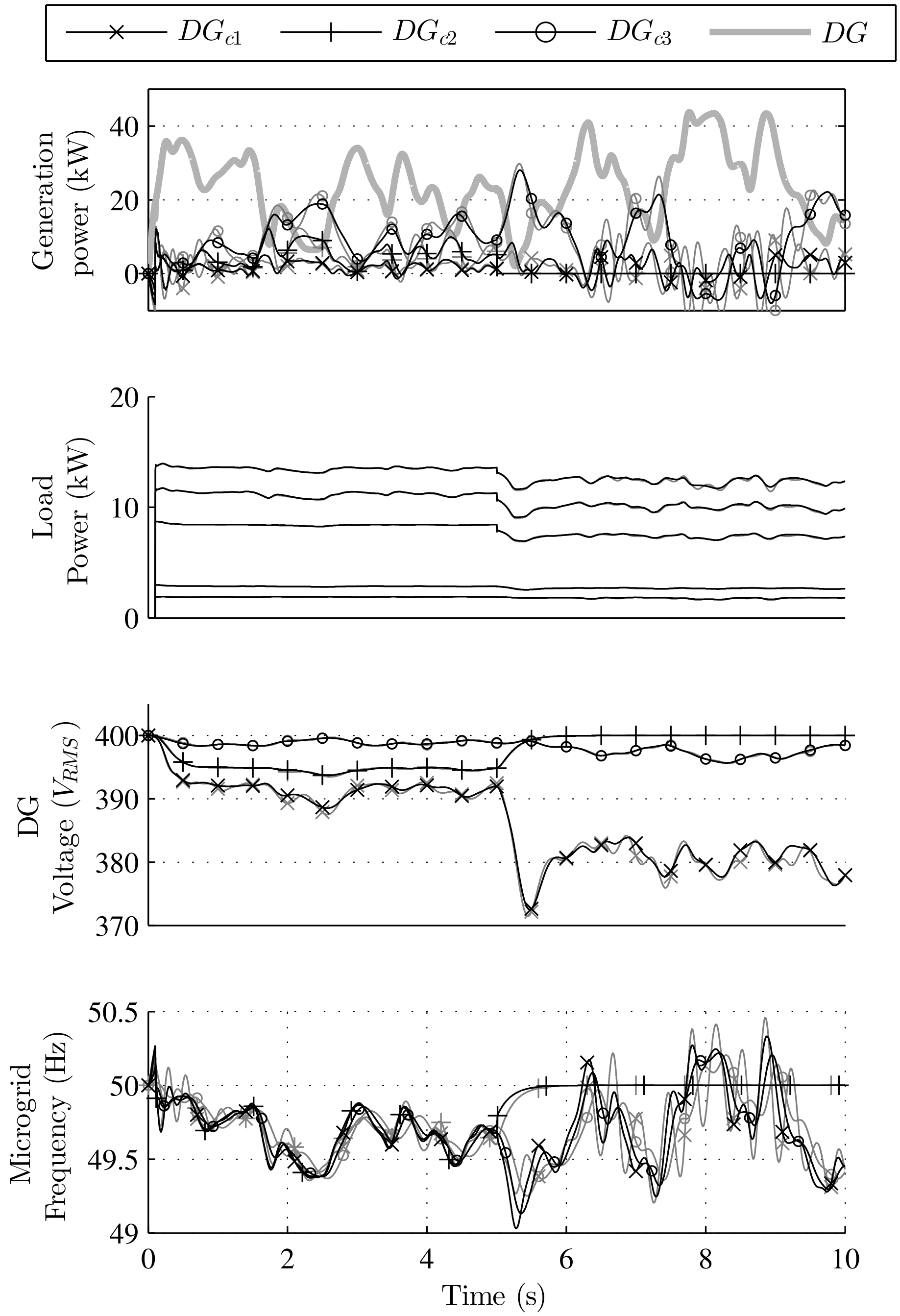

Figure 8.6.: Scenario 3 results: full load at $t = 0.1$ s; the DG_{uc} (a 45 kVA wind turbine) is connected to the microgrid injecting fluctuating power as a consequence of a turbulent wind profile; at $t = 5$ s DG_{c2} is disconnected. Black lines correspond to the proposed control design and gray lines correspond to conventional droop without derivative term.

8.6. Conclusion of the chapter

This chapter has presented a design procedure for the decentralized field control of microgrids. The control starts from the conventional droop scheme and incorporates a low pass filter introducing fictitious inertia, and a derivative term capable to improve the microgrid stability margins without affecting the steady state power share. The problem of decentralized control design has been cast as a decentralized output feedback problem of the subsystem '$\jmath$-th' with non-linear interconnections with the microgrid. The design of the derivative term gain is achieved by solving an LMI optimization problem. The feasibility of the proposed design procedure is shown by the design of three decentralized controllers and illustrated by numerical simulation in a sample microgrid. The numerical simulation shows the correct operation of the sample microgrid in three representative scenarios, including the loading of the microgrid from 0 to 100 %, and the balance between generation-demand with fluctuating renewable power generation and constant impedance loads.

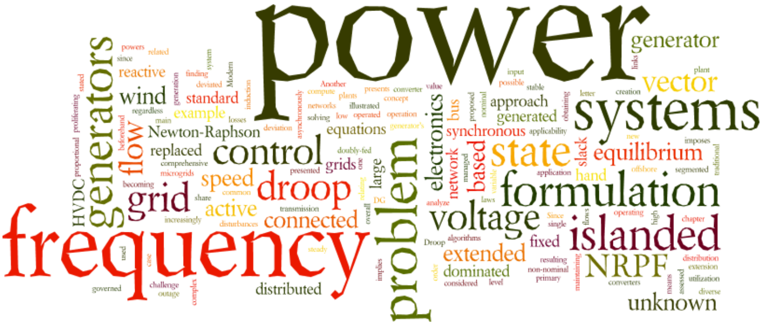

9

Power flow calculation with extended Newton-Raphson method for islanded grids with droop control

This chapter presents an extension of the Newton-Raphson power flow problem formulation for its application to islanded power systems governed with droop control. The standard state vector is extended to compute the unknown equilibrium frequency and the resulting active and reactive power of the droop generators. The formulation applicability is illustrated with a comprehensive example.

9.1. Introduction

As discussed in the introductory Chapter 1, the concept of microgrids based on power electronics converters is proliferating. It can be stated, that all the islanded systems that are based on power electronics (regardless the voltage level where they are connected) share the challenge of maintaining a stable voltage and frequency for the overall grid. The common operation approach is to have a primary control which links active power to frequency and reactive power to voltage by means of droop control laws, as seen in Chapter 3. In order to analyse the power flows in such systems, the standard power flow algorithms cannot be used, since the frequency cannot be considered as an input, but as a state variable related to converter active powers. Solving the power flow problem has been a requirement, for instance, to initialize numerical simulations of microgrids performed in Chapter 8, or to linearise the electrical equations around the equilibrium point for small signal stability studies and design purposes.

In traditional power systems dominated by synchronous generators, the problem of finding the steady state equilibrium frequency after large disturbances has been assessed in [97], where the state vector of the Newton-Raphson power flow (NRPF) problem [164] has been extended with the unknown network frequency. In their formulation, the slack bus is replaced by generator's equations relating the generated power with the grid frequency, obtaining the equilibrium frequency after a generator outage. Another approach to the NRPF problem with deviated frequency from the nominal value, has been presented in [30]. Their problem formulation is for power systems with large wind power plants with fixed speed or doubly-fed induction generators. The state vector of the NRPF problem is extended with the grid frequency, and the generator speed in case of fixed speed generators.

In this chapter, a formulation for solving the power flow problem with non-nominal operating frequency for islanded grids dominated by distributed generation managed with droop control is proposed. In this formulation, for islanded grids, the slack bus is replaced by the droop equations of the distributed generators (DG). Droop control [32] imposes a frequency deviation proportional to the generated power. Since network losses are unknown beforehand, the state vector of the NRPF problem has been extended with the power generated by DGs, and the grid frequency.

9.2. Problem formulation

Assume a grid with $n = n_{slk} + n_{DR} + n_{PV} + n_{PQ}$ buses, grouped and labeled in the following categories:

1. Slack bus is label 0, with $n_{slk} \in \{0, 1\}$ depending whether there is a slack bus in the grid under study or not.
2. Droop controlled buses are $\mathbb{N}_{DR} = \{1, \ldots, n_{DR}\}$.
3. Active power, voltage source buses are $\mathbb{N}_{PV} = \{n_{DR}+1, \ldots, n_{DR}+n_{PV}\}$.
4. Active and reactive power source buses are $\mathbb{N}_{PQ} = \{n_{DR} + n_{PV} + 1, \ldots, n\}$.

Note that some of the groups might be empty if there are no buses of a certain type.

Let us define the new state vector for the extended NRPF problem

$$\mathbf{x} = \begin{bmatrix} \mathbf{P}^T & \mathbf{Q}^T & \mathbf{\Theta}^T & \mathbf{V}^T & \omega \end{bmatrix}^T,$$

where bold symbols denotes vectors, with $\mathbf{P}, \mathbf{Q} \in \mathbb{R}^{n_{DR}}$ are the vectors of active and reactive power, respectively, corresponding to droop generators, $\mathbf{\Theta} \in \mathbb{R}^{n-1}$ and $\mathbf{V} \in \mathbb{R}^{n-n_{PV}-n_{slk}}$ are the bus angle and voltage vectors, and ω is the equilibrium electrical frequency of the island grid, *i.e.* when there is no slack bus. In total, the extended NRPF problem has a total of $2n + 2n_{DR} - n_{PV} - 2n_{slk}$ unknowns.

The power system can be expressed as the following functions, which the methodology seeks to equal to zero

$$f_i(\mathbf{P}, \mathbf{\Theta}, \mathbf{V}) = V_i \sum_{j=1}^{n} V_j \left(G_{ij}\cos(\theta_{ij}) + B_{ij}\sin(\theta_{ij})\right) - P_i,$$
$$g_i(\mathbf{Q}, \mathbf{\Theta}, \mathbf{V}) = V_i \sum_{j=1}^{n} V_j \left(G_{ij}\sin(\theta_{ij}) - B_{ij}\cos(\theta_{ij})\right) - Q_i,$$

where $\theta_{ij} = \theta_j - \theta_i$ is the angle difference between i-th and j-th buses, $f_i, \forall i \in \mathbb{N}_{DR} \cup \mathbb{N}_{PV} \cup \mathbb{N}_{PQ}$ and $g_i, \forall i \in \mathbb{N}_{DR} \cup \mathbb{N}_{PQ}$ are the classical power flow equations, and G_{ij}, B_{ij} the real and imaginary parts of the element in the bus admittance matrix B, corresponding to the i-th row and j-th column. The system equations are extended with the droop controlled generators expressions

$$
\begin{aligned}
h_i(\mathbf{P},\omega) &= \omega^* - \omega - k_{p_i}(P_i - P_i^*),\\
l_i(\mathbf{Q},\mathbf{V}) &= V^* - V_i - k_{q_i}(Q_i - Q_i^*),
\end{aligned}
$$

where $h_i, l_i, \forall i \in \mathbb{N}_{DR}$ are the droop control equations, with ω^*, V^*, P_i^* and Q_i^* the frequency, voltage, active and reactive power set-points for the droop generators.

To solve the extended NRPF problem, let us define the following jacobian matrix

$$
J = \begin{bmatrix}
\dfrac{\partial \mathbf{f}(x)}{\partial \mathbf{P}} & 0 & \dfrac{\partial \mathbf{f}(x)}{\partial \mathbf{\Theta}} & \dfrac{\partial \mathbf{f}(x)}{\partial \mathbf{V}} & 0\\
0 & \dfrac{\partial \mathbf{g}(x)}{\partial \mathbf{Q}} & \dfrac{\partial \mathbf{g}(x)}{\partial \mathbf{\Theta}} & \dfrac{\partial \mathbf{g}(x)}{\partial \mathbf{V}} & 0\\
\dfrac{\partial \mathbf{h}(x)}{\partial \mathbf{P}} & 0 & 0 & 0 & \dfrac{\partial \mathbf{h}(x)}{\partial \omega}\\
0 & \dfrac{\partial \mathbf{l}(x)}{\partial \mathbf{Q}} & 0 & \dfrac{\partial \mathbf{l}(x)}{\partial \mathbf{V}} & 0
\end{bmatrix},
$$

where each element is a matrix of appropriate dimensions. The frequency dependency of admittance matrix B, $\partial B/\partial\omega$, is much smaller than the rest of derivatives present in J. For this reason, and for the sake of simplicity, B is assumed constant for the formulation of the extended NRPF. The derivatives of the extended elements in J are

$$
\begin{aligned}
\frac{\partial f_i}{\partial P_j} &= -1, & \frac{\partial g_i}{\partial Q_j} &= -1, & \frac{\partial h_i}{\partial \omega} &= -1,\\
\frac{\partial h_i}{\partial P_j} &= -k_{pi}, & \frac{\partial l_i}{\partial Q_j} &= -k_{qi}, & \frac{\partial l_i}{\partial V_j} &= -1,
\end{aligned}
$$

$\forall i = j$, with i, j in the appropriate group of buses, and zero the off-diagonal elements ($i \neq j$) of the extended matrices. Parameters k_{pi} and k_{qi} are the active and reactive power droop coefficients respectively. Then, the k-th iteration of the solving process can be computed with

$$
\begin{bmatrix}
\mathbf{P}^{(k+1)}\\ \mathbf{Q}^{(k+1)}\\ \mathbf{\Theta}^{(k+1)}\\ \mathbf{V}^{(k+1)}\\ \omega^{(k+1)}
\end{bmatrix}
=
\begin{bmatrix}
\mathbf{P}^{k}\\ \mathbf{Q}^{k}\\ \mathbf{\Theta}^{k}\\ \mathbf{V}^{k}\\ \omega^{k}
\end{bmatrix}
+ \left[J^k\right]^{-1}
\begin{bmatrix}
-\mathbf{f}(\mathbf{P}^k, \mathbf{\Theta}^k, \mathbf{V}^k)\\
-\mathbf{g}(\mathbf{Q}^k, \mathbf{\Theta}^k, \mathbf{V}^k)\\
-\mathbf{h}(\mathbf{P}^k, \omega^k)\\
-\mathbf{l}(\mathbf{Q}^k, \mathbf{V}^k)
\end{bmatrix}.
$$

9.3. Numerical example

The proposed extended NRPF algorithm has been applied to the sample microgrid shown in Figure 9.1, composed by 5 buses, 3 DG controlled with droop scheme, and a DG with constant power output. The configuration parameters for the sample microgrid are included in the illustration. The nominal voltage and frequency of operation of the microgrid are 400 V and 50 Hz respectively. In the evaluated scenario, power references to droop generators are zero.

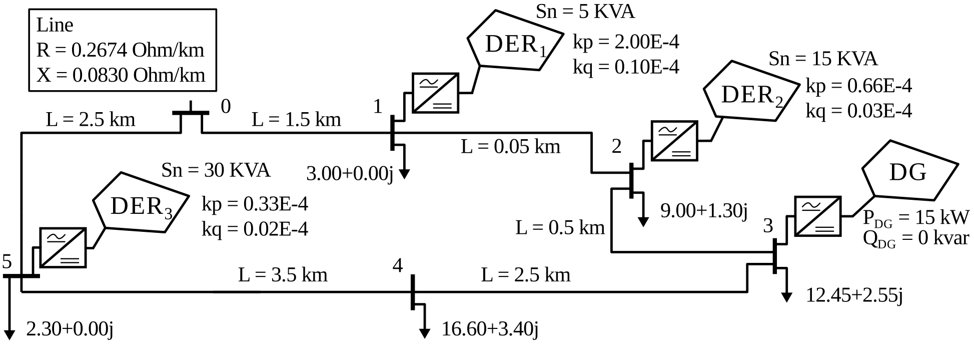

Figure 9.1.: Low voltage sample microgrid under study, with the electrical parameters, demand and generation indicated.

The steady state operating points are summarized in Table 9.1. As expected, the resulting frequency for the proposed scenario is deviated from the nominal frequency, since the electrical demand and the power set-points to droop controllers are unbalanced. The evolution of the objective functions f_i, g_i, h_i, l_i in the successive iterations can be seen in Figure 9.2.

9.4. Conclusion of the chapter

A new formulation for an extended Newton-Raphson power flow problem has been proposed to obtain the steady state operating points for droop controlled islanded microgrids. The formulation extends the classical state vector to obtain the equilibrium frequency and the droop generators active and reactive powers.

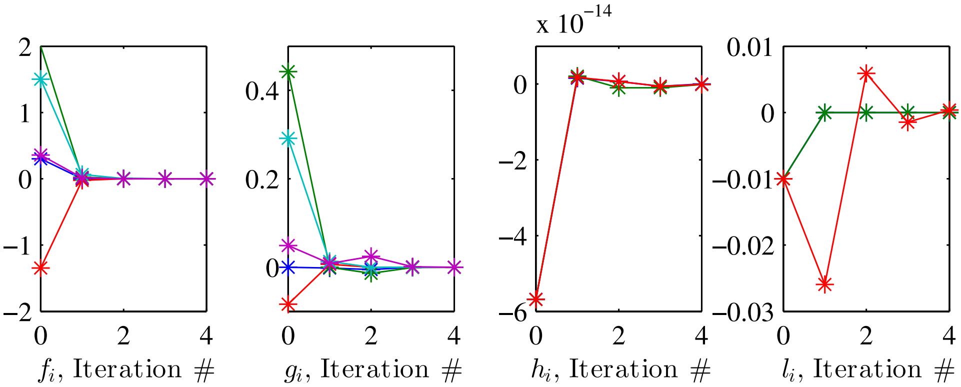

Figure 9.2.: Evaluation of functions f_i, g_i, h_i, l_i from initial guess to 4^{th} and last iteration.

	Frequency	Voltage	Angle	Generation	
Node	Hz	V	°	kW	kvar
1	49.4159	390.9322	0.0000	2.921	2.267
2	49.4159	390.7837	0.0078	8.762	6.912
3	49.4159	388.7543	0.2151	15.000	0.000
4	49.4159	375.6036	0.4985	0.000	0.000
5	49.4159	401.2504	1.5065	17.524	-1.870

Table 9.1.: Power flow results for the sample droop controlled microgrid.

10

Conclusions

The improvement and proliferation of power electronics based converters along with enhanced energy storage technologies are permitting the development of microgrids. This thesis has covered some important issues regarding the implementation of droop based microgrids. In particular, this thesis has addressed the control of the power electronics converters, and the control and management of energy storage devices, proposing control strategies and design methodologies.

The large scale integration of renewable energy sources into distribution grids is facing important challenges in its implementation. One of the most relevant challenges presented in islanded microgrids is the coordinated control of energy storage systems aimed to electrically stabilize the network. To this end, the droop control has already been proposed, providing promising results. However, its performance has a strong dependence with the grid impedance and topology, leading the research community to propose modifications to classical droop control. Although there are different droop alternatives, not so many design procedures for modified droop ensuring the stability of the grid has been found.

Moreover, the design and stability analysis of droop control microgrids makes assumptions on the converter topology and dynamics. In particular, a back-to-back converter is typically used for interfacing renewable energy sources and energy storage devices. The droop control, implemented in the grid side converter, assumes an ideal DC–link voltage connecting with the renewable energy source or storage. New control strategies for the control of renewable source side converter has been proposed to integrate energy storage systems in microgrids.

In addition, microgrids are typically low voltage grids with high penetration of renewable energy sources. These sources are variable by nature, introducing electrical disturbances into the grid. A common disturbance is the voltage oscillation, referred as flicker phenomena when the oscillation exceed a certain threshold. This issue has been addressed in this thesis.

In summary, the contributions presented in this thesis can be classified in three different types:

- Contributions on advanced control schemes for power electronics converters used in storage systems applications for microgrids.
  - Sliding mode control of DC–DC converter for fast and robust operation of ESS.
  - Use reset control to improve DC-link voltage regulation in relation to linear control.
- Contributions on advanced design methodologies for droop control in islanded microgrids.
  - Proposed a methodology to analytically obtain the equilibrium frequency and power flow for islanded grids with droop control.
  - Proposed new methods to design droop control for DG.
- Contributions on the improvement of the power quality in weak grids with high penetration of RES.

Regarding the first contribution group, the new control strategies based on SM control has been experimentally validated for ESS interfaced with power electronic converters. The SM based controllers offer a robust in front of uncertainties, such as variable operating voltage and unknown impedances. In addition, sliding mode control offers a good performance on tracking of reference signals, improving the overall performance of the system compared with linear control.

Droop based control is the *de facto* control strategy for islanded microgrids in the literature. With this premise, some tools have been developed to contribute to the field implementation of droop control based microgrids. Most of the stability analysis methods found in the literature are based on the linearisation around the equilibrium point. A tool to analytically obtain the operating point (power flow), without the need of detailed simulations, has been proposed. With the microgrid topology, loading conditions, and DG and droop parameters, the tool obtains the power flow and equilibrium frequency. In addition to the power flow calculation, methodologies for the design of droop controllers have been proposed. The resulting controllers guarantee stability and increase the robustness of droop control.

Finally, in addition to the use of ESS for islanded microgrids, a power smoothing method has been proposed for weak networks. In this application, an ESS based on supercapacitors is used to mitigate the flicker present in weak distribution grids with high penetration of RES. The supercapacitors can handle a high number of charge and discharge cycles, making them a good candidate for such applications. This power smoothing scheme has been experimentally verified in a laboratory test bench, showing the supercapacitors capability.

As a general conclusion, microgrids are a feasible paradigm for the large scale introduction of renewable energy sources, although all the required technology is not yet mature. Several topics should be addressed before its commercialization; these topics have been identified and summarized as possible future research lines.

10.1. Further work

Throughout this thesis, future research lines have arisen for the further development of microgrids, which appear listed following.

- Continuing with the experimental work developed in Chapters 4 and 5, it would be interesting the experimental validation of droop control design proposed in Chapter 8. The experimental validation of droop control strategies would require to overcome several practical aspects, such as the need for specialized protections and the use of specific hardware for the power electronics.

- Related with Chapter 8, it has been identified the need to improve the reactive power sharing among DG units in droop controlled microgrids. An interesting approach might be the use of distributed control, perhaps using consensus-based methods [73, 150].

- From the investigation on the interaction between microgrids and distribution networks done in [C3], a possible interesting research could be on the protection scheme for power electronic based grids and microgrids. Different aspects can be considered:

  - The interconnection switch design in coordination with distribution grid protections.
  - The internal protections of microgrid units; a new mechanisms to detect faults needs to be investigated. A possible approach might be the design of protections based on low voltage detected instead of current based detection.

- In Chapters 4 and 5, a ESS for supercapacitors and Li-ion battery has been designed independently. The design of unique ESS coordinating both storage technologies would permit to implement advanced strategies to improve transient performance in islanded microgrids.

Bibliography

[1] C. Abbey and G. Joos, "Supercapacitor Energy Storage for Wind Energy Applications", *IEEE Transactions on Industry Applications*, vol. 43, no. 3, pp. 769–776, 2007.

[2] M. Agrawal, "Micro grid technological activities across the globe: A review", *International Journal of Research & Reviews in Applied Sciences*, vol. 7, no. May, pp. 147–152, 2011.

[3] H. Akagi, E. Hirokazu Watanabe, and M. Aredes, *Instantaneous Power Theory and Applications to Power Conditioning.* Wiley-IEEE Press, 2007, p. 379.

[4] E. H. Allen and M. D. Ilic, "Interaction of transmission network and load phasor dynamics in electric power systems", *IEEE Transactions on Circuits and Systems I: Fundamental Theory and Applications*, vol. 47, no. 11, pp. 1613–1620, 2000.

[5] Alstom. (2014). Microrid project, [Online]. Available: `http://www.alstom.com/press-centre/2014/11/alstom-awarded-microgrid-project-by-the-us-energy-department/` (visited on Apr. 14, 2015).

[6] K. J. Åström and T. Hägglund, *PID controllers: theory, design and tuning, 2nd edition*, I. International, Ed. Research Triangle Park, 1995, p. 343.

[7] ——, *Advanced PID control.* Research Triangle Park, USA: ISA Society, 2006.

[8] J. Aubry, P. Bydlowski, B. Multon, *et al.*, “Energy Storage System Sizing for Smoothing Power Generation of Direct Wave Energy Converters”, in *Proc. of the 3rd International Conference on Ocean Energy*, 2010, pp. 1–7.

[9] A. Baños and A. Barreiro, *Reset Control Systems.* London, UK: Springer-Verlag, 2012.

[10] A. Baños and A. Vidal, “Design of Reset Control Systems: The PI+CI Compensator”, *J. Dyn. Sys., Meas., Control*, vol. 134, no. 5, 2012.

[11] M. E. Baran, S. Teleke, L. Anderson, *et al.*, “STATCOM with energy storage for smoothing intermittent wind farm power”, *Proc. of the Power and Energy Society General Meeting*, pp. 1–6, Jul. 2008.

[12] M. Barnes, J Kondoh, H Asano, *et al.*, “Real-World MicroGrids - An Overview”, in *Proc. of the IEEE Int. Conf. on SoSE*, 2007, pp. 1–8.

[13] J. A. Barrado, A. E. Aroudi, H. Valderrama-blavi, *et al.*, “Analysis of a Self-Oscillating Bidirectional DC - DC Converter in Battery Energy Storage Applications”, *IEEE Transactions on Power Delivery*, vol. 27, no. 3, pp. 1292–1300, 2012.

[14] H.-P. Beck and R. Hesse, “Virtual synchronous machine”, in *Proc. of the 9th International Conference on Electrical Power Quality and Utilisation (EPQU)*, IEEE, Ed., 2007, pp. 1–6.

[15] O. Beker, C. V. Hollot, Y. Chait, *et al.*, “Fundamental properties of reset control systems”, *Automatica*, vol. 40, no. 6, pp. 905–915, 2004.

[16] R. Belmans, “Smart Grids in the European Framework”, in *3rd IEEE PES ISGT Europe*, 2012.

[17] F. D. Bianchi, H. D. Battista, and R. J. Mantz, “On the Stability of DC-to-DC Converters in PV Systems Undergoing Sliding Motions”, *Int. Journal of Systems Science*, pp. 637–647, 2004.

[18] F. D. Bianchi, A. Egea-Alvarez, A. Junyent-Ferré, *et al.*, “Optimal control of voltage source converters under power system faults”, *Control Eng. Practice*, vol. 20, pp. 539–546, 2012.

[19] M. Bollen and F. Hassan, *Integration of Distributed Generation in the Power System*. John Wiley & Sons Inc., Hoboken, New Jersey, 2011.

[20] U. Borup, F. Blaabjerg, and P. Enjeti, “Sharing of nonlinear load in parallel-connected three-phase converters”, *IEEE Transactions on Industry Applications*, vol. 37, no. 6, pp. 1817–1823, 2001.

[21] S. Boyd, L. E. Ghaoui, E. Feron, *et al.*, *Linear Matrix Inequalities in System and Control Theory*. Society for Industrial and Applied Mathematics (SIAM), 1994, p. 205.

[22] K. D. Brabandere, B. Bolsens, J. Van den Keybus, *et al.*, “A Voltage and Frequency Droop Control Method for Parallel Inverters”, *IEEE Transactions on Power Electronics*, vol. 22, no. 4, pp. 1107–1115, Jul. 2007.

[23] K. D. Brabandere, K. Vanthournout, J. Driesen, *et al.*, “Control of Microgrids”, in *2007 IEEE Power Engineering Society General Meeting*, IEEE, Jun. 2007, pp. 1–7.

[24] T. K. A. Brekken, A. Yokochi, A. von Jouanne, *et al.*, “Optimal Energy Storage Sizing and Control for Wind Power Applications”, *IEEE Transactions on Sustainable Energy*, vol. 2, no. 1, pp. 69–77, Jan. 2010.

[25] S. Buller, M. Thele, R. De Doncker, *et al.*, “Impedance-based simulation models of supercapacitors and Li-ion batteries for power electronic applications”, vol. 41, no. 3, pp. 742–747, 2005.

[26] X. Cao, Q.-c. Zhong, and W.-l. Ming, “Ripple Eliminator to Smooth DC-Bus Voltage and Reduce the Total Capacitance Required”, *IEEE Transactions on Industrial Electronics*, vol. 62, no. 4, pp. 2224–2235, 2015.

[27] R. Cardenas, R. Pena, G. Asher, *et al.*, “Control strategies for enhanced power smoothing in wind energy systems using a flywheel driven by a vector-controlled induction machine”, *IEEE Transactions on Industrial Electronics*, vol. 48, no. 3, F. Maurice, Ed., pp. 625–635, Jun. 2001.

[28] R. Cardenas, R. Pena, G. Asher, *et al.*, “Control strategies for power smoothing using a flywheel driven by a sensorless vector-controlled induction machine operating in a wide speed range”, vol. 51, no. 3, pp. 603–614, 2004.

[29] F. Caricchi, F. Crescimbini, F. Giulii Capponi, *et al.*, “Study of bi-directional buck-boost converter topologies for application in electrical vehicle motor drives”, in *Proc. of Applied Power Electronics Conference and Exposition (APEC)*, 1998, 287 –293 vol.1.

[30] L. M. Castro, C. R. Fuerte-Esquivel, and J. H. Tovar-Hernandez, “Solution of Power Flow With Automatic Load-Frequency Control Devices Including Wind Farms”, vol. 27, no. 4, pp. 2186–2195, 2012.

[31] CERTS. (2015). Certs project, [Online]. Available: `http://certs.lbl.gov/certs-der-micro.html` (visited on Apr. 15, 2015).

[32] M. C. Chandorkar, D. Divan, and R. Adapa, “Control of parallel connected inverters in standalone AC supply systems”, *IEEE Transactions on Industry Applications*, vol. 29, no. 1, pp. 136–143, 1993.

[33] C.-T. Chen, *Linear System Theory and Design*, 3rd. New York, NY, USA: Oxford University Press, Inc., 1998.

[34] F. Ciccarelli and D. Lauria, “Sliding-mode control of bidirectional DC-DC converter for supercapacitor energy storage applications”, in *Proc. of the Int. SPEEDAM*, 2010, pp. 1119–1122.

[35] A. Colet-Subirachs, A. Ruiz-Álvarez, O. Gomis-Bellmunt, *et al.*, “Centralized and Distributed Active and Reactive Power Control of a Utility Connected Microgrid Using IEC61850”, *IEEE Systems Journal*, vol. 6, no. 1, pp. 58–67, 2012.

[36] E. Commission. (2013). Horizon 2020, [Online]. Available: `http://ec.europa.eu/programmes/horizon2020/en/h2020-section/secure-clean-and-efficient-energy` (visited on Apr. 14, 2015).

[37] CORDIS. (2005). Microgrids, [Online]. Available: `http://cordis.europa.eu/project/rcn/67577\_en.html` (visited on Apr. 14, 2015).

[38] ——, (2011). More Microrids, [Online]. Available: `http://cordis.europa.eu/project/rcn/75085\_en.html` (visited on Apr. 15, 2015).

[39] ——, (2015). IDE4L project, [Online]. Available: `http://cordis.europa.eu/project/rcn/109372\_en.html` (visited on Apr. 15, 2015).

[40] C. A. R. Crusius and A. Trofino, “Sufficient LMI conditions for output feedback control problems”, *IEEE Transactions on Automatic Control*, vol. 44, no. 5, pp. 1053–1057, May 1999.

[41] J. Dannehl, C. Wessels, and F. W. Fuchs, “Limitations of voltage - oriented PI current control of grid - connected PWM rectifiers with LCL filters”, *IEEE Transactions on Industrial Electronics*, vol. 56, no. 2, pp. 380–388, 2009.

[42] S. D’Arco and J. A. Suul, “Equivalence of virtual synchronous machines and frequency-droops for converter-based Microgrids”, *IEEE Transactions on Smart Grid*, vol. 5, no. 1, pp. 394–395, 2014.

[43] M. B. Delghavi and A. Yazdani, “Islanded-Mode Control of Electronically Coupled Distributed-Resource Units Under Unbalanced and Nonlinear Load Conditions”, *IEEE Transactions on Power Delivery*, vol. 26, no. 2, pp. 661–673, Apr. 2011.

[44] ——, “A Unified Control Strategy for Electronically Interfaced Distributed Energy Resources”, *IEEE Transactions on Power Delivery*, vol. 27, no. 2, pp. 803–812, Apr. 2012.

[45] T. Demiray and A. Göran, “Simulation of Power Systems Dynamics using Dynamic Phasor Models”, in *Proc. of the 10th symposium of specialists in electric operational and expansion planning*, 2006, pp. 0–9.

[46] E. N. Dialynas, N. C. Koskolos, and D. Agoris, “Reliability assessment of autonomous power systems incorporating HVDC interconnection links”, *IEEE Transactions on Power Delivery*, vol. 11, no. 1, pp. 519–525, 1996.

[47] G. Díaz, C. Gonzalez-Moran, J. Gomez-Aleixandre, *et al.*, “Composite Loads in Stand-Alone Inverter-Based Microgrids — Modeling Procedure and Effects on Load Margin”, *IEEE Transactions on Power Systems*, vol. 25, no. 2, pp. 894–905, 2010.

[48] F. Díaz-González, F. D. Bianchi, A. Sumper, *et al.*, “Control of a flywheel energy storage system for power smoothing in wind power plants”, *IEEE Transactions on Energy Conversion*, vol. 29, no. 1, pp. 204–214, 2014.

[49] F. Díaz-González, A. Sumper, O. Gomis-Bellmunt, *et al.*, "A review of energy storage technologies for wind power applications", *Renewable and Sustainable Energy Reviews*, vol. 16, no. 4, pp. 2154–2171, 2012.

[50] P. H. Divshali, A. Alimardani, S. H. Hosseinian, *et al.*, "Decentralized Cooperative Control Strategy of Microsources for Stabilizing Autonomous VSC-Based Microgrids", *IEEE Transactions on Power Systems*, vol. 27, no. 4, pp. 1949–1959, Nov. 2012.

[51] P. Dondi, D. Bayoumi, C. Haederli, *et al.*, "Network integration of distributed power generation", *Journal of Power Sources*, vol. 106, no. 2, pp. 1–9, 2002.

[52] J. C. Doyle, B. Francis, and A. Tannenbaum, *Feedback Control Theory*. Macmillan Publishing Co., 1990, p. 202.

[53] J. Driesen and F. Katiraei, "Design for distributed energy resources", *IEEE Power and Energy Magazine*, vol. 6, no. 3, pp. 30–40, May 2008.

[54] W. DU, H. Wang, and H. Cai, "Modelling a grid-connected SOFC power plant into power systems for small-signal stability analysis and control", *European Transactions on Electrical Power*, n/a–n/a, Jan. 2012.

[55] Y. Du, J. Su, M. Mao, *et al.*, "Autonomous controller based on synchronous generator dq0 model for micro grid inverters", in *Proc. of the 8th Int. Conf. on Power Electronics - ECCE Asia*, IEEE, May 2011, pp. 2645–2649.

[56] A El Aroudi, B Robert, and R Leyva, "Sliding mode control of a high voltage DC-DC buck converter", in *Proc. of the European Conference onCircuit Theory and Design*, vol. 3, 2005.

[57] S. Elloumi and E. Braiek, "Robust decentralized control for multimachine power systems-the LMI approach", in *Proc. of the IEEE Int. Conf. on Systems, Man and Cybernetics*, vol. vol.6, IEEE, 2002, p. 5.

[58] S. Emamian, M. Hamzeh, K. Paridari, *et al.*, "Robust decentralized voltage control of an islanded microgrid under unbalanced and nonlinear load conditions", in *Proc. of the Int. Conf. on Ind. Tec. (ICIT)*, IEEE, Feb. 2013, pp. 1825–1830.

[59] A. Engler, "Applicability of droops in low voltage grids", *DER journal*, no. 1, pp. 1–5, 2005.

[60] ENTSO-E, “Network Code for Requirements for Grid Connection Applicable to all Generators”, Tech. Rep., 2012.

[61] D. C. Erb, O. C. Onar, and A. Khaligh, “Bi-directional charging topologies for plug-in hybrid electric vehicles”, in *Proc. of Applied Power Electronics Conference and Exposition (APEC)*, IEEE, Feb. 2010, pp. 2066–2072.

[62] A. Etxeberria, I. Vechiu, H. Camblong, *et al.*, “Comparison of three topologies and controls of a hybrid energy storage system for microgrids”, *Energy Conversion and Management*, vol. 54, no. 1, pp. 113–121, Feb. 2012.

[63] F. Freijedo, A. Vidal, A. G. Yepes, *et al.*, “Tuning of Synchronous-Frame PI Current Controllers in Grid-Connected Converters Operating at a Low Sampling Rate by MIMO Root Locus”,

[64] A. M. Gee, F. V. Robinson, and R. W. Dunn, “Analysis of Battery Lifetime Extension in a Small-Scale Wind-Energy System Using Supercapacitors”, vol. PP, no. 99, pp. 1–10, 2013.

[65] H. Geng, D Xu, B. Wu, *et al.*, “Active Damping for PMSG-Based WECS With DC-Link Current Estimation”, *IEEE Transactions on Industrial Electronics*, vol. 58, no. 4, pp. 1110–1119, 2011.

[66] J. M. Guerrero, M. C. Chandorkar, T.-l. Lee, *et al.*, “Advanced Control Architectures for Intelligent Microgrids—Part I: Decentralized and Hierarchical Control”, *IEEE Transactions on Industrial Electronics*, vol. 60, no. 4, pp. 1254–1262, Apr. 2013.

[67] J. M. Guerrero, L. García de Vicuña, J. Matas, *et al.*, “A wireless controller to enhance dynamic performance of parallel inverters in distributed generation systems”, *IEEE Transactions on Power Electronics*, vol. 19, no. 5, pp. 1205–1213, Sep. 2004.

[68] ——, “Output Impedance Design of Parallel-Connected UPS Inverters With Wireless Load-Sharing Control”, *IEEE Transactions on Industrial Electronics*, vol. 52, no. 4, pp. 1126–1135, 2005.

[69] J. M. Guerrero, P. C. Loh, T.-l. Lee, *et al.*, “Advanced Control Architectures for Intelligent Microgrids—Part II: Power Quality, Energy Storage, and AC/DC Microgrids”, *IEEE Transactions on Industrial Electronics*, vol. 60, no. 4, pp. 1263–1270, 2013.

[70] J. M. Guerrero, J. Matas, L. García De Vicuña, *et al.*, "Wireless-Control Strategy for Parallel Operation of Distributed-Generation Inverters", *IEEE Transactions on Industrial Electronics*, vol. 53, no. 5, pp. 1461–1470, 2006.

[71] J. M. Guerrero, J. C. Vázquez Quintero, J. Matas, *et al.*, "Control Strategy for Flexible Microgrid Based on Parallel Line-Interactive UPS Systems", *IEEE Transactions on Industrial Electronics*, vol. 56, no. 3, pp. 726–736, Mar. 2009.

[72] J. M. Guerrero, J. C. Vázquez Quintero, J. Matas, *et al.*, "Hierarchical control of droop-controlled AC and DC microgrids - A general approach toward standardization", *IEEE Transactions on Industrial Electronics*, vol. 58, no. 1, pp. 158–172, 2011.

[73] F. Guo, C. Wen, J. Mao, *et al.*, "Distributed Secondary Voltage and Frequency Restoration Control of Droop-Controlled Inverter-Based Microgrids", *IEEE Transactions on Industrial Electronics*, vol. 0046, no. c, pp. 1–1, 2014.

[74] F. Habibi, A. H. Naghshbandy, and H. Bevrani, "Robust voltage controller design for an isolated Microgrid using Kharitonov's theorem and D-stability concept", *International Journal of Electrical Power & Energy Systems*, vol. 44, no. 1, pp. 656–665, Jan. 2013.

[75] L. Harnefors and H.-P. Nee, "Model-based current control of AC machines using the internal model control method", vol. 34, no. 1, pp. 133–141, 1998.

[76] N. D. Hatziargyriou, H. Asano, R. Iravani, *et al.*, "Microgrids: An Overview of Ongoing Research, Development, and Demonstration Projects", *IEEE power & energy magazine*, p. 17, 2007.

[77] N. D. Hatziargyriou, N. Jenkins, G Strbac, *et al.*, "Microgrids - Large Scale Integration of Microgeneration to Low Voltage Grids", in *CIGRE C6-309*, 2006, Cigre 2006.

[78] N. D. Hatziargyriou, S. A. Papathanassiou, and M. P. Papadopoulos, "Decision trees for fast security assessment of autonomous power systems with a large penetration from renewables", *IEEE Transactions on Energy Conversion*, vol. 10, no. 2, pp. 315–325, 1995.

[79] W. House. (2012). Department of energy, [Online]. Available: `https://www.whitehouse.gov/omb/factsheet\_department\_energy/` (visited on Apr. 16, 2015).

[80] A. Saez-de Ibarra, A. Milo, H. Gaztanaga, *et al.*, "Analysis and comparison of battery energy storage technologies for grid applications", in *PowerTech (POWERTECH), 2013 IEEE Grenoble*, 2013, pp. 1–6.

[81] C. . IEEE Standards Coordinating, "Application Guide for IEEE Std 1547, IEEE Standard for Interconnecting Distributed Resources with Electric Power Systems", Tech. Rep. April, 2009, p. 219.

[82] L. Igualada-González, C. Corchero-Garcia, and M. Cruz-Zambrano, "Sistema de gestión energético óptimo para edificios inteligentes con sistemas de generación renovable integrados", in *Proc. of I Congreso de Edificios Inteligentes*, 2013, n.a.

[83] IMERGY. (2015). Microgrid project, [Online]. Available: `http://www.imergy.com/blog/2015/2/chabot-las-positas-community-college-district-imergy-power-systems-and-geli-awarded-cec-grant-to-provide-energy-storage-technology-for-las-positas-college-microgrid-project` (visited on Apr. 13, 2015).

[84] F. A. Inthamoussou, R. J. Mantz, and H. D. Battista, "Flexible power control of fuel cells using sliding mode techniques", *Journal of Power Sources*, vol. 205, no. 0, pp. 281–289, 2012.

[85] S. D. G. Jayasinghe and D. M. Vilathgamuwa, "Flying supercapacitors as power smoothing elements in wind generation", *IEEE Transactions on Industrial Electronics*, vol. 60, no. 7, pp. 2909–2918, 2013.

[86] Y. Jia, J. Zhao, and X. Fu, "Direct grid current control of LCL-filtered grid-connected inverter mitigating grid voltage disturbance", *IEEE Transactions on Power Electronics*, vol. 29, no. 3, pp. 1532–1541, 2014.

[87] H. Jiang, H. Cai, J. F. Dorsey, *et al.*, "Toward a globally robust decentralized control for large-scale power systems", *IEEE Transactions on Control Systems Technology*, vol. 5, no. 3, pp. 309–319, May 1997.

[88] H. Jiayi, J. Chuanwen, and X. Rong, "A review on distributed energy resources and MicroGrid", *Renewable and Sustainable Energy Reviews*, vol. 12, no. 9, pp. 2472–2483, Dec. 2008.

[89] H. Jung, H. Wang, and T. Hu, “Control design for robust tracking and smooth transition in power systems with battery/supercapacitor hybrid energy storage devices”, *Journal of Power Sources*, vol. 267, pp. 566–575, 2014.

[90] A. Kahrobaeian and Y. A.-R. I. Mohamed, “Suppression of Interaction Dynamics in DG Converter-Based Microgrids Via Robust System-Oriented Control Approach”, *IEEE Transactions on Smart Grid*, vol. 3, no. 4, pp. 1800–1811, Dec. 2012.

[91] R. M. Kamel, A. Chaouachi, and K. Nagasaka, “Wind power smoothing using fuzzy logic pitch controller and energy capacitor system for improvement Micro-Grid performance in islanding mode”, *Energy*, vol. 35, no. 5, pp. 2119–2129, May 2010.

[92] K Kankanamge and N Kularatna, “Improving the End-to-End Efficiency of DC-DC Converters Based on a Supercapacitor-Assisted Low-Dropout Regulator Technique”, vol. 61, no. 1, pp. 223–230, 2014.

[93] F. Katiraei and R. Iravani, “Power Management Strategies for a Microgrid With Multiple Distributed Generation Units”, *IEEE Transactions on Power Systems*, vol. 21, no. 4, pp. 1821–1831, Nov. 2006.

[94] ——, “Small-signal dynamic model of a micro-grid including conventional and electronically interfaced distributed resources”, *Generation, Transmission and Distribution*, vol. 1, no. 3, pp. 369–378, 2007.

[95] F. Katiraei, R. Iravani, N. D. Hatziargyriou, *et al.*, “Microgrids management”, *IEEE Power and Energy Magazine*, vol. 6, no. 3, pp. 54–65, May 2008.

[96] H. J. Khasawneh and M. S. Illindala, “Battery cycle life balancing in a microgrid through flexible distribution of energy and storage resources”, *Journal of Power Sources*, vol. 261, no. 0, pp. 378–388, 2014.

[97] Z. Kremens and M. Labuzek, “Load flow analysis incorporating frequency as a state vector variable”, *Ninth International Conference on Harmonics and Quality of Power. Proceedings (Cat. No.00EX441)*, vol. 2, pp. 526–530, 2000.

[98] N Kroutikova, C. Hernandez-Aramburo, and T. C. Green, “State-space model of grid-connected inverters under current control mode”, *IET Electric Power Applications*, vol. 1, no. 3, p. 329, 2007.

[99] P. Kundur, *Power System Stability and Control.* McGraw-Hill Professional, 1994, p. 1176.

[100] A Kuperman, U Levy, J Goren, *et al.*, “Battery Charger for Electric Vehicle Traction Battery Switch Station”, *IEEE Transactions on Industrial Electronics*, vol. 60, no. 12, pp. 5391–5399, Dec. 2013.

[101] R. H. Lasseter, “Microgrids [distributed power generation]”, in *Proc. of the IEEE Power Engineering Society Winter Meeting. Conference Proceedings*, vol. 1, IEEE, 2001, pp. 146–149.

[102] A. Laub, M. Heath, C. Paige, *et al.*, “Computation of system balancing transformations and other applications of simultaneous diagonalization algorithms”, *IEEE Transactions on Automatic Control*, vol. 32, no. 2, pp. 115–122, Feb. 1987.

[103] Y Levron, J. M. Guerrero, and Y Beck, “Optimal Power Flow in Microgrids With Energy Storage”, vol. 28, no. 3, pp. 3226–3234, 2013.

[104] J. Li and M. A. Danzer, “Optimal charge control strategies for stationary photovoltaic battery systems”, *Journal of Power Sources*, vol. 258, no. 0, pp. 365–373, 2014.

[105] N. W. a. Lidula and a. D. Rajapakse, *Microgrids research: A review of experimental microgrids and test systems*, 2011.

[106] X. Liu, P. C. Loh, P. Wang, *et al.*, “A Direct Power Conversion Topology for Grid Integration of Hybrid AC/DC Energy Resources”, vol. 60, no. 12, pp. 5696–5707, 2013.

[107] Z. Liu, J. Liu, and Y. Zhao, “A unified control strategy for three-phase inverter in distributed generation”, *IEEE Transactions on Power Electronics*, vol. 29, no. 3, pp. 1176–1191, 2014.

[108] J. Löfberg, “YALMIP : A Toolbox for Modeling and Optimization in MATLAB”, in *Proc. of the CACSD Conference*, Taipei, Taiwan, 2004.

[109] J. Lunze, *Feedback Control of Large-Scale Systems*, Prentice-H, M. J. Grimble, Ed. Prentice-Hall International (UK) ltd, 1992, p. 344.

[110] R. R. Majumder, B. Chaudhuri, A. Ghosh, *et al.*, “Improvement of Stability and Load Sharing in an Autonomous Microgrid Using Supplementary Droop Control Loop”, *IEEE Transactions on Power Systems*, vol. 25, no. 2, pp. 796–808, May 2010.

[111] V. Mariani and F. Vasca, “Stability analysis of droop controlled inverters via dynamic phasors and contraction theory”, in *Control Conference (ECC), 2013 European*, IEEE, 2013, pp. 1505–1510.

[112] V. Mariani, F. Vasca, and J. M. Guerrero, “Dynamic-phasor-based nonlinear modelling of AC islanded microgrids under droop control”, *2014 IEEE 11th International Multi-Conference on Systems, Signals and Devices, SSD 2014*, pp. 1–6, 2014.

[113] F. Marra, G. Yang, C. Traeholt, *et al.*, “A Decentralized Storage Strategy for Residential Feeders With Photovoltaics”, *IEEE Trans. on Smart Grid*, vol. PP, no. 99, pp. 1–8, 2013.

[114] J. G. D. Matos, L. Antonio, D. S. Ribeiro, *et al.*, “Power Control in AC Isolated Microgrids with Renewable Energy Sources and Energy Storage Systems”, *IEEE Transactions on Industrial Electronics*, vol. PP, no. 99, in–press, 2014.

[115] A. Mehrizi-Sani and R. Iravani, “Potential-Function Based Control of a Microgrid in Islanded and Grid-Connected Modes”, vol. 25, no. 4, pp. 1883–1891, 2010.

[116] M. Meiqin, L. Chang, and D. Ming, “Integration and intelligent control of micro-grids with multi-energy generations: A review”, in *2008 IEEE International Conference on Sustainable Energy Technologies*, IEEE, Nov. 2008, pp. 777–780.

[117] Y. A.-R. I. Mohamed and E. F. El-Saadany, “Adaptive Decentralized Droop Controller to Preserve Power Sharing Stability of Paralleled Inverters in Distributed Generation Microgrids”, *IEEE Transactions on Power Electronics*, vol. 23, no. 6, pp. 2806–2816, Nov. 2008.

[118] Y. A.-R. I. Mohamed and A. a. Radwan, “Hierarchical Control System for Robust Microgrid Operation and Seamless Mode Transfer in Active Distribution Systems”, *IEEE Transactions on Smart Grid*, vol. 2, no. 2, pp. 352–362, Jun. 2011.

[119] A. Mohd, E. Ortjohann, D. Morton, *et al.*, “Review of control techniques for inverters parallel operation”, *Electric Power Systems Research*, vol. 80, no. 12, pp. 1477–1487, Dec. 2010.

[120] D. B. Murray, J. G. Hayes, D. L. O’Sullivan, *et al.*, “Supercapacitor Testing for Power Smoothing in a Variable Speed Offshore Wave Energy Converter”, *IEEE Journal of Oceanic Engineering*, vol. 37, no. 2, pp. 301–308, Apr. 2012.

[121] C. Nichita, D. Luca, B. Dakyo, *et al.*, “Large band simulation of the wind speed for real time wind turbine simulators”, *IEEE Transactions on Energy Conversion*, vol. 17, no. 4, pp. 523–529, Dec. 2002.

[122] G. G. Oggier, G. O. Garcia, and A. R. Oliva, “Modulation strategy to operate the dual active bridge DC-DC converter under soft switching in the whole operating range”, vol. 26, no. 4, pp. 1228–1236, 2011.

[123] D. E. Olivares, A. Mehrizi-Sani, A. H. Etemadi, *et al.*, “Trends in microgrid control”, *IEEE Transactions on Smart Grid*, vol. 5, no. 4, pp. 1905–1919, 2014.

[124] J. A. Peças Lopes, C. L. Moreira, and A. G. Madureira, “Defining Control Strategies for MicroGrids Islanded Operation”, *IEEE Transactions on Power Systems*, vol. 21, no. 2, pp. 916–924, May 2006.

[125] J. Pegueroles-Queralt, F. D. Bianchi, and O. Gomis-Bellmunt, “A Power Smoothing System Based on Supercapacitors for Renewable Distributed Generation”, *IEEE Transactions on Industrial Electronics*, vol. 62, no. 1, pp. 343 –350, 2014.

[126] J. Pegueroles-Queralt, L. Igualada-González, C. Corchero-Garcia, *et al.*, “Coordination of control and energy management methods for microgrid systems”, in *Proc. of the 5th IEEE PES Innovative Smart Grid Technologies (ISGT)*, F. Maurice, Ed., 2014, in–press.

[127] L. F. A. Pereira, J. V. Flores, G. Bonan, *et al.*, “Multiple Resonant Controllers for Uninterruptible Power Supplies—A Systematic Robust Control Design Approach”, *IEEE Transactions on Industrial Electronics*, vol. 61, no. 3, pp. 1528–1538, Mar. 2014.

[128] W. Perruquetti and J. P. e. Barbot, *Sliding Mode Control in engineering.* Marcel Dekker, 2002.

[129] T. Petru and T. Thiringer, “Modeling of wind turbines for power system studies”, *IEEE Transactions on Power Systems*, vol. 17, no. 4, pp. 1132–1139, Nov. 2002.

[130] E. Planas, A. Gil-de Muro, J. Andreu, *et al.*, “General aspects, hierarchical controls and droop methods in microgrids: A review”, *Renewable and Sustainable Energy Reviews*, vol. 17, pp. 147–159, Jan. 2013.

[131] N. Pogaku, M. Prodanovic, and T. C. Green, “Modeling, analysis and testing of autonomous operation of an inverter-based microgrid”, *IEEE Transactions on Power Electronics*, vol. 22, no. 2, pp. 613–625, 2007.

[132] M. Popov, H. Karimi, H. Nikkhajoei, *et al.*, “Modeling, control and islanding detection of microgrids with passive loads”, in *Proc. of the 14th International Power Electronics and Motion Control Conference EPE-PEMC 2010*, IEEE, Sep. 2010.

[133] M. Prodanovic and T. C. Green, “High-Quality Power Generation Through Distributed Control of a Power Park Microgrid”, *IEEE Transactions on Industrial Electronics*, vol. 53, no. 5, pp. 1471–1482, Oct. 2006.

[134] A. Purvins and M. Sumner, “Optimal management of stationary lithium-ion battery system in electricity distribution grids”, *Journal of Power Sources*, vol. 242, no. 0, pp. 742–755, 2013.

[135] H. Qian, J. Zhang, and W. Yu, “A High-Efficiency Grid-Tie Battery Energy Storage System”, *IEEE Transactions on Power Electronics*, vol. 26, no. 3, pp. 886–896, Mar. 2011.

[136] D. Rastler, “Electricity Energy Storage Technology Options”, Electric Power Research Institute, Palo Alto, Tech. Rep., 2010, p. 170.

[137] P. K. Ray, S. R. Mohanty, and N. Kishor, “Classification of Power Quality Disturbances Due to Environmental Characteristics in Distributed Generation System”, *IEEE Transactions on Sustainable Energy*, vol. 4, no. 2, pp. 302–313, Apr. 2013.

[138] “Recommended Practices and Requirements for Harmonic Control in Electrical Power Systems”, *IEEE Std 519-1992*, section 10.5, 1993.

[139] REN 21 Steering Commitee, “RENEWABLES 2014 GLOBAL STATUS REPORT”, REN 21, Tech. Rep., 2014, pp. 67–69.

[140] M Reza, D Sudarmadi, F. Viawan, *et al.*, "Dynamic Stability of Power Systems with Power Electronic Interfaced DG", in *2006 IEEE PES Power Systems Conference and Exposition*, IEEE, 2006, pp. 1423–1428.

[141] J. Rocabert, A. Luna, F. Blaabjerg, *et al.*, "Control of Power Converters in AC Microgrids", *IEEE Transactions on Power Electronics*, vol. 27, no. 11, pp. 4734–4749, Nov. 2012.

[142] A. Ruiz-Álvarez, A. Colet-Subirachs, F. Álvarez-Cuevas Figuerola, *et al.*, "Operation of a Utility Connected Microgrid Using an IEC 61850-Based Multi-Level Management System", *IEEE Transactions on Smart Grid*, vol. 3, no. 2, pp. 858–865, 2012.

[143] D. M. Sable, F. C. Lee, and B. O. H. Cho, "A Zero-Voltage-Switching Bidirectional Battery Charger / Discharger for the NASA EOS Satellite", in *Proc. of Applied Power Electronics Conference and Exposition, APEC*, 1992, pp. 614–621.

[144] SAFT. (2011). SYNERION 24M, Medium power lithium-ion module, [Online]. Available: `http://www.saftbatteries.com/`.

[145] R. H. Salim, M. Oleskovicz, and R. Ramos, "Power quality of distributed generation systems as affected by electromechanical oscillations – definitions and possible solutions", *IET Generation, Transmission & Distribution*, vol. 5, no. 11, p. 1114, 2011.

[146] A. S. Satpathy, N. K. Kishore, D Kastha, *et al.*, "Control Scheme for a Stand-Alone Wind Energy Conversion System", vol. PP, no. 99, pp. 1–8, 2014.

[147] J. Schiffer, A. Anta, T. D. Trung, *et al.*, "On power sharing and stability in autonomous inverter-based microgrids", in *2012 IEEE 51st IEEE Conference on Decision and Control (CDC)*, IEEE, Dec. 2012, pp. 1105–1110.

[148] J. Schiffer, D. Goldin, J. Raisch, *et al.*, "Synchronization of droop-controlled microgrids with distributed rotational and electronic generation", in *Proc. of the IEEE 52nd Annual Conference on Decision and Control (CDC)*, 2013, n.a.

[149] J. Schiffer, R. Ortega, A. Astolfi, *et al.*, "Conditions for stability of droop-controlled inverter-based microgrids", *Automatica*, vol. 50, no. 10, pp. 2457–2469, 2014.

[150] J. Schiffer, T. Seel, J. Raisch, *et al.*, “Voltage Stability and Reactive Power Sharing in Inverter-Based Microgrids With Consensus-Based Distributed Voltage Control”, *IEEE Transactions on Control Systems Technology*, pp. 1–1, 2015.

[151] I. Serban and C. Marinescu, “Control strategy of three-phase battery energy storage systems for frequency support in microgrids and with uninterrupted supply of local loads”, *IEEE Transactions on Power Electronics*, vol. 29, no. 9, pp. 5010–5020, 2014.

[152] Siemens, “Microgrids: white paper”, *Refocus*, vol. 7, no. 4, pp. 1–11, Jul. 2011.

[153] J. W. Simpson-Porco, F. Dörfler, and F. Bullo, “Synchronization and power sharing for droop-controlled inverters in islanded microgrids”, *Automatica*, vol. 49, no. 9, pp. 2603–2611, Sep. 2013.

[154] H Sira-Ramírez, “On the dynamical sliding mode control of nonlinear systems”, *Int. Journal of Control*, vol. 57, no. 5, pp. 1039–1061, 1993.

[155] T. Skjellnes, A. Skjellnes, and L. E. Norum, “Load sharing for parallel inverters without communication”, in *Proc. of the Nordic Workshop on Power and Industrial Electronics (NORPIE)*, 2002, pp. 12–14.

[156] A.-I. Stan, M. Swierczynski, D.-I. Stroe, *et al.*, “Lithium ion battery chemistries from renewable energy storage to automotive and back-up power applications — An overview”, in *Optimization of Electrical and Electronic Equipment (OPTIM), 2014 International Conference on*, 2014, pp. 713–720.

[157] K. Strunz, “Developing benchmark models for studying the integration of distributed energy resources”, in *Proc. of the IEEE Power Engineering Society General Meeting*, 2006, p. 2.

[158] J. Sturm, “Using SeDuMi 1.02, a Matlab toolbox for optimization over symmetric cones”, *Optim. Method Softw.*, vol. 11-12, pp. 625–653, 1999.

[159] G. O. Suvire, M. G. Molina, and P. E. Mercado, “Improving the Integration of Wind Power Generation Into AC Microgrids Using Flywheel Energy Storage”, *IEEE Transactions on Smart Grid*, vol. 3, no. 4, pp. 1945–1954, Dec. 2012.

[160] S.-C. Tan, Y. M. Lai, and C. K. Tse, “An Evaluation of the Practicality of Sliding Mode Controllers in DC-DC Converters and Their General Design Issues”, in *Proc. of the 37th IEEE PESC*, 2006, pp. 1–7.

[161] ——, “General Design Issues of Sliding-Mode Controllers in DC-DC Converters”, vol. 55, no. 3, pp. 1160–1174, 2008.

[162] X. Tang, W. Deng, and Z. Qi, “Investigation of the Dynamic Stability of Microgrid”, *Power Systems, IEEE Transactions on*, vol. 29, no. 2, pp. 698–706, 2014.

[163] T. Thringer and J.-A. Dahlberg, “Periodic pulsations from a three-bladed wind turbine”, *IEEE Transactions on Energy Conversion*, vol. 16, no. 2, pp. 128–133, Jun. 2001.

[164] W. F. Tinney and C. E. Hart, “Power Flow Solution by Newton’s Method”, *Power Apparatus and Systems, IEEE Transactions on*, vol. PAS-86, no. 11, pp. 1449–1460, 1967.

[165] L. Trilla, F. D. Bianchi, and O. Gomis-bellmunt, “Optimal Control of VSC for STATCOM Applications”, in *8th PP&PSC (Power Plant and Power System Control) Symposium*, 2012.

[166] V. Utkin, J. Guldner, and J. Shi, *Sliding Mode Control in Electro-Mechanical Systems, Second Edition.* CRC Press, 2009.

[167] V. Valouch, M. Bejvl, P. Simek, *et al.*, “Power Control of Grid Connected Converters Under Unbalanced Voltage Conditions”, *IEEE Transactions on Industrial Electronics*, vol. PP, no. 99, in–press, 2014.

[168] N. Vazquez, C. Hernandez-Aramburo, J. Alvarez, *et al.*, “Sliding mode control for DC-DC converters: a new sliding surface”, in *Proc. of IEEE ISIE*, vol. 1, 2003, pp. 422–426.

[169] S. Vazquez, S. M. Lukic, E. Galvan, *et al.*, “Energy storage systems for transport and grid applications”, *IEEE Transactions on Industrial Electronics*, vol. 57, no. 12, pp. 3881–3895, 2010.

[170] V. Venkatasubramanian, H. Schattler, and J. Zaborszky, “Fast time-varying phasor analysis in the balanced three-phase large electric power system”, *IEEE Transactions on Automatic Control*, vol. 40, no. 11, pp. 1975–1982, 1995.

[171] D. D. Šiljak, *Decentralized Control of Complex Systems.* Boston, MA: Academic Press, 1991, p. 527.

[172] Y. Wang, Z. Lu, Y. Min, *et al.*, “Comparison of the voltage and frequency control schemes for voltage source converter in autonomous microgrid”, in *The 2nd International Symposium on Power Electronics for Distributed Generation Systems*, IEEE, Jun. 2010, pp. 220–223.

[173] E. Wu and P. Lehn, “Digital current control of a voltage source converter with active damping of LCL resonance”, in *Twentieth Annual IEEE Applied Power Electronics Conference and Exposition, 2005. APEC 2005.*, vol. 3, IEEE, 2005, pp. 1642–1649.

[174] W. Yao, M. Chen, J. Matas, *et al.*, “Design and Analysis of the Droop Control Method for Parallel Inverters Considering the Impact of the Complex Impedance on the Power Sharing”, *IEEE Transactions on Industrial Electronics*, vol. 58, no. 2, pp. 576–588, Feb. 2011.

[175] K. Yoshimoto, T. Nanahara, and G. Koshimizu, “New Control Method for Regulating State-of- Charge of a Battery in Hybrid Wind Power/Battery Energy Storage System”, in *2006 IEEE PES Power Systems Conference and Exposition*, vol. 8165, IEEE, 2006, pp. 1244–1251.

[176] A. I. Zecevic and D. D. Šiljak, “Design of Robust Static Output Feedback for Large-Scale Systems”, *IEEE Transactions on Automatic Control*, vol. 49, no. 11, pp. 2040–2044, Nov. 2004.

[177] Q.-c. Zhong, “Robust Droop Controller for Accurate Proportional Load Sharing Among Inverters Operated in Parallel”, *IEEE Transactions on Industrial Electronics*, vol. 60, no. 4, pp. 1281–1290, Apr. 2013.

[178] H. Zhu, J.-S. Lai, A. R. Hefner, *et al.*, “Modeling-based examination of conducted EMI emissions from hard and soft-switching PWM inverters”, vol. 37, no. 5, pp. 1383–1393, 2001.

A

List of Publications

This appendix provides the list of publications both journals and conferences papers derived from the development of the thesis.

Journal articles

[J1] Jordi Pegueroles-Queralt, Fernando D. Bianchi and O. Gomis-Bellmunt, *“Sliding mode control of a lithium battery storage system for microgrid applications"* published to Journal of Power Sources, Volume 272, no. 25, Pages 531-540, December 2014.
DOI: 10.1016/j.jpowsour.2014.08.087.

[J2] Fernando Inthamoussou, Jordi Pegueroles-Queralt and Fernando D. Bianchi, *“Control of a supercapacitor energy storage system for microgrid applications"* published to IEEE Transactions on Energy Conversion, Volume 28, no.3, Pages 690-697, May 2013.
DOI: 10.1109/TEC.2013.2260752.

[J3] Jordi Pegueroles-Queralt, Fernando D. Bianchi and Oriol Gomis-Bellmunt, *“A power smoothing system based on supercapacitors for renewable distributed generation"* published to IEEE Transactions on Industrial Electronics, Volume 62, issue 1, Pages 343-350, May 2014.
DOI: 10.1109/TIE.2014.2327554.

[J4] Jordi Pegueroles-Queralt, Ramon Costa-Castelló and Fernando D. Bianchi, *“Reset control of a power converter"* submitted to IEEE Transactions on Industrial Electronics.

[J5] Jordi Pegueroles-Queralt, Fernando D. Bianchi and O. Gomis-Bellmunt, *“Robust decentralized voltage and frequency control design for islanded microgrids"* submitted to IEEE Transactions on Control Systems Technologies.

Conference articles

[C1] J. Pegueroles-Queralt, F. Bianchi and O. Gomis-Bellmunt, *“Optimal Droop Control for Voltage Source Converters in Islanded Microgrids"*, published to IFAC Power Plant & Power Systems Control conference.
DOI: 10.3182/20120902-4-FR-2032.00099.

[C2] Fernando Inthamoussou, Jordi Pegueroles-Queralt and Fernando Bianchi, *“Control por modo deslizante de un convertidor DC/DC bidireccional para aplicaciones en microredes: Implementación en baja potencia"* presented to RPIC Conference.

[C3] Jordi Pegueroles-Queralt, Cristina Corchero-Garcia, Miquel Cruz-Zambrano, Gerard del-Rosario-Calaf and Lucia Igualada-Gonzalez *“Economical and technical aspects of microgrid systems"* presented in the 5^{th} IEEE PES Innovative Smart Grid Technologies (ISGT) European Conference.
DOI: 10.1109/ISGTEurope.2014.7028836.

Other publications

[O1] Jordi Pegueroles-Queralt and Ignasi Cairo-Molins *“Power Routing Strategies for Dense Electrical Grids"* published in the 11th International Multi-Conference on Systems, Signals & Devices (SSD),
DOI: 10.1109/SSD.2014.6808859.

[O2] Jordi Pegueroles-Queralt, Mike Barnes, Oriol Gomis-Bellmunt, Antony Beddard, Fernando D. Bianchi. *“Small signal analysis of CIGRE HVDC grid"* presented in the 12th Deep Sea Offshore Wind R&D Conference, EERA DeepWind.

[O3] Francisco Díaz-González, Jordi Pegueroles-Queralt, Gerard del Rosario, Albert Ruiz, J.-Ignasi Cairó-Molins, Francesc Girbau-Llistuellay and Oriol Gomis-Bellmunt *“Short-term Energy Storages for Power Quality Improvement in Weak MV Grids with Distributed Renewable Generation"* submitted to the 6th IEEE PES Innovative Smart Grid Technologies (ISGT) European Conference.

[O4] J.-Ignasi Carió-Molins, Jordi Pegueroles-Queralt, Fernando Martin and Maite Hormigo, *“Consideration of DER in the PLC communication channel"* accepted to 23rd International Conference on Electricity Distribution, CIRED.

B

Background in control tools

The aim of this thesis is to apply advanced control techniques to power converters in order to improve the performance of power systems with high power electronics penetration. This section will provide the reader with a general overview of the main control techniques employed throughout this thesis.

B.1. Concepts of robust control

The most elementary feedback control system has three different components:

- a plant G: the subject to be controlled,
- a controller C: the component that generates the plant input signals or signals,
- a sensor F and an actuator: the elements to measure the signal/s to be controlled, and to convert the control signal/s into physical magnitudes, respectively.

Typically, actuators and sensors are lumped in with the plant for simplicity. The elementary control system is depicted in Figure B.1, with the labeled signals having the following interpretation:

- r, reference or command input
- d, external disturbance

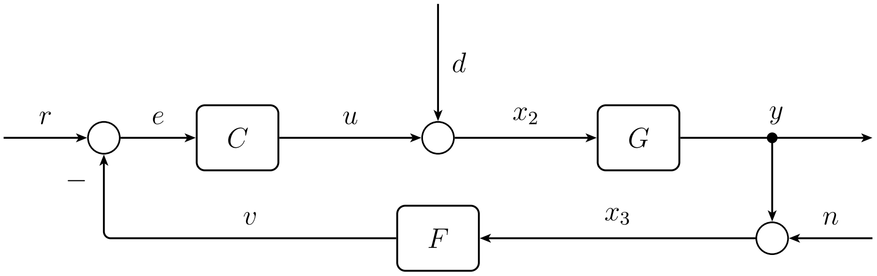

Figure B.1.: Generic feedback control loop.

- n, sensor noise
- y, plant output signal
- u, actuator signal
- v, sensor output
- e, tracking error

The three signals from the outside, r, d, n are called *exogenous inputs.* Based on these signals one can write the equations at the summing junctions as

$$e = r - F\,v, \qquad x_2 = d + C\,u, \qquad x_3 = n + G\,y,$$

which in matrix form are

$$\begin{bmatrix} 1 & 0 & F \\ -C & 1 & 0 \\ 0 & -G & 1 \end{bmatrix} \begin{pmatrix} e \\ x_2 \\ x_3 \end{pmatrix} = \begin{pmatrix} r \\ d \\ n \end{pmatrix}. \tag{B.1}$$

Assuming the system is well-posed, this is that the matrix in (B.1) is nonsingular, it can be obtained the transfer functions from the external inputs as

$$\begin{pmatrix} e \\ x_2 \\ x_3 \end{pmatrix} = \frac{1}{1+GCF} \begin{bmatrix} 1 & -GF & -F \\ C & 1 & -CF \\ PC & G & 1 \end{bmatrix} \begin{pmatrix} r \\ d \\ n \end{pmatrix}.$$

Some of these transfer functions are of important relevance in the design and analysis of control systems. Let L denote the *loop transfer function,*

$$L \triangleq GC.$$

Then, the transfer function from input r to tracking error e is

$$S \triangleq \frac{1}{1+LF},$$

called *sensitivity function.* Let T denote the *complementary sensitivity function*

$$T \triangleq 1 - S = \frac{LF}{1+LF},$$

this is the transfer function from r to y. The idea of the sensitivity function comes from the quantification of how sensitive T is to variations in G. This is, taking to the limit perturbations $\Delta T/T$ relative to perturbations $\Delta G/G$, one gets

$$\lim_{\Delta G \to 0} \frac{\Delta T/T}{\Delta G/G} = \frac{dT}{dG}\frac{G}{T},$$

where the right hand evaluates to S.

Performance of control systems can be specified in terms of the size of certain signals. In order to size signals and system's transfer functions, usually these are measured with the *norms for signals and systems.* The two most common norms are

	2-norm	∞-norm
signal u(t)	$\sqrt{\int_{-\infty}^{\infty} u(t)^2 dt}$,	$\max_t \lvert u(t)\rvert$,
system G(s)	$\lVert G\rVert_2 \triangleq \sqrt{\frac{1}{2\pi}\int_{-\infty}^{\infty} \lvert G(j\omega)\rvert^2 d\omega}$,	$\lVert G\rVert_\infty \triangleq \max_\omega \lvert G(j\omega)\rvert$,

where $\|G\|_\infty$ equals the peak magnitude in the bode diagram of G. With these measuring tools, one can think of a mechanism to specify the performance of a control system. Consider weighting transfer function W_e to bound the maximum error of e for a tracking problem. Then, the nominal performance condition is

$$\|W_e S\|_\infty.$$

For instance, suppose that good performance is known to be achieved if the plot of $|S(\jmath\omega)|$ lies under a certain curve, then it can be expressed as

$$|S(\jmath\omega)| < |W_e(\jmath\omega)|^{-1}, \qquad \forall\omega.$$

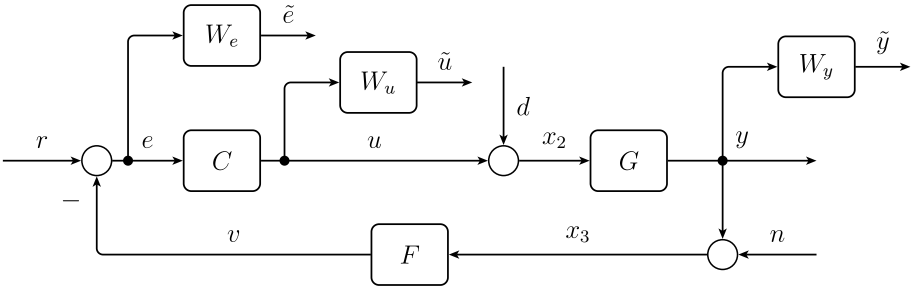

Figure B.2.: Augmented control system with weighting functions.

B.1.1. Robust stability and performance

No physical system can be exactly modelled using a mathematical system. The modelling errors might degrade the control performance. For this reason, the modelling errors should be quantified. Consider Δ a variable transfer function such that $||\Delta||_\infty < 1$. Suppose a nominal plant with transfer function G is perturbed resulting in

$$\tilde{G} = (1 + \Delta W_y)G,$$

where W_y is a weighting function. Weighting functions can be seen in Figure B.2.

Consider $\mathcal{G}$ the set of perturbed plants G. Then, a controller C provides *robust stability* if it provides internal stability for every plant $G \in \mathcal{G}$. Then, it can be proved that C provides robust stability iff

$$\|W_y T\|_\infty < 1.$$

If G is perturbed to $(1 + \Delta W_y)G$, then, S is perturbed to

$$\frac{1}{1 + (1 + \Delta W_y)L} = \frac{S}{1 + \Delta W_y T}.$$

Clearly, the robust performance should be

$$\|W_y T\|_\infty < 1 \qquad \text{and} \qquad \left\| \frac{W_e S}{1 + \Delta W_y T} \right\|_\infty < 1 \qquad \forall \Delta.$$

Then, it can be demonstrated that a necessary and sufficient condition for robust performance is

$$\| |W_e S| + |W_y T| \|_\infty < 1. \tag{B.2}$$

B.1.2. Loopshaping

Loopshaping is a graphical technique for designing a controller to achieve robust performance for a stable and minimum-phase plant. The idea of loopshaping is to construct the loop transfer function L to achieve (B.2) approximately. Then, the controller C can be obtained via

$$C = L/G.$$

For more details on robust control, see *e.g.* [52].

B.2. Sliding mode control

Sliding mode techniques provide powerful control tools, especially for DC/DC converters [34, 56, 160]. In this case, the controller implementation results quite simple and direct because the whole control strategy is basically a commutation law that commands the closing and opening of electronic switches. In the sequel, a brief background is presented and then the proposed SM control is introduced.

Consider a scalar switched system of the form

$$\left\{ \begin{array}{l} \dot{x} = f(x) + g(x)u, \\ y = \mathcal{S}(x), \end{array} \right. \tag{B.3}$$

where x is the vector state, u is the control action and y is the output to be controlled. The function $\mathcal{S}(x)$ is assumed of relative degree 1, i.e. $< \nabla\mathcal{S}, g > \neq 0$ with $\nabla\mathcal{S}$ being the gradient of $\mathcal{S}(x)$ and $< \cdot, \cdot >$ is the dot product. Furthermore, suppose without loss of generality that $< \nabla\mathcal{S}, g >< 0$. Let the switching law be

$$u(x) = \text{sign}(\mathcal{S}(x)) := \left\{ \begin{array}{ll} 1 & \text{if } \mathcal{S}(x) > 0, \\ 0 & \text{otherwise.} \end{array} \right. \tag{B.4}$$

Suppose also that, as a result of this switching law, the reaching condition

$$\mathcal{S}(x)\dot{\mathcal{S}}(x) < 0, \tag{B.5}$$

locally holds around the manifold $\mathcal{S} = \{x | \mathcal{S}(x) = 0\}$. That is, all state trajectories originated close enough to $\mathcal{S}$ will locally point toward it. Then, the control action will switch at (ideally) infinite frequency as the state trajectory crosses the manifold in both directions. This particular mode of operation is called sliding regime or sliding mode. Among other attractive features, SM exhibits robust properties and reduces the order of the system dynamics.

From the invariance conditions $\mathcal{S}(x) = 0$ and $\dot{\mathcal{S}}(x) = 0$, a fictitious smooth equivalent control action can be defined as

$$u_{eq}(x) = -\frac{\langle \nabla \mathcal{S}(x), f(x) \rangle}{\langle \nabla \mathcal{S}(x), g(x) \rangle}. \tag{B.6}$$

By substituting the control action in equation (B.3) with u_{eq}, the SM dynamics is obtained. A necessary condition for u_{eq} to be well defined is that the system has a relative degree of one. The necessary and sufficient condition for SM existence can be written in terms of the equivalent control as follows

$$0 < u_{eq}(x) < 1. \tag{B.7}$$

The equivalent control is a fictitious continuous signal that produces the same effect as the discontinuous control.

A VSS presents another mode of operation: the reaching mode (RM). With no restrictions on the control effort, a continuous control action can be designed to reach the sliding surface with a prescribed reaching dynamics. However, the convergence of all state trajectories to the manifold is generally not ensured for bounded inputs. Sometimes, several changes of structure may occur before the sliding regime is finally established. In this article, we investigate the domain of attraction of the proposed sliding surfaces and the sliding domains, i.e. the regions of the sliding surfaces where SM exists.

In real applications, switching frequency is deliberately bounded to avoid undesirable effects and losses. A simple method consists in incorporating hysteresis to the switching law. A constant amplitude ripple on the controlled output is therefore obtained whereas the switching frequency is kept bounded.

C

Practical considerations of VSC

C.1. VSC modulation and harmonic emission

Most of the residential renewable energy source (RES) are interfaced with the power distribution grid through power electronic converters. Power electronic converters control power flow by modulating voltage and current, to optimally suit user requirements. Typically, RES generates power in form of DC voltage or variable frequency AC voltage, so the power converter is in charge convert this voltage to inject this power to the AC distribution network. Hereafter we will refer to power electronic DC/AC converters as inverters. This section describes the types of converter available to interface RES with the electrical grid. Analytical expressions of the harmonic content due to voltage modulation are also provided.

Inverters have been used in industrial applications since the late 1980s. Semiconductor manufacture development resulted in many power devices such as gate turn-off thyristor (GTO), triac, bipolar transistor (BT), insulated gate bipolar transistor (IGBT) and MOSFETS, suitable for power applications with switching frequencies from few kHz, like GTO to hundreds of kHz, like MOSFETs. Nowadays, the vast majority of power electronic devices for residential applications are based on IGBT or MOSFETS[165]. Inverters have three supply methods: i) voltage source, ii) current source, and iii) impedance source. However, in RES applications, only voltage source inverters are considered. Among the DC/AC voltage source converters (VSC), it can be found different topologies:

- Single-phase full-bridge VSC
- Three-phase full-bridge VSC

The election of the VSC topology depends on the power level required by the RES installation. Typically, single-phase VSC covers the power range of hundreds of watt to several kilo-watts. Residential three-phase VSC are rated up to few tens of kilo-watts.

C.1.1. Voltage modulation techniques

The most straightforward modulation technique is the naturally sampled pulse width modulation (PWM). This technique compares a low frequency target reference signal, typically a sinusoid, against a high-frequency carrier waveform. Typically, the carrier waveform is triangular. The crossing of both signals determines pulse generation instant and duration. However, the majority of the commercial converters are controlled using a digital modulation system, where naturally sampled PWM strategies are difficult to implement. To overcome this point, a popular alternative is to implement a regular sampled PWM strategy, where the low frequency reference waveform are sampled and held constant during each carrier interval. These sampled values are compared against the triangular carrier signal to control the switching process of each leg. We define the amplitude modulation index for inverters as

$$M_a = v_o/(V_{DC}),$$

where v_o is the amplitude of fundamental component of the output voltage, and V_{DC} is the amplitude of the DC voltage source, typically referred to as the DC–link voltage . In general, amplitude modulation index M_a is considered smaller than unity, *i.e.* operation is in linear region. We also define the frequency modulation index as

$$M_f = f_{sw}/f_o,$$

where f_{sw} is the switching frequency of the converter and the frequency of the carrier waveform, and f_o is the fundamental frequency of the output voltage.

Single-phase full-bridge VSC

A single-phase full bridge VSC is shown in Figure C.1. Two big capacitors may be used to generate a neutral point N, although it is not strictly necessary. Since the output voltage is no referenced to the neutral point, but is the voltage difference between branches, the effective output voltage can be greater than input DC voltage V_{DC}. However, linear operation limits the output voltage to the DC–link voltage. The modulation of the full-bridge is different from the half-bridge VSC described above. For the modulation of this converter, a reference sinusoidal signal is applied to one branch, and the same reference signal with opposite sign is applied on the other branch. A graphical representation of the PWM generation is shown in Figure C.3.

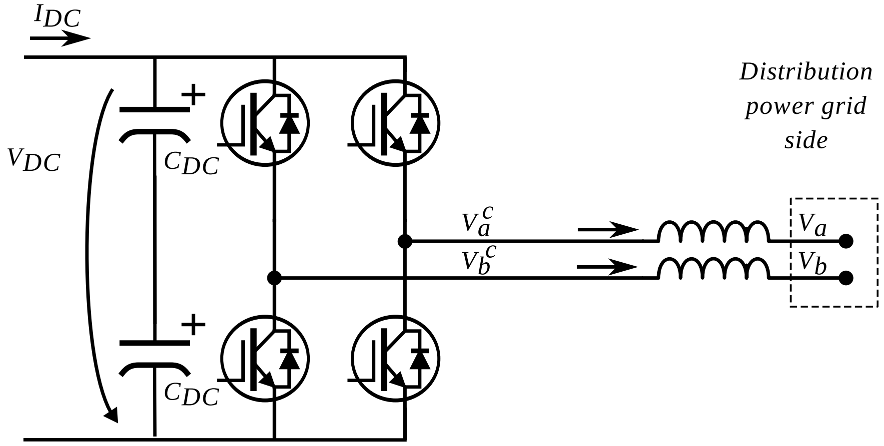

Figure C.1.: Single phase full-bridge VSC.

Single-phase full-bridge VSC are commonly modulated with triangular regular sampled PWM. The complete harmonic solution for symmetrical regular sampled modulation with double-edge carrier (triangular) of a single-phase full-bridge VSC leads to express the output voltage v^c_{ab}, *i.e.* the line to line voltage $v^c_b - v^c_a$, in terms of the harmonic components as

$$v^c_{ab}(t) = \frac{8V_{DC}}{\pi} \sum_{\substack{m=0\\ m>0}}^{\infty} \left(\sum_{\substack{n=1\\ n=-\infty}}^{\infty} (\frac{1}{q} J_n(q\frac{\pi}{2}M_a)) \sin([q+n]\frac{\pi}{2}) \sin(n\frac{\pi}{2}) \right)$$
$$\times \cos(m[\omega_{sw}t+\theta_{sw}] + n[\omega_0 t+\theta_0]),$$

with the parameters as previously defined.

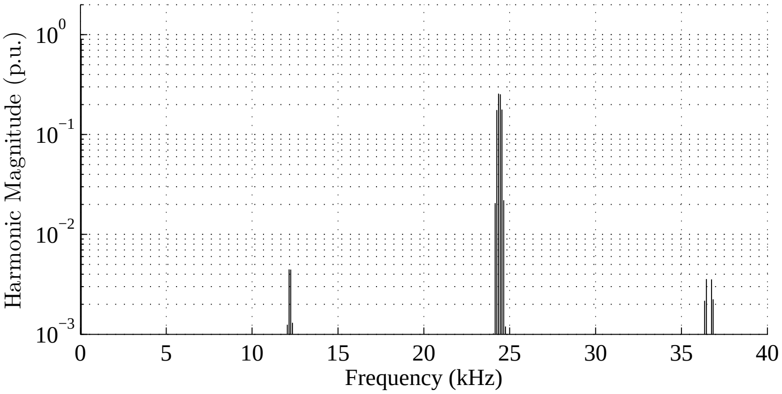

Figure C.2.: Harmonic components of leg-to-leg voltage of a single-phase full-bridge VSC with triangular carrier waveform.

In Figure C.2 it can be seen the harmonic content of the line to line output voltage of a single phase full bridge voltage source converter (VSC). In contrast with the half bridge converter harmonics, the full bridge has a reduced harmonic amplitude due to the cancellation of side band harmonics.

Three-phase full-bridge VSC

A three-phase full-bridge converter is shown if Figure C.4. As in the other topologies, two big capacitors may be used to generate a neutral point N, although it is not strictly necessary. In this converter, six switches are capable to modulate three AC voltage waveforms $v_{a,b,c}$.

Three-phase full-bridge VSC are commonly modulated with symmet-

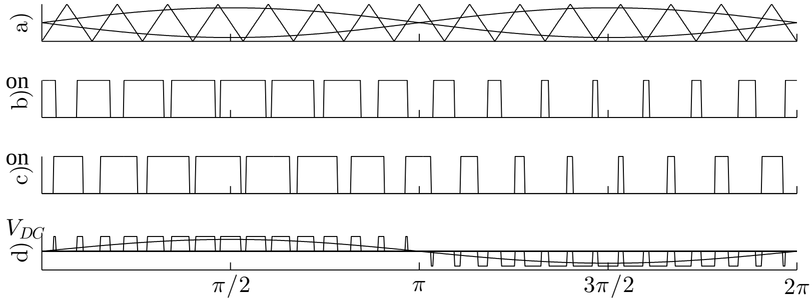

Figure C.3.: Waveforms for a single-phase full-bridge VSC.

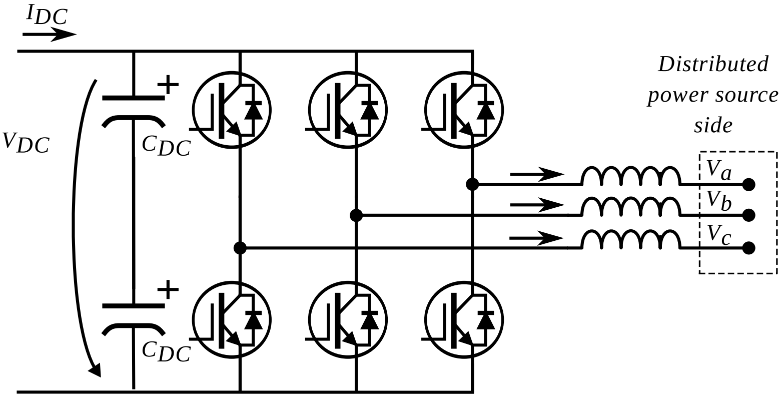

Figure C.4.: Three phase full-bridge VSC.

rical regularly sampled space vector modulation (SVM) . The complete harmonic solution for symmetrical regular sampled SVM for a three-phase full-bridge VSC can be expressed in terms of the harmonic components as

$$\frac{8V_{DC}}{m\pi^2}\left[\begin{array}{l} \frac{6}{\pi}\sin\left([q+n]\frac{\pi}{2}\right)\left\{J_n\left(q\frac{3\pi}{4}M_a\right)+2\cos\left(n\frac{\pi}{6}J_n\left[q\frac{\sqrt{3}\pi}{4}M_a\right]\right)\right\} \\ \frac{1}{n}\sin\left(q\frac{\pi}{2}\right)\cos\left(n\frac{\pi}{2}\right)\sin\left(n\frac{\pi}{6}\right)\left\{J_0\left(q\frac{3\pi}{4}M_a\right)-J_0\left(q\frac{\sqrt{3}\pi}{4}M_a\right)\right\}\Big|_{n\neq 0} \\ +\sum_{\substack{k=1\\k\neq -n}}^{\infty}\left[\begin{array}{l} \frac{1}{n+k}\sin\left([q+k]\frac{\pi}{2}\right)\cos\left([n+k]\frac{\pi}{2}\right)\sin\left([n+k]\frac{\pi}{6}\right) \\ \times\left\{J_k\left(q\frac{3\pi}{4}M_a\right)+2\cos\left([2n+3k]\frac{\pi}{6}\right)J_k\left(q\frac{\sqrt{3}\pi}{4}M_a\right)\right\} \end{array}\right] \\ +\sum_{\substack{k=1\\k\neq n}}^{\infty}\left[\begin{array}{l} \frac{1}{n-k}\sin\left([q+k]\frac{\pi}{2}\right)\cos\left([n-k]\frac{\pi}{2}\right)\sin\left([n-k]\frac{\pi}{6}\right) \\ \times\left\{J_k\left(q\frac{3\pi}{4}M_a\right)+2\cos\left([2n-3k]\frac{\pi}{6}\right)J_k\left(q\frac{\sqrt{3}\pi}{4}M_a\right)\right\} \end{array}\right] \end{array}\right]$$

where $q = m+n(\omega_0/\omega_c)$, $\omega_0 = 2\pi f_0$, $\omega_{sw} = 2\pi f_{sw}$, m is the carrier index, and n is the sideband harmonic order, and J_n is the Bessel function.

The SVM generated reference waveform can be seen in Figure C.5 a). This waveform is compared with the carrier signal, a triangular waveform in this example, and the result is the switching pulses for every IGBT of the VSC. Then, by comparing the pulses of two legs of the converter, it can be obtained the output square voltage waveform of the VSC, as shown in Figure C.5 b).

The theoretical harmonic content of the three phase VSC has been compared with experimental measurements. The results are shown in Figure C.6, where the black lines are the analytical results, and the

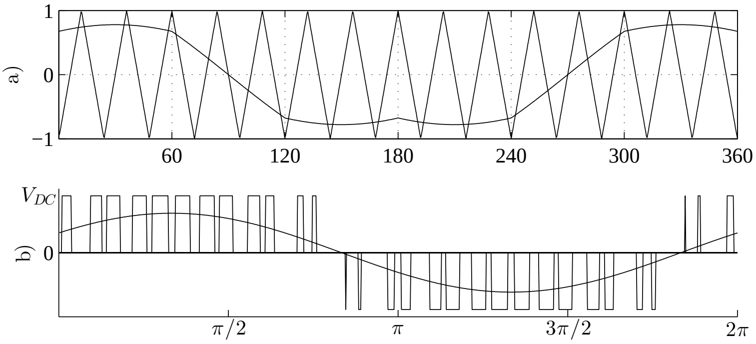

Figure C.5.: Waveforms for a three-phase full-bridge VSC.

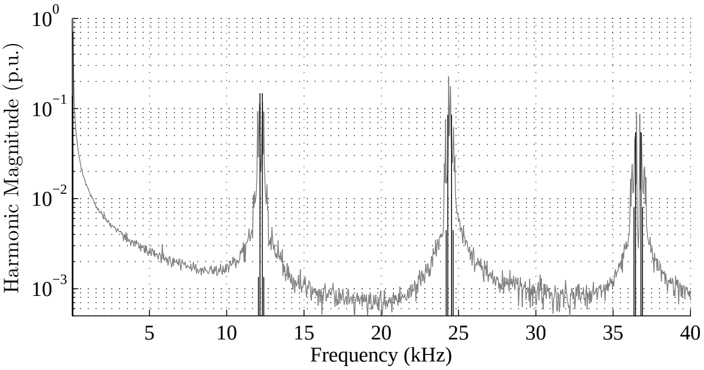

Figure C.6.: Harmonic components of leg-to-leg voltage of a three-phase full-bridge VSC with triangular carrier waveform.

grey line corresponds to the spectrum obtained from the experimental measurement of a 400 V line to line VSC.

C.1.2. Typical output filters

In residential RES applications, VSC are typically interfaced with a single low-frequency inductor with the distribution grid. This output filter is designed to reduce the voltage components at the switching frequency. The output impedance of the power inverter is thus dominated by the output filter.

Although all inductors consist of a coil of wire, many variations on the actual method of device construction exist. The core of low-frequency inductors are often made of stacks of thin steel sheets or laminations oriented parallel to the field, with an insulating coating on the surface, preventing eddy currents between the sheets with the aim of reducing the energy losses. In order to characterize the output filter behavior, the equivalent inductor circuit will be compared with the experimental measurement of a real power electronic converter output filter.

The resistance of the inductor's coils is considered a parasitic component of the inductor impedance and is designated as $R_{parasitic}$. The proximity of the adjacent inductor coils introduces a parasitic capacitance component into the inductor equivalent impedance. This parasitic capacitance, designated as $C_{parasitic}$, increases significantly when space saving winding techniques (such as multiple layers of coils) are employed. The equivalent model can be expressed as a series combination of the element inductance and the parasitic resistance

$$Z_s = j\omega L + R_{parasitic}$$

in parallel with the parasitic capacitance of the inductor

$$Z_p = 1/(j\omega C_{parasitic}),$$

resulting in

$$Z_{VSC} = \frac{j\omega L + R_{para.}}{1 + j\omega^2 L C_{para.} + j\omega R_{para.} C_{para.}}$$

In Figure C.7 it can be seen the comparison between a real 4.6 mH inductor and the previous model with the proper parameter values. In the same figure it can also be seen the impedance for different inductance values.

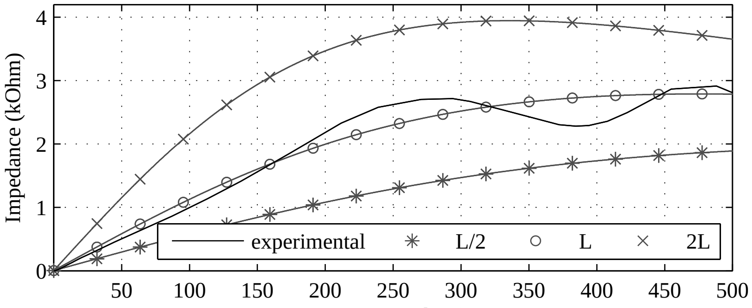

Figure C.7.: Comparison of a real L=4.6 mH VSC output filter and the theoretical model.

D

IREC test facility for microgrids

This section summarizes the technical details of the real elements used throughout this thesis for experimental validation.

D.1. Power electronic converter for experimental tests

The parameters of the power electronics converters used in chapters 4, 5, 6 and 7 are summarized in Table D.1. A picture of the set-up can be seen in Figure D.1.

Parameter	Value	Units	Description
V_{DC}^{ref}	750	V	Nominal DC-link voltage
C_{DC}	2.024	mF	Capacity of the DC-link bus
L_B	4.29	mH	Inductance of the battery branch
L_f	4.66	mH	Inductance of the AC filter
R_f	0.29	Ω	Resistance of the AC filter
$f_{sw_{GSC}}$	12.2	kHz	GSC switching frequency (fixed)
$f_{sw_{ESSC}}$	[7-10]	kHz	ESSC switching frequency (variable)

Table D.1.: Main parameters of the three-phase VSC used for experimental validation.

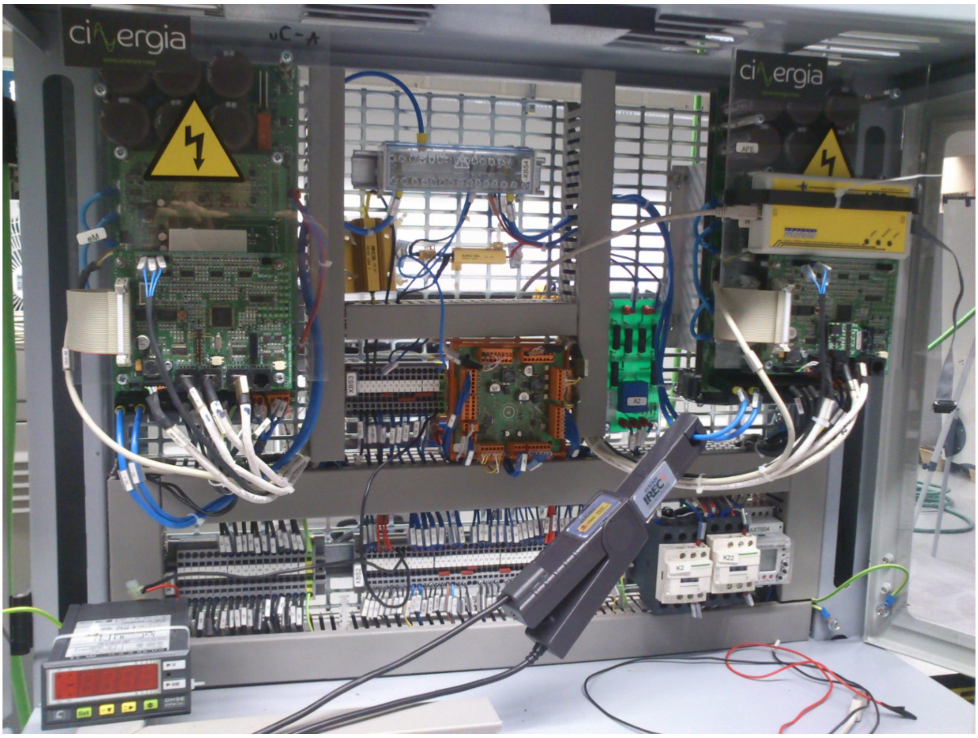

Figure D.1.: Power electronics converters in back-to-back configuration available in IREC microgrid laboratory.

D.2. Li-ion based energy storage system at IREC facilities

The IREC laboratory includes a high power and high capacity energy storage system based on li-ion batteries, which can be seen in Figure D.2. Throughout the development of this thesis, a power converter energy storage system (ESS) has been designed to permit the integration of the Li-ion battery for microgrid operations. The summary of the main figures of the battery are listed in Table D.2.

---

[1] Depth of discharge

Figure D.2.: Picture of a Li-ion battery used throughout the thesis related works.

Parameter	Value	Units	Description
E_B	20	kWh	Nominal capacity of the battery
V_B	250	V	Nominal battery voltage
$V_{B_{\min}}, V_{B_{\max}}$	$[210, 280]$	V	Voltage operation range
$P_{B_{\max}}$	80	kW	Maximum discharge power
Ψ_B	3000	cycles	Nominal cycles at 80% DoD[1]

Table D.2.: Main parameters of IREC laboratory Li-ion battery.

D.3. Supercapacitor based energy storage system at IREC facilities

The IREC laboratory includes a high power and high capacity energy storage system based on supercapacitors, which can be seen in Figure D.3. Throughout the development of this thesis, a power converter ESS has been designed to permit the integration of the supercapacitor bank for microgrid operations. The summary of the main figures of the supercapacitor bank are listed in Table D.3.

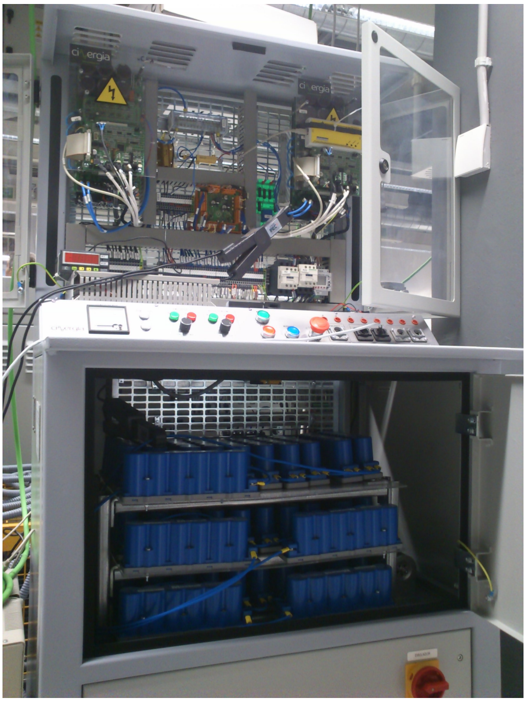

Figure D.3.: Picture of a supercapacitor bank used in diffrent experiments in this thesis.

Parameter	Value	Units	Description
E_{SC}	60	Wh	Nominal capacity of the battery
$V_{SC_{\min}}, V_{SC_{\max}}$	$[250, 500]$	V	Voltage operation range
C_{SC}	1.702	F	Capacity
$I_{SC_{\max}}$	20	A	Maximum current
$P_{SC_{\max}}$	10	kW	Maximum power

Table D.3.: Main parameters of IREC's supercapacitor bank.

Index